5-2013

VIBRATION BASED DAMAGE IDENTIFICATION OF TIME-VARYING DYNAMICAL SYSTEMS

Jie Zhao
jzhao11@utk.edu

To the Graduate Council:

I am submitting herewith a dissertation written by Jie Zhao entitled "VIBRATION BASED DAMAGE IDENTIFICATION OF TIME-VARYING DYNAMICAL SYSTEMS." I have examined the final electronic copy of this dissertation for form and content and recommend that it be accepted in partial fulfillment of the requirements for the degree of Doctor of Philosophy, with a major in Mechanical Engineering.

Hans A. DeSmidt, Major Professor

We have read this dissertation and recommend its acceptance:

J. A. M. Boulet, Seddik M. Djouadi, Xiaopeng Zhao

Accepted for the Council:
Dixie L. Thompson

Vice Provost and Dean of the Graduate School

(Original signatures are on file with official student records.)

Vibration Based

Damage Identification of

Time-varying Dynamical Systems

A Dissertation Presented for

the Doctor of Philosophy

Degree

The University of Tennessee, Knoxville

Jie Zhao

May 2013

ACKNOWLEDGEMENTS

I would like to appreciate the seamless guidance given by my major advisor Dr. Hans A. DeSmidt during my PhD study. Also, I would like to thank the committee members: Dr. J. A. M. Boulet, Dr. Seddik M. Djouadi and Dr. Xiaopeng Zhao for giving me so many insightful suggestions.

This research was supported by a grant from the National Science Foundation (Grant Number: NSF-CMMI-0748022) under the Dynamical Systems Program directed by Dr. Eduardo A. Misawa.

DEDICATION

My Soul Mate

Jingbo Jia

My Parents

Yuewu Zhao & Cuie Wang

My Mother-in-law

Jiangyun Lu

My Grandmother-in-law

Qinying Fang

My adorable son

Jason R. Zhao

ABSTRACT

This thesis develops and explores two new kinds of vibration-based damage identification methodologies suitable for dynamical systems with periodically time-varying coefficients; 1) a Floquet based method (Methodology I) and, 2) a Sideband Frequency Response Function (FRF) method (Methodology II). One important class of dynamical systems where periodic time-varying parametric terms naturally arise is rotordynamic systems. For the case of a flexible shaft-rotor system with multiple open cracks, this thesis explores a new Least Squares damage identification approach based on Floquet theory with iterative eigenvector estimate updating. It is found that this method is able to detect the location and severity of multiple cracks with the assistance of control inputs from an Active Magnetic Bearing (AMB). However, it is also found that this method could not effectively identify the crack angle. To overcome this shortcoming, the new Sideband FRF based methodology is developed which utilizes the measured changes in transfer function magnitude and phase due to structural damage at the primary and side-band frequencies of the damaged periodically time-varying dynamical system. This method provides the advantages of arbitrary interrogation frequency and multiple inputs/outputs which greatly enriches the dataset for damage identification. This damage identification algorithm utilizes an iterative least square approach combined with a Newton-Raphson technique to estimate the damage parameters. The effectiveness of this method is thoroughly explored for a flexible rotor system and a planar truss both with breathing cracks. In each case, damage estimation is performed using time-domain vibration data taken from full nonlinear simulations of the cracked structures. The results

show that this new method successfully estimated the crack depths, locations and angles for the case of multiple simultaneous damages.

TABLE OF CONTENTS

LIST OF TABLES

LIST OF FIGURES

Chapter I

INTRODUCTION

1.1 Background

With the rapid development of modern industry, Rotating machinery is widely used in gas turbine engine, aviation, industrial compressors and various motor devices and plays a very important role in power, aviation, mechanical, chemical engineering and other areas. It is easy to leave initial crack sources, like dents and fissures on the rotating machinery due to equipment installation, maintenance and operation errors. Together with its increasing development towards high speed and power, heavy duty, and long cycle direction, rotor usually runs in a harsh condition. Thus, severe vibration may result in acceleration of crack propagation which will aggravate vibration. Sometimes, severe vibration can even cause rotor breaking and magnificent accident. Usually, transverse cracks may be produced if the rotor runs under long-term switching bending; spiral cracks may be appeared when the rotor was applied strong bending moment and torsion. Rotor's running condition has a straight effect on the energy consumption and operation safety of the entire unit. Therefore, the real-time health monitoring and fault diagnosis are very essential for conducting maintenance, reducing the accidental risk and unplanned downtime, which makes the system efficient, safe, stable and reliable.

In the aspects of damage detection, lots of damage detection techniques have been developed, such as ultrasound, X-ray, magnetic powder inspection, etc., but they are belonged to the category of downtime detection method and not effective for real-time damage detection. Vibration based damage detection methods have been rapidly

developing in recent decades because of its advantage in online health monitoring. Generally, the rotor's faults can be reflected by the abnormal vibration. Engineers are able to get a lot of repeatable and reliable information from the vibration and spectrum analysis. Therefore, the vibration signals can be main parameters of health monitoring and fault diagnosis. In addition, it is easy to implement real-time monitoring and diagnosis by using vibration signal testing/processing methods including time domain, frequency domain, amplitude domain, envelope demodulation and wavelet analysis, etc. Among these methods, time and frequency methods are most widely used. Once the rotor has cracks, structure parameters, i.e. local stiffness, will change and then lead to the change of natural frequency and dynamic characteristics of the entire rotor system. Analyzing these changes of vibration signals and dynamic characteristics could help us to detect damage and diagnose faults of cracked structures.

1.2 State of the Art: Rotor Dynamics

Differential equations of motion of rotor system can be written as:

$$M\ddot{Z} + (C + G)\dot{Z} + KZ = F \tag{1.1}$$

Where Z is the vector of the generalized system coordinates; M is the mass matrix; C is the damping matrix; G gyroscopic matrix: K is stiffness matrix and F is generalized external force acting on the system. During the development of rotor dynamics over the past century, many topics have been studied including critical speed, damped natural frequency (complex eigenvalue), imbalance response, transient response, nonlinear response, instability, parametric excitation, rubbing, bearings and vibration monitoring.

The analysis of disk-shaft coupling vibration analysis is one of the main contents of the

rotor dynamics. Shahab and Tomas [1] used the finite element method and the rotation period to discuss the coupling effects of disk and shaft in a multiple disk-shaft system. Wu and Flowers [2] employed the transformation matrix method to study the coupling effects of the flexible dish-shaft by adding additional items. Sakta et al [3] applied the finite element method to study the vibration characteristics of the flexible disk-shaft system with elastic supports. Wu and Flowers [4] tested and inspected the dynamic behaviors of the elastic plate in a rotor system. Chun and Lee [5] analyzed vibration modes of the rotating elastic blades by using sub-structure synthesis method and the assumed mode method. Loewy R.G. and Khader N. [6] investigated the coupling vibration characteristics of the blades and flexible shaft in a rotating impeller. Imbalanced response of the rotor system is one of the basic problems in rotor dynamics. The studies on the imbalance response mainly focus on the steady-state response with constant rotating speed and transient response with variable rotating speed. The rotor imbalance is one of the most important excitation sources for rotating machinery. Currently, the common methods for rotor balance research include modal balance method, the influence coefficient method, and hybrid method [7-8].

With the increasingly wide application of the high-speed and flexible rotors, the stability of the rotor system has attracted more and more attention. Many factors could be able to affect rotor stability, such as the oil film force, the sealing force, shaft stiffness asymmetry, shaft viscoelastic material, shaft structural damping, and cracked rotor, etc. McLaclan [9] studied the Mathieu equation and built the mathematical foundation for the stability problems of the parametric vibration. Bolton [10] completed the most comprehensive summary on this research branch for previous 15 years and provided a

theoretical foundation for the dynamic stability problem of parameter vibration according to Floquet's[11] concept of dynamic instability region proposed 75 years ago the. Since then, many scholars achieved a large number of fruitful researches in terms of dynamic stability problem of parametric excitation system, especially the dynamic stability of the rotor system under periodic loads. A. Unger [12] analyzed the dynamic stability of simply supported and clamped shaft under periodic loads and obtained 2T periodic solution according to the concept of dynamic instability region defined by the Floquet. J.W. Lund [13] used transfer matrix method to study the imbalanced response of flexible rotor and compared it with the experimental data. In 1970, Ruhl [14] first applied finite element method to study the stability of the rotor system. Then, Booker [15] did the similar work.

Another important topic of rotor dynamics is health monitoring and fault diagnosis of the rotor system. Generally, the main faults of rotating machinery are: initial bending, misalignment, stiffness asymmetry, oil whirl, crack and sealing instability, etc. In past, engineer prevented the machine failures by frequent maintenance, but this is a passive way. In recent years, a lot of damage detection methods have been developed and successfully applied on health monitoring and faults diagnosis. C.A. Papalopoulos [16] studied coupled dynamic response of the Jeffcott rotor with open crack. S.C. Huang [17] studied the lateral Vibration of shaft with breathing cracks and discussed the effects on the steady-state response and amplitude caused by cracks. A.S. Sekkar [18] analyzed the dynamic response of the Jeffcott rotor with open crack under viscoelastic supports and the variation of the bending stress versus rotating speed. Kim at el. [19] and Ji at el. [20] used harmonic balance method and multiple scales method to discuss vibration

characteristics of Jeffcott rotor under nonlinear viscoelastic support, respectively. C.O. Chang [21] studied the vibration response and stability of a slender shaft and rigid disk system while considering the geometric nonlinearity.

1.3 Development of Crack Model

Crack model is the key of dynamic modeling and analysis of cracked structure [22-25]. For the 1D beam structure in the engineering, the common crack models include: the equivalent beam segment model, local flexibility model, continuous beam theory, breathing crack model. Generally, it is assumed that the presence of the cracks only affects structural stiffness distribution and does not result in the change of mass distribution.

(1) Equivalent beam segment model

Equivalent beam segment model assumes that the structural stiffness reduction can be represented by a beam segment. The length of beam segment can be obtained by modal test. Kirmsher [26] and Thomson [27] first proposed this method and studied the vibration characteristics of a notched beam. Subsequently, Isalik [28] studied the free vibration of the cracked concrete beams based on this model. Petroski [29] established static and dynamic equations of a cracked elastic beam. Ku and Chen [30] analyzed the dynamic stability of a damaged shaft-drive system. Wendtland [31] compared the natural frequency changes of the cracked beam with different geometries and boundary conditions through a large number of experiments. In the experiment, he used the artificial notch instead of a real crack. However, this confused the concept of crack and notch. Without considering the singularity on the crack tip, the local flexibility produced

by a notch is usually smaller than that caused by a crack in the same condition. Cawley and Ray [32] pointed out that decreasing rate of the fundamental frequency increases with the gap width. Silva and Gomez [33, 34] gave the further conclusions: the decreasing rate of natural frequency caused by a crack is approximately 2 times of that caused by a notch with a small depth.

Equivalent beam segment model is simple, intuitive and easy to use, but this model has no strict definition on the length of equivalent beam segment. The length needs to be corrected according to the experiment results. In addition, it fails to give the specific crack location and depth in the damage identification process.

(2) Local flexibility model

The local flexibility model comes out with the linear elastic fracture mechanics and stress intensity factor theory. Irwin [35] first studied the local flexibility of cracked structure and successfully linked it with stress intensity factor. The Liebowitz and Ocamura [36-38] calculated local rotary flexibility of the rectangular cross-section beams with transverse cracks and studied the stability Cracked Beam according to the changes of tested bending moments. For those crack types not including in the stress intensity factor manual, the local flexibility can be obtained by calculating the strain energy through numerical methods like multi-dimensional finite element method [39]. Rice and Levy [40] studied the local flexibility in matrix form under axial and bending forces. Dimarogonas [41] gave the method to calculate the local flexibility matrix of cracked beam under multiple loads. He [42, 43] calculated the dynamic response of the Euler beam based on the local flexibility model of fracture mechanics. He [44] also analyzed the coupled vibration of cracked Timoshenko beam under stretching, twisting, bending excitation and gave the

relationship between frequency changes and the crack parameters. Ostachowicz and Krawczuk [45, 46] derived the local flexibility of elastic and elastoplastic crack according to the stress intensity factor.

The advantages of this model are the local flexibility is uniquely determined by the depth of the crack and crack location and depth can be obtained in the damage identification.

(3) Continuous cracked beam theory

Continuous beam theory assumes that the presence of the crack affects the whole distribution of the beam stiffness, rather than the sole crack location. It can be characterized by a continuous function of the stiffness distribution. According to the extended Hu-Washizu generalized variation principle, Christidest and Barr [47, 48] first proposed the theory which assumes that the stress in the crack region decayed exponentially. Shen and Pierre [49, 50] used similar method to study Euler beam with bilateral and unilateral crack. Chondrost and Dimarogonas [51-57] established continuous displacement distribution function of cracked beam according to fracture mechanics and derived the differential control equation for longitudinal, lateral and torsional vibration combining extended Hu-Washizu generalized variation principles. Carneiro [58] derived the continuous equations of motion of cracked Timoshenko beam. Swamidas and Yang [59, 60] assumed strain energy distribution function as a particular function and obtained the equivalent continuous bending stiffness function along the longitudinal direction of the beam according to the energy balance relation in fracture mechanics.

Relative to equivalent beam segment and local flexibility model, the theory is more suitable for the problems of modal extension, variable boundary conditions as well as

lateral and torsional coupled vibration. However, the derivation of vibration equations is very complicated using this theory. Moreover, the stiffness distribution results in the inconvenience of finite element analysis.

(4) Breathing crack model

For the previous models, cracks were assumed to be open. For the real vibration, crack is not always open. It opens and closes periodically due to the gravity or other factors. Thus, the structural stiffness varies with the time and the dynamic response of the structure exhibits nonlinear characteristics. There are several breathing crack model:

a) Bilinear model: In this model, the crack only have two states: fully open and fully closed. It assumes that the opening and closing of the cracks and the shaft stiffness changes can be represented by step function which has the following expression:

$$f(\Omega t)=\begin{cases}1 & 2k\pi-\pi/2\le\Omega t\le 2k\pi+\pi/2\\ 0 & 2k\pi+\pi/2\le\Omega t\le 2k\pi+3\pi/2\end{cases}\qquad (k=0,1,2\cdots) \tag{1.2}$$

Fourier series expansion of the equation (1.2) is:

$$f(\Omega t)=\frac{1}{2}+\frac{1}{2\pi}\cos(\Omega t)-\frac{2}{3\pi}\cos(3\Omega t)+\frac{2}{5\pi}\cos(5\Omega t)-\frac{2}{7\pi}\cos(7\Omega t)+\cdots \tag{1.3}$$

Crack stiffness matrix in the fixed coordinate system is:

$$K=\begin{bmatrix}k_0 & 0\\ 0 & k_0\end{bmatrix}-\frac{1}{2}f(\Omega t)\Delta k\begin{bmatrix}1+\cos(2\Omega t) & \sin(2\Omega t)\\ \sin(2\Omega t) & 1-\cos(2\Omega t)\end{bmatrix} \tag{1.4}$$

Where k_0 is the bending stiffness of nominal shaft; Δk is the maximum decreasing amount of shaft stiffness along the crack direction, Ω is the rotating speed.

Ibrahim et al [61] used bilinear spring model and numerical integration method and verified the difference between the experimental frequency Gudmunson [39] found and the results obtained by open crack model. Pugno and Ruotolo [62, 63] studied

the dynamic response of breathing cracked beam under harmonic excitation. Chondros [64, 65] and Shen [66] analyzed the vibration frequency of cracked beam using bilinear model and continuous crack beam theory.

b) The cosine wave model: This model reflects the transition between the crack opening and closing, which has the following expression:

$$f(\Omega t) = \frac{1}{2}[1 + \cos(\Omega t)] \tag{1.5}$$

Cheng [67] analyzed the dynamic response of a 1-DOF cracked beam using cosine wave model. Douka and Loutridis [68, 69] proposed a time-frequency signal processing damage detection method based on the simulation results of Cheng's cracked beam model.

c) Contact model: compared with the two previous approaches, contact model is closer to the real situation. Kisa and Brandon [70] used two-dimensional finite element analysis to calculate the additional stiffness of the crack surface. Andreaus [71] and Kogl et al [72] analyzed the non-linear characteristics of cracked beam under harmonic excitation using frictionless contact model. Hirose and Achenbach [73] employed the boundary element method to obtain the high-order harmonics caused by the crack contact.

Existing research results show that the natural frequency of beam with a breathing crack locates between that of nominal beam and that of beam with an equal-depth open crack. Sub-harmonic and super-harmonic components usually appear in the dynamic response, which is especially obvious under harmonic excitation. The nonlinear behavior of breathing crack model has a very important meaning for engineering, especially for the application of damage identification method. However, the model has issues about

computational complexity of the dynamic response, the nonlinear weakness in the real structures and identification difficulty.

1.4 Cracked Rotor Dynamics Overview

1.4.1 Cracked Shaft Vibration Analysis Methods

In this section, several analysis methods for cracked shaft vibration are introduced.

(1) Semi-analytical

The method assumes that the cracked beam breaks at the crack location and defines the displacements of beam sections as the analytical function with undetermined coefficients. By satisfying the compatibility and equilibrium conditions, vibration equations for different boundary conditions can be obtained. Chondros [57], Rizos [76], Ostachowicz [59], Narkis [77], Maiti [74, 78-80], Kasper [81] analyzed different types of cracked beam vibration problem using this method.

(2) The transfer matrix method

When the beam has multiple cracks, semi-analytical method will result in high-order frequency equations while the transfer matrix method is able to avoid this problem. Lin [82], Khiem [83, 84], Patil [75] used this method in their research.

(3) Dynamic Stiffness Matrix Method

Similar with the finite element method, this method uses dynamic stiffness matrix with a frequency parameter to solve the higher order frequencies. The dynamic stiffness matrix of nominal beam can be obtained by the analytical solution as well as assumed displacement method. Khiem [85, 86] used this method to investigate the free vibration and damage identification problem of multi-cracked beam. Viola [87, 88] studied the

vibration characteristics of T-shaped cross-section beam and cracked Timoshenko beam with axial loading.

(4) Finite element method

The finite element method is widely used in the dynamic analysis of the cracked beam. Gounaris and Dimarogonas [89] proposed a cracked beam element with full degree-of-freedom including tensile, bending and torsional directions. Chinchalkar [90] analyzed the vibration characteristics of a cracked beam with variable cross-section using crack element and variable cross-section beam element. Kisa, Brandon [70, 91-94] applied substructure method and finite element method to study the vibration characteristics of the homogeneous beam and the composite beam with rectangular/circular cross-section, and with a single crack/multiple cracks.

1.4.2 Cracked Shaft Vibration

(1) Linear torsional vibrations of cracked shafts

Papadopoulos and Dimarogonas [95, 96] studied the torsional vibration response of the single-disk rotor with a transverse crack. They concluded that the frequency response becomes stronger with the increase of the crack depth and produces a certain degree of harmonic resonance. The crack location and depth can be determined by measuring the first three natural frequencies of nominal and damaged rotor. In addition, cracks lead to the coupling vibration between axial and lateral directions which can be used in damage detection.

(2) Stability analysis of cracked shafts

Papadopoulos and Dimarogonas [95] and Huang [97] used Floquet theory to study the dynamic stability of a cracked rotor. The results show that the system is unstable when the rotating speed is $2\Omega/n$ (n=1, 2, 3, 4…) where Ω is the critical speed. The angle between the crack direction and the eccentricity has no impact on the stability of the system. Lee [98] considered the effect of nonlinear eddy and found the system only has one unstable zone (near Ω), and the angle has a great influence on the stability of the system.

(3) Transient response of cracked shafts

Prabhu [99] and Zheng [100] studied the transient response of the cracked rotor. They pointed out that the forced vibration response of the cracked rotor includes transient component, which can be used to identify cracks. Sekhar at el. [101, 102] monitored the transient vibration response when the cracked shaft passed through its critical speed. Monitoring the transient response during passage through the critical speed could give an indication of crack existence.

(4) Damped vibrations of cracked shafts-thermal effects

The material damping in a cracked structure increases due to the reciprocity of the temperature rise and strain. This increase is correlated to the vibration mode and the magnitude of the existing crack in the structure by Panteliou et al. [103]. The analytical determination of the dynamic characteristics of the cracked structure yielded the damping factor of the bar, the material damping factor, and a good correlation of crack depth with the damping factor. Experimental results on cracked bars are in good correlation with the analysis. Similar results are presented by Zhang and Testa in [104].

Bachschmid et al. [105] introduced an original, simplified model that allows cracks of various shapes to be modeled and thermal stresses to be taken into account, as they may influence the opening and closing mechanism. The proposed method was validated by 3D FEM analysis and by an equivalent cracked beam. In both cases, there was a good agreement in the results.

Bovsunovsky [106], in an experimental investigation of specimens with an edge fatigue crack loaded in bending (mode I), concluded that the energy dissipation in a non-propagating crack is caused mainly by the elastoplastic area around the crack tip and practically is not related to the friction between the crack surfaces. They stated that the level of energy dissipation in a crack is determined uniquely as a function of the cyclic (nominal) SIF range and is not affected by the initial level of damping in an intact specimen. This function can be used for the prediction of damping change caused by crack initiation and growth and for damage diagnostics based on the prediction of damping change. The closing of the crack-introduced contact effects are presented by Kisa and Brandon [70].

(5) Vibrations of cracked structures in viscous liquid

When a cracked shaft is rotating in a viscous fluid, then there is a change in the critical speeds and the amplitudes of vibration. Behera et al. [107] and Parhi and Behera [108, 109] analyzed the effect of the fluid using the Navier-Stokes equations. The damping effect and virtual mass effect are also taken into account through the Navier-Stokes equation. Gounaris et al. [110] applied the fail-safe criterion to a floating, ship-like, Timoshenko beam moving forward in waves, including both hydrodynamic and structural damping. The nominal stress near the crack, needed as input to the Paris equation for the

evaluation of the cycles required to failure, is computed assuming known values for the SIF. The resulting fail-safe diagrams indicate the effect of various parameters of the problem.

1.5 Damage Detection Methodologies

Currently, vibration based damage identification methods can be classified in several ways, such as characteristic parameters, time/frequency domain, linear/nonlinear and so on.

1.5.1 Identification based on Characteristic Parameters

Any structure can be considered as a dynamical system with structural parameters such as stiffness, mass and damping, etc. Structural damage will result in the change of structural parameters as well as modal parameters and the frequency response function. Hence, the modal parameters (frequencies, mode shapes and damping) can be seen as a sign of structural damage. Choosing the characteristic parameters is a key step for direct identification method based on the characteristic parameters. Here lists some dynamic characteristic parameters which are commonly used:

(1) Frequency, including inherent frequency and anti-resonance. Due to easy measurement and high accuracy of low-order frequencies, inherent frequency has long been using to detect structural cracks. Salawu [111] and Cawley [112] used the changes of natural frequencies to detect the structural damage. Dharmaraju [113] and Dilena [114, 115] detected the crack location and depth using antiresonance. Nikolakopoulos et al. [116,117] examined the problem of identification of crack depth and position in frame

structures, using eigenfrequency measurements. Lee and Chung [98] presented a nondestructive evaluation procedure for identifying a crack in a one-dimensional beam-type structure using the natural frequency data and FEM. Lele and Maiti [118] presented the forward (determination of frequencies of beams knowing the crack parameters) and inverse problem (determination of crack location knowing the natural frequencies) in a Timoshenko beam while representing the crack by a rotational spring. Ratan et al. measured the amplitudes at the peaks of the Fourier transform in order to use them in a "residue" vector to identify and locate the crack [119]. Frequency contours with respect to crack depths and locations can be used to identify the crack [107].

(2) Modes, including mode shape, the strain mode, curvature mode, Modal assurance criteria (MAC) and coordinate modal assurance criteria (COMAC). Strain mode, the first derivative of mode shape, can be obtained by measuring structural strain. Curvature mode, the second derivative of mode shape, can be obtained by taking center differentiation of displacement modes. MAC examines the existence of damage by comparing the mode shapes before and after the damage occurrence. COMAC could further identify the coordinates of inconsistencies. These two criteria are not sensitive enough for damage detection in the early stage. Rizos et al. [120] used two measurements at two different positions of the beam vibrating near the first resonance. An on-line rotor crack detection and monitoring system have been reported by Imam et al. [121] in 1989. Seibold and Weinert [122] used the Extended Kalman Filter to present the localization of cracks in rotating machinery based on measured vibrations. Dong et al. [123] used a continuous model for vibration analysis and parameter identification of a static (non-rotating) rotor with an open crack. Karthikeyan et al. [124] identify the crack in a beam based on free

and forced response measurements. Gounaris and Papadopoulos [125] used a method based on the basic observation that the eigenmodes of any cracked structure are different from those of the uncracked one.

(3) Frequency response function. Frequency response function is related with mass, stiffness. Therefore, the structural characteristics can be directly obtained from the frequency response function. Different from modal parameters, frequency response function needs not to identify modal parameter and therefore avoids the identification error. However, it should be attended that signal truncation may distort the frequency response function while transforming the time-domain signal to frequency domain. Ishida et al. [126] used external excitations of rotating cracked shafts, thus causing the excitation of nonlinear characteristics of the crack in order to identify it. The Hwang's and Kim's idea was to minimize the measured and calculated FRF data [127] in order to identify the damage. Simple beam and helicopter rotor blades are used and cracks successfully identified. Sekhar and Prabhu [102] found the changes of an adequate number of natural frequencies (with FEM) and used these differences to detect the crack.

(4) Parameters of coupled vibration. When a transverse surface crack exists on a shaft, then coupling between different modes of vibration exists. This phenomenon was first reported for longitudinal and bending vibrations by Papadopoulos and Dimarogonas [16] and then for bending and torsional vibrations [44]. Gounaris et al. [128] used the coupling phenomenon as an identification tool for the determination of the depth and the location of a transverse surface crack in a Timoshenko beam. Gounaris and Papadopoulos [129] used the property of coupled vibrations introduced by a crack in order to identify a crack in a rotating cracked shaft. The simple Jeffcott or de Laval rotor model is considered by

Darpe et al. in [130] analyzing the response of a rotor with constant angular velocity under axial excitation of different frequencies. Continuing this effort, Darpe et al. [131] examined this phenomenon experimentally. They proved the above analytical results for both rotating and non-rotating shafts, exciting them by axial excitation of different frequencies. Dado and Abuzeid [132] presented the vibration behavior of a beam with rectangular cross section carrying end mass and rotary inertia. Al-Said et al. [133] proposed a simple model that describes the flexural vibration characteristics of a rotating, cracked Timoshenko beam.

(5) Compliance matrix. Structural damage reflects the stiffness reduction and flexibility increase of the structure. It is more effective to use compliance matrix for damage detection than stiffness matrix because compliance matrix converges very fast with the increase of the frequency. So, a few low-order modes enable good estimate of the compliance matrix. In addition, flexibility matrix method does not require the establishment of a structural analysis model and can diagnose the damage according to the experimental modal data. In 2001, Saavedra and Cuitino [134,135] calculated the local compliance matrix, then calculated a finite element model of the cracked element, and used it to accomplish detection of cracked beams and rotor.

(6) Damping. In comparison with frequency and mode, using damping for damage detection is relatively less. When the material is put under alternating stress, the thermo-elastic effect will result in temperature oscillation and irreversible thermal conductivity will cause entropy increase. In general, damping is not sensitive to the change and uncertainty of boundary conditions, so using damping for damage detection has its

advantages compared to using frequency and modes. However, damping is difficult to determine in practical applications.

Characteristic parameter method can be implemented easily and is able to detect the severity of damage. However, it is hard to locate the damage by this method. With the improvement of measuring tools and weak signal detection techniques, characteristic parameter based damage detection method will be applied to more and more structures.

1.5.2 Model-based Identification

At present, most of methods which can realize quantitative crack identification are based on the dynamical model. These methods take full advantages of theoretical and experimental modeling: establish a dynamical model at first; then repeat dynamic analysis according to the test data; finally, match simulated and experimental structural responses as close as possible by adjusting the crack parameters. The final crack parameters can be used for the quantitative identification of structural cracks. Therefore, damage detection problem based on the dynamical model is usually considered as an optimization problem.

The three key steps for dynamical model based damage identification method are objective function determination, optimization parameter selection and optimization algorithm application. Determination of the objective function usually depends on the sensitivity of characteristic parameters and engineering feasibility. Optimization parameters are crack location and depth. Optimization algorithms have two categories: one is the classical gradient optimization methods [136] and the other is the intellectual optimization algorithm [137]. Classical optimization method has limited application

because it requires the derivative information of the model which is hard to get in the practical application. Intellectual optimization algorithms, such as genetic algorithm, immune algorithm, particle swarm and ant colony algorithm, provide new ideas and tools for complicated problems. They are very robust and do not require the model to be continuous, and are especially suitable to deal with the realistic engineering problems with complexity and nonlinearity. The method was first presented by Isermann [138] for fault detection of technical processes. This method was applied based on the information extracted from direct measured signals, from signal models, and process models. Bachschmid and Dellupi [139] used a model-based identification procedure to identify the nonlinear forces of linearized and nonlinear oil films in two lobe journal bearings. Bachschmid et al. [140] introduced a method based on vibration measurements for the identification of the position and the depth of a transverse crack in a rotor system. The model-based method was also presented by Markert et al. [141] to solve the on-line identification of malfunctions in rotor systems. Dharmaraju et al. [142,143] applied inverse engineering techniques to estimate the system model parameters from the experimental force–response measurements. Sekhar [144] applies the model-based ID for a rotor-bearing system, whereas in [145] the rotor bearing system has been modeled using FEM, while the crack is considered through local flexibility change. Pennacchi et al. [146] presented a model-based identification method suitable for industrial machines.

1.5.3 Signal based Identification

The dynamical characteristic parameters are not going to fluctuate obviously when the crack is small or nonlinear response is very week. At this time, signal based damage

detection methods are needed to analyze the signal details in order to get the clear and usable data. Commonly used signal processing method includes Fourier transform, wavelet analysis, Hilbert-Huang transform (HHT).

Fourier transform is a classical signal processing method, which gives the frequency spectrum of time-domain signal and can not distinguish the variation of frequency components. For the small damage, Fourier transforms of the response have no big difference before and after damage appearance.

The wavelet analysis method is a time-frequency analysis technology. Wavelet transform has the ability to characterize the local signal in the time domain and frequency domains. It has strong ability to deal with non-steady state signal and therefore is able to obtain more signal information than Fourier analysis. In recent years, many researchers used wavelet analysis method to identify the crack location and depth of cracked beams [122-125].

HHT is a time-frequency analysis method for nonlinear and non-steady time signal. It is developed by N.E. Huang based on Hilbert transform. Compared to wavelet transform, Hilbert-Huang transform is able to better depict the signal energy distribution over time and frequency. This method was applied to damage detection and fault diagnosis of the rotor system and beam structure.

1.5.4 Identification based on Artificial Intelligence

Artificial intelligence (AI) is a comprehensive discipline that contains the knowledge of computer science, control theory, information theory, systems theory, nonlinear science and other disciplines. Artificial intelligence has been used for damage

identification, such as expert system, neural networks, fuzzy theory, etc. Among these, expert system is able to diagnose the location and severity of structural damage through human-computer interaction. Fuzzy theory has the ability to deal with uncertain information and can be used with expert system as preprocessing and post processing respectively. Neural network technique is very suitable for fault classification and pattern recognition due to its powerful parallel computing capability, self-learning function and associative ability.

Theoretically, artificial intelligence can detect damage without dynamical model and parameter recognition. However, the training samples of above methods are obtained from the analysis of dynamical model. Meanwhile, a large number of training samples may cause too long training time and converging difficulty for large and complicated structures.

1.5.5 Statistics based Identification

In the damage detection process, various types of error and uncertainties have great impact on the accuracy and reliability of the results. Statistics-based identification considers the uncertainty and statistical distribution of characteristic parameters. It uses stochastic models to analyze the eigenvalue problem and evaluate the damage. The statistical properties of spectrum density estimation can also be used to get corrected density function of modal parameters and then estimate the damage. The commonly used methods are generalized Bayes statistical methods, Monte-Carlo methods, etc. Not much research has been reported in this field, but it may have further development in the future.

1.6 Thesis Contribution

As cited above, many damage detection methods have been developed in recent years. To advance state-of-the-art, this thesis explores two new vibration-based damage identification methodologies: Floquet based method (Methodology I) and Frequency Response Function (FRF) based method (Methodology II). Subsequently, FRF based damage identification method are applied to identify the breathing transverse cracks existed on truss and rotor system. The system model is built based on energy method and the equations of motion are derived by applying assumed modes method and Lagrange theorem. In addition, the crack model is based on the Strain Energy Release Rate (SERR) concept in fracture mechanics.

Based on the assumption that the transverse crack is always open during operation, natural frequency-based damage detection methodology is developed to utilize the natural frequency shifts induced by damage to estimate the damage. This approach is based on Floquet theory and utilizes measured changes in the system natural frequencies to estimate the severity and location of shaft structural cracks during operation. The damage detection algorithms are developed and demonstrated via several damage cases existed on linear time-invariant and time-varying rotor system. Active Magnetic Bearing is introduced to break the symmetric structure of rotor system and the tuning range of proper stiffness/virtual mass gains is studied.

To overcome the shortcoming of natural frequency-based method, Chapter IV proposes another vibration-based damage identification method: FRF based method. This method utilizes the changes of transfer function between nominal and damaged system to detect the cracks. The magnitude and phase shifts of transfer function are all used in this

method instead of only natural frequency shifts in Floquet based method. The characteristics of frequency spectrum are studied first and then the algorithm for linear time-invariant rotor system is developed and validated through two damage sets. Subsequently, by interrogating the system near-field/far-field resonances, the sensitivity of transfer function is studied and the damage identification is demonstrated via a linear damage case.

In Chapter V and VI, FRF based damage identification methodology is used to identify the breathing cracks existed in truss and rotor systems. The nonlinear behavior of breathing crack is investigated and the nonlinear breathing functions are simulated by reasonable linear approximation. Then, the damage detection algorithms are developed and validated in frequency domain. Finally, the vibration of breathing cracked system is simulated in the Simulink. The vibration response signal is processed and used for damage identification of breathing cracks.

Chapter II

DEVELOPMENT OF ROTORDYNAMIC SYSTEM MODEL

2.1 Introduction

To describe the state-space of motion and to obtain angular velocity expression of a rigid body, Cardan angle transformation [147] is used in this chapter. Assumed mode method and Lagrange principle are applied to derive the dynamical equations of flexible shaft/disk system. Finally, crack model is built using Strain Energy Release Rate (SERR) method based on the fracture mechanics.

2.2 Rigid Body Dynamics

The transformation from the fixed coordinate system {n} to the rotating coordinate system {a} (Fig. 2.1) can be denoted as T:

$$\begin{bmatrix} \mathbf{c}_1 \\ \mathbf{c}_2 \\ \mathbf{c}_3 \end{bmatrix} = \mathrm{T} \begin{bmatrix} \mathbf{n}_1 \\ \mathbf{n}_2 \\ \mathbf{n}_3 \end{bmatrix} \tag{2.1}$$

where n_1, n_2, n_3 and a_1, a_2, a_3 are the coordinate vectors of {n} and {a}, respectively.

Cardan angles θ_1, θ_2 and θ_3 are shown in Fig. 2.1. θ_1 is the angle between axis b_2 and c_2; θ_2 is the angle between axis n_3 and a_3; θ_3 is the angle between axis a_1 and b_1. The coordinate system {n} is transformed from coordinate system {c} by following the below three rotations:

1) {n}→{a} by rotating coordinate system {n} θ_2 degree around axis n_2

$$\begin{bmatrix}\mathbf{a}_1\\ \mathbf{a}_2\\ \mathbf{a}_3\end{bmatrix}=\begin{bmatrix}\cos\theta_2 & 0 & -\sin\theta_2\\ 0 & 1 & 0\\ \sin\theta_2 & 0 & \cos\theta_2\end{bmatrix}\begin{bmatrix}\mathbf{n}_1\\ \mathbf{n}_2\\ \mathbf{n}_3\end{bmatrix}=T_1(\theta_2)\begin{bmatrix}\mathbf{n}_1\\ \mathbf{n}_2\\ \mathbf{n}_3\end{bmatrix} \tag{2.2}$$

2) {a}→{b} by rotating coordinate system {a} θ_3 degree around axis a_3

$$\begin{bmatrix}\mathbf{b}_1\\ \mathbf{b}_2\\ \mathbf{b}_3\end{bmatrix}=\begin{bmatrix}\cos\theta_3 & \sin\theta_3 & 0\\ -\sin\theta_3 & \cos\theta_3 & 0\\ 0 & 0 & 1\end{bmatrix}\begin{bmatrix}\mathbf{a}_1\\ \mathbf{a}_2\\ \mathbf{a}_3\end{bmatrix}=T_2(\theta_3)\begin{bmatrix}\mathbf{a}_1\\ \mathbf{a}_2\\ \mathbf{a}_3\end{bmatrix} \tag{2.3}$$

3) {b}→{c} by rotating coordinate system {b} θ_1 degree around axis b_1

$$\begin{bmatrix}\mathbf{c}_1\\ \mathbf{c}_2\\ \mathbf{c}_3\end{bmatrix}=\begin{bmatrix}1 & 0 & 0\\ 0 & \cos\theta_1 & \sin\theta_1\\ 0 & -\sin\theta_1 & \cos\theta_1\end{bmatrix}\begin{bmatrix}\mathbf{b}_1\\ \mathbf{b}_2\\ \mathbf{b}_3\end{bmatrix}=T_3(\theta_1)\begin{bmatrix}\mathbf{b}_1\\ \mathbf{b}_2\\ \mathbf{b}_3\end{bmatrix} \tag{2.4}$$

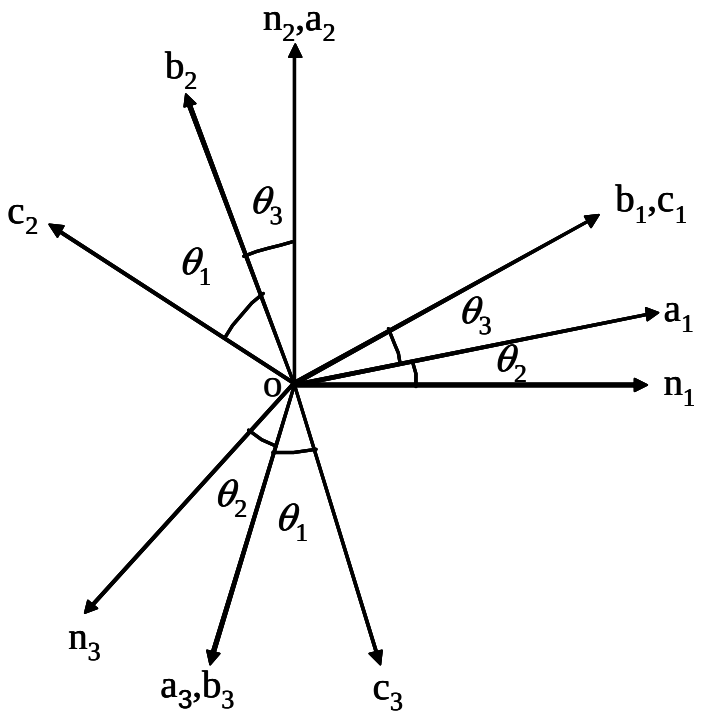

Fig. 2.1 Cardan Angles

The transformation matrix *T* can be expressed as:

$$T = T_3(\theta_1)T_2(\theta_3)T_1(\theta_2)$$
$$= \begin{bmatrix} \cos\theta_2\cos\theta_3 & \sin\theta_3 & -\sin\theta_2\cos\theta_3 \\ \sin\theta_1\sin\theta_2 - \cos\theta_1\cos\theta_2\sin\theta_3 & \cos\theta_1\cos\theta_3 & \sin\theta_1\cos\theta_2 + \cos\theta_1\sin\theta_2\sin\theta_3 \\ \cos\theta_1\sin\theta_2 + \sin\theta_1\cos\theta_2\sin\theta_3 & -\sin\theta_1\cos\theta_3 & \cos\theta_1\cos\theta_2 - \sin\theta_1\sin\theta_2\sin\theta_3 \end{bmatrix}$$

(2.5)

The angular velocity of rigid body is:

$$\omega_c = \dot{\theta}_2\hat{\mathbf{n}}_2 + \dot{\theta}_3\hat{\mathbf{b}}_3 + \dot{\theta}_1\hat{\mathbf{c}}_1$$
$$= (\dot{\theta}_2\sin\theta_3 + \dot{\theta}_1)\hat{\mathbf{c}}_1 + (\dot{\theta}_2\cos\theta_1\cos\theta_3 + \dot{\theta}_3\sin\theta_1)\hat{\mathbf{c}}_2 + (-\dot{\theta}_2\sin\theta_1\cos\theta_3 + \dot{\theta}_3\cos\theta_1)\hat{\mathbf{c}}_2$$

(2.6)

where upper index (.) denotes the derivative with respect to time. In rotating coordinate system {c}, the moments of inertia are defined as J_{c1}, J_{c2} and J_{c3}. The rotational energy of rigid body is:

$$T_{rot} = \frac{1}{2}(J_{c1}\omega_{c1}^2 + J_{c2}\omega_{c2}^2 + J_{c3}\omega_{c3}^2)$$
$$= \frac{1}{2}[J_{c1}(\dot{\theta}_2\sin\theta_3 + \dot{\theta}_1)^2 + J_{c2}(\dot{\theta}_2\cos\theta_1\cos\theta_3 + \dot{\theta}_3\sin\theta_1)^2 \qquad (2.7)$$
$$\cdots + J_{c3}(-\dot{\theta}_2\sin\theta_1\cos\theta_3 + \dot{\theta}_3\cos\theta_1)^2]$$

2.3 Energy Method

In this section, the kinetic and potential energy of flexible shaft/disk system is derived based on energy method.

2.3.1 System Specifications and Assumptions

The shaft is assumed to rotate at constant angular speed Ω and have structural damping proportional to shaft stiffness. A circular shaft with length *L* and radius *R* rotating about its longitudinal axis, *x*, is shown in Fig. 2.2. The transverse shaft

deflections in the synchronous rotating-frame directions c_2 and c_3 are denoted $v(x, t)$ and $w(x, t)$ while the lateral rotations about the axes c_2 and c_3 are $\theta_2(x, t)$ and $\theta_3(x, t)$ respectively.

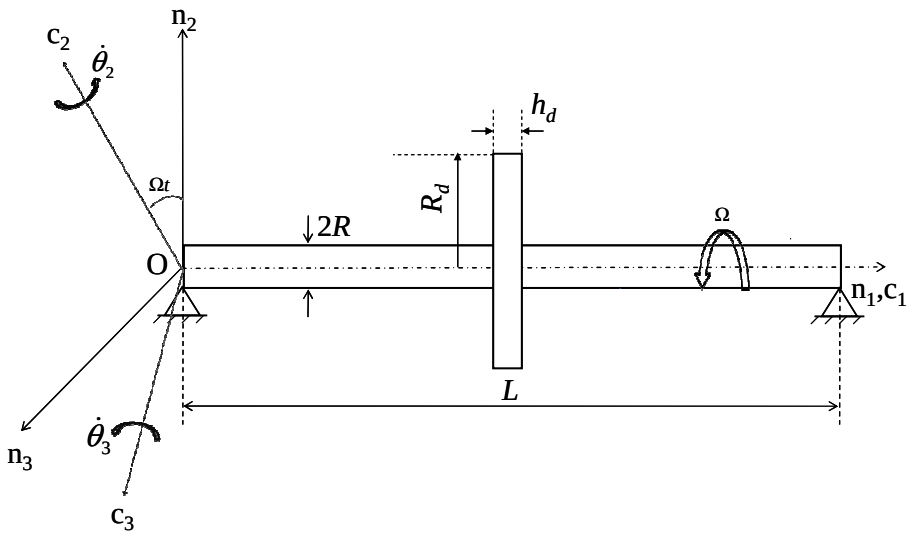

Fig. 2.2 Shaft-disk rotor system specifications

To simplify the system, we made the following assumptions:

(1) Simulate the shaft using Rayleigh beam model and neglect the effect of shear stress.

(2) Rigid connection between the shaft and the disk. The disk is fixed to the shaft and the normal direction of disk is perpendicular to the tangent of shaft modes.

(3) The disk is rigid and neglects the elastic deformation of disk.

2.3.2 Rotational Energy

First of all, we take a piece of shaft and look at the rotational energy of this small piece. Then, the rotational energy of the whole shaft can be obtained by integrating over the shaft length.

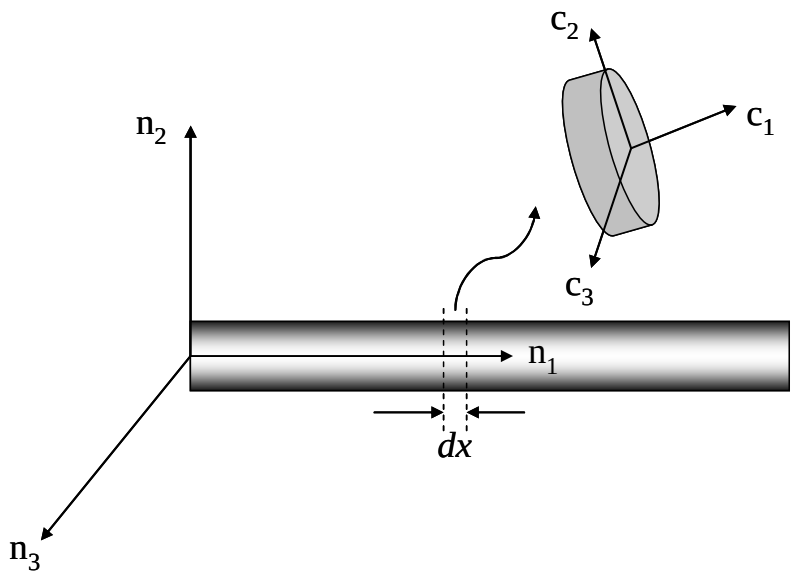

Fig. 2.3 Flexible shaft

For the symmetric structure shown in Fig. 2.3, the moment of inertia J_{c2} is the same as $J_{c3.}$ By assuming θ_2 and θ_3 are small and neglecting the high-order terms, the rotational energy in Eq. (2.7) can be simplified as:

$$T_{rot} = \frac{1}{2} J_{c1}(\Omega^2 + 2\Omega\int_0^L \dot{\theta}_2\theta_3 dx) + \frac{1}{2} J_{c2}\int_0^L (\dot{\theta}_2^2 + \dot{\theta}_3^2)dx \tag{2.8}$$

2.3.3 Translational Energy

The transverse shaft deflections in the synchronous rotating-frame directions c_2 and c_3 are denoted $v(x, t)$ and $w(x, t)$ while the lateral rotations about the axes c_2 and c_3 are $\theta_2(x, t)$ and $\theta_3(x, t)$ respectively. The translational energy of the shaft piece is

$$T_{trans} = \frac{1}{2}\rho A\int_0^L \left(\dot{v}^2 + \dot{w}^2\right)dx \tag{2.9}$$

Where ρ is density, A is cross-section area.

2.3.4 Strain Energy

In Fig. 2.4, the deflections in c_2, c_3, n_2 and n_3 directions are defined as v, w, v_s and w_s, respectively.

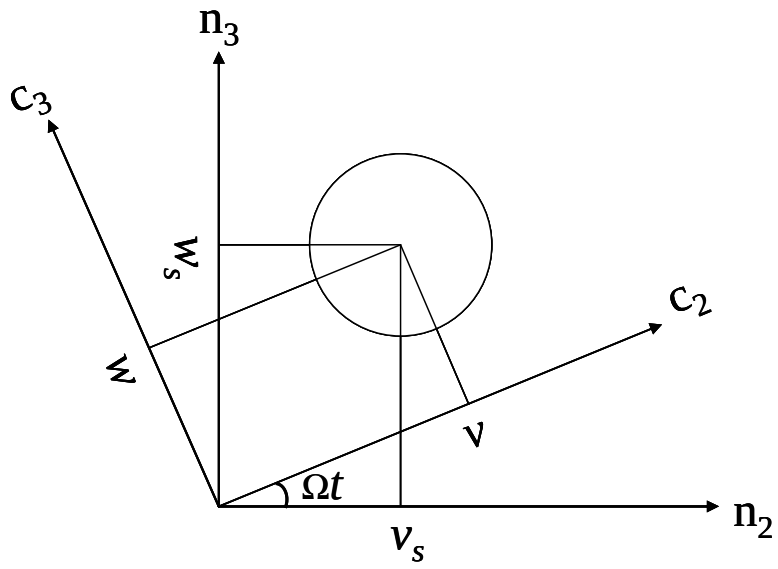

Fig. 2.4 Coordinate transformation

The deflections can be transformed by the following equation:

$$\begin{bmatrix} v \\ w \end{bmatrix} = \begin{bmatrix} \cos(\Omega t) & \sin(\Omega t) \\ -\sin(\Omega t) & \cos(\Omega t) \end{bmatrix} \begin{bmatrix} v_s \\ w_s \end{bmatrix} \tag{2.10}$$

The strain energy of undamaged system is

$$U_s = \frac{1}{2} EI_y \int_0^L \left(v''^2 + w''^2 \right) dx = \frac{1}{2} EI_y \int_0^L \left(v_s''^2 + w_s''^2 \right) dx \tag{2.11}$$

Where is E elastic modulus. The upper index (") denotes the second derivative of displacement with respect to x.

2.3.5 Kinetic Energy of Disk

The kinetic energy of the disk is

$$T_{rot}^{d} = \frac{1}{2} M_d (\dot{v}_d^{\,2} + \dot{w}_d^{\,2}) + \frac{1}{2} J_{dc2} \left(\dot{\theta}_{2d}^{\,2} + \dot{\theta}_{3d}^{\,2} \right) + \frac{1}{2} J_{dc1} (\Omega^2 + 2\Omega \dot{\theta}_{2d} \theta_{3d}) \qquad (2.12)$$

Where M_d is the disk mass, I_{dc1} and I_{dc2} are disk moments of inertia, $v_d(t)$ and $w_d(t)$ are disk transverse deflections, $\theta_{2d}(t)$ and $\theta_{3d}(t)$ are the disk lateral rotations respectively in the rotating frame {c}.

2.4 Assumed Modes Method

The assumed modes assume a solution to the boundary value problem as [148]

$$y(x,t) = \sum_{i=1}^{n} \varphi_i(x) q_i(t) \qquad (2.13)$$

where φ_i are trial functions and q_i are generalized coordinates. The Convenience of equation (2.13) as it applies to conversation leads to

$$[M]\{\ddot{q}\} + [K]\{q\} = \{0\} \qquad (2.14)$$

where [M] and [K] are the corresponding mass and stiffness matrices, respectively. It can be further used to solve the eigenvalue problem and find the forced response to dynamic systems due to external forces or initial impulses.

Since the assumed mode method is popular in the dynamics of flexible multibody systems, it is important to note that its popularity stems from the fact that the admissible functions (trial functions) are approximated by taking these from continuous system such beams, which in general provide a good approximation.

For the rotor system, the deflections in two lateral directions are assumed as:

$$v = \sum_{m=1}^{n} \varphi_m(x) q_{1m}(t)$$
$$w = \sum_{m=1}^{n} \varphi_m(x) q_{2m}(t) \tag{2.15}$$

And for the small θ_2 and θ_3, we have

$$\theta_2 \approx -w' \text{ and } \theta_3 \approx v' \tag{2.16}$$

where the symbol (') indicates d/dx, n is number of assumed modes, $\varphi_m(x)$ is an assumed modeshape and $q_{1m}(x)$ and $q_{2m}(x)$ are the modal coordinates associated with the v and w deflections respectively.

2.5 Lagrange Theorem

For a collection of particles with conservative forces described by a potential, we have in inertial Cartesian coordinates

$$m\ddot{x}_i = F_i \tag{2.17}$$

The left hand side of this equation is determined by the kinetic energy function as the time derivative of the momentum $p_i = \partial T/\partial \dot{x}_i$, while the right hand side is a derivative of the potential energy, $\partial U/\partial x_i$. As T is independent of x_i and U is independent of $\dot{x}_i$ in these coordinates, we can write both sides in terms of the Lagrangian $L = T - U$, which is then a function of both the coordinates and their velocities. Thus we have established

$$\frac{d}{dt}\frac{\partial L}{\partial \dot{x}_i} - \frac{\partial L}{\partial x_i} = 0 \tag{2.18}$$

which, once we generalize it to arbitrary coordinates, will be known as Lagrange's equation.

Lagrangian dynamics, as described thus far, provides a very powerful means to determine the equations of motion for complicated discrete (finite degree-of-freedom) systems. However, there are two primary kinematical requirements which must be achieved before the determination of the potential functions, and subsequent application of Lagrange's equation.

(1) Coordinate choice:

(a) The choice of coordinates must be independent and orthogonal. While it is possible to use non-orthogonal coordinates, the additional complexity incurred is not worth the effort in discrete models. Examples of orthogonal coordinate choices include: Cartesian – x, y and z; cylindrical – r, θ and z; spherical – r, θ and φ.

(b) The coordinates must locate the body with respect to an inertial reference frame. An inertial reference frame is simply one which is not accelerating.

(2) Translational and rotational energy:

In rigid bodies, both the translational and rotational kinetic energy must be accounted for. Three cases exist:

(a) Pure rotation – An object which is in pure rotation has at least one point or line which has zero translational velocity. In this case, all of the kinetic energy is rotational, so only the rotational kinetic potential function need be accounted for.

(b) Pure translation – An object is said to be in pure translation if it has no rotation. In this case only the translational kinetic potential function need be accounted for, so only the velocity of the center of mass is needed.

(c) Translation and rotation – A body which is both translating and rotating exhibits no stationary points as does a body in pure rotation. However, a translating and rotating

body can exhibit instantaneous centers of rotation which have zero velocity with respect to an inertial reference for an instant.

2.6 Crack Model

2.6.1 Basic Crack Modes

If the plastic area of the crack tip is small, linear elastic method can be used to analyze the stress and strain of the cracked structure. The stress and strain field can be determined by solving the equations with boundary conditions. The real crack can be divided into three basic modes due to different types of external loads: opening mode, sliding mode and shearing mode.

Opening mode (mode I): the upper and lower surface of crack move along y direction and cause the crack open and close, as shown in Fig. 2.5.

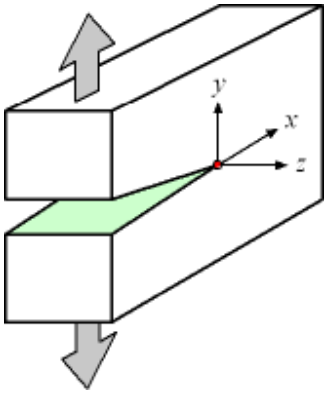

Fig. 2.5 Stress Intensity Factor, Mode I [149]

Sliding mode (mode II): the upper and lower surface of crack move along x direction and cause the crack slide-open, as shown in Fig. 2.6.

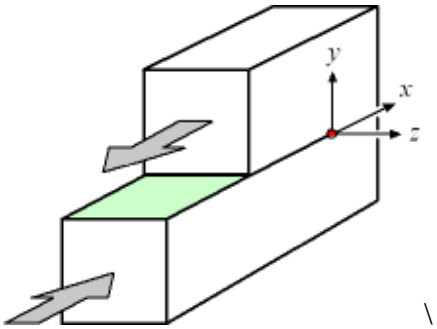

Fig. 2.6 Stress Intensity Factor, Mode II [149]

Shearing mode (mode III): the upper and lower surface of crack move along z direction and cause the crack shear-open, as shown in Fig. 2.7.

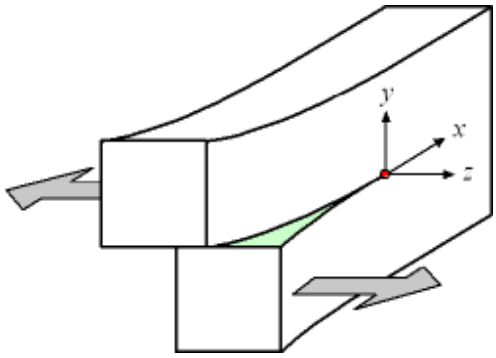

Fig. 2.7 Stress Intensity Factor, Mode III [149]

2.6.2 Displacement and Stress Field of Crack

The total deformation of the crack tip can be obtained through the superposition of deformations for three basic modes. Hence, here gives the displacement and stress fields of crack tip for each mode [149]:

Mode I:

$$
\begin{aligned}
\sigma_x &= \frac{K_I}{\sqrt{2\pi r}}\cos\frac{\theta}{2}[1-\sin\frac{\theta}{2}\sin\frac{3\theta}{2}] \\
\sigma_y &= \frac{K_I}{\sqrt{2\pi r}}\cos\frac{\theta}{2}[1+\sin\frac{\theta}{2}\sin\frac{3\theta}{2}] \\
\tau_{xy} &= \frac{K_I}{\sqrt{2\pi r}}\sin\frac{\theta}{2}\cos\frac{\theta}{2}\cos\frac{3\theta}{2} \\
u_x &= \frac{K_I}{\mu}\sqrt{\frac{r}{2\pi}}\cos\frac{\theta}{2}[\frac{\kappa-1}{2}+\sin^2\frac{\theta}{2}] \\
u_y &= \frac{K_I}{\mu}\sqrt{\frac{r}{2\pi}}\sin\frac{\theta}{2}[\frac{\kappa+1}{2}-\cos^2\frac{\theta}{2}]
\end{aligned}
\qquad (2.19)
$$

Mode II:

$$
\begin{aligned}
\sigma_x &= \frac{K_{II}}{\sqrt{2\pi r}}\sin\frac{\theta}{2}[2+\cos\frac{\theta}{2}\cos\frac{3\theta}{2}] \\
\sigma_y &= \frac{K_{II}}{\sqrt{2\pi r}}\sin\frac{\theta}{2}\cos\frac{\theta}{2}\cos\frac{3\theta}{2} \\
\tau_{xy} &= \frac{K_{II}}{\sqrt{2\pi r}}\cos\frac{\theta}{2}[1-\sin\frac{\theta}{2}\sin\frac{3\theta}{2}] \\
u_x &= \frac{K_{II}}{\mu}\sqrt{\frac{r}{2\pi}}\sin\frac{\theta}{2}[\frac{\kappa+1}{2}+\cos^2\frac{\theta}{2}] \\
u_y &= \frac{K_{II}}{\mu}\sqrt{\frac{r}{2\pi}}\cos\frac{\theta}{2}[\frac{1-\kappa}{2}+\sin^2\frac{\theta}{2}]
\end{aligned}
\qquad (2.20)
$$

Mode II:

$$
\begin{aligned}
\tau_{xz} &= -\frac{K_{III}}{\sqrt{2\pi r}}\sin\frac{\theta}{2} \\
\tau_{xy} &= -\frac{K_{III}}{\sqrt{2\pi r}}\cos\frac{\theta}{2} \\
u_z &= \frac{K_{III}}{\mu}\sqrt{\frac{r}{2\pi}}\sin\frac{\theta}{2}
\end{aligned}
\qquad (2.21)
$$

2.6.3 Stress Intensity Factor

The stresses at the crack tip for three basic modes are given in the Eq. (2.19), (2.20) and (2.21). It could be seen that the stress goes to infinity at the crack tip ($r \rightarrow 0$). This

feature is known as the stress singularity at the crack tip. The stress coefficients K_N ($N = I, II, III$) are independent of the coordinates and characterize the singularity of the stress field. Therefore, these coefficients are named as stress intensity factors in fracture mechanics, wherein K_I, K_{II}, K_{III} denote the stress intensity factor for opening, sliding and shearing mode respectively. They can be expressed as [149]:

$$K_N = \sqrt{2\pi r}\sigma_{ij}^N f_{ij}^N(\theta) \tag{2.22}$$

where $f_{ij}^N(\theta)$ is function of the θ, which is called shape correction function in fracture mechanics. The stress at the crack tip is decomposed into three components corresponding to three modes:

$$\sigma_{ij}(r,\theta) = \sum_N \sigma_{ij}^N = \frac{1}{\sqrt{2\pi r}}[K_I f_{ij}^I(\theta) + K_{II} f_{ij}^{II}(\theta) + K_{III} f_{ij}^{III}(\theta)] \tag{2.23}$$

Since stress intensity factor at the crack tip is significant for the crack propagation and material destruction, we should study the stress and corresponding stress intensity factor at the crack tip besides the displacement and stress fields. The calculation methods of the stress intensity factor are divided into analytical, numerical method and experimental methods.

2.6.4 Energy Release

The concept of energy release was first proposed by Griffith in 1920 and then was improved by Irwin. Consider a shaft element containing a transverse surface crack of depth a as shown in Fig. 2.8. The length of the shaft is l and the depth of the crack is a. In a general case, the shaft is loaded with axial force P_1, shear forces P_2 and P_3, bending moments P_4 and P_5 and torque P_6.

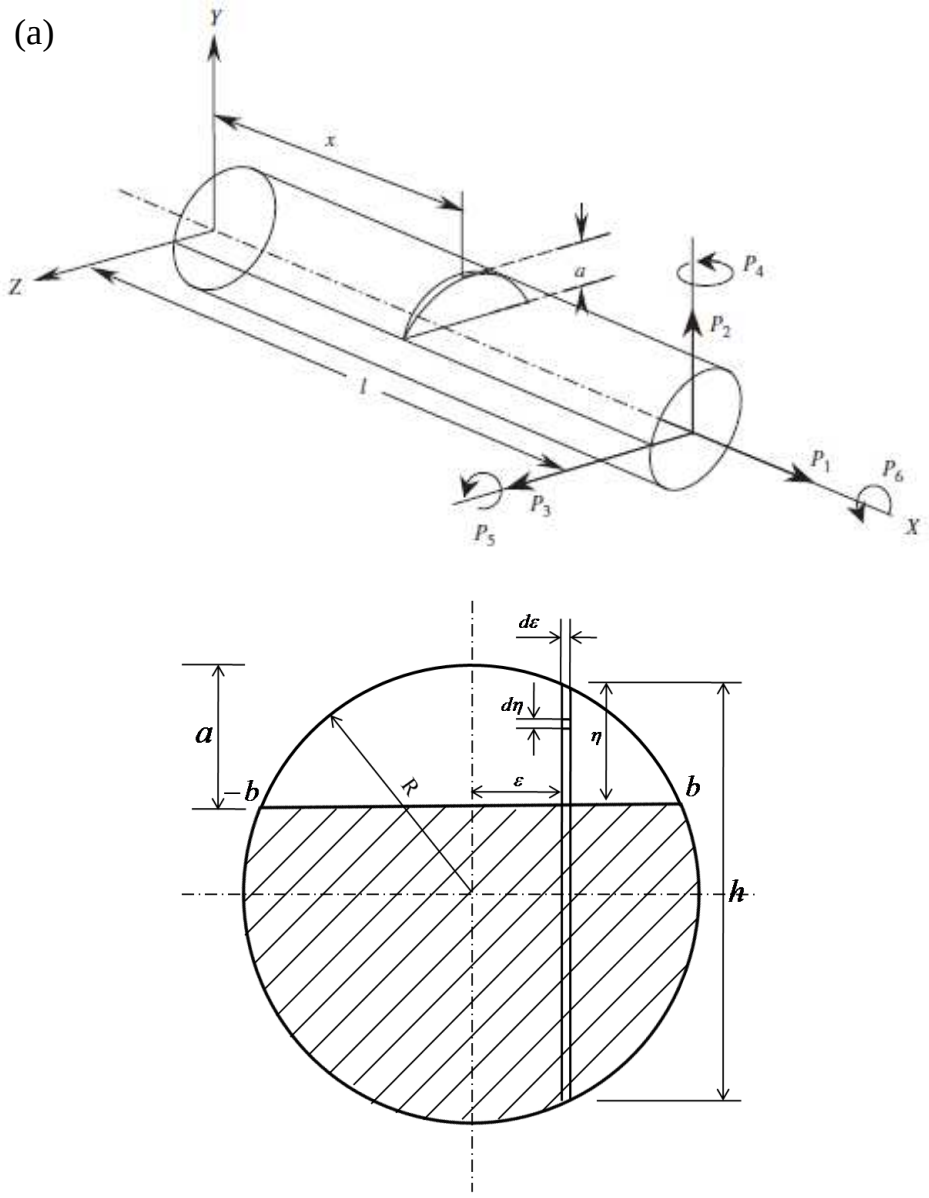

Fig. 2.8 (a) A cracked shaft in general loading [150] (b) Cracked shaft cross-section

The released strain energy due to crack is given by the following expression [150]:

$$U_c = \frac{1}{E'}\int_A J dA \tag{2.24}$$

Where J is strain energy density function expressed as:

$$J = \left(\sum_{i=1}^{6} K_{Ii}\right)^2 + \left(\sum_{i=1}^{6} K_{IIi}\right)^2 + (1+\nu)\left(\sum_{i=1}^{6} K_{IIIi}\right)^2 \tag{2.25}$$

Where K_{Ii}, K_{IIi} and K_{IIIi} are the stress intensity factors (SIF) corresponding to opening mode, sliding mode and shearing mode, i=1-6; $E^{'} = E/(1-\nu^2)$ for plane strain and $E^{'} = E$ for plane stress; ν is Poisson ratio.

These stress intensity factors are given as follows [150]:

SIF for mode I:

$$\begin{aligned} K_{I1} &= \sigma_1\sqrt{\pi\eta}F_1(\eta/h) = \frac{P_1}{\pi R^2}\sqrt{\pi\eta}F_1(\eta/h) \\ K_{I4} &= \sigma_4\sqrt{\pi\eta}F_1(\eta/h) = \frac{4(P_5+P_2x)\eta}{\pi R^4}\sqrt{\pi\eta}F_2(\eta/h) \\ K_{I5} &= \sigma_5\sqrt{\pi\eta}F_1(\eta/h) = \frac{4(P_3x-P_4)\varepsilon}{\pi R^4}\sqrt{\pi\eta}F_1(\eta/h) \\ K_{I2} &= K_{I3} = K_{I6} = 0 \end{aligned} \tag{2.26}$$

SIF for mode II:

$$\begin{aligned} K_{II2} &= \sigma_2\sqrt{\pi\eta}F_{II}(\eta/h) = \frac{kP_2}{\pi R^2}\sqrt{\pi\eta}F_{II}(\eta/h) \\ K_{II6} &= \sigma_{6II}\sqrt{\pi\eta}F_{II}(\eta/h) = \frac{2P_6\varepsilon}{\pi R^4}\sqrt{\pi\eta}F_{II}(\eta/h) \\ K_{II1} &= K_{II3} = K_{II4} = K_{I5} = 0 \end{aligned} \tag{2.27}$$

SIF for mode III:

$$\begin{aligned} K_{III3} &= \sigma_3\sqrt{\pi\eta}F_{III}(\eta/h) = \frac{kP_3}{\pi R^2}\sqrt{\pi\eta}F_{III}(\eta/h) \\ K_{III6} &= \sigma_{6III}\sqrt{\pi\eta}F_{III}(\eta/h) = \frac{2P_6\eta}{\pi R^4}\sqrt{\pi\eta}F_{III}(\eta/h) \\ K_{III1} &= K_{III2} = K_{III4} = K_{III5} = 0 \end{aligned} \tag{2.28}$$

where,

$$F_1(\eta/h) = \sqrt{\frac{\tan\lambda}{\lambda}}\frac{[0.752+2.02(a/h)+0.37(1-\sin\lambda)^3]}{\cos\lambda} \tag{2.29}$$

$$F_2(\eta/h) = \sqrt{\frac{\tan\lambda}{\lambda}}\,\frac{[0.923 + 0.199(1-\sin\lambda)^4]}{\cos\lambda} \tag{2.30}$$

$$F_{II}(\eta/h) = \frac{1.122 - 0.561(2\lambda/\pi) + 0.085(2\lambda/\pi)^2 + 0.18(2\lambda/\pi)^3}{\sqrt{1-2\lambda/\pi}} \tag{2.31}$$

$$F_{III}(\eta/h) = \sqrt{\frac{\tan\lambda}{\lambda}} \tag{2.32}$$

For the shaft-disk rotor system shown in Fig. 2.3, $P_1 = P_2 = P_3 = P_6 = 0$. Therefore, the crack energy equation (2.24) can be simplified as:

$$\begin{aligned} U_c &= \frac{1}{E'}\int_A \left(K_{I4} + K_{I5}\right)^2 dA \\ K_{I4} &= E\sqrt{R^2-\varepsilon^2}\,\sqrt{\pi\eta}\,F_2(\eta/h)v_c'' \\ K_{I5} &= E\varepsilon\sqrt{\pi\eta}\,F_1(\eta/h)w_c'' \end{aligned} \tag{2.33}$$

where v_c and w_c are the shaft deflections at crack location in y and z direction.

2.7 Equation of Motion

By taking Eq. (2.15) and (2.16) into Eq. (2.8), (2.9) and (2.11) and employing Lagrange's equation, the nominal shaft system equations-of-motion are given as:

$$[M_s]\ddot{q} + [C_s + G_s]\dot{q} + [K_s]q = 0 \tag{2.34}$$

where M_s, C_s, G_s and K_s are the shaft mass, damping, gyroscopic and stiffness matrices with the following expressions:

$$M_s = \begin{bmatrix} \rho A\int_0^L \varphi^T\varphi dx + \rho I\int_0^L \varphi'^T\varphi' dx & 0 \\ 0 & \rho A\int_0^L \varphi^T\varphi dx + \rho I\int_0^L \varphi'^T\varphi' dx \end{bmatrix} \tag{2.35}$$

$$K_s = \begin{bmatrix} EI\int_0^L \varphi''^T\varphi'' dx & 0 \\ 0 & EI\int_0^L \varphi''^T\varphi'' dx \end{bmatrix} \tag{2.36}$$

$$G_s = 2\Omega \begin{bmatrix} 0 & \rho I \int_0^L \varphi'^T \varphi' dx \\ -\rho I \int_0^L \varphi'^T \varphi' dx & 0 \end{bmatrix} \tag{2.37}$$

$$C_s = cK_s = c \begin{bmatrix} EI \int_0^L \varphi''^T \varphi'' dx & 0 \\ 0 & EI \int_0^L \varphi''^T \varphi'' dx \end{bmatrix} \tag{2.38}$$

where ρ is shaft density, A is shaft cross-section area, I is moment of inertia in c_2 direction, E is elastic modulus, c is proportional structural damping coefficient.

If the system has a transverse crack, the strain energy of damaged system can be obtained by deducting the crack released strain energy from strain energy of nominal system. The equation of motion for damaged system is given as:

$$[M_s]\ddot{q} + [C_s + G_s]\dot{q} + [K_s - K_{c\theta}]q = 0 \tag{2.39}$$

where $K_{c\theta}$ is the stiffness perturbation matrix due to the shaft crack damage. Its expression is given as:

$$K_{c\theta} = \begin{bmatrix} [2A_c^p \cos^2\theta + 2B_c^p \sin^2\theta - 2C_c^p \sin 2\theta]\varphi(x_c)^T \varphi(x_c) & [(A_c^p - B_c^p)\sin 2\theta + 2C_c^p \cos 2\theta]\varphi(x_c)^T \varphi(x_c) \\ [(A_c^p - B_c^p)\sin 2\theta + 2C_c^p \cos 2\theta]\varphi(x_c)^T \varphi(x_c) & [2A_c^p \sin^2\theta + 2B_c^p \cos^2\theta + 2C_c^p \sin 2\theta]\varphi(x_c)^T \varphi(x_c) \end{bmatrix} \tag{2.40}$$

where A_c^p, B_c^p, C_c^p are crack parameters which are given as follows:

$$\begin{aligned} A_c^p &= E \int_0^{\sqrt{a^2-\varepsilon^2}-(R-a)} \int_{-b}^{b} (R^2 - \varepsilon^2)\pi\eta F_2^2(\eta/h) d\varepsilon d\eta \\ B_c^p &= E \int_0^{\sqrt{a^2-\varepsilon^2}-(R-a)} \int_{-b}^{b} \varepsilon^2 \pi\eta F_1^2(\eta/h) d\varepsilon d\eta \\ C_c^p &= E \int_0^{\sqrt{a^2-\varepsilon^2}-(R-a)} \int_{-b}^{b} \varepsilon\sqrt{R^2-\varepsilon^2}\,\pi\eta F_1(\eta/h) F_2(\eta/h) d\varepsilon d\eta \end{aligned} \tag{2.41}$$

θ is the angle between crack coordinate and rotating coordinate {c} (Fig. 2.9); x_c is the crack location.

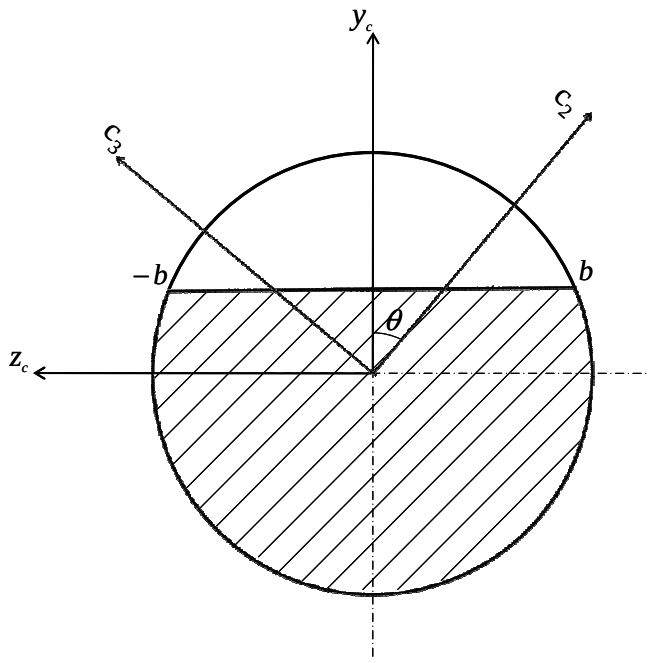

Fig. 2.9 Coordinate transformation for crack

For the damaged shaft-disk system with the shaft cracks, the equation-of-motion becomes:

$$[M_s + M_d]\ddot{q} + [C_s + G_s + G_d]\dot{q} + [K_s - K_{c\theta}]q = 0 \tag{2.42}$$

where,

$$M_d = \begin{bmatrix} \rho_d A_d h_d \varphi(x_d)^T \varphi(x_d) + \rho_d I_d \varphi(x_d)'^T \varphi(x_d)' & 0 \\ 0 & \rho_d A_d h_d \varphi(x_d)^T \varphi(x_d) + \rho_d I_d \varphi(x_d)'^T \varphi(x_d)' \end{bmatrix} \tag{2.43}$$

$$G_d = 2\Omega \begin{bmatrix} 0 & \rho_d I_d \varphi(x_d)'^T \varphi(x_d)' \\ -\rho_d I_d \varphi(x_d)'^T \varphi(x_d)' & 0 \end{bmatrix} \tag{2.44}$$

where ρ_d is disk density, A_d is disk cross-section area, I_d is disk moment of inertia in c_2 direction, h_d is disk thickness.

Chapter III

METHODOLOGY I: NATURAL FREQUENCY-BASED DAMAGE IDENTIFICATION OF ROTOR SYSTEM WITH OPEN CRACKS

3.1 Introduction

A new vibration-based damage identification methodology for cracked rotor systems with is developed and demonstrated on a shaft-disk system. This approach is based on Floquet theory and utilizes measured changes in the system natural frequencies to estimate the severity and location of shaft structural cracks during operation [151-154]. The damage identification is enhanced through the use of an Active Magnetic Bearing with adjustable support stiffness and acceleration feedback. Here, a novel symmetry-breaking closed-loop control is employed during the iterative damage identification process to enrich the data set by removing the Eigen degeneracy of the symmetric shaft structure. This approach enables full damage identification from a single sensor and hence without requiring measured modeshape information. The method is synthesized via harmonic balance and numerical examples for a shaft/disk system demonstrate the effectiveness in detecting both location and severity of the structural damage.

3.2 Open Crack Parameters

To develop the damage identification method and understand how the cracks affect the structural system, the features of crack parameters are studied first. The cracks on the shaft/disk system are assumed to be open in this chapter. The breathing crack mechanism will be studied in the following chapters.

First of all, the variation of crack parameters A_c^p, B_c^p and C_c^p is studied for increasing crack depth in crack coordinate system. The non-dimensional form of crack parameters is given as follows:

$$\begin{aligned}
\bar{A}_c^p &= ER^5 \int_0^{\sqrt{\bar{a}^2-\bar{\varepsilon}^2}-(1-\bar{a})} \int_{-\bar{b}}^{\bar{b}} (1-\bar{\varepsilon}^2)\pi\bar{\eta}F_2^2(\bar{\eta}/\bar{h})d\bar{\varepsilon}d\bar{\eta} \\
\bar{B}_c^p &= ER^5 \int_0^{\sqrt{\bar{a}^2-\bar{\varepsilon}^2}-(1-\bar{a})} \int_{-\bar{b}}^{\bar{b}} \bar{\varepsilon}^2\pi\bar{\eta}F_1^2(\bar{\eta}/\bar{h})d\bar{\varepsilon}d\bar{\eta} \\
\bar{C}_c^p &= ER^5 \int_0^{\sqrt{\bar{a}^2-\bar{\varepsilon}^2}-(1-\bar{a})} \int_{-\bar{b}}^{\bar{b}} \bar{\varepsilon}\sqrt{R^2-\bar{\varepsilon}^2}\pi\bar{\eta}F_1(\bar{\eta}/\bar{h})F_2(\bar{\eta}/\bar{h})d\bar{\varepsilon}d\bar{\eta}
\end{aligned} \tag{3.1}$$

where,

$$\bar{a} = \frac{a}{R}, \bar{b} = \frac{b}{R}, \bar{\varepsilon} = \frac{\varepsilon}{R}, \bar{\eta} = \frac{\eta}{R}, \bar{h} = \frac{h}{R} \tag{3.2}$$

It can be seen from Fig. 3.1 that crack parameters A_c^p and B_c^p are keeping increasing when the crack depth varies from 0 to shaft radius R while the parameter C_c^p remaining at 0.

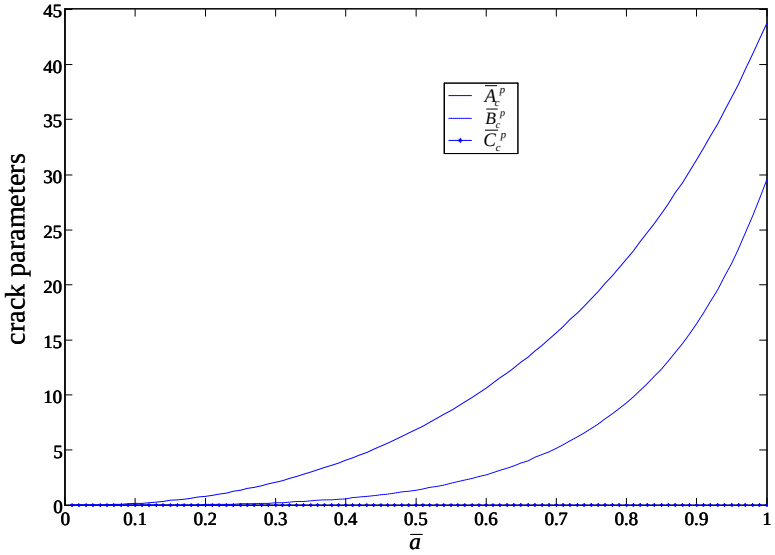

Fig. 3.1 Open crack parameters variation

It is also noticed that the parameter in straight-open direction (y_c in Fig. 2.9) is always larger than that in shearing-open direction (z_c in Fig. 2.9), which means the stiffness reduction in y_c direction is larger. Furthermore, the crack does not cause any stiffness reduction in cross-coupling direction in crack coordinate system. In another words, no stiffness reduction is produced in cross-coupling direction when the crack coordinate system coincides with rotating frame {c}.

Next, the stiffness variation in rotating frame {c} is analyzed while the crack angle θ varying from 0 to 2π. Here, we define the stiffness reduction parameters in c_2, c_3 and the cross-coupling directions as $A_{c\theta}^p$, $B_{c\theta}^p$ and $C_{c\theta}^p$, respectively.

$$\begin{aligned} A_{c\theta}^p &= 2A_c^p \cos^2\theta + 2B_c^p \sin^2\theta - 2C_c^p \sin 2\theta \\ B_{c\theta}^p &= 2A_c^p \sin^2\theta + 2B_c^p \cos^2\theta + 2C_c^p \sin 2\theta \\ C_{c\theta}^p &= (A_c^p - B_c^p)\sin 2\theta + 2C_c^p \cos 2\theta \end{aligned} \tag{3.3}$$

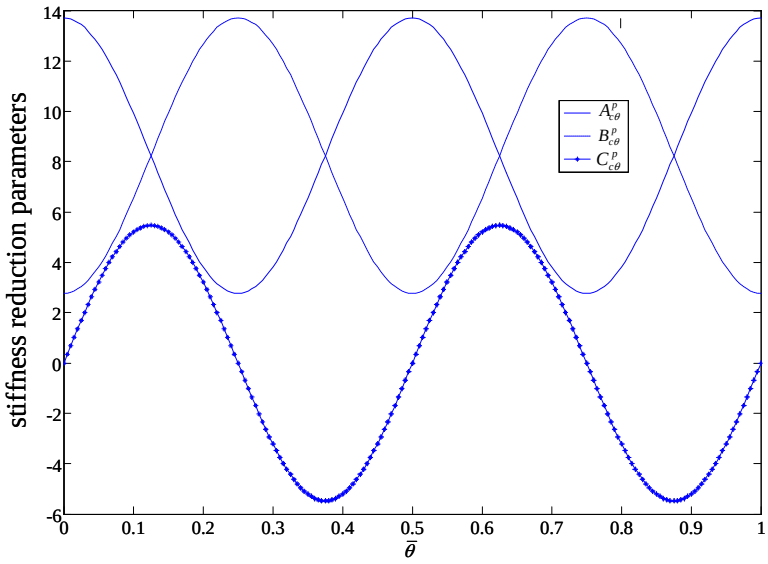

Fig. 3.2 Stiffness reduction parameters for $\bar{a} = 0.5$

With the change of crack angle, the stiffness reduction parameters vary periodically with the period π. It can be found that the summation of parameters in two lateral directions is a certain number for a crack with certain depth no matter what the crack angle is. In addition, the parameter in cross-coupling direction is zero when the crack angle is $n\pi/2$ (n=0, 1, 2,…) and it will reach its maximum or minimum value when the crack angle is $n\pi/4$ (n=1, 3, 5,…).

From the point of view of moment of inertia, the moment of inertia at crack position is reduced by $\Delta I_{y\theta}$, $\Delta I_{z\theta}$ *and* $\Delta I_{yz\theta}$ with respect to rotating frame {c}. According to transformation principle of moment of inertia from crack coordinate system to rotating frame {c} (Fig. 2.9), $\Delta I_{y\theta}$, $\Delta I_{z\theta}$ and $\Delta I_{yz\theta}$ have the relation as following:

$$2\Delta I_{yz\theta} = (\Delta I_{z\theta} - \Delta I_{y\theta})\tan(2\theta) \tag{3.4}$$

We can see from Eq. (3.4) three parameters are needed to describe the damage because of their nonlinear relation. Thus, it is assumed that the change of stiffness due to damage is approximated as

$$\Delta K = \sum_{j=1}^{Ne}\left(\delta_{y,j}\Delta K^{e}_{y,j} + \delta_{z,j}\Delta K^{e}_{z,j} + \delta_{yz,j}\Delta K^{e}_{yz,j}\right) \tag{3.5}$$

where N_e is number of elements, and $\Delta K^{e}_{y,j}$, $\Delta K^{e}_{z,j}$ and $\Delta K^{e}_{yz,j}$ are stiffness perturbation matrices in y, z, and cross-coupling directions of j^{th} element, respectively; $\delta_{y,j}$, $\delta_{z,j}$ and $\delta_{yz,j}$ describe the stiffness reduction of j^{th} element in y, z, and coupling directions respectively, which have the relation of

$$2\delta_{yz,j} = (\delta_{y,j} - \delta_{z,j})\tan(2\theta) \tag{3.6}$$

The stiffness perturbation matrices, and $\Delta K^{e}_{y,j}$, $\Delta K^{e}_{z,j}$ and $\Delta K^{e}_{yz,j}$ can be assigned any perturbation form, such as midpoint, average, etc.

3.3 Floquet Based Damage Identification of Time-Invariant System

In this section, the Floquet based damage identification method is developed for time-invariant rotor system as shown in Fig. 3.3.

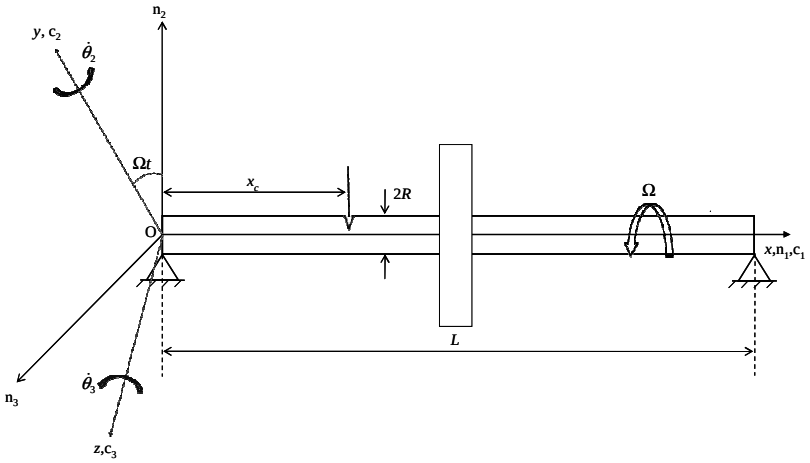

Fig. 3.3 Time-invariant shaft system

3.3.1 Damage Identification Algorithm

To develop the damage detection methodology, the equations-of-motion (2.39) is recast into the following state-space form with state vector $\mathbf{x} = [q^T \quad \dot{q}^T]^T \in \Re^{N_x \times 1}$

$$\dot{\mathbf{x}} = \left(\mathbf{A} + \sum_{k=1}^{N_d} \Delta\mathbf{A}_k \delta_k \right) \mathbf{x} \tag{3.7}$$

Here the system and damage matrices, $\mathbf{A}$, and $\Delta\mathbf{A}_k$, are given as:

$$\mathbf{A} = \begin{bmatrix} 0 & I \\ -M_s^{-1}K_s & -M_s^{-1}(C_s + G_s) \end{bmatrix} \qquad \Delta\mathbf{A}_k = \begin{bmatrix} 0 & 0 \\ -M_s^{-1}K_{c\theta}^k & 0 \end{bmatrix} \tag{3.8}$$

where N_d is the number of damage. The homogeneous solution of the linear system can be expressed as

$$\mathbf{x}_i(t) = \mathrm{X}_i e^{\lambda_i t} \tag{3.9}$$

with complex characteristic (Floquet) exponents, $\lambda_i = \alpha_i + j\omega_i$ and corresponding eigenvector, X_i. The following eigenvalue problems whose solutions characterize the nominal and damaged system spectra are given as:

$$[\lambda_i \mathbf{I} - \mathbf{A}]\mathrm{X}_i = \mathbf{0} \tag{3.10}$$

$$[(\lambda_i + \Delta\lambda_i)\mathbf{I} - (\mathbf{A} + \sum_{j=1}^{N_d} \Delta\mathbf{A}_j \delta_j)](\mathrm{X}_i + \Delta\mathrm{X}_i) = \mathbf{0} \tag{3.11}$$

Here, $\Delta\lambda_i$ and $\Delta\mathrm{X}_i$ are damage induced perturbations in the characteristic exponents and mode shapes. Utilizing left and right eigenvector orthogonality, where $\mathrm{Y}_i(t)$ is the left eigenvector,

$$\mathrm{Y}_i^{\,T} \mathrm{X}_j = \delta_{ij} \tag{3.12}$$

Using a 1st order perturbation approach that neglects the effect of $\Delta\mathrm{X}_i$, the damage identification is formulated in terms of the following frequency-shift sensitivity matrix *S*,

$$\begin{aligned} \Delta\boldsymbol{\lambda} &= S\,\boldsymbol{\delta} \\ [S_{ij}] &= \mathrm{Y}_i^{\,T} \Delta\mathbf{A}_j \mathrm{X}_i \end{aligned} \tag{3.13}$$

where $\Delta\boldsymbol{\lambda} = [\Delta\lambda_1 \quad \ldots \quad \Delta\lambda_{Nmeas}]^T$ is a vector of measured Floquet characteristic exponent shifts obtained by comparing FRFs of the damaged and undamaged systems and $\boldsymbol{\delta} = [\delta_1 \quad \ldots \quad \delta_{N_d}]^T$ is the vector of unknown damage parameters which can be estimated in the least-squares sense as

$$\boldsymbol{\delta}_{est} = [S^T S]^{-1} S^T \Delta\boldsymbol{\lambda} \tag{3.14}$$

Using (3.14) as an initial damage estimate, subsequent estimates can be iteratively improved by including the effect of the damage induced modeshape perturbations $\Delta \mathrm{X}_i$. Specifically, based on the k^{th} estimate of the damage parameters $\boldsymbol{\delta}_{est}^{(k)} = [\delta_1^{(k)} \quad \dots \quad \delta_{N_d}{}^{(k)}]^T$, the k^{th} estimate of the damaged system mode shapes $\tilde{\mathrm{X}}_i^{(k)}$ can be determined from

$$[(\lambda_i + \Delta\lambda_i)\mathbf{I} - (\mathbf{A} + \sum_{j=1}^{N_d} \Delta\mathbf{A}_j \delta_j^{(k)})]\tilde{\mathrm{X}}_i^{(k)} = \mathbf{0} \tag{3.15}$$

Using this, the k^{th} estimate of the damage induced mode shape perturbations are $\Delta\tilde{\mathrm{X}}_i^{(k)} = \tilde{\mathrm{X}}_i^{(k)} - \mathrm{X}_i$. Expanding (3.15) and using the estimates $\Delta\tilde{\mathrm{X}}_i^{(k)}$ and $\boldsymbol{\delta}_{est}^{(k)}$ results in the following iterative damage estimation approach.

$$\boldsymbol{\delta}_{est}^{(k+1)} = [S^{(k)^T} S^{(k)}]^{-1} S^{(k)^T} P^{(k)} \Delta\boldsymbol{\lambda} \tag{3.16}$$

with

$$S^{(k)} = [S_{ij}^{(k)}] = \mathrm{Y}_i{}^T \Delta\mathbf{A}_j (\mathrm{X}_i + \Delta\tilde{\mathrm{X}}_i^{(k)}) \tag{3.17}$$

and

$$P^{(k)} = [P_{ij}^{(k)}] = (1 + \mathrm{Y}_i{}^T \Delta\tilde{\mathrm{X}}_i^{(k)})\delta_{ij} \tag{3.18}$$

Since the initial estimate $\boldsymbol{\delta}_{est}^{(1)}$ is determined from (3.14), the damage estimation algorithm only relies on the measured resonance frequency shifts $\Delta\lambda$. Due to limited measurement of the higher frequencies, the number of measured natural frequency shifts is typically less than the total number of damage parameters, i.e. $N_d > N_{meas}$. Thus, (3.14) and (3.16) become under-determined.

To overcome this problem, we use N_{rs} shaft rotating speeds to form the composite estimation matrices $\overline{S}$ and $\overline{P}$ such that the estimation problem becomes over determined

(i.e. $N_{meas}N_{rs} > N_d$) and enables complete estimation of $\boldsymbol{\delta}$ without the need to measure all the frequency shifts, particularly the higher modes.

$$\begin{bmatrix} P(\mathbf{p}_1)\Delta\boldsymbol{\lambda}(\mathbf{p}_1) \\ P(\mathbf{p}_2)\Delta\boldsymbol{\lambda}(\mathbf{p}_2) \\ \vdots \\ P(\mathbf{p}_{N_{rs}})\Delta\boldsymbol{\lambda}(\mathbf{p}_{N_{rs}}) \end{bmatrix} = \begin{bmatrix} S(\mathbf{p}_1) \\ S(\mathbf{p}_2) \\ \vdots \\ S(\mathbf{p}_{N_{rs}}) \end{bmatrix} \boldsymbol{\delta} = \overline{P} \begin{bmatrix} \Delta\boldsymbol{\lambda}(\mathbf{p}_1) \\ \Delta\boldsymbol{\lambda}(\mathbf{p}_2) \\ \vdots \\ \Delta\boldsymbol{\lambda}(\mathbf{p}_{N_{rs}}) \end{bmatrix} = \overline{S}\boldsymbol{\delta} \tag{3.19}$$

To measure the damage identification effectiveness, the actual and estimated crack energy ratios r_i and $\tilde{r}_i$ in the i^{th} shaft damage cell element are

$$r_i = \frac{\sum_{j=1}^{n_m} U_{i,j}^c}{\sum_{j=1}^{n_m} U_{i,j}^e} \quad \text{and} \quad \tilde{r}_i = \frac{\sum_{j=1}^{n_m} \tilde{U}_{i,j}^c}{\sum_{j=1}^{n_m} U_{i,j}^e} \tag{3.20}$$

with

$$\begin{aligned} U_{i,j}^c &= \delta_i \varphi_j^{"T}(x_c)\varphi_j^{"}(x_c) \\ \tilde{U}_{i,j}^c &= \tilde{\delta}_i \varphi_j^{"T}(x_c)\varphi_j^{"}(x_c) \\ U_{i,j}^e &= EI \int_{l_i} \varphi_j^{"T} \varphi_j^{"} dx \end{aligned} \tag{3.21}$$

Here $\tilde{U}_{i,j}^c$, $U_{i,j}^c$, and $U_{i,j}^e$ are the estimated crack strain energy, actual crack strain energy and total shaft damage cell element strain energy associated with the j^{th} system modeshape.

3.3.2 Damage Identification: Open Cracked Shaft

Table 3.1 gives the material property parameters of shaft system.

Table 3.1 Shaft parameters

Parameter	Value	Units
Shaft length, L	0.4	m
Shaft radius, R	0.01	m
Shaft density, ρ	7800	kg/m^3
Shaft elastic modulus, E	200	GPa
Number of shaft modes, n	12	--
Number of damage cells, N	10	--

In order to ensure that all the damage parameters can be estimated from the measured frequency shifts $\Delta\lambda$, multiple shaft rotating speeds are utilized to enrich the data and make the problem overdetermined as shown in equation (3.19). The speed set and two damage sets (not known by the detection algorithm) are given in Table 3.2 and Table 3.3.

Table 3.2 Shaft rotating speed set

	trial 1	trial 2	trial 3	trial 4	trial 5
Ω (Hz)	100	200	300	400	500

Table 3.3 Shaft Crack Damages I

Case I			Case II		
Cell No.	Crack Depth	Crack Angle	Cell No.	Crack Depth	Crack Angle
1	0	N/A	1	0	N/A
2	0	N/A	2	0	N/A
3	0	N/A	3	0	N/A
4	1.0 mm	0°	4	1.0 mm	0°
5	0	N/A	5	0	N/A
6	0	N/A	6	0	N/A
7	0	N/A	7	0.8 mm	60°
8	0	N/A	8	0	N/A
9	0	N/A	9	0	N/A
10	0	N/A	10	0	N/A

Figs. 3.4 and 3.5 show the damage identification results for the damaged shaft system with single transverse open crack (Case I). Specifically, Fig. 3.4 shows the actual and

converged estimates of the crack energy ratios r_i and $\tilde{r}_i$, wherein the blue and red bar denote the actual and estimated energy ratio respectively.

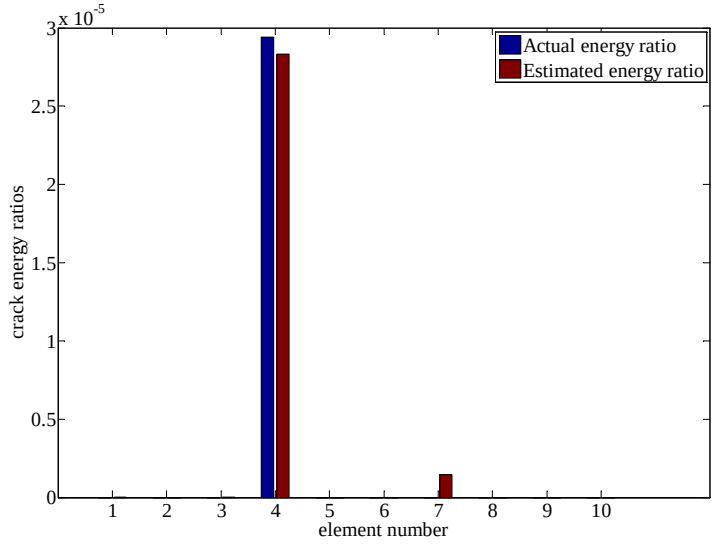

Fig. 3.4 Converged shaft crack damage energy ratio estimates: Case I

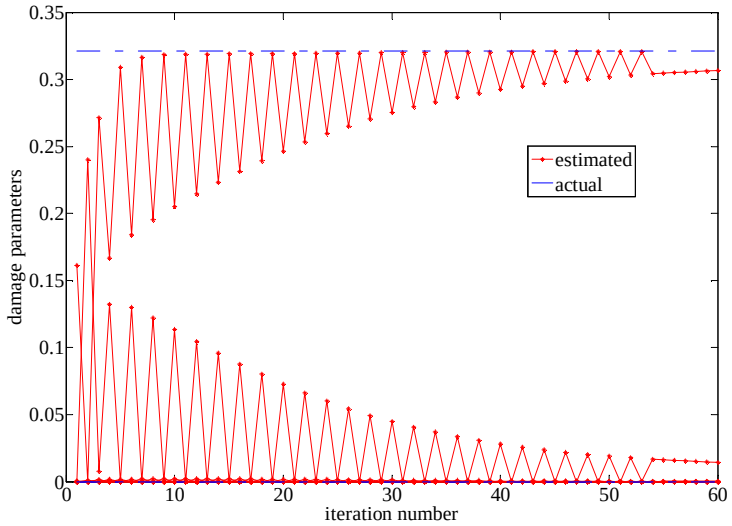

Fig. 3.5 Estimated shaft damage parameters vs iteration number: Case I

Furthermore, Fig. 3.5 shows the shaft damage parameter iteration history, wherein the blue dash line and red star line denote the actual and estimated damage parameters respectively. The results show that the proposed damage identification method works

well to detect single transverse open crack on the shaft system. It can be seen from Fig. 3.4 that the algorithm detects relatively small damage in 7^{th} cell which is in a symmetric position of real damage cell with respect to shaft mid-center. This phenomenon can be further showed in Fig. 3.5 that estimated damage parameters in 4^{th} and 7^{th} cells oscillate at the beginning of iteration and gradually converge to the actual values.

Figs. 3.6 and 3.7 show the damage identification results for the damaged shaft system with duel transverse open cracks (Case II). Specifically Fig. 3.6 shows the actual and converged estimates of the crack energy ratios r_i and $\tilde{r}_i$, wherein the blue and red bar denote the actual and estimated energy ratio respectively.

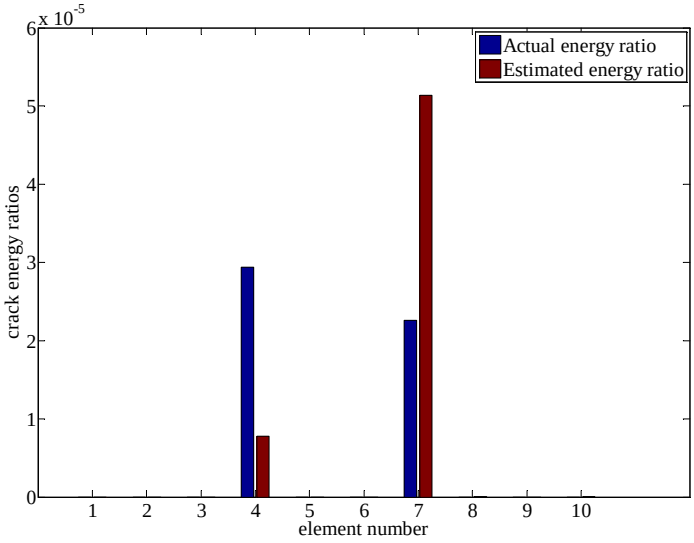

Fig. 3.6 Converged shaft crack damage energy ratio estimates: Case II

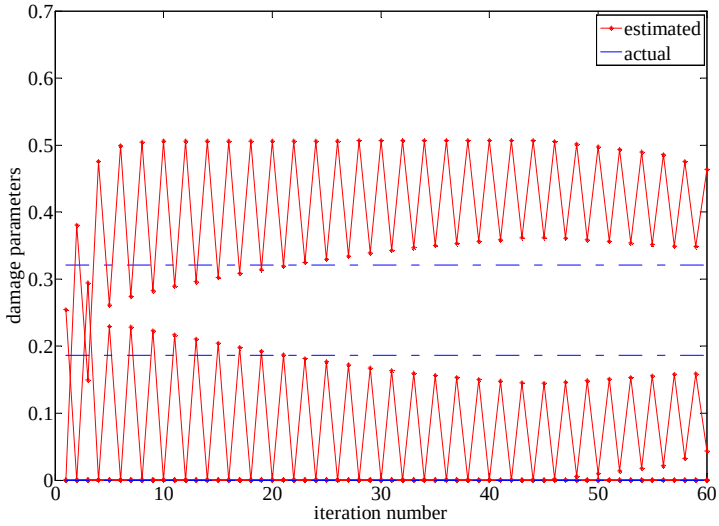

Fig. 3.7 Estimated shaft damage parameters vs. iteration number: Case II

Furthermore, Fig. 3.7 shows the shaft damage parameter iteration history, wherein the blue dash line and red star line denote the actual and estimated damage parameters respectively. The results show that the algorithm fails to detect duel cracks on the shaft system. In Fig. 3.6, we can see that the estimated crack energy ratios are far away from the actual ones for both damaged cells. The estimated damage parameters still oscillate during the iteration, but what is different from the single crack case is that they did not converge to the actual values (as seen in Fig. 3.7). An interesting phenomenon is that the sum of estimates for both damaged cells is almost equal to that of actual values even though the individual estimate is not able to converge. This is caused by some reason so that the algorithm cannot distinguish the multiple cracks, especially for the damages in symmetric cells.

To clarify the reason, we look into the variation of the eigenvalue versus crack location and angle. The eigenvalue shifts for a single cracked shaft system is investigated while the crack location and angle varying.

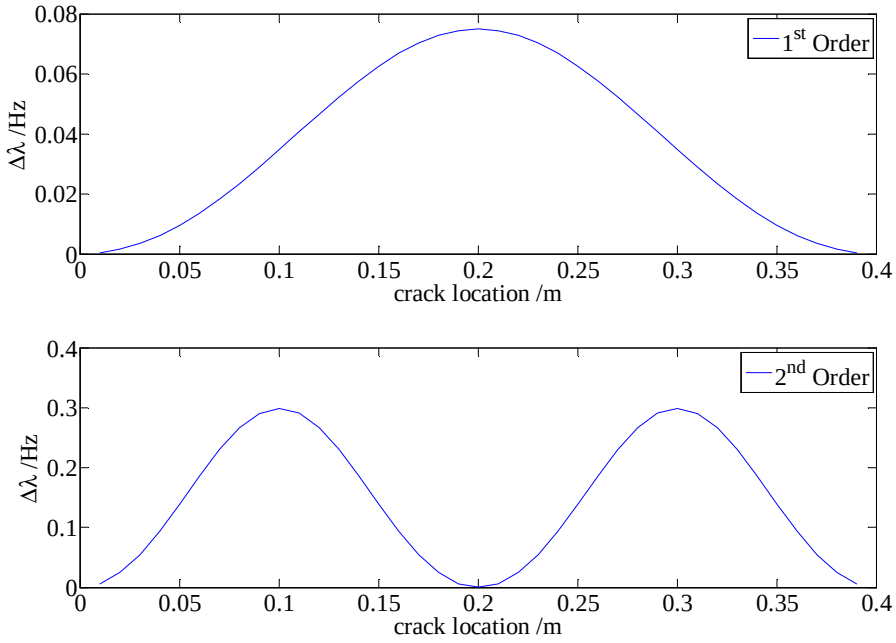

Fig. 3.8 Eigenvalue variations vs. crack location: a=1mm, θ=0°, Ω=100Hz

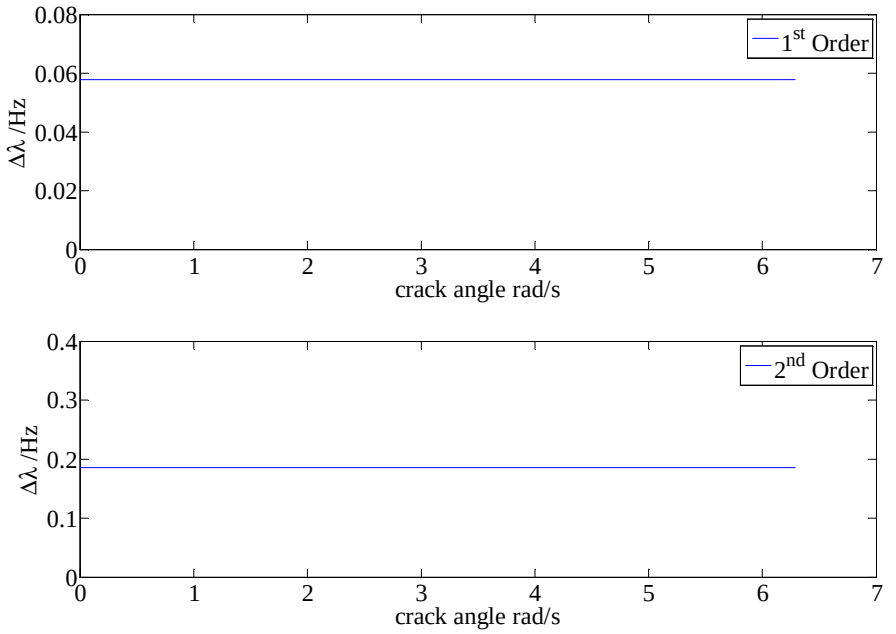

Fig. 3.9 Eigenvalue variations vs. crack angle: a=1mm, x_c=0.14m, Ω=100Hz

The changes of first and second eigenvalues are symmetric with respect to the midpoint of shaft, which means the crack located at the symmetric cells induces the same eigenvalue changes. Due to this reason, the algorithm is not able to distinguish the cracks

in symmetric positions. It is also found that the method is limited to detect the multiple cracks. In Fig. 3.9, it is obvious to see that eigenvalue shifts are independent on the crack angle. No matter what the crack angle is, it does not affect the eigenvalue and therefore current method could not be able to detect the crack angle correctly.

3.3.3 Damage Identification: Open Cracked Shaft with AMB

According to above analysis, we concluded that the damage detection failure is caused by the symmetric structure of shaft system which leads to the Eigen degeneracy. To overcome this problem, an active magnetic bearing (AMB) is introduced to break the symmetry. For simplicity, we assume that AMB device is providing the constant stiffness gains k_{bv} and k_{bw} in rotating frame {c} which makes the whole system time-invariant. The system diagram is shown in Fig. 3.10.

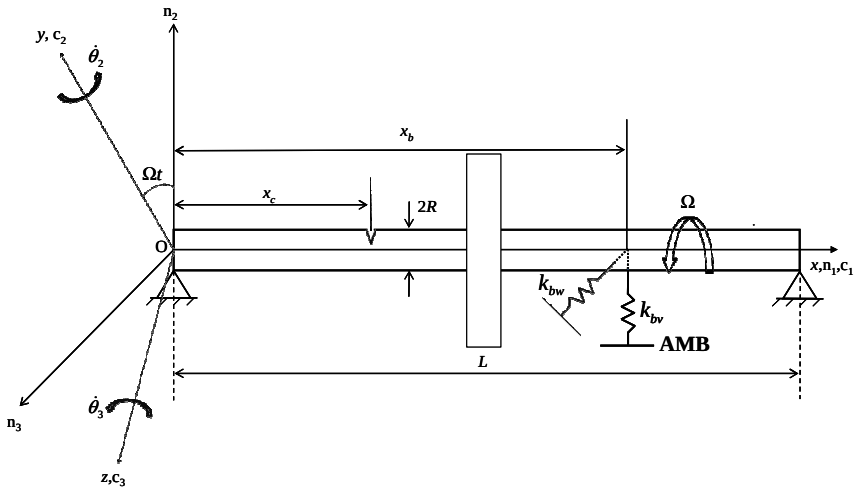

Fig. 3.10 Time-invariant shaft-bearing system

The AMB device is introduced into the shaft system to break the structural symmetry by making the adjustable AMB stiffness values of two lateral directions different. As

shown in Fig. 3.10, k_{bv} and k_{bw} are the adjustable AMB lateral stiffness values and x_b is the AMB location.

Figs. 3.11 and 3.12 show the damage identification results for the damaged shaft – bearing system with single transverse open crack (Case I).

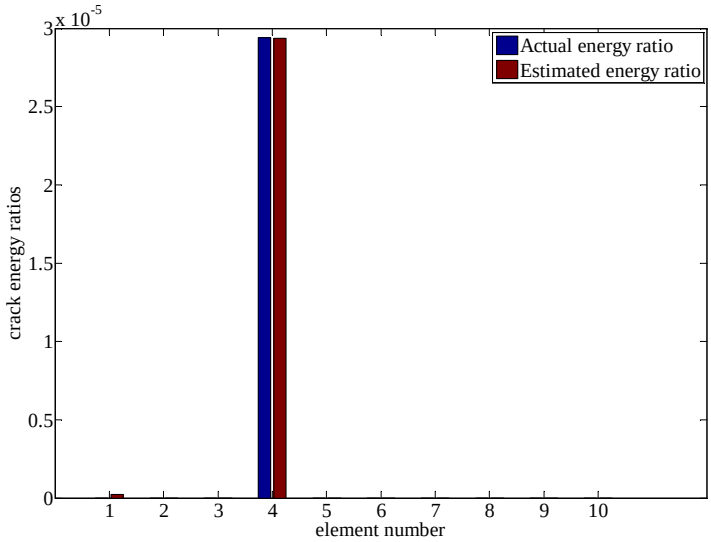

Fig. 3.11 Converged shaft-bearing crack damage energy ratio estimates: Case I

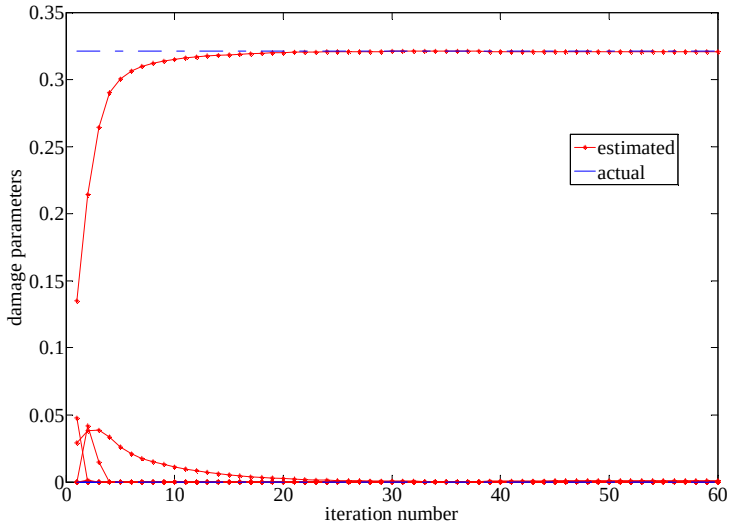

Fig. 3.12 Estimated shaft-bearing damage parameters vs iteration number: Case I

The results show that introducing AMB does improve the damage estimation for single transverse open crack on the shaft system. We can see that the damage in 7th cell estimated in Fig. 3.4 is not showing in Fig. 3.11. In addition, the damage parameter iterations become much smoother and converge much faster to the actual values.

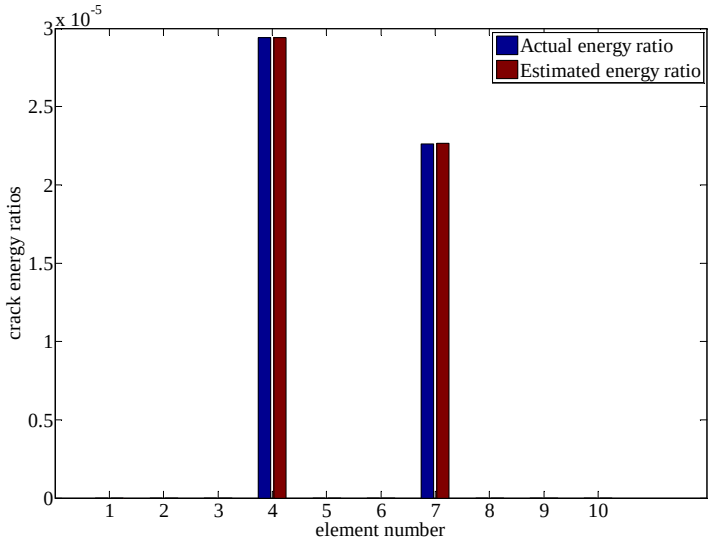

Fig. 3.13 Converged shaft-bearing crack damage energy ratio estimates: Case II

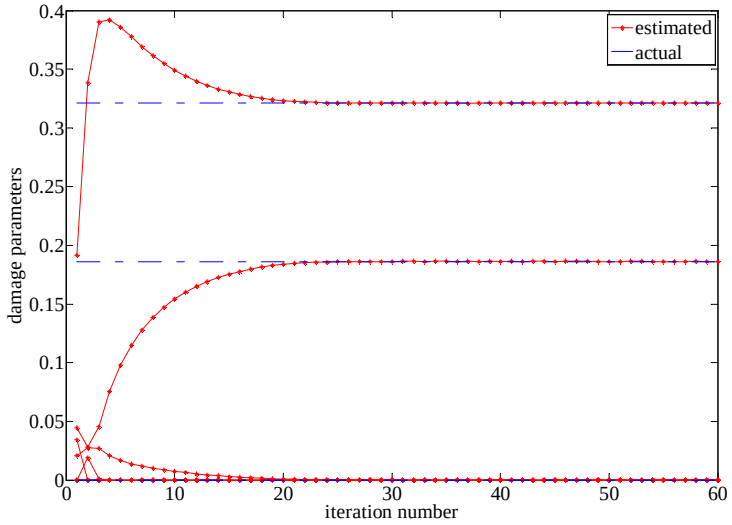

Fig. 3.14 Estimated shaft-bearing damage parameters vs. iteration number: Case II

Figs. 3.13 and 3.14 show the damage identification results for the damaged shaft system with duel transverse open cracks (Case II). Same as case I, the damage estimation

of case II improves greatly. The crack energy ratios and damage parameters quickly go to the actual values without oscillation. Therefore, breaking symmetry plays an essential role in distinguishing the multiple cracks on the shaft system. Similar as the eigenvalue analysis we did in the previous section, we want to study it again to investigate what makes things different.

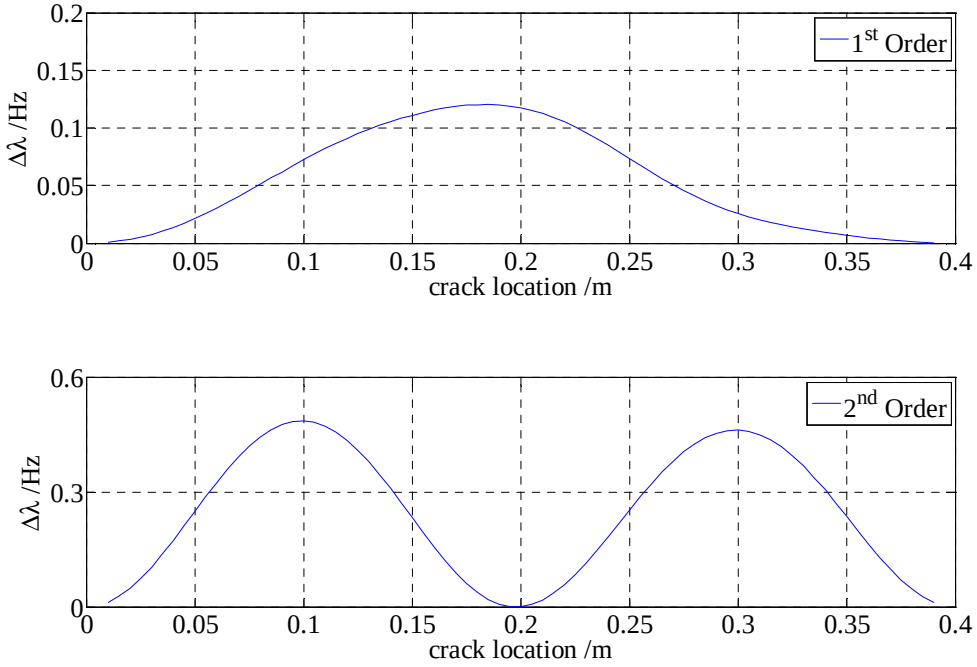

Fig. 3.15 Eigenvalue variations vs. crack location
a=1mm, θ=0°, Ω=100Hz, k_{bv}=10^6N/m, k_{bw}=0N/m, x_b=0.3m

The changes of first and second eigenvalues are not symmetric with respect to the midpoint of shaft since AMB breaks the structural symmetry as shown in Fig. 3.15. In Fig. 3.16, eigenvalue changes in a harmonic way while the crack angle is varying from 0 to 2π. Compare to the system in 3.3.2, the eigenvalue changes are not independent with the crack angle any more. However, crack angle is still not able to detect in this case

because the mapping is not unique from eigenvalue changes to crack angle. We can see from Fig. 3.16 that one $\Delta\lambda$ could have four corresponding crack angles.

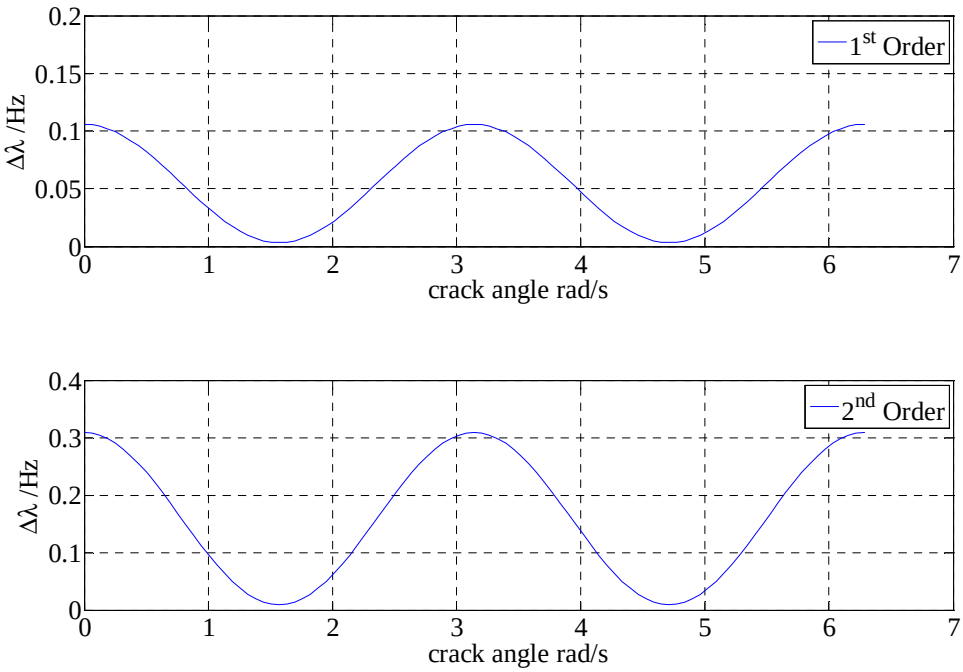

Fig. 3.16 Eigenvalue variations vs. crack angle
a=1mm, x_c=0.14m, Ω=100Hz, k_{bv}=10^6N/m, k_{bw}=0N/m

Although rotating AMB could break the structural symmetry of rotor system and get very good damage estimation results, it is not feasible to provide constant AMB stiffness in rotating frame. Usually, active magnetic bearing is installed in fixed frame and it is easier to provide the constant stiffness in fixed frame which produces the time-varying term in rotating frame. Hence, we are going to develop the damage identification method for shaft system with stationary active magnetic bearing in next section.

3.4 Floquet based Damage Identification of Time-Varying Rotor System

The system studied in this section is a cracked shaft system with active magnetic bearing in stationary coordinate system {n}.

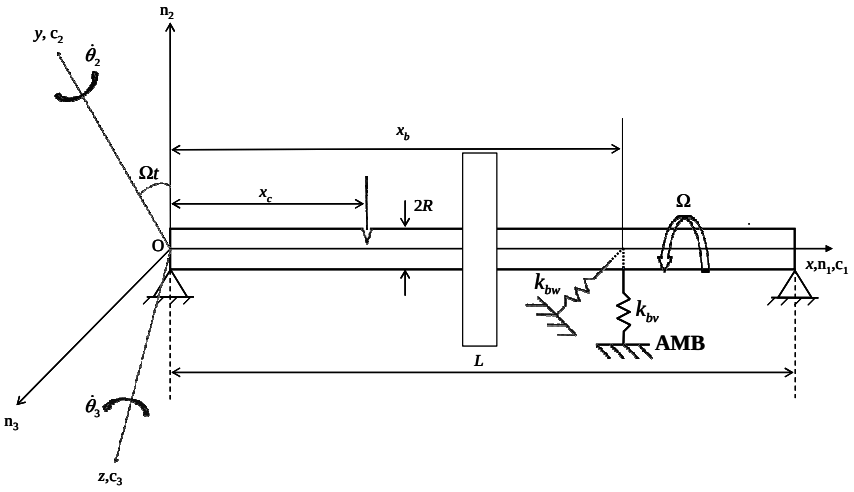

Fig. 3.17 Time-varying shaft-bearing system

3.4.1 Active Bearing Model

In the system, an Active Magnetic Bearing (AMB) is introduced to break the modal symmetry with respect to the center point of shaft, to eliminate symmetry of Eigen modes and to enhance the accuracy of crack detection results. Here the feature of adjustable bearing stiffness or virtual added mass in two lateral directions is used to break the transverse modal symmetry. When the system is perturbed by bearing stiffness, the additional potential energy due to the active bearing in rotating frame {c} is

$$\begin{aligned} U_b &= \frac{1}{2}k_{bv}(v_b\cos(\Omega t) - w_b\sin(\Omega t))^2 \\ &+ \frac{1}{2}k_{bw}(v_b\sin(\Omega t) + w_b\cos(\Omega t))^2 \end{aligned} \tag{3.22}$$

When the system is perturbed by bearing mass, the additional kinetic energy produced by bearing in rotating frame {c} is:

$$T_b = \frac{m_{bv}}{2}([\dot{v}_b - w_b\Omega]\cos(\Omega t) - [\dot{w}_b + v_b\Omega]\sin(\Omega t))^2 + \frac{m_{bw}}{2}([\dot{v}_b - w_b\Omega]\sin(\Omega t) + [\dot{w}_b + v_b\Omega]\cos(\Omega t))^2 \quad (3.23)$$

where $v_b(t)$ and $w_b(t)$ are shaft deflections at the bearing position as measured from fixed frame {n}. Furthermore, k_{bv} and k_{bw} are the adjustable AMB lateral stiffness values and m_{bv} and m_{bw} are synthetic mass values due to acceleration feedback control. The system equations-of-motion are obtained via Lagrange's method and are given as:

$$[M_s + M_b(t)]\ddot{q} + [C_s + G_s]\dot{q} + [K_s + K_b(t) - K_{c\theta}]q = 0 \quad (3.24)$$

with

$$M_b(t) = M_0 + M_{-2}e^{-j2\Omega t} + M_2 e^{j2\Omega t} \quad (3.25)$$

$$K_b(t) = K_0 + K_{-2}e^{-j2\Omega t} + K_2 e^{j2\Omega t} \quad (3.26)$$

Note since the equations are formulated in the rotating frame {c}, both the shaft and the crack damage matrices are time-invariant; however the asymmetric AMB stiffness in the fixed frame introduces periodic parametric terms. The applied asymmetric bearing stiffness and inertia feedback terms are used in the damage detection process to break the symmetries associated with the two transverse shaft deflection planes enabling identification from natural frequency measurements without direct modeshape information.

3.4.2 Stiffness Perturbed Damage Identification Methodology

To develop the damage detection methodology, the equations-of-motion are recast into the following state-space form with state vector $\mathbf{x} = [q^T \quad \dot{q}^T]^T \in \Re^{N_x \times 1}$

$$\dot{\mathbf{x}} = \left(\mathbf{A}(t) + \sum_{k=1}^{N_d} \Delta\mathbf{A}_k(t)\delta_k \right)\mathbf{x} \tag{3.27}$$

Here the periodic system and damage matrices, $\mathbf{A}(t)$, and $\Delta\mathbf{A}_k(t)$, are expanded in the complex exponential series as:

$$\mathbf{A}(t) = \sum_{n=-N_h}^{N_h} \mathbf{A}_n e^{jn\Omega t} \quad \text{and} \quad \Delta\mathbf{A}_k(t) = \sum_{n=-N_h}^{N_h} \Delta\mathbf{A}_{n,k} e^{jn\Omega t} \tag{3.28}$$

Where N_h is the number of system harmonics. In the case of the shaft-bearing system, N_h = 2. Utilizing Floquet theory, the homogeneous solution of the linear periodically time-varying system can be expressed as

$$\mathbf{x}_h(t) = \sum_{k=1}^{N_x} c_k \mathbf{u}_k(t) e^{\lambda_k t} \quad \text{with} \quad \mathbf{u}_k(t) = \sum_{n=-\infty}^{\infty} \mathbf{u}_{k,n} e^{jn\Omega t} \tag{3.29}$$

With complex characteristic (Floquet) exponents, $\lambda_k = \alpha_k + j\omega_k$ and corresponding periodic modeshapes, $\mathbf{u}_k(t)$. After performing harmonic balance, the following hyper-dimensional eigenvalue problems whose solutions characterize the nominal and damaged system spectra are given as.

$$[\lambda_k \hat{\mathbf{I}} - \hat{\mathbf{A}}]\mathbf{U}_k = \mathbf{0} \tag{3.30}$$

$$[(\lambda_k + \Delta\lambda_k)\hat{\mathbf{I}} - (\hat{\mathbf{A}} + \sum_{j=1}^{N_d} \Delta\hat{\mathbf{A}}_j \delta_j)](\mathbf{U}_k + \Delta\mathbf{U}_k) = \mathbf{0} \tag{3.31}$$

Here, $\mathbf{U}_k$ is the Fourier coefficient vector of the k^{th} nominal right eigenvector (modeshape), $\hat{\mathbf{A}}$ and $\Delta\hat{\mathbf{A}}_k$ are the hyper-dimensional nominal system matrix and damage perturbation matrix given by,

$$\hat{\mathbf{A}} = \begin{bmatrix} \ddots & & & \vdots & & & \iddots \\ \cdots & \mathbf{A}_0 - j2\Omega\mathbf{I} & \mathbf{A}_{-1} & \mathbf{A}_{-2} & \cdots & & \\ \cdots & \mathbf{A}_{+1} & \mathbf{A}_0 - j\Omega\mathbf{I} & \mathbf{A}_{-1} & \mathbf{A}_{-2} & \cdots & \\ \cdots & \mathbf{A}_{+2} & \mathbf{A}_{+1} & \mathbf{A}_0 & \mathbf{A}_{-1} & \mathbf{A}_{-2} & \cdots \\ & \cdots & \mathbf{A}_{+2} & \mathbf{A}_{+1} & \mathbf{A}_0 + j\Omega\mathbf{I} & \mathbf{A}_{-1} & \cdots \\ & & \cdots & \mathbf{A}_{+2} & \mathbf{A}_{+1} & \mathbf{A}_0 + j2\Omega\mathbf{I} & \cdots \\ \iddots & & & \vdots & & & \ddots \end{bmatrix} \tag{3.32-a}$$

$$\Delta\hat{\mathbf{A}}_k = \begin{bmatrix} \ddots & & & \vdots & & & \iddots \\ \cdots & \Delta\mathbf{A}_{0,k} & \Delta\mathbf{A}_{-1,k} & \Delta\mathbf{A}_{-2,k} & \cdots & & \\ \cdots & \Delta\mathbf{A}_{+1,k} & \Delta\mathbf{A}_{0,k} & \Delta\mathbf{A}_{-1,k} & \Delta\mathbf{A}_{-2,k} & \cdots & \\ \cdots & \Delta\mathbf{A}_{+2,k} & \Delta\mathbf{A}_{+1,k} & \Delta\mathbf{A}_{0,k} & \Delta\mathbf{A}_{-1,k} & \Delta\mathbf{A}_{-2,k} & \cdots \\ & \cdots & \Delta\mathbf{A}_{+2,k} & \Delta\mathbf{A}_{+1,k} & \Delta\mathbf{A}_{0,k} & \Delta\mathbf{A}_{-1,k} & \cdots \\ & & \cdots & \Delta\mathbf{A}_{+2,k} & \Delta\mathbf{A}_{+1,k} & \Delta\mathbf{A}_{0,k} & \cdots \\ \iddots & & & \vdots & & & \ddots \end{bmatrix} \tag{3.32-b}$$

$$\mathbf{U}_k = \begin{bmatrix} \cdots & \mathbf{u}_{k,-2}{}^T & \mathbf{u}_{k,-1}{}^T & \mathbf{u}_{k,0}{}^T & \mathbf{u}_{k,+1}{}^T & \mathbf{u}_{k,+2}{}^T & \cdots \end{bmatrix}^T \tag{3.33}$$

Furthermore, $\Delta\lambda_k$ and $\Delta\mathbf{U}_k$ are damage induced perturbations in the characteristic exponents and mode shapes. Utilizing left and right eigenvector orthogonality where $\mathbf{v}_i(t)$ is the left periodic eigenvector,

$$\mathbf{v}_k(t) = \sum_{n=-\infty}^{\infty} \mathbf{v}_{k,n} e^{jn\Omega t} \tag{3.34-a}$$

$$\mathbf{v}_i(t)^T \mathbf{u}_j(t) = \delta_{ij} \Rightarrow \mathbf{V}_i^T \mathbf{U}_j = \delta_{ij} \tag{3.34-b}$$

and using a 1st order perturbation approach that neglects the effect of $\Delta\mathbf{U}_k$, the damage identification is formulated in terms of the following frequency-shift sensitivity matrix S,

$$\Delta\boldsymbol{\lambda} = S\,\boldsymbol{\delta} \quad \text{with} \quad [S_{ij}] = \mathbf{V}_i^T \Delta\hat{\mathbf{A}}_j \mathbf{U}_i \tag{3.35}$$

where $\Delta\boldsymbol{\lambda} = [\Delta\lambda_1 \quad \ldots \quad \Delta\lambda_{Nmeas}]^T$ is a vector of measured Floquet characteristic exponent shifts obtained by comparing FRFs of the damaged and undamaged systems and

$\boldsymbol{\delta} = [\delta_1 \quad \dots \quad \delta_{N_d}]^T$ is the vector of unknown damage parameters which can be estimated in the least-squares sense as

$$\boldsymbol{\delta}_{est} = [S^T S]^{-1} S^T \Delta\boldsymbol{\lambda} \tag{3.36}$$

Using (3.36) as an initial damage estimate, subsequent estimates can be iteratively improved by including the effect of the damage induced modeshape perturbation $\Delta\mathbf{U}_i$. Specifically, based on the k[th] estimate of the damage parameters $\boldsymbol{\delta}_{est}^{(k)} = [\delta_1^{(k)} \quad \dots \quad \delta_{N_d}{}^{(k)}]^T$, the k[th] estimate of the damaged system mode shapes $\tilde{\mathbf{U}}_i^{(k)}$ can be determined from

$$[(\lambda_i + \Delta\lambda_i)\hat{\mathbf{I}} - (\hat{\mathbf{A}} + \sum_{j=1}^{N_d} \Delta\hat{\mathbf{A}}_j \delta_j^{(k)})]\tilde{\mathbf{U}}_i^{(k)} = \mathbf{0} \tag{3.37}$$

Using this, the k[th] estimate of the damage induced mode shape perturbations are $\Delta\tilde{\mathbf{U}}_i^{(k)} = \tilde{\mathbf{U}}_i^{(k)} - \mathbf{U}_i$. Expanding (3.31) and using the estimates $\Delta\tilde{\mathbf{U}}_i^{(k)}$ and $\boldsymbol{\delta}_{est}^{(k)}$ results in the following iterative damage estimation approach.

$$\boldsymbol{\delta}_{est}^{(k+1)} = [S^{(k)T} S^{(k)}]^{-1} S^{(k)T} P^{(k)} \Delta\boldsymbol{\lambda} \tag{3.38-a}$$

with

$$S^{(k)} = [S_{ij}^{(k)}] = \mathbf{V}_i^T \Delta\hat{\mathbf{A}}_j (\mathbf{U}_i + \Delta\tilde{\mathbf{U}}_i^{(k)}) \tag{3.38-b}$$

and

$$P^{(k)} = [P_{ij}^{(k)}] = (1 + \mathbf{V}_i^T \Delta\tilde{\mathbf{U}}_i^{(k)})\delta_{ij} \tag{3.38-c}$$

Since the initial estimate $\boldsymbol{\delta}_{est}^{(1)}$ is determined from (3.36), the damage estimation algorithm only relies on the measured resonance frequency shifts $\Delta\boldsymbol{\lambda}$. Note this iterative approach is

very similar to the iterative approach developed in section 3.3 for the time-invariant second order system case.

By taking advantage of the adjustability of the active support stiffness and damping provided by the AMB, the natural frequency shift measurements can be performed at various PD feedback gain settings to enrich the data-set and enable complete estimation of the damage parameters.

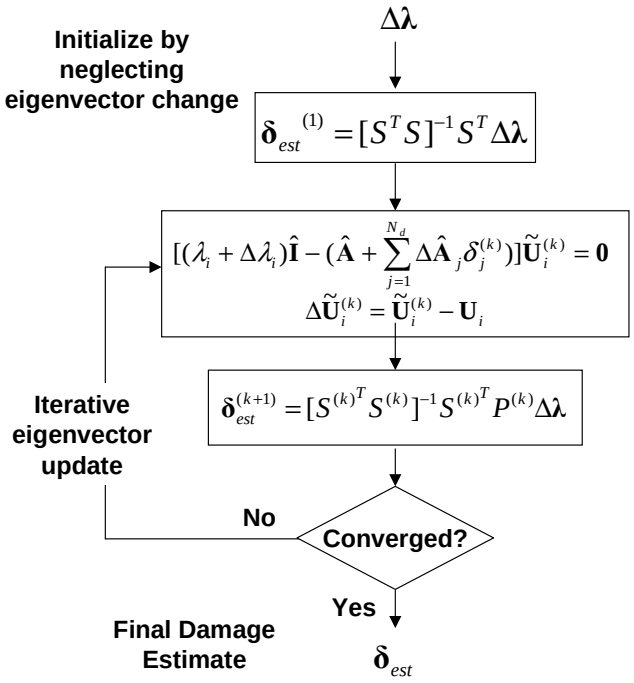

Fig. 3.18 Iterative damage identification process

Specifically, the natural frequencies, $\lambda(\mathbf{p})$, the damage induced frequency-shifts and mode shape perturbations $\Delta\lambda(\mathbf{p})$ and $\Delta\mathbf{U}(\mathbf{p})$ are implicitly functions of the active bearing support stiffness values $\mathbf{p} = [k_{bv}, k_{bw}]$. By tuning $\mathbf{p}$ to N_c different settings, we obtain N_c sets of linearly independent equations which each characterize the effect of the damage $\boldsymbol{\delta}$.

$$\begin{bmatrix} P(\mathbf{p}_1)\Delta\boldsymbol{\lambda}(\mathbf{p}_1) \\ P(\mathbf{p}_2)\Delta\boldsymbol{\lambda}(\mathbf{p}_2) \\ \vdots \\ P(\mathbf{p}_{N_c})\Delta\boldsymbol{\lambda}(\mathbf{p}_{N_c}) \end{bmatrix} = \begin{bmatrix} S(\mathbf{p}_1) \\ S(\mathbf{p}_2) \\ \vdots \\ S(\mathbf{p}_{N_c}) \end{bmatrix} \boldsymbol{\delta} = \overline{P} \begin{bmatrix} \Delta\boldsymbol{\lambda}(\mathbf{p}_1) \\ \Delta\boldsymbol{\lambda}(\mathbf{p}_2) \\ \vdots \\ \Delta\boldsymbol{\lambda}(\mathbf{p}_{N_c}) \end{bmatrix} = \overline{S}\boldsymbol{\delta} \tag{3.39}$$

By forming the composite estimation matrices $\overline{S}$ and $\overline{P}$ and measuring N_{meas} modal frequency-shifts, $\Delta\lambda(\mathbf{p}_i)$, at N_c different control settings such that the estimation problem becomes over determined (i.e. $N_{meas}N_c > N_d$) enables complete estimation of $\boldsymbol{\delta}$ without the need to measure all the frequency shifts, particularly the higher modes.

3.4.3 Virtual Mass Perturbed Damage Identification Methodology

To develop the damage detection methodology, the equations-of-motion are recast into the following state-space form with state vector $\mathbf{x} = [q^T \quad \dot{q}^T]^T \in \Re^{N_x \times 1}$

$$\mathrm{E}(t)\dot{\mathbf{x}} = \left(\mathrm{Z}(t) + \sum_{k=1}^{N_d} \Delta\mathrm{Z}_k(t)\delta_k \right)\mathbf{x} \tag{3.40}$$

Here the periodic system mass, stiffness and damage matrices, E(t), Z(t), and $\Delta\mathrm{Z}_k(t)$, are expanded in the complex exponential series as:

$$\mathrm{E}(t) = \sum_{n=-N_h}^{N_h} \mathrm{E}_n e^{jn\Omega t} \quad \mathrm{Z}(t) = \sum_{n=-N_h}^{N_h} \mathrm{Z}_n e^{jn\Omega t} \ , \ \Delta\mathrm{Z}_k(t) = \sum_{n=-N_h}^{N_h} \Delta\mathrm{Z}_{n,k} e^{jn\Omega t} \tag{3.41}$$

where N_h is the number of system harmonics. In the case of the shaft-bearing system, N_h = 2. Using the same solution as Eq. (3.29) and performing harmonic balance, the followin g hyper-dimensional eigenvalue problems whose solutions characterize the nominal and d amaged system spectra are given as.

$$[\lambda_k \hat{\mathrm{E}} - \hat{\mathrm{Z}}]\mathbf{U}_k = \mathbf{0} \tag{3.42}$$

$$[(\lambda_k + \Delta\lambda_k)\hat{\mathrm{E}} - (\hat{\mathrm{Z}} + \sum_{j=1}^{N_d} \Delta\hat{\mathrm{Z}}_j \delta_j)](\mathbf{U}_k + \Delta\mathbf{U}_k) = \mathbf{0} \tag{3.43}$$

Here, $\hat{\mathrm{Z}}$ and $\hat{\mathrm{E}}$ are the hyper-dimensional nominal system stiffness and mass matrices given by,

$$\hat{\mathrm{Z}} = \begin{bmatrix} \ddots & & \vdots & & & & \iddots \\ \cdots & \mathrm{Z}_0 - j2\Omega\mathrm{E}_0 & \mathrm{Z}_1 - j\Omega\mathrm{E}_1 & \cdots & & & \\ \cdots & \mathrm{Z}_{-1} - j2\Omega\mathrm{E}_{-1} & \mathrm{Z}_0 - j\Omega\mathrm{E}_0 & \mathrm{Z}_1 & \cdots & & \\ & \cdots & \mathrm{Z}_{-1} - j\Omega\mathrm{E}_{-1} & \mathrm{Z}_0 & \mathrm{Z}_1 + j\Omega\mathrm{E}_1 & \cdots & \\ & & \cdots & \mathrm{Z}_{-1} & \mathrm{Z}_0 + j\Omega\mathrm{E}_0 & \mathrm{Z}_1 + j2\Omega\mathrm{E}_1 & \cdots \\ & & & \cdots & \mathrm{Z}_{-1} + j\Omega\mathrm{E}_{-1} & \mathrm{Z}_0 + j2\Omega\mathrm{E}_0 & \cdots \\ \iddots & & & & \vdots & & \ddots \end{bmatrix} \tag{3.44-a}$$

$$\hat{\mathrm{E}} = \begin{bmatrix} \ddots & & \vdots & & & & \iddots \\ \cdots & \mathrm{E}_0 & \mathrm{E}_1 & \cdots & & & \\ \cdots & \mathrm{E}_{-1} & \mathrm{E}_0 & \mathrm{E}_1 & \cdots & & \\ & \cdots & \mathrm{E}_{-1} & \mathrm{E}_0 & \mathrm{E}_1 & \cdots & \\ & & \cdots & \mathrm{E}_{-1} & \mathrm{E}_0 & \mathrm{E}_1 & \cdots \\ & & & \cdots & \mathrm{E}_{-1} & \mathrm{E}_0 & \cdots \\ \iddots & & & & \vdots & & \ddots \end{bmatrix} \tag{3.44-b}$$

By taking the same steps as in section 3.4.2, the iterative damage parameters are obtained by the following equation:

$$\boldsymbol{\delta}_{est}^{(k+1)} = [S^{(k)^T} S^{(k)}]^{-1} S^{(k)^T} P^{(k)} \Delta\boldsymbol{\lambda} \tag{3.45-a}$$

with

$$S^{(k)} = [S_{ij}^{(k)}] = \mathbf{V}_i^T \Delta\hat{\mathbf{Z}}_j (\mathbf{U}_i + \Delta\tilde{\mathbf{U}}_i^{(k)}) \tag{3.45-b}$$

and

$$P^{(k)} = [P_{ij}^{(k)}] = \mathbf{V}_i^T \hat{\mathrm{E}} (\mathbf{U}_i + \Delta\tilde{\mathbf{U}}_i^{(k)}) \tag{3.45-c}$$

Specifically, the natural frequencies, $\lambda(\mathbf{p})$, the damage induced frequency-shifts and mode shape perturbations $\Delta\lambda(\mathbf{p})$ and $\Delta\mathbf{U}(\mathbf{p})$ are implicitly functions of the active bearing

support virtual mass values $\mathbf{p} = [m_{bv}, m_{bw}]$. By tuning $\mathbf{p}$ to N_c different settings, we obtain N_c sets of linearly independent equations which each characterize the effect of the damage $\boldsymbol{\delta}$.

In the case of the shaft/disk system, the feedback tuning plays a critical role in overcoming indeterminacy induced by structural symmetry. Specifically, the axi-symmetric nature of the shaft-disk system results in repeated natural frequency and modeshape pairs, one corresponding to each lateral plane. As a result of this symmetry, each mode pair has identical damage sensitivity to a crack at a given axial location resulting in a rank reduction of the sensitivity formulations. This situation is problematic for the damage identification approach due to the fact that the method only utilizes frequency shift information, and no measured modeshape data.

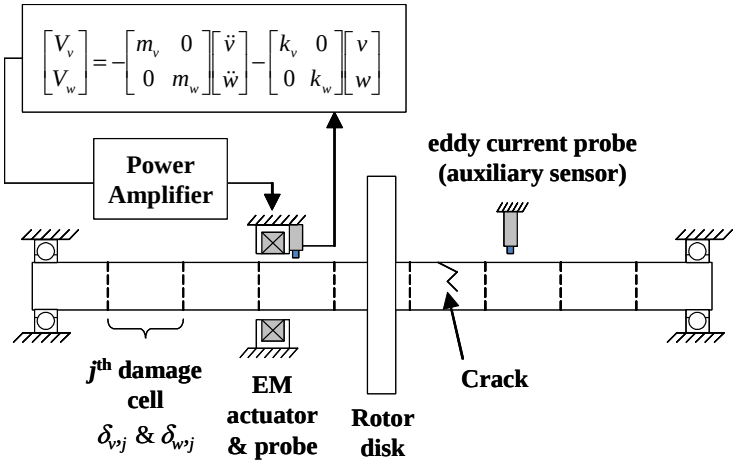

Fig. 3.19 Shaft/Disk system with symmetry breaking feedback control

To address this, a symmetry breaking active feedback control is utilized to remove the modal degeneracy during the damage identification process. Here, as shown in Fig. 3.19, the AMB applies a localized asymmetric position and acceleration feedback control of the form

$$\begin{bmatrix} f_v \\ f_w \end{bmatrix} = -\begin{bmatrix} m_{bv} & 0 \\ 0 & m_{bw} \end{bmatrix}\begin{bmatrix} \ddot{v} \\ \ddot{w} \end{bmatrix} - \begin{bmatrix} k_{bv} & 0 \\ 0 & k_{bw} \end{bmatrix}\begin{bmatrix} v \\ w \end{bmatrix} \tag{3.46}$$

where f_{bv} and f_{bw} are actuation forces applied on the shaft in both lateral directions with acceleration feedback (inertia) gains m_{bv} and m_{bw} and position feedback (stiffness) gains k_{bv} and k_{bw}. By performing the damage identification under multiples sets of asymmetric gain values i.e. $m_{bv} \neq m_{bw}$ and $k_{bv} \neq k_{bw}$, the modal symmetry is broken and (3.39) can be rendered fully determinate.

3.4.4 AMB Stiffness and Virtual Mass Tuning

The aim of tuning AMB stiffness is to gather more frequency shifts which can be used for damage estimation. We can achieve this goal by looking for the suitable AMB stiffness ranges in which the frequencies shift strongly. To choose a suitable set of AMB stiffness and virtual mass tuning gains, it is proposed that they should be selected from the range in which there is strong frequency-shift damage sensitivity.

Figs. 3.20 and 3.21 show the natural frequency variation due to a 1 mm crack as a function of crack location and AMB stiffness gain k_{bv} (with $k_{bw} = 0$). Here Figs. 3.20 and 3.21 show the 1st and 2nd mode variation of the non-rotating shaft (Ω=0 RPM). Regardless of damage location along the shaft (i.e. the damage element number), the 1st and 2nd mode natural frequencies are most sensitive to damage for AMB stiffness values in the range [10^5 - 10^8] N/m.

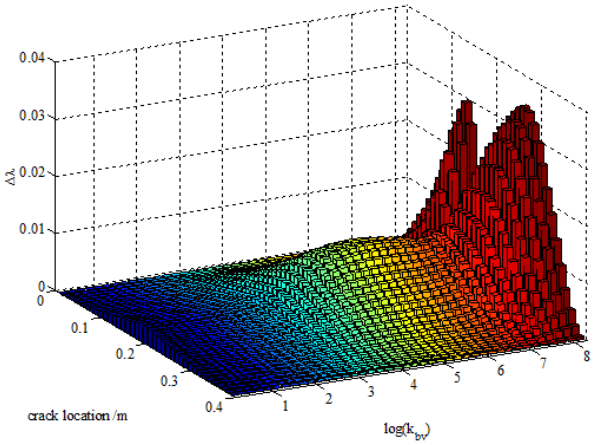

Fig. 3.20 Natural frequency variation due to 1 mm crack vs AMB stiffness gain k_{bv} and damage location with k_{bw} = 0 N/m, Ω = 0 RPM, AMB location $x = 0.375L$, 1st mode

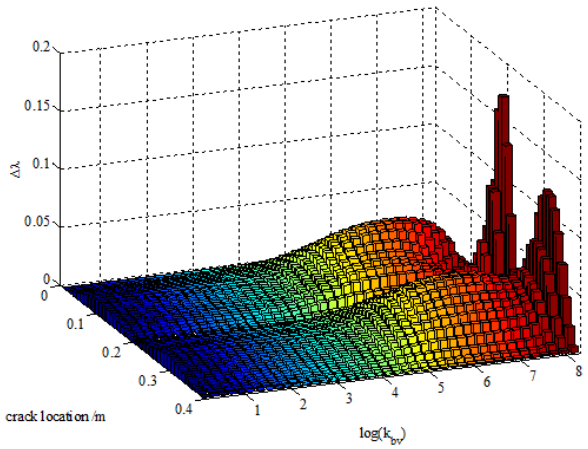

Fig. 3.21 Natural frequency variation due to 1 mm crack vs AMB stiffness gain k_{bv} and damage location with k_{bw} = 0 N/m, Ω = 0 RPM, AMB location $x = 0.375L$, 2nd mode

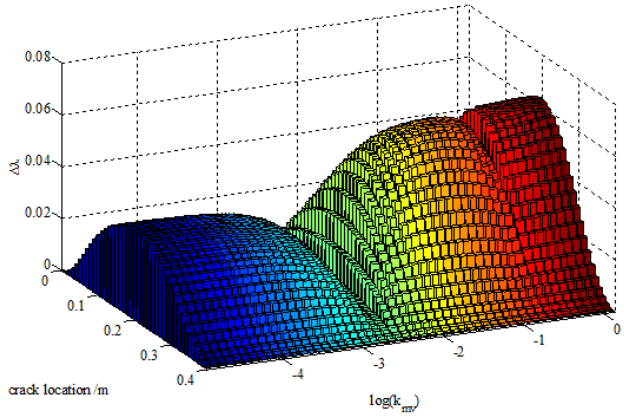

Fig. 3.22 Natural frequency variation due to 1 mm crack vs AMB virtual mass gain m_{bv} and damage location with m_{bw} = 0 Kg, Ω = 0 RPM, AMB location $x = 0.375L$, 1st mode

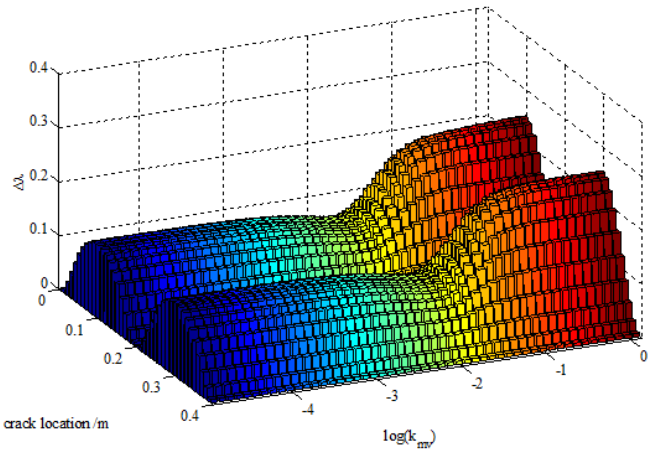

Fig. 3.23 Natural frequency variation due to 1 $\hat{}$mm crack vs AMB virtual mass gain m_{bv} and damage location with m_{bw} = 0 Kg, Ω = 0 RPM, AMB location $x = 0.375L$, 2nd mode

Figs. 3.22 and 3.23 show natural frequency variation of the first two modes induced by 1mm crack as a function of crack location and virtual mass gain m_{bv} (with $m_{bw} = 0$). We can see from these figures that the frequency shifts have little change when the bearing mass is tuned in the range [10^{-5}~10^{-3}] Kg and fluctuate stronger when the bearing stiffness is tuned in the range from [10^{-2}~10^{-1}] Kg.

Using this range as a guide, two different sets of AMB active stiffness/mass tuning gains are utilized in the damage identification process. Most critically, the first tuning set consists of purely symmetric AMB stiffness/mass gains while the second set consists of asymmetric stiffness/mass gains. These two tuning sets are given in Tables 3.4 and 3.5.

Table 3.4 Symmetric AMB stiffness tuning set

	trial 1	trial 2	Trial 3	trial 4
k_{bv} (N/m)	0	10^5	10^6	10^7
k_{bw} (N/m)	0	10^5	10^6	10^7
m_{bv} (Kg)	0	0.01	0.05	0.1
m_{bw} (Kg)	0	0.01	0.05	0.1

Table 3.5 Asymmetric AMB stiffness tuning set

	trial 1	trial 2	Trial 3	trial 4
k_{bv} (N/m)	10^5	0	10^7	10^5
k_{bw} (N/m)	0	10^5	10^5	10^7
m_{bv} (Kg)	0.1	0	0.05	0.1
m_{bw} (Kg)	0	0.1	0.1	0..05

3.4.5 Case Study

In this section, a damage case is studied using two stiffness/mass tuning sets proposed in section 3.4.4. Table 3.6 shows the damage parameters.

Table 3.6 Shaft Crack Damages II

Cell No.	Crack Depth	Crack Angle
1	0.1 mm	0°
2	0.2 mm	80°
3	0.3 mm	160°
4	0.4 mm	240°
5	0.5 mm	320°
6	0.6 mm	10°
7	0.7 mm	80°
8	0.8 mm	60°
9	0.9 mm	40°
10	1.0 mm	20°

(a) Stiffness tuning sets

Figs. 3.24 and 3.25 show the damage identification results for the symmetric and asymmetric stiffness tuning sets. Specifically, Figs. 3.24-a and 3.25-a show the actual and converged estimates of the crack energy ratios r_i and $\tilde{r}_i$ of symmetric and asymmetric stiffness tuning sets, respectively. Figs. 3.24-b and 4.25-b show the shaft damage parameter iteration history for the symmetric and asymmetric stiffness tuning sets, respectively.

It can be obtained from Eq. (2.40) that a transverse crack on the shaft-bearing system induces stiffness reduction in both lateral directions and their cross-coupling direction.

The sum of reduction in both lateral directions is invariant for a given crack depth and the stiffness cross-coupling depends on the crack phase angle. Since the Floquet based method is independent of the orientation angle of crack, only two damage parameters are needed per cell to estimate the stiffness reduction of both lateral directions.

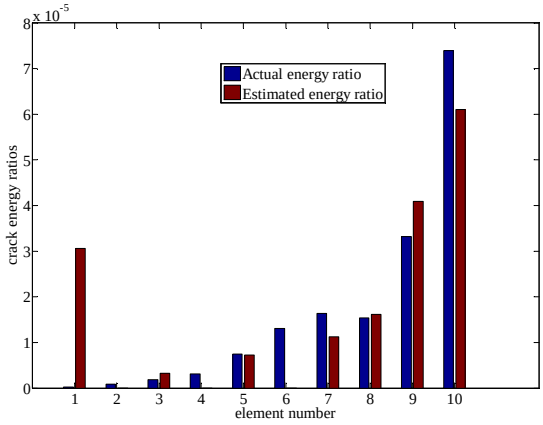

Fig. 3.24-a Converged shaft crack damage energy ratio estimates; symmetric AMB stiffness tuning set, AMB location $x = 0.375L$, $\Omega = 3600$ RPM.

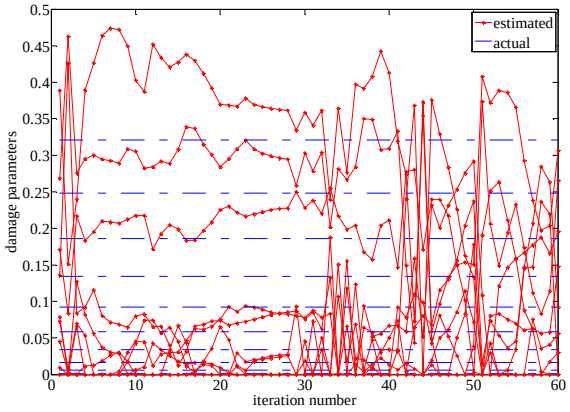

Fig. 3.24-b Estimated shaft damage parameters vs. iteration number; symmetric AMB stiffness tuning set, AMB location $x = 0.375L$, $\Omega = 3600$ RPM.

These results clearly show the importance of utilizing an asymmetric stiffness tuning set. With symmetric AMB stiffness, the damage estimates do not converge to the actual values and the modal degeneracy prevents the estimates form converging. However, with

asymmetric stiffness, the damage estimates indeed converge to their true values within approximately 20 iteration steps.

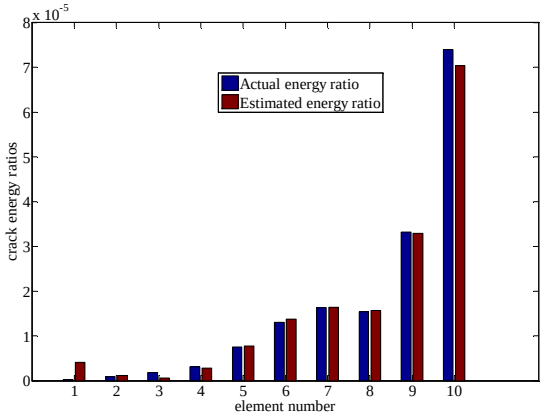

Fig. 3.25-a Converged shaft crack damage energy ratio estimates; asymmetric AMB stiffness tuning set, AMB location $x = 0.375L$, $\Omega = 3600$ RPM.

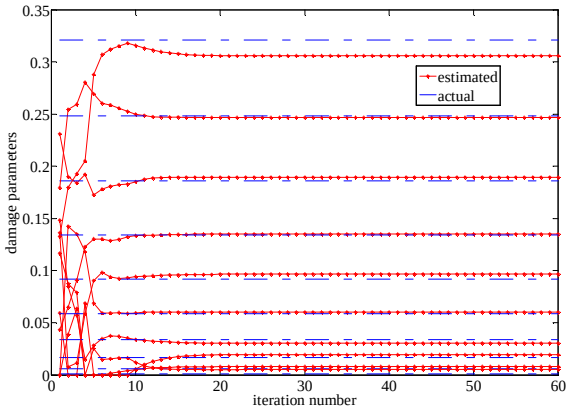

Fig. 3.25-b Estimated shaft damage parameters vs. iteration number; asymmetric AMB stiffness tuning set, AMB location $x = 0.375L$, $\Omega = 3600$ RPM.

(b) Mass tuning sets

Figs. 3.26 and 3.27 show the damage identification results for the symmetric and asymmetric mass tuning sets. Specifically, Figs 3.26-a, 3.27-a show the actual and converged estimates of the crack energy ratios r_i and $\tilde{r}_i$. Figs. 3.26-b and 3.27-b show

the shaft damage parameter iteration history for the symmetric and asymmetric mass tuning sets, respectively.

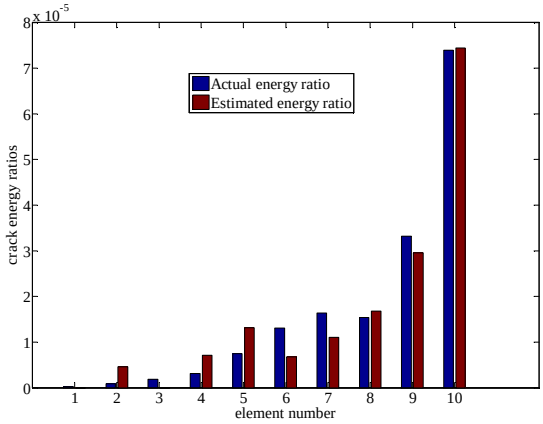

Fig. 3.26-a Converged shaft crack damage energy ratio estimates; symmetric AMB mass tuning set, AMB location $x = 0.375L$, $\Omega = 900$ RPM.

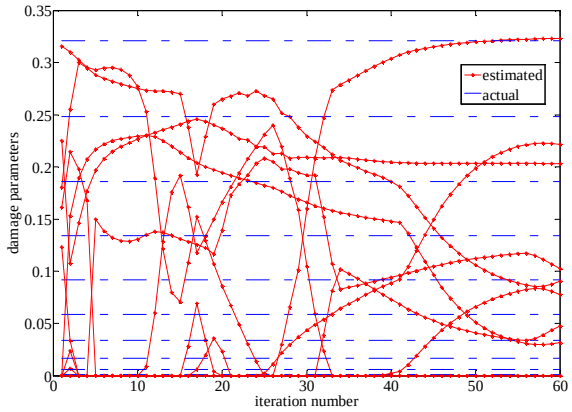

Fig. 3.26-b Estimated shaft damage parameters vs. iteration number; symmetric AMB mass tuning set, AMB location $x = 0.375L$, $\Omega = 900$ RPM.

The similar results are obtained using AMB mass tuning sets, which shows the damage estimates are not able to converge to the actual damage values with symmetric tuning set while they indeed converge to their true values within approximately 20 iteration steps with asymmetric mass tuning set.

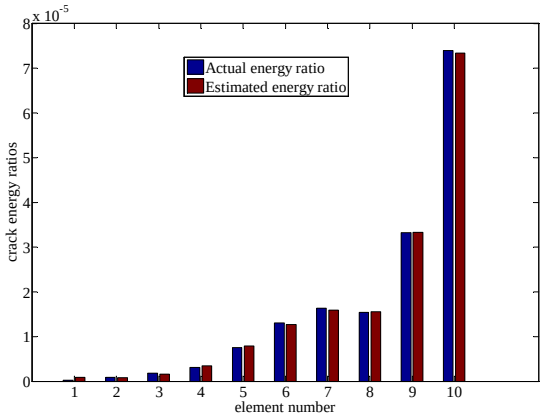

Fig. 3.27-a Converged shaft crack damage energy ratio estimates; asymmetric AMB mass tuning set, AMB location $x = 0.375L$, $\Omega = 900$ RPM.

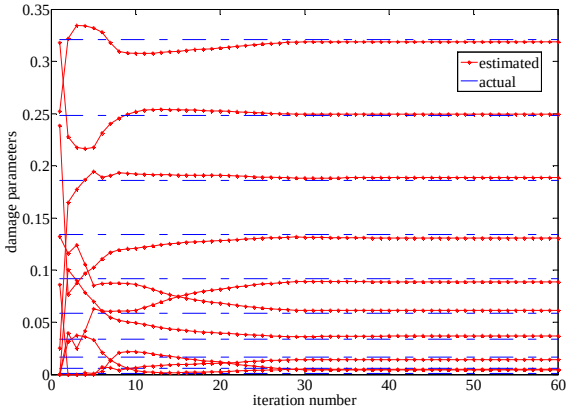

Fig. 3.27-b Estimated shaft damage parameters vs. iteration number; symmetric AMB mass tuning set, AMB location $x = 0.375L$, $\Omega = 900$ RPM

3.4.6 Asymmetric AMB Stiffness Role

It is important to note that the requirement of asymmetric tuning necessarily demands the ability to conduct damage identification of a periodically time-varying system. Specifically, the equations-of-motion become periodically time varying in both the rotating frame (due to AMB stiffness/mass asymmetry) and fixed frame (due to the presence of crack damage). Here, we are going to analyze the role of AMB stiffness/mass tuning in damage identification by studying two simple damage cases listed in Table 3.7.

Table 3.7 Shaft Crack Damages III

Case III			Case IV		
Cell No.	Crack Depth	Crack Angle	Cell No.	Crack Depth	Crack Angle
1	0	N/A	1	0	N/A
2	1.0 mm	0°	2	1.0 mm	0°
3	0	N/A	3	0	N/A
4	0	N/A	4	0	N/A
5	0	N/A	5	0	N/A
6	0	N/A	6	0	N/A
7	0	N/A	7	0	N/A
8	0	N/A	8	0	N/A
9	0	N/A	9	1.0 mm	60°
10	0	N/A	10	0	N/A

Case III is a single crack located at 2nd cell and Case IV is duel cracks located at 2nd with crack angle=0° and 9th cell with crack angle=60°. The symmetric and asymmetric sets, listed in Table 3.8, are used to detect the damage separately.

Table 3.8 Symmetric and asymmetrical sets

Tuning set No.		1	2	3	4
Symmetric sets	k_{bv}(N/m)	10^8	10^7	10^6	0
	k_{bw} (N/m)	10^8	10^7	10^6	0
Asymmetrical sets	k_{bv}(N/m)	10^7	10^6	10^5	0
	k_{bw}(N/m)	10^8	10^7	10^6	0

Fig. 3.28 shows the estimated errors on each cell as a function of bearing locations for case III. Fig. 3.28-a shows the energy ratio error for each cell when the damage is detected by symmetric set and Fig. 3.28-b shows the energy ratio error for each cell when the damage is detected by asymmetric set. The lines depict the error between estimated and actual energy ratio for corresponding i^{th} cell. We can see from Fig. 3.28 that the plots are basically smooth for most of the bearing location and both tuning sets work well for single crack identification.

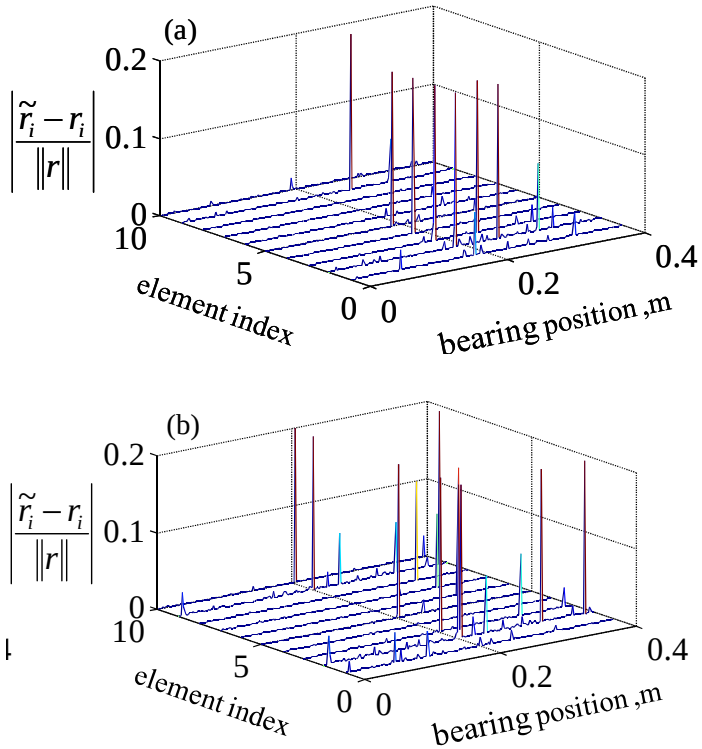

Fig. 3.28 Energy ratio errors for case III (a) Symmetric (b) Asymmetric

Fig. 3.29 shows the estimated errors on each cell as a function of bearing locations for case IV. Fig. 3.29-a shows the energy ratio error for each cell when the damage is detected by symmetric set and Fig. 3.29-b shows the energy ratio error for each cell when the damage is detected by asymmetric set.

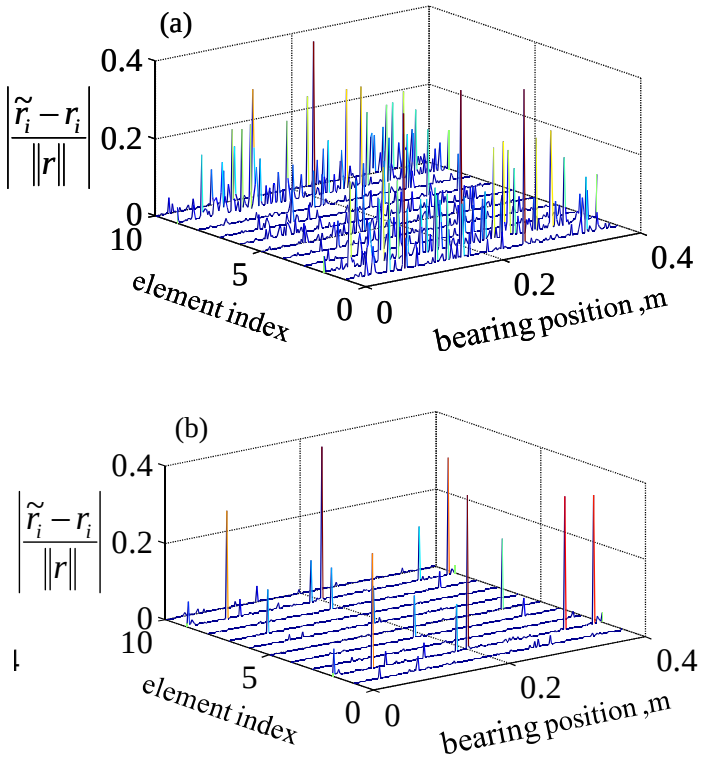

Fig. 3.29 Energy ratio errors for case IV (a) Symmetric (b) Asymmetric

It is clear to observe the role of asymmetrical supports when the system has multiple cracks. Since no modeshape information is utilized in the damage estimation process (only frequency shift data from a single sensor FRF) the shaft modal symmetry in the two lateral planes renders the estimation indeterminate. Physically, this is due to the fact that a given crack can produce the same frequency shift in either lateral mode depending on the crack phase. Hence asymmetric stiffness tuning gains are required to break the modal symmetry.

3.5 Summary

In this chapter, a new vibration-based damage identification methodology for cracked rotor systems with periodically time-varying dynamics is developed and demonstrated on a shaft-bearing system. Since the crack is assumed to be always open during operation,

the crack parameters A_c^p, B_c^p and C_c^p are constant in crack coordinate system $\{x_c, y_c, z_c\}$. Through the coordinate transformation, the crack parameters $A_{c\theta}^p$, $B_{c\theta}^p$ and $C_{c\theta}^p$ are dependent on the crack phase θ in rotating coordinate system {c}. Based on the damage identification results of linear time-invariant rotor system, the usage of natural frequency shifts is not enough to distinguish the crack located on symmetric cells with respect to shaft midpoint. Consequently, Active Magnetic Bearing (AMB) is introduced to break structural symmetry which gives the system stiffness/acceleration feedback. Through proper tuning, AMB is able to provide adjustable stiffness or virtual mass gains to enrich the dataset for damage identification and hence removes the Eigen degeneracy of the symmetric shaft structure. It is found that natural frequency shifts are sensitive in the AMB stiffness range [10^5~10^8] N/m or AMB virtual mass range [10^{-2}~10^{-1}] Kg. With symmetric and asymmetric AMB stiffness/virtual mass gains, the damage parameters are estimated by damage detection algorithm based on least square and eigenvector updating methods. The asymmetric support plays an important role in damage identification which gives more accurate results. However, this method is limited to detect the crack phase, though it works well to estimate the location and depth of transverse open cracks. This problem will be addressed in Chapter IV.

Chapter IV

METHODOLOGY II: SIDEBAND FREQUENCY RESPONSE FUNCTION BASED DAMAGE IDENTIFICATION OF ROTOR SYSTEM WITH OPEN CRACKS

4.1 Introduction

This chapter develops a damage detection method which is aimed to estimate the structural damage by utilizing the influence of cracks on dynamical property. It has been known the crack on the structure will cause the change of natural frequencies. In fact, it also induces the change of frequency response function. This method explores the characteristics of frequency response function (FRF) of time-invariant/varying systems. The same crack model is used in this chapter as chapter III and the cracks are assumed to be open all the time during operation. The Least Square and Newton-Raphson methods are used to solve the initial guess and the following iteration, respectively. Finally, numerical examples demonstrate the effectiveness and accuracy of this method in detecting both the magnitude and phase of the structural damage.

4.2 Damaged FRF Characteristics

First of all, we focus on the transfer function derivation of time-invariant stationary beam system and recast the equations-of-motion into the following state-space form with state vector $\mathbf{x} = [q^T \quad \dot{q}^T]^T \in \Re^{N_x \times 1}$

$$\begin{aligned} \dot{\mathbf{x}} &= \left(\mathbf{A} + \sum_{k=1}^{N_d} \Delta \mathbf{A}_k \right) \mathbf{x} + \mathrm{B}_u \mathbf{u}(t) \\ \mathbf{y} &= \mathbf{C}_y \mathbf{x} \end{aligned} \tag{4.1}$$

where B_u is input matrix and C_y is output matrix. The general form of input and output matrix is given as:

$$\mathrm{B}_u = \begin{bmatrix} \overbrace{0 \quad \cdots \quad 0}^{2n} & M^{-1}\begin{bmatrix} \varphi(x_b) & \overbrace{0 \quad \cdots \quad 0}^{n} \end{bmatrix} \\ \overbrace{0 \quad \cdots \quad 0}^{2n} & M^{-1}\begin{bmatrix} \overbrace{0 \quad \cdots \quad 0}^{n} & \varphi(x_b) \end{bmatrix} \end{bmatrix}^T \tag{4.2}$$

$$\mathbf{C}_y = \begin{bmatrix} \varphi(x_s) & \overbrace{0 \quad \cdots \quad 0}^{n} & \overbrace{0 \quad \cdots \quad 0}^{2n} \\ \overbrace{0 \quad \cdots \quad 0}^{n} & \varphi(x_s) & \overbrace{0 \quad \cdots \quad 0}^{2n} \end{bmatrix} \tag{4.3}$$

where M is the mass matrix, x_b is the input location and x_s is the sensor location. Here, the external excitation **u(t)** are expanded in the complex exponential series as:

$$\mathbf{u}(t) = \mathbf{u}e^{j\omega t} \tag{4.4}$$

Then, the solution of the system can be expressed as

$$\mathbf{x}(t) = \mathrm{X}e^{j\omega t} \tag{4.5}$$

Substituting Eq. (4.2) and (4.3) back into Eq. (4.1), the transfer function of damaged system is given as:

$$\tilde{\mathbf{T}}_{yu} = \mathbf{C}_y(j\omega\mathbf{I} - \mathbf{A} - \sum_{k=1}^{N_d}\Delta\mathbf{A}_k)^{-1}\mathbf{B}_u \tag{4.6}$$

To study the characteristics of transfer function, the transfer function is calculated for the damaged beam system as shown in Fig. 4.1. The system is assumed to be stationary and have a 1mm crack with 0 crack angle.

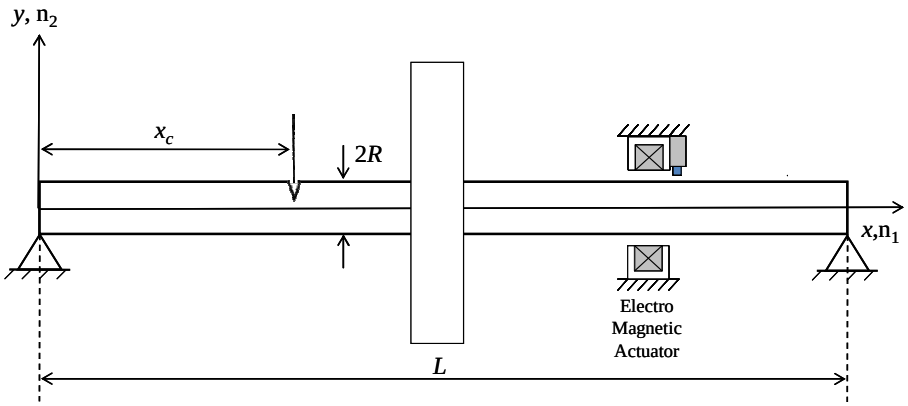

Fig. 4.1 Non-rotating beam with EM actuator for interrogation

Fig. 4.2 shows $|\Delta T_{yu}|$ variations while the excitation frequency varying from 0 to 1000 Hz. The blue and red line denotes the transfer function difference observed at the sensor location x_s in two lateral directions, respectively. The transfer function shifts ΔT_{yu} are obtained by subtracting the transfer function of nominal system from the damaged transfer function. It is obvious to see that $|\Delta T_{yu}|$ have peaks when the system is excited near resonance.

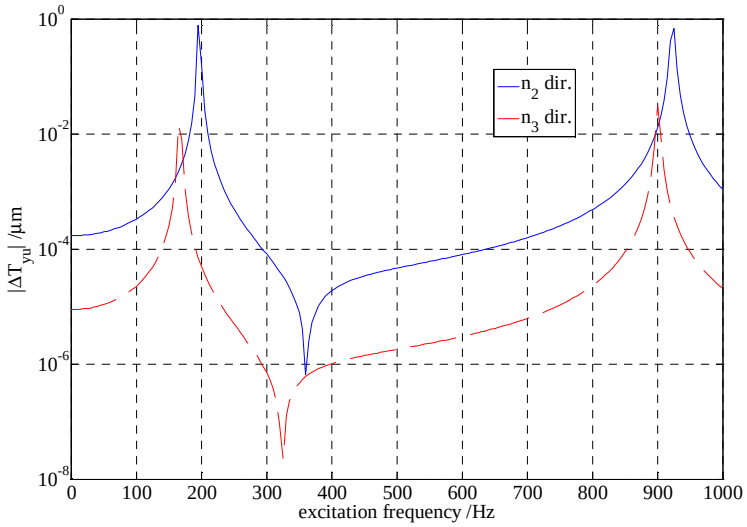

Fig. 4.2 $|\Delta T_{yu}|$ variations vs. excitation frequency;
x_f=3/4L, x_s=1/4L, a=1mm, x_c=0.14m

Next, we investigate how the magnitude and phase of transfer function change versus crack location and angle. Fig. 4.3 and 4.4 show the magnitude and phase of transfer function shifts as a function of crack location for the shaft-disk system with a 1mm transverse crack.

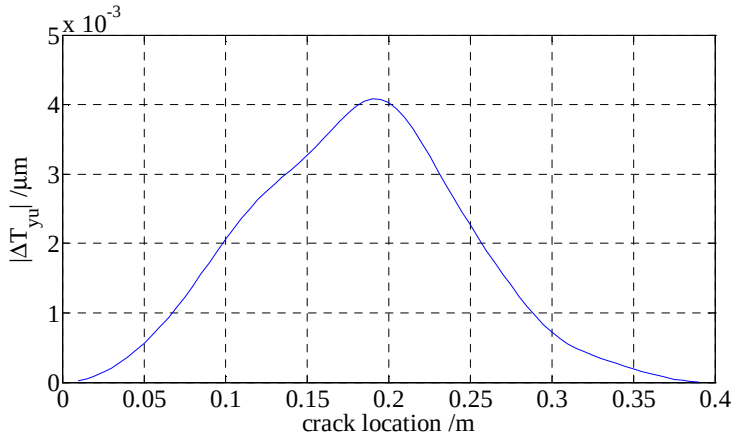

Fig. 4.3 $|\Delta T_{yu}|$ variations vs. crack location;
x_f=3/4L, x_s=1/4L, a=1mm, ω=170 Hz

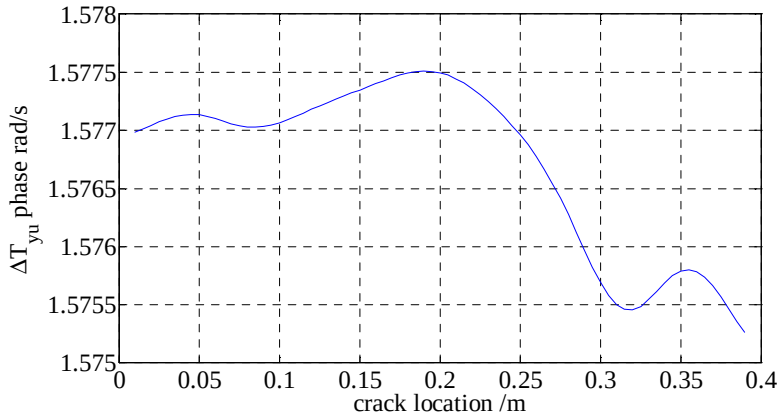

Fig. 4.4 ΔT_{yu} phases vs. crack location;
x_f=3/4L, x_s=1/4L, a=1mm, ω=170 Hz

Unlike the symmetric eigenvalue changes with respect to the midpoint of the shaft in Fig. 3.8, the magnitude and phase of ΔT_{yu} is not symmetric which eliminate the limitation

of symmetric structure of rotor system and therefore makes it possible to distinguish the cracks located at symmetric cells.

In Chapter III, we concluded that the eigenvalue shifts are independent of the crack angle, which means the damage detection algorithm based on the Floquet theory is not able to detect the crack angle of the cracks. Thus, it is important to investigate that if the transfer function shifts are affected by the crack angle. A 1mm crack with varying angle is put on a fixed location on the shaft-disk system and the transfer function is observed in n_2 and n_3 directions while the system is excited in n_2 direction. Fig. 4.5 shows the magnitude and phase of ΔT_{yu} in n_2 direction as a function of crack angle. Fig. 4.6 shows the magnitude and phase of ΔT_{yu} in n_3 direction as a function of crack.

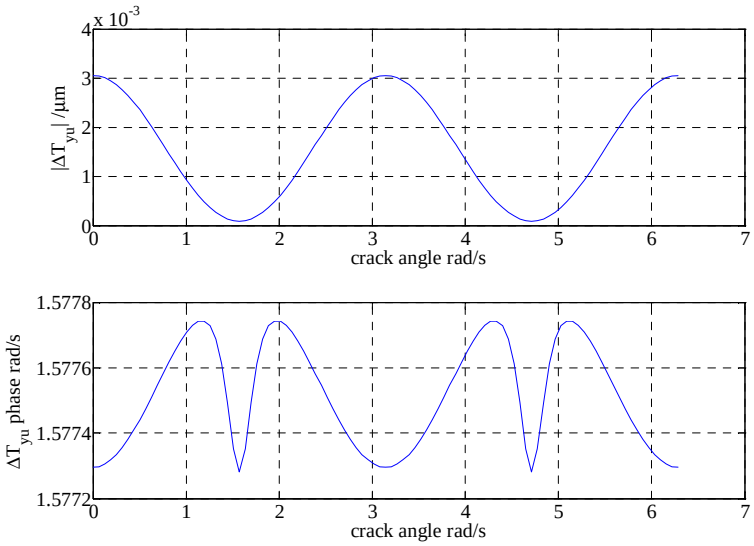

Fig. 4.5 ΔT_{yu} variations vs. crack angle, n_2 dir.;
x_f=3/4L, x_s=1/4L, a=1mm, x_c=0.14m, ω=170 Hz

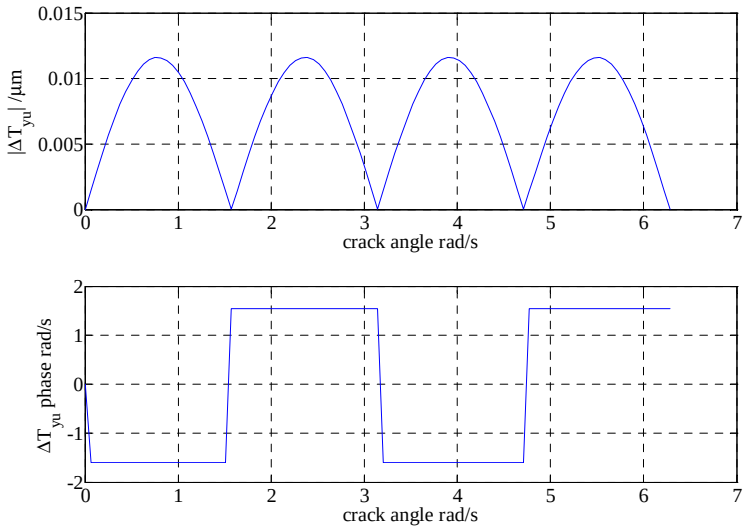

Fig. 4.6 ΔT_{yu} variations vs. crack angle, n_3 dir.;
x_f=3/4L, x_s=1/4L, a=1mm, x_c=0.14m, ω=170 Hz

In Fig. 4.5, the magnitude and phase of ΔT_{yu} are symmetrically distributed and periodically changing, which could not tell the difference of auxiliary angle. For example, a crack with crack angle 1/3π can not be distinguished from a crack whose angle is 2/3π only using ΔT_{yu} observed in n_2 direction. However, phase of ΔT_{yu} behaves like step function and is not symmetric any more in n_3 direction (Fig. 4.6), which enables the possibility of identifying the crack angle.

4.3 Newton-Raphson Method

4.3.1 Introduction

The Newton-Raphson method [155], or Newton Method, is a powerful technique for solving equations numerically. Like so much of the differential calculus, it is based on the simple idea of linear approximation. The Newton Method, properly used, usually homes in on a root with devastating efficiency.

Let $f(x)$ be a well-behaved function, and let r be a root of the equation $f(x) = 0$. We start with an estimate x_0 of r. From x_0, we produce an improved-we hope-estimate x_1. From x_1, we produce a new estimate x_2. We go on until we are 'close enough' to r--or until it becomes clear that we are getting nowhere. The above general style of proceeding is called iterative. Of the many iterative root-finding procedures, the Newton-Raphson method, with its combination of simplicity and power, is widely used.

4.3.2 Newton-Raphson Iteration

Let x_0 be a good estimate of r and let $r = x_0 + h$. Since the true root is r, and $h = r - x_0$, the number h measures how far the estimate x_0 is from the truth.

Since h is 'small', we can use the linear (tangent line) approximation to conclude that

$$0 = f(r) = f(x_0 + h) \approx f(x_0) + hf'(x_0) \tag{4.7}$$

and therefore, unless $f'(x_0)$ is close to 0,

$$h \approx -\frac{f(x_0)}{f'(x_0)} \tag{4.8}$$

It follows that

$$r = x_0 + h \approx x_0 - \frac{f(x_0)}{f'(x_0)} \tag{4.9}$$

Our new improved estimate x_1 of r is therefore given by

$$x_1 \approx x_0 - \frac{f(x_0)}{f'(x_0)} \tag{4.10}$$

The next estimate x_2 is obtained from x_1 in exactly the same way as x_1 was obtained from x_0:

$$x_2 \approx x_1 - \frac{f(x_1)}{f'(x_1)} \tag{4.11}$$

Continue in this way. If x_n is the current estimate, then the next estimate x_{n+1} is given by

$$x_{n+1} \approx x_n - \frac{f(x_n)}{f'(x_n)} \tag{4.12}$$

4.3.3 Geometric Interpretation

In the picture below, the curve $y = f(x)$ meets the x-axis at r. Let a be the current estimate of r. The tangent line to $y = f(x)$ at the point $(a, f(a))$ has equation:

$$y = f(a) + (x - a) f'(a) \tag{4.13}$$

Let b be the x-intercept of the tangent line. Then

$$b \approx a - \frac{f(a)}{f'(a)} \tag{4.14}$$

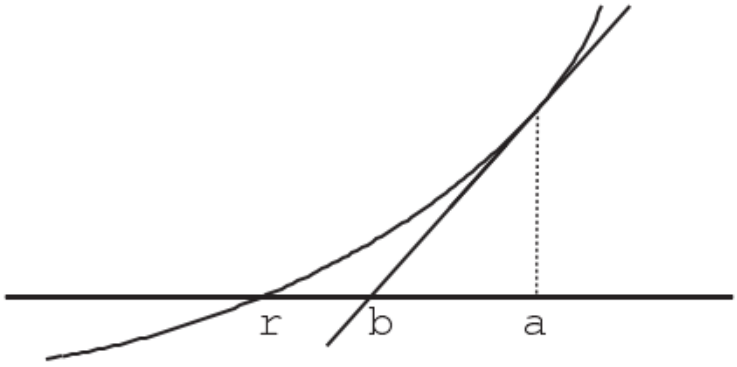

Fig. 4.7 Newton method [155]

Compare with Eq. (4.12): b is just the 'next' Newton-Raphson estimate of r. The new estimate b is obtained by drawing the tangent line at $x = a$, and then sliding to the x-axis along this tangent line. Now draw the tangent line at $(b, f(b))$ and ride the new tangent line to the x-axis to get a new estimate c. Repeat.

We can use the geometric interpretation to design functions and starting points for which the Newton Method runs into trouble. It would be wrong to think of the Newton Method simply in terms of tangent lines. The Newton Method is used to find complex roots of polynomials and roots of systems of equations in several variables, where the geometry is far less clear, but linear approximation still makes sense.

4.3.4 The Convergence of the Newton Method

The argument that led to Equation (4.7) used the informal and imprecise symbol ≈. We probe this argument for weaknesses.

No numerical procedure works for all equations. For example, let $f(x) = x^2 + 17$ if $x \neq 1$, and let $f(1) = 0$. The behavior of $f(x)$ near 1 gives no clue to the fact that $f(1) = 0$. Thus no method of successive approximation can arrive at the solution of $f(x) = 0$. To make progress in the analysis, we need to assume that $f(x)$ is in some sense smooth. We will suppose that $f''(x)$ (exists and) is continuous near r.

The tangent line approximation is an approximation. Let's try to get a handle on the error. Imagine a particle travelling in a straight line, and let $f(x)$ be its position at time x. Then $f'(x)$ is the velocity at time x. If the acceleration of the particle were always 0, then the change in position from time x_0 to time x_0+h would be $hf'(x_0)$. So the position at time x_0+h would be $f(x_0) + hf'(x_0)$—|note that this is the tangent line approximation, which we can also think of as the zero-acceleration approximation.

If the velocity varies in the time from x_0 to $x_0 + h$, that is, if the acceleration is not 0, then in general the tangent line approximation will not correctly predict the displacement at time $x_0 + h$. And the bigger the acceleration is, the bigger the error is. It can be shown

that if f is twice differentiable then the error in the tangent line approximation is $(1/2)h^2f''(c)$ for some c between x_0 and $x_0 + h$. In particular, if $|f''(x)|$ is large between x_0 and $x_0 + h$, then the error in the tangent line approximation is large. Thus we can expect large second derivatives to be bad for the Newton Method.

In the argument for Equation (4.7), from $0 \approx f(x_0)+hf'(x_0)$ we concluded that $h \approx -f(x_0)/f'(x_0)$. This can be quite wrong if $f'(x_0)$ is close to 0: note that 3.01 is close to 3, but $3{:}01/10^{-8}$ is not at all close to $3/10^{-8}$. Thus we can expect first derivatives close to 0 to be bad for the Newton Method.

4.4 FRF based Damage Identification of Time-Invariant System

The basic idea of FRF based damage identification method is to utilize the transfer function shifts between nominal and damaged system to detect the damage. To achieve this, Newton-Raphson method is employed to iterate the initial guess obtained by least square method. The rotor system we studied is assumed to be static in this section and hence it is a time-invariant system as shown in Fig. 4.1.

4.4.1 Damage Identification Algorithm

Starting from Eq. (4.4), the transfer function shift is given as

$$\Delta\mathbf{T}_{yu} = \tilde{\mathbf{T}}_{yu} - \mathbf{T}_{yu} = \mathbf{C}_y\left(i\omega\mathbf{I} - \mathbf{A} - \Delta\mathbf{A}\right)^{-1}\mathbf{B}_u - \mathbf{C}_y\left(i\omega\mathbf{I} - \mathbf{A}\right)^{-1}\mathbf{B}_u \qquad (4.15)$$

It can be approximated after taking Taylor expansion of the first term,

$$\Delta\mathbf{T}_{yu} = \mathbf{C}_y\left(i\omega\mathbf{I} - \mathbf{A}\right)^{-1}\Delta\mathbf{A}\left(i\omega\mathbf{I} - \mathbf{A}\right)^{-1}\mathbf{B}_u \qquad (4.16)$$

with

$$\Delta\mathbf{A} = \sum_{j=1}^{N_d}\left(\delta_{y,j}\Delta\mathbf{A}^e_{y,j} + \delta_{z,j}\Delta\mathbf{A}^e_{z,j} + \delta_{yz,j}\Delta\mathbf{A}^e_{yz,j}\right) \qquad (4.17)$$

With the transfer function shifts, the 1st damage estimate is formulated by substituting Eq. (4.17) into Eq. (4.15),

$$S\delta^{(1)} = P \tag{4.18}$$

with $\boldsymbol{\delta} = [\delta_{y,1} \quad \dots \quad \delta_{y,N_d} \; \delta_{z,1} \quad \dots \quad \delta_{z,N_d} \; \delta_{yz,1} \quad \dots \quad \delta_{yz,N_d}]^T$ is the vector of unknown damage parameters which can be estimated by using least-square method.

$$\delta_{est}^{(1)} = \left(S^T S\right)^{-1} S^T P \tag{4.19}$$

Similar as the way to enrich the dataset in Floquet based damage identification method, multiple sensors and/or excitation frequencies can be used to remove the rank deficiency of Eq. (4.19).

$$S = \begin{bmatrix} S(1) \\ S(2) \\ \vdots \\ S(N_f) \end{bmatrix} \quad P = \begin{bmatrix} P(1) \\ P(2) \\ \vdots \\ P(N_f) \end{bmatrix} \tag{4.20}$$

Starting the iteration by $\boldsymbol{\delta}_{est}^{(1)}$, the new solutions are calculated by Newton-Raphson method.

$$\delta^{(i+1)} = \delta^{(i)} - \left[J_E\left(\delta^{(i)}\right)\right]^{-1} E(\delta^{(i)}) \tag{4.21}$$

Where

$$\begin{aligned} E(\delta^{(i)}) &= \mathbf{C}_y \left(j\omega \mathbf{I} - \mathbf{A} - \Delta\tilde{\mathbf{A}}^{(i)} \right)^{-1} \mathbf{B}_u - \mathbf{T}_{\mathbf{yu}} \\ \Delta\tilde{\mathbf{A}}^{(i)} &= \sum_{j=1}^{N_d} \left(\delta_{y,j}^{(i)} \Delta\mathbf{A}_{y,j}^{e} + \delta_{y,j}^{(i)} \Delta\mathbf{A}_{z,j}^{e} + \delta_{yz,j}^{(i)} \Delta\mathbf{A}_{yz,j}^{e} \right) \end{aligned} \tag{4.22}$$

4.4.2 Damage Identification: Open Cracked Beam

Two damage cases listed in Table 4.1 are studied in this section. The shaft and disk parameters are listed in Table 3.1 and Table 4.2.

Table 4.1 Shaft Crack Damages

Case V			Case VI		
Cell No.	Crack Depth	Crack Angle	Cell No.	Crack Depth	Crack Angle
1	0	N/A	1	0	N/A
2	0	N/A	2	0	N/A
3	0	N/A	3	0	N/A
4	1.0 mm	45°	4	1.0 mm	45°
5	0	N/A	5	0	N/A
6	0	N/A	6	0	N/A
7	0	N/A	7	0.8 mm	60°
8	0	N/A	8	0	N/A
9	0	N/A	9	0	N/A
10	0	N/A	10	0	N/A

Table 4.2 Disk parameters

Parameters	Value	Units
Disk position	0.2	m
Disk outer radius	0.05	m
Disk thickness	0.01	m
Disk density	7800	kg/m^3
Disk elastic modulus	200	GPa

In order to ensure that all the damage parameters can be estimated from the measured transfer function shift information ΔT_{yu}, multiple (N_f =4) excitation frequencies and sensors are utilized to enrich the data and make the problem over-determined as shown in equation (4.20). The excitation frequency set and sensor location set are given in Table 4.3 and 4.4, respectively.

Table 4.3 Interrogation frequency set

	trial 1	trial 2	trial 3	trial 4
ω (Hz)	150	300	600	900

Table 4.4 Sensor location set

pair	Sensor 1	Sensor 2	Sensor 3
x_s (m)	1/8L	3/8L	5/8L

Fig. 4.8 and 4.9 show the damage identification results for the damaged shaft system with single transverse open crack (Case V). Specifically Fig. 4.9 shows the actual and converged estimates of the crack energy ratios and crack angles, wherein the blue and red bar denotes the actual and estimated value respectively.

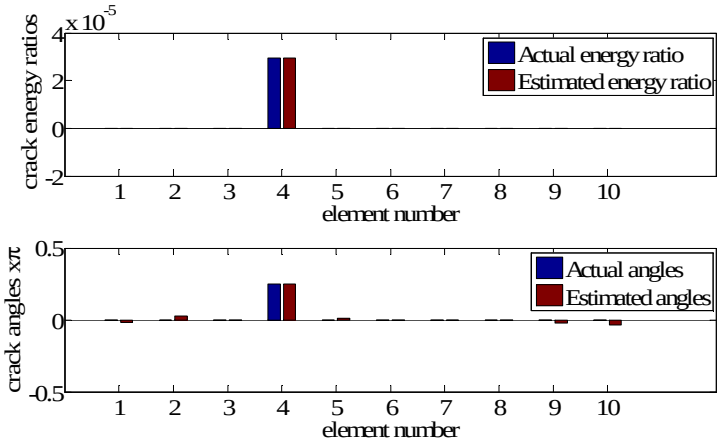

Fig. 4.8 Converged shaft crack damage energy ratio estimates: Case V

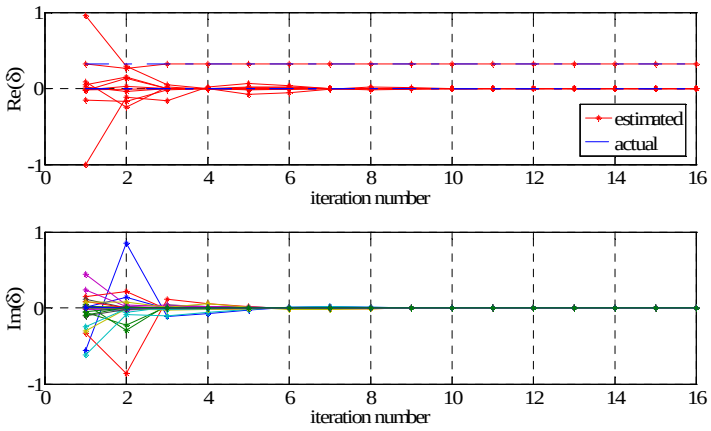

Fig. 4.9 Estimated shaft damage parameters vs. iteration number: Case V

Furthermore, Fig. 4.9 shows the shaft damage parameter iteration history, wherein the blue dash line and red star line denotes the actual and estimated damage parameters respectively. Compared with the results in Chapter 3, the results show that the FRF based damage identification method works better and more efficient to detect the magnitude

and crack angle. The real part of damage parameters converges to the actual value very quickly while the imaginary part goes down to zero. As we analyzed in last section, the symmetric structure does not lead to the wrong estimation any longer in this case since we utilize the magnitude and phase of transfer function shifts.

Fig. 4.10 and 4.11 show the damage identification results for the damaged shaft system with duel transverse open cracks (Case VI). Specifically Fig. 4.10 shows the actual and converged estimates of the crack energy ratios and crack angles, wherein the blue and red bar denotes the actual and estimated energy ratio respectively.

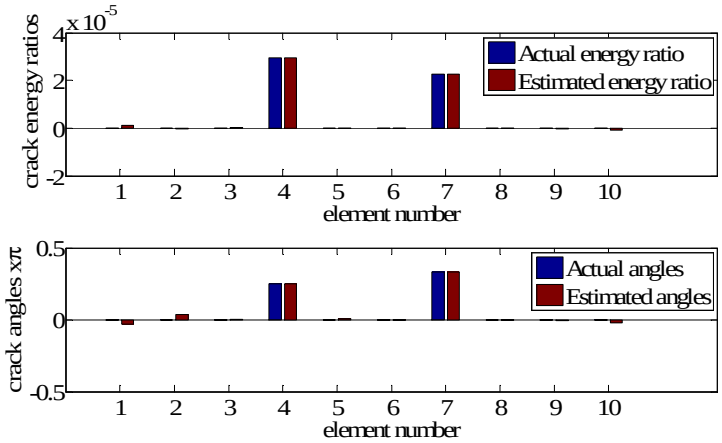

Fig. 4.10 Converged shaft crack damage energy ratio estimates: Case VI

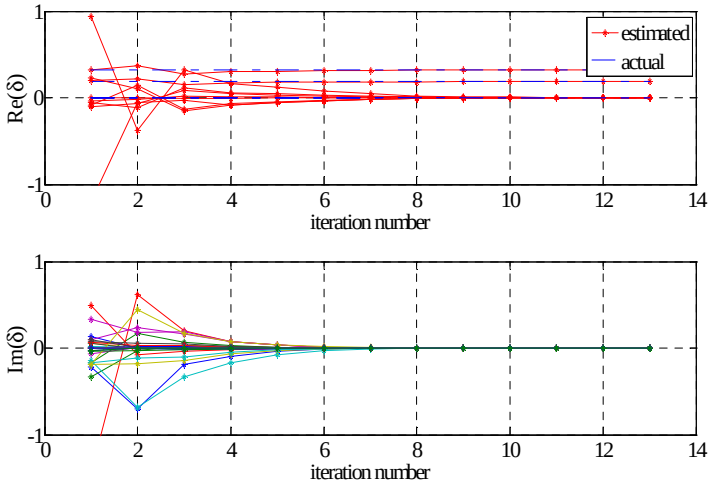

Fig. 4.11 Estimated shaft damage parameters vs. iteration number: Case VI

Furthermore, Fig. 4.11 shows the shaft damage parameter iteration history, wherein the blue dash line and red star line denotes the actual and estimated damage parameters respectively. Again, this method works well to detect dual cracks located at the symmetric cells with different crack angles.

4.5 FRF based Damage Identification of Time-Varying Rotor System

For the damaged system shown in Fig. 4.12, time-varying term will always appear in the equation of motion regardless which coordinate system the EOM is based on, if bearing stiffness is asymmetric. Specifically, crack rotating with shaft leads to time-varying term in fixed frame {n} and so does asymmetric bearing stiffness for rotating frame {c}. Based on the damage identification method developed for time-invariant system, the method for time-varying system is proposed in this section.

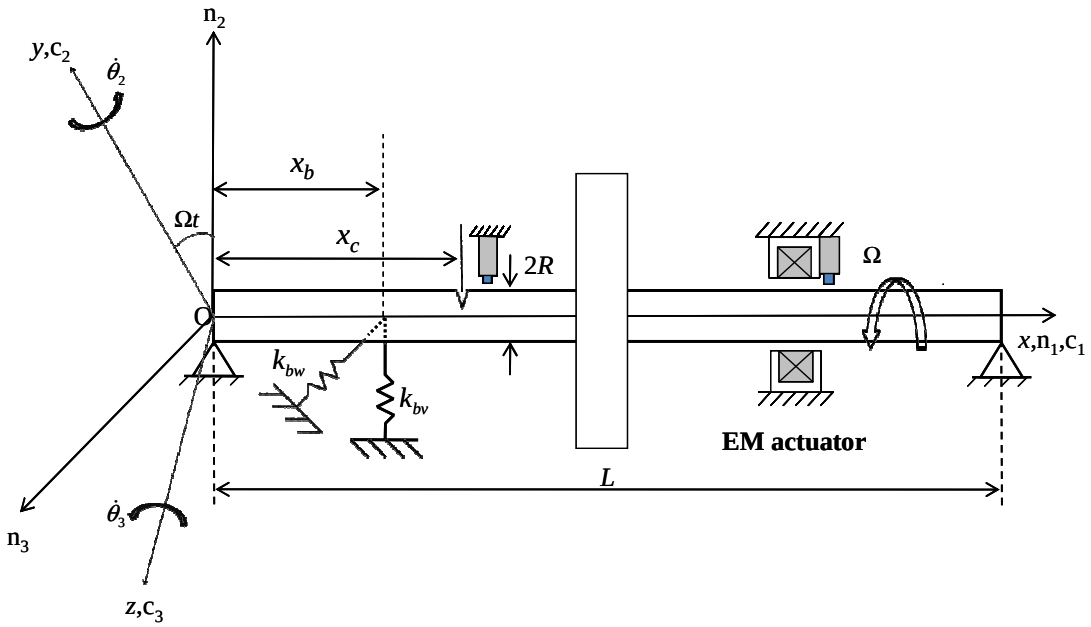

Fig. 4.12 Rotating rotor/shaft system with EM actuator

4.5.1 Damage Identification Algorithm

To develop the damage detection methodology, the equations-of-motion are recast into the following state-space form with state vector $\mathbf{x} = \begin{bmatrix} q^T & v_1 & \cdots & \dot{q}^T & \dot{v}_1 & \cdots \end{bmatrix}^T$

$$\begin{aligned} \dot{\mathbf{x}} &= \left(\mathbf{A}(t) + \sum_{k=1}^{N_d} \Delta\mathbf{A}_k(t) \right) \mathbf{x} + \mathrm{B}_u \mathbf{u}(t) \\ \mathbf{y} &= \mathbf{C}_y \mathbf{x} \end{aligned} \tag{4.23}$$

In this section, the EOM is derived in fixed frame {n}. Hence, the system matrix **A** is time-invariant. Here the external excitation and damage matrices, **u(t)**, and $\Delta\mathbf{A}_k(t)$, are expanded in the complex exponential series as:

$$\begin{aligned} \mathbf{u}(t) &= \mathbf{u} e^{j\omega t} \\ \Delta\mathbf{A}_k(t) &= \sum_{n=-N_h}^{N_h} \Delta\mathbf{A}_{n,k} e^{jn\Omega t} \end{aligned} \tag{4.24}$$

where N_h is the number of system harmonics. In the case of the shaft-disk system, $N_h = 2$. The solution of the linear periodically time varying system can be expressed as

$$\mathbf{x}(t) = \sum_{n=-Nx}^{N_x} \mathbf{x}_n e^{jn\Omega t} e^{j\omega t} \tag{4.25}$$

After performing harmonic balance, the following hyper-dimensional problems whose solutions characterize the nominal and damaged system transfer function matrices are given as:

$$\mathbf{T} = \hat{\mathbf{C}} \hat{\mathbf{A}}^{-1} \hat{\mathbf{B}} \tag{4.26}$$

$$\tilde{\mathbf{T}} = \hat{\mathbf{C}} (\hat{\mathbf{A}} - \sum_{k=1}^{N_d} \Delta\hat{\mathbf{A}}_{\mathbf{k}})^{-1} \hat{\mathbf{B}} \tag{4.27}$$

Here, $\hat{\mathbf{A}}$ and $\Delta\hat{\mathbf{A}}_k$ are the hyper-dimensional nominal system matrix and damage perturbation matrix given by,

$$\hat{\mathbf{A}}=\begin{bmatrix} \ddots & & \vdots & & & \iddots \\ \cdots & j(\omega-2\Omega)\mathbf{I}-\mathbf{A}_0 & -\mathbf{A}_{-1} & -\mathbf{A}_{-2} & \cdots & \\ \cdots & -\mathbf{A}_{+1} & j(\omega-\Omega)\mathbf{I}-\mathbf{A}_0 & -\mathbf{A}_{-1} & -\mathbf{A}_{-2} & \cdots \\ \cdots & -\mathbf{A}_{+2} & -\mathbf{A}_{+1} & j\omega\mathbf{I}-\mathbf{A}_0 & -\mathbf{A}_{-1} & -\mathbf{A}_{-2} \\ & \cdots & -\mathbf{A}_{+2} & -\mathbf{A}_{+1} & j(\omega+\Omega)\mathbf{I}-\mathbf{A}_0 & -\mathbf{A}_{-1} \\ & & \cdots & -\mathbf{A}_{+2} & -\mathbf{A}_{+1} & j(\omega+2\Omega)\mathbf{I}-\mathbf{A}_0 \\ \iddots & & & \vdots & & \ddots \end{bmatrix} \quad (4.28\text{-a})$$

$$\Delta\hat{\mathbf{A}}_k=\begin{bmatrix} \ddots & & \vdots & & & \iddots \\ \cdots & \Delta\mathbf{A}_{0,k} & \Delta\mathbf{A}_{-1,k} & \Delta\mathbf{A}_{-2,k} & \cdots & \\ \cdots & \Delta\mathbf{A}_{+1,k} & \Delta\mathbf{A}_{0,k} & \Delta\mathbf{A}_{-1,k} & \Delta\mathbf{A}_{-2,k} & \cdots \\ \cdots & \Delta\mathbf{A}_{+2,k} & \Delta\mathbf{A}_{+1,k} & \Delta\mathbf{A}_{0,k} & \Delta\mathbf{A}_{-1,k} & \Delta\mathbf{A}_{-2,k} \\ & \cdots & \Delta\mathbf{A}_{+2,k} & \Delta\mathbf{A}_{+1,k} & \Delta\mathbf{A}_{0,k} & \Delta\mathbf{A}_{-1,k} \\ & & \cdots & \Delta\mathbf{A}_{+2,k} & \Delta\mathbf{A}_{+1,k} & \Delta\mathbf{A}_{0,k} \\ \iddots & & & \vdots & & \ddots \end{bmatrix} \quad (4.28\text{-b})$$

Using the Taylor expansion on Eq. (4.27), the damage identification is formulated in terms of the following sensitivity matrix *S*,

$$\tilde{\mathbf{T}}-\mathbf{T}\approx\hat{\mathbf{C}}\hat{\mathbf{G}}^{-1}\Big(\sum_{k=1}^{N_d}\Delta\hat{\mathbf{A}}_{\mathbf{k}}\Big)\hat{\mathbf{G}}^{-1}\hat{\mathbf{B}}=\hat{\mathbf{C}}\hat{\mathbf{G}}^{-1}\Big(\sum_{k=1}^{N_d}\delta_k\hat{\mathbf{A}}_{\mathbf{k}}\Big)\hat{\mathbf{G}}^{-1}\hat{\mathbf{B}} \quad (4.29)$$

$$\Downarrow$$

$$\Delta\mathbf{T}_{yu}=S\delta_{est} \quad (4.30)$$

with

$$S_k=\hat{\mathbf{C}}\hat{\mathbf{G}}^{-1}\hat{\mathbf{A}}_{\mathbf{k}}\hat{\mathbf{G}}^{-1}\hat{\mathbf{B}} \quad (4.31)$$

$\hat{\mathrm{B}}$ is hyper-dimensional input matrix and $\hat{\mathbf{C}}$ is hyper-dimensional output matrix.

$$\begin{aligned}\hat{\mathbf{B}}&=\begin{bmatrix}0 & 0 & \mathbf{B}_u & 0 & 0\end{bmatrix}^T\\ \hat{\mathbf{C}}&=(2n_h+1)\otimes\mathbf{C}_y\end{aligned} \quad (4.32)$$

The following iterative process is similar with the process for time-invariant system. Note that the Jacobian and iterative error matrices are hyper-dimensional.

4.5.2 Damage Identification: Time-varying Shaft/Disk System

In this section, the parametric study is done to find the sensitive range of transfer function. To do this, the excitation frequency is divided into three categories: near-resonance, near-sidebands and far-off-resonance. First, the frequency response functions of the system shown in Fig. 4.13 are calculated by applying force at 3/4*L* and placing the sensor at 3/8*L*. The system is assumed to have the damage listed in Table 3.6.

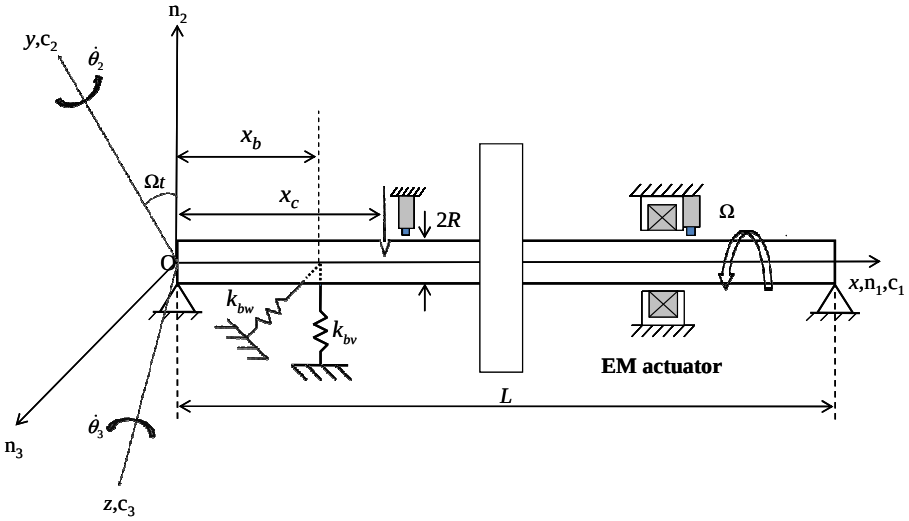

Fig. 4.13 Rotor system for damage detection: x_f=3/4*L*, x_s=3/8*L*, k_{bv}=10^6, k_{bw} =0, Ω=3000 RPM

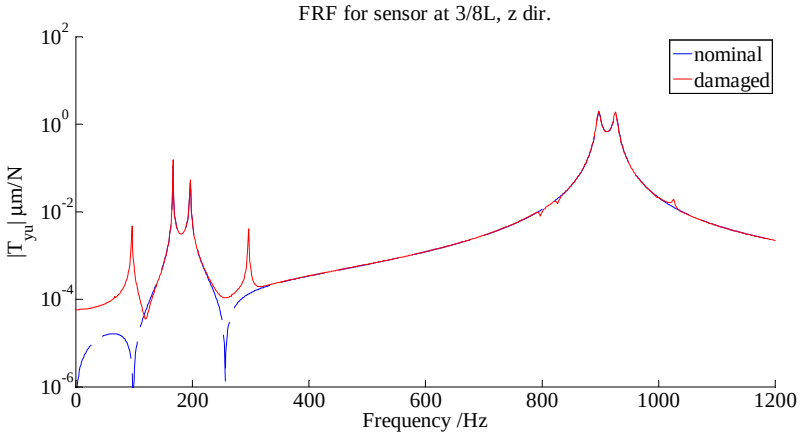

Fig. 4.14-a Frequency response function magnitude

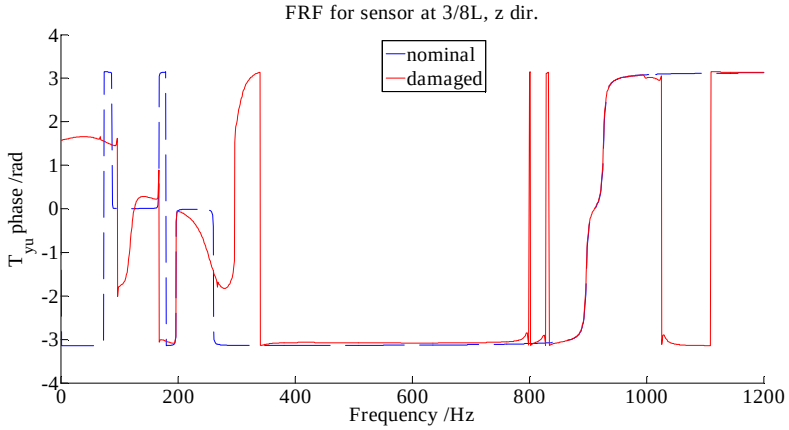

Fig. 4.14-b Frequency response function phase

Fig. 4.14-a and 4.14-b show the magnitude and phase of frequency response function of nominal and damaged rotor system. Several resonances can be seen from Fig. 14-a and their corresponding frequencies are around 170, 200, 900, 930 Hz. Note that damaged FRF has several sidebands around 70, 300, 800, 830, 1030 Hz due to the damage and the sidebands for second mode is relatively small for this specific case.

According to above analysis, three excitation frequency sets are designated as near-resonance, near-sideband & resonance and far-off-resonance set in Table 4.5, 4.6 and 4.7 respectively.

Table 4.5 Near-resonance frequency set

	trial 1	trial 2	trial 3
ω (Hz)	160	190	890

Table 4.6 Near-sideband & resonance frequency set

	trial 1	trial 2	trial 3
Set II	70	300	890

Table 4.7 Far-off-resonance frequency set

	trial 1	trial 2	trial 3
Set III	400	500	600

Fig. 4.15, 4.16 and 4.17 show the damage estimation results for using near-resonance, near-sideband & resonance and far-off-resonance frequency set, respectively. For each

Fig., it includes the subplots of energy ratios, twice of crack angle, damage parameter iteration history and estimated error history. Note here that twice of crack angle is adopted as a parameter since the crack parameters derived in previous chapters are represented in terms of 2θ.

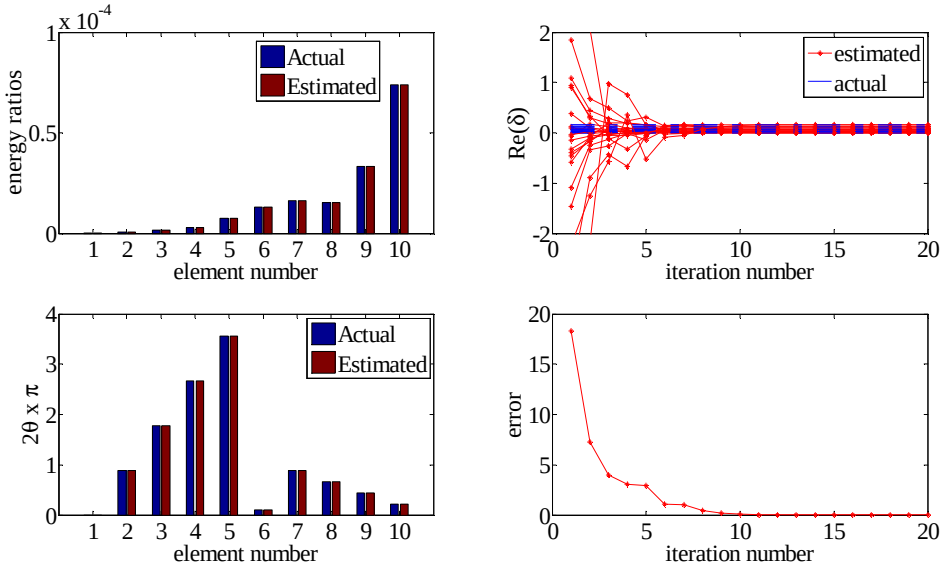

Fig. 4.15 Damage estimates for near-resonance set (a) crack damage energy ratio estimates (b) crack angle estimates (c) damage parameter iteration history (d) estimated error history

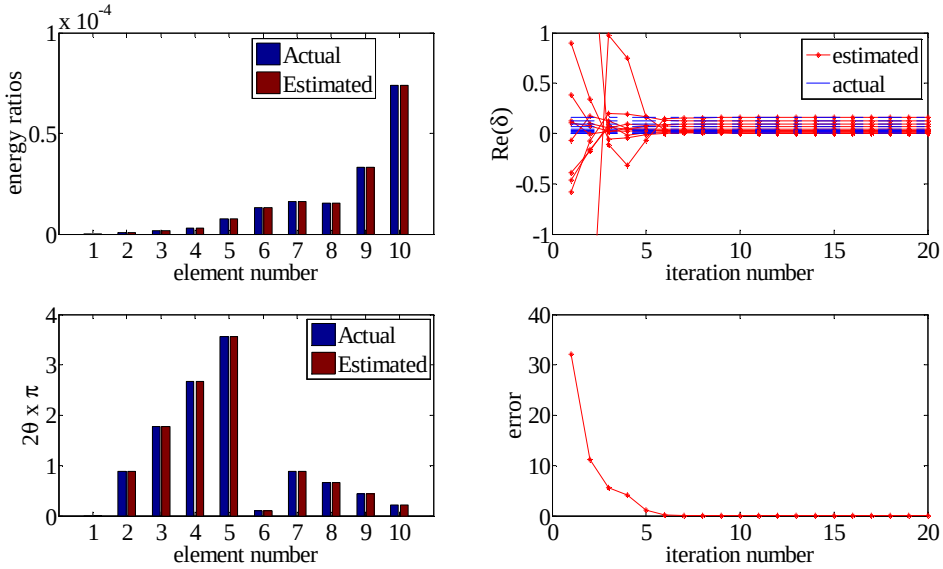

Fig. 4.16 Damage estimates for near-sideband & resonance set: (a) crack damage energy ratio estimates (b) crack angle estimates (c) damage parameter iteration history (d) estimated error history

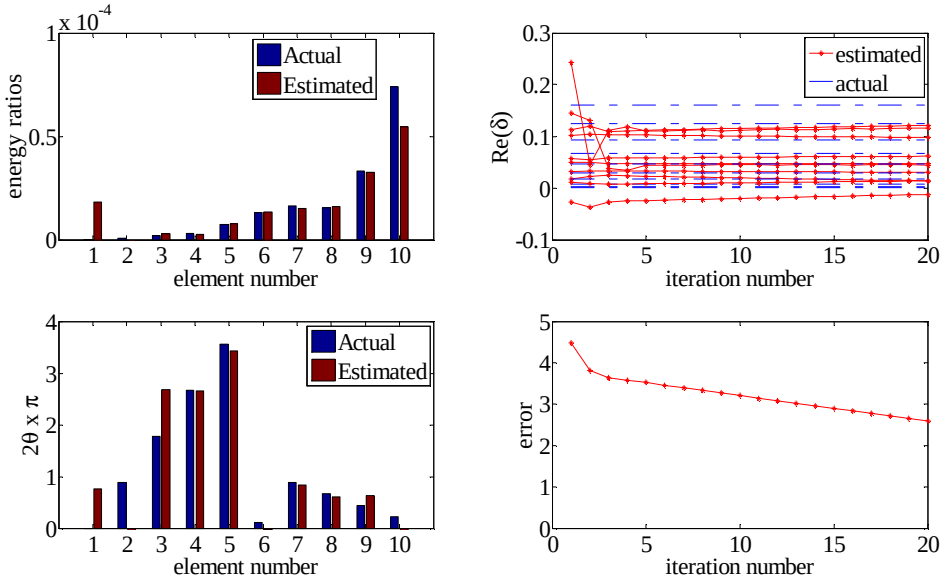

Fig. 4.17 Damage estimates for far-off-resonance set (a) crack damage energy ratio estimates (b) crack angle estimates (c) damage parameter iteration history (d) estimated error history

With near-resonance and near-sideband excitation frequency, the estimated energy ratios, twice of crack angle and damage parameters converge to their actual values within several steps. Meanwhile, the estimated error goes to zero quickly. However, the estimation results are not good with far-off-resonance excitation frequency. The estimated error starts from around 500% and ends around 250% in 20 steps. For energy ratio, the algorithm fails to estimate the correct values for 1st and 10th cells. For crack angle, big discrepancy appears for 1st, 2nd, 3rd cells and angles for 6th and 10th cells is not be able to be recognized.

With above observation, it is obvious to get the conclusion that better damage estimation results can be obtained using near-resonance and near sideband excitation

frequency. What is the reason behind this conclusion? The answer will be revealed by the transfer function data obtained from three frequency sets shown in Fig. 4.18, 4.19, 4.20.

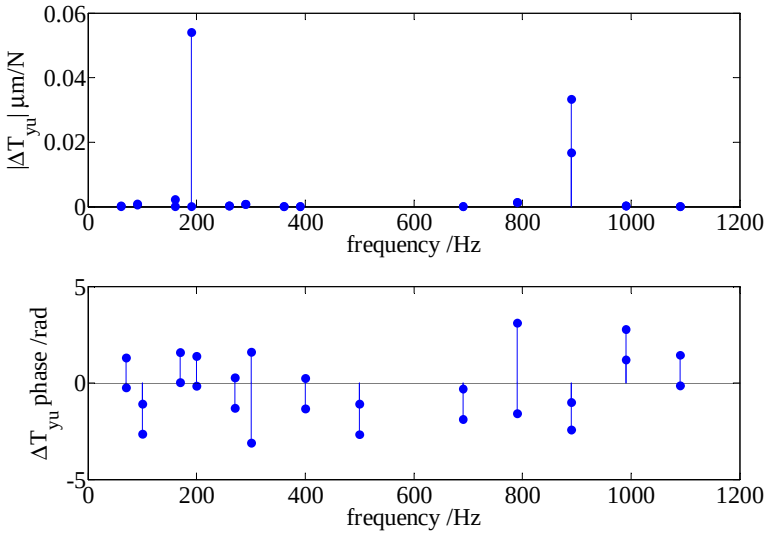

Fig. 4.18 Transfer function shift data from near-resonance set

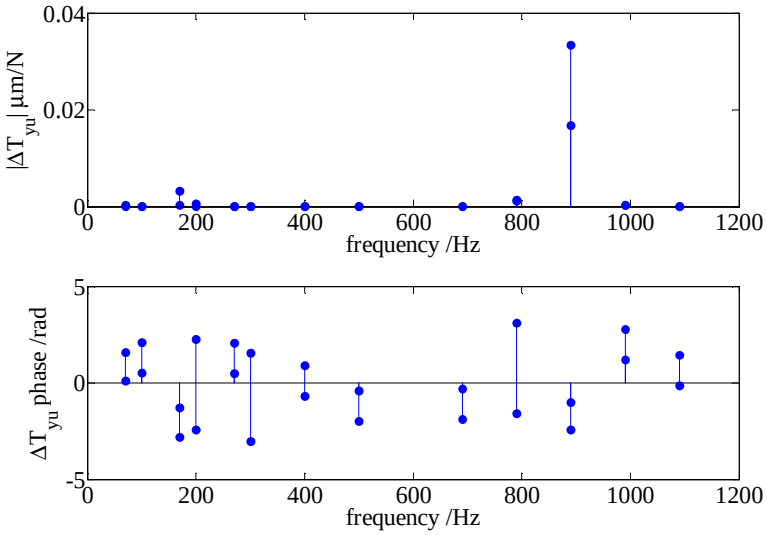

Fig. 4.19 Transfer function shift data from near-sideband & resonance set

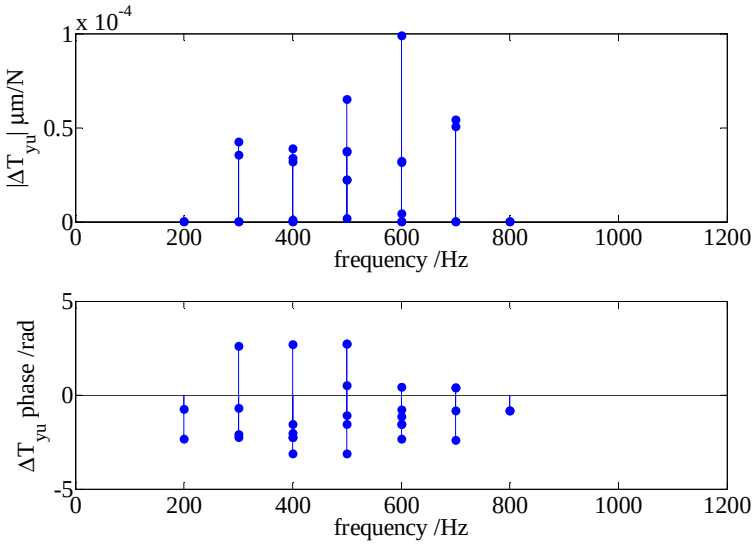

Fig. 4.20 Transfer function shift data from far-off-resonance set

Figs. 4.18-4.20 show the magnitude and phase of transfer function shifts at the excitation frequencies and their sidebands. The data from main peak and sidebands were all used for damage detection. For near-resonance and near-sideband sets, $|\Delta T_{yu}|$ are around the magnitude of $10^{-2} \sim 10^{-1}$ μm/N. For far-off-resonance set, the values fall in the range $[10^{-5} \sim 10^{4}]$ μm/N. Thus, the transfer function shifts are much stronger when the system is excited near resonance or sideband. On the other hand, the transfer function shifts are not very sensitive in the far-off-resonance region which results in worse estimation results.

4.6 Summary

As stated in Chapter III, Floquet based method only utilizes the natural frequency shifts which is independent of crack phase for the single cracked system without AMB. Also, the shifts are same for the symmetric positions with respect to the midpoint of shaft. However, these conclusions do not hold any more for Frequency Response Function

(FRF) based method which uses the magnitude and phase of transfer function shifts to detect the damage. Since the magnitude and phase of transfer function shifts are not symmetric versus crack location and angle, this method enables the possibility of distinguishing the multiple cracks and detecting crack angle. The damage detection algorithms are explored for both time-invariant and time-varying systems. For the time-varying system, stronger transfer function shifts can be obtained by exciting the system near resonances or sidebands and consequently benefit the damage identification.

Chapter V

DAMAGE IDENTIFICATION OF BREATHING CRACKS IN TRUSS SYSTEM

5.1 Introduction

In this chapter, FRF based damage identification methodology is developed for a truss system to detect the mass and stiffness uncertainties as well as the breathing cracks. This approach is based on the Newton-Raphson method and utilizes damage-induced changes of frequency response functions to estimate the severity and location of structural damage. The dynamical model of truss system is built using the finite element method [156] and the crack model is based on fracture mechanics. First, the method is synthesized via numerical examples to illustrate the essentiality of considering the existence of mass uncertainty besides stiffness uncertainty. Then, the linear damage detection algorithm is developed in frequency domain on the premise of assumptions and used to identify the damage of truss system. Finally, the nonlinear breathing cracked truss system is simulated in the time domain and the vibration signal is processed and used for nonlinear damage identification of breathing cracks.

5.2 Truss Model

A truss is one of the simplest and most widely used structural members. It is a straight bar that is designed to take only axial forces, therefore it deforms only in its axial direction. The cross-section of the bar can be arbitrary, but the dimensions of the cross-section should be much smaller than that in the axial direction. Finite element equations for such truss members will be developed in this topic. The element developed is

commonly known as the truss element or bar element. Such elements are applicable for analysis of the skeletal type of truss structural systems both in two-dimensional planes and in three-dimensional space.

In planar trusses, there are two components in the *x* and *y* directions for the displacements as well as for the forces. For space trusses, however, there will be three components in the *x*, *y* and *z* directions for both displacements and forces. In skeletal structures consisting of truss members, the truss members are joined together by pins or hinges (not by welding), so that there are only forces (not moments) transmitted between the bars. For the purpose of explaining the concepts more clearly, this topic will assume that the truss elements have a uniform cross-section. Therefore, to deal with bars with varying cross-sections, one should develop equations for a truss element with a varying cross-section, which can also be done very easily following the procedure for uniform truss elements. Note that there is no reason from the mechanics viewpoint to use bars with a varying cross-section, as the force in a bar is uniform.

5.2.1 Shape Function Construction

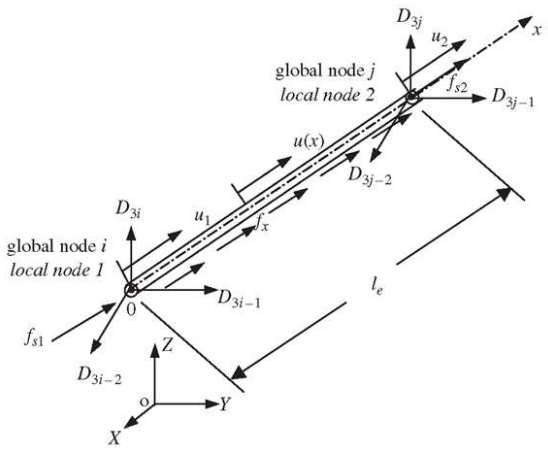

Fig. 5.1 Truss element and the coordinate system [156]

Consider a structure consisting of a number of trusses or bar members. Each of the members can be considered as a truss/bar element of uniform cross-section bounded by two nodes (n_d = 2). Consider a bar element with nodes 1 and 2 at each end of the element, as shown in Fig. 5.1. The length of the element is l_e. The local x-axis is taken in the axial direction of the element with the origin at node 1.

In the local coordinate system, there is only one DOF at each node of the element, and that is the axial displacement. Therefore, there is a total of two DOFs for the element. In the FEM discussed in the previous topic, the displacement in an element should be written in the form

$$u^h(x) = N(x)d_e \tag{5.1}$$

where u^h is the approximation of the axial displacement within the element, N is a matrix of shape functions that possess the properties described and d_e should be the vector of the displacements at the two nodes of the element:

$$d_e = \begin{Bmatrix} u_1 \\ u_2 \end{Bmatrix} \tag{5.2}$$

The axial displacement in the truss element can be given in a general form

$$u^h(x) = \alpha_0 + \alpha_1 x = \begin{bmatrix} 1 & x \end{bmatrix} \begin{bmatrix} \alpha_0 \\ \alpha_1 \end{bmatrix} = p^T \alpha \tag{5.3}$$

where α is the vector of two unknown constants, α_0 and α_1, and p is the vector of polynomial basis functions (or monomials). For this particular problem, we use up to the first order of polynomial basis. Depending upon the problem, we could use a higher order of polynomial basis functions. The order of polynomial basis functions up to the n^{th} order can be given by

$$p^T = \begin{bmatrix} 1 & x & \cdots & x^n \end{bmatrix} \tag{5.4}$$

The number of terms of basis functions or monomials we should use depends upon the number of nodes and degrees of freedom in the element. Since we have two nodes with a total of two DOFs in the element, we choose to have two terms of basis functions, which gives Eq. (5.3). Note that we usually use complete orders of polynomial basis functions, meaning no lower order term is skipped while constructing Eq. (5.3). This is to ensure that the shape functions will be able to reproduce complete polynomials up to n^{th} order. If k^{th} order term of a polynomial basis is skipped, the shape function will only be able to ensure a consistency of $(k\text{-}1)^{th}$ order, regardless of how many higher orders of monomials are included in the basis.

In deriving the shape function**,** we use the fact that

$$\begin{aligned} u(x)|_{x=0} &= u_1 \\ u(x)|_{x=l_e} &= u_2 \end{aligned} \tag{5.5}$$

Using Eq. (5.3), we then have

$$\begin{Bmatrix} u_1 \\ u_2 \end{Bmatrix} = \begin{bmatrix} 1 & 0 \\ 1 & l_e \end{bmatrix} \begin{Bmatrix} \alpha_0 \\ \alpha_1 \end{Bmatrix} \tag{5.6}$$

Solving the above equation for α, we have

$$\begin{Bmatrix} \alpha_0 \\ \alpha_1 \end{Bmatrix} = \begin{bmatrix} 1 & 0 \\ -1/l_e & 1/l_e \end{bmatrix} \begin{Bmatrix} u_1 \\ u_2 \end{Bmatrix} \tag{5.7}$$

Substituting the above equation into Eq. (5.3), we obtain

$$u(x) = p^T \alpha = \begin{bmatrix} 1 & x \end{bmatrix} \begin{Bmatrix} \alpha_0 \\ \alpha_1 \end{Bmatrix} = \begin{bmatrix} 1 - x/l_e & x/l_e \end{bmatrix} \begin{Bmatrix} u_1 \\ u_2 \end{Bmatrix} = N(x) d_e \tag{5.8}$$

The matrix of shape functions is then obtained in the form

$$N(x) = \begin{bmatrix} N_1(x) & N_2(x) \end{bmatrix} = \begin{bmatrix} 1 - x/l_e & x/l_e \end{bmatrix} \tag{5.9}$$

We obtained two shape functions because we have two DOFs in the truss elements.

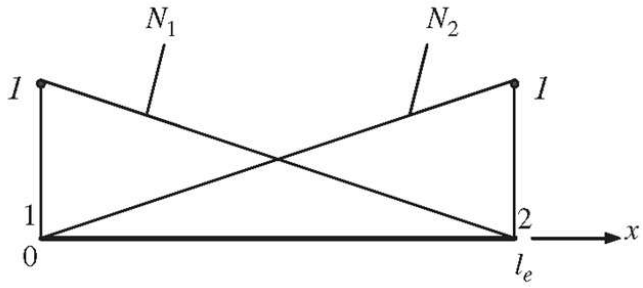

Fig. 5.2 Linear shape functions [156]

The graphic representation of the linear shape functions is shown in Fig. 5.2. It is clearly shown that N_i gives the shape of the contribution from nodal displacement at node *i*. In this case, the shape functions vary linearly across the element, and they are termed linear shape functions. Substituting Eq. (5.9) and (5.2) into Eq. (5.1), we have

$$u(x) = N_1(x)u_1 + N_2(x)u_2 = u_1 + \frac{u_2 - u_1}{l_e}x \tag{5.10}$$

There is only one stress component σ_x in a truss, and the corresponding strain can be obtained by

$$\varepsilon_x = \frac{\partial u}{\partial x} = \frac{u_2 - u_1}{l_e} = Bd_e \tag{5.11}$$

where the strain matrix *B* has the following form for the truss element:

$$B = \frac{\partial}{\partial x}\begin{bmatrix} N_1(x) & N_2(x) \end{bmatrix} = \begin{bmatrix} -1/l_e & 1/l_e \end{bmatrix} \tag{5.12}$$

5.2.2 Element Matrix in the Local Coordinate System

Once the strain matrix *B* is obtained, the stiffness matrix for truss elements can be expressed as:

$$\mathbf{k}_e = \int_{V_e} B^T c B dV = A\int_0^{l_e} \begin{bmatrix} -1/l_e \\ 1/l_e \end{bmatrix} E\begin{bmatrix} -1/l_e & 1/l_e \end{bmatrix} dx = \frac{EA}{l_e}\begin{bmatrix} 1 & -1 \\ -1 & 1 \end{bmatrix} \tag{5.13}$$

where A is the area of the cross-section of the truss element. Note that the material constant matrix c reduces to the elastic modulus, E, for the one-dimensional truss element..

The mass matrix for truss elements can be obtained as:

$$\mathbf{m}_e = \int_{V_e} \rho N^T N dV = A\rho\int_0^{l_e} \begin{bmatrix} N_1N_1 & N_1N_2 \\ N_2N_1 & N_2N_2 \end{bmatrix} dx = \frac{A\rho l_e}{6}\begin{bmatrix} 2 & -1 \\ -1 & 2 \end{bmatrix} \tag{5.14}$$

5.2.3 Element Matrices in the Global Coordinate System

Element matrices in Eq. (5.12) and (5.13) were formulated based on the local coordinate system, where the x-axis coincides with the neutral axis of the bar, shown in Fig. 5.1. In practical trusses, there are many bars of different orientations and at different locations. To assemble all the element matrices to form the global system matrices, a coordinate transformation has to be performed for each element to formulate its element matrix based on the global coordinate system for the whole truss structure. The following performs the transformation for both spatial and planar trusses.

(a) Spatial trusses

Assume that the local nodes 1 and 2 of the element correspond to the global nodes i and j, respectively, as shown in Fig. 5.1. The displacement at a global node in space should have three components in the X, Y and Z directions, and numbered sequentially. For example, these three components at the i^{th} node are denoted by D_{3i-2}, D_{3i-1} and D_{3i}. The coordinate transformation gives the relationship between the displacement vector de

based on the local coordinate system and the displacement vector $\mathbf{D}_e$ for the same element, but based on the global coordinate system *XYZ*:

$$d_e = \mathbf{T}\mathbf{D}_e \tag{5.15}$$

where

$$\mathbf{D}_e = \begin{Bmatrix} D_{3i-2} \\ D_{3i-1} \\ D_{3i} \\ D_{3j-2} \\ D_{3j-1} \\ D_{3j} \end{Bmatrix} \tag{5.16}$$

and $\mathbf{T}$ is the transformation matrix for the truss element, given by

$$\mathbf{T} = \begin{bmatrix} l_{ij} & m_{ij} & n_{ij} & 0 & 0 & 0 \\ 0 & 0 & 0 & l_{ij} & m_{ij} & n_{ij} \end{bmatrix} \tag{5.17}$$

in which

$$\begin{aligned} l_{ij} &= \cos(x, X) = \frac{X_j - X_i}{l_e} \\ m_{ij} &= \cos(x, Y) = \frac{Y_j - Y_i}{l_e} \\ n_{ij} &= \cos(x, Z) = \frac{Z_j - Z_i}{l_e} \end{aligned} \tag{5.18}$$

are the direction cosines of the axial axis of the element. The length of the element, l_e, can be calculated using the global coordinates of the two nodes of the element by

$$l_e = \sqrt{(X_j - X_i)^2 + (Y_j - Y_i)^2 + (Z_j - Z_i)^2} \tag{5.19}$$

The transformation matrix also applies to the force vectors between the local and global coordinate systems:

$$\mathbf{f}_e = \mathbf{T}\mathbf{F}_e \tag{5.20}$$

where

$$\mathbf{F}_e = \begin{Bmatrix} F_{3i-2} \\ F_{3i-1} \\ F_{3i} \\ F_{3j-2} \\ F_{3j-1} \\ F_{3j} \end{Bmatrix} \tag{5.21}$$

in which $F_{3i-2}, F_{3i-1}, F_{3i}$ stand for the three components of the force vector at node *i* based on the global coordinate system.

The global stiffness and mass matrices are:

$$\mathbf{K}_e = \mathbf{T}^T\mathbf{k}_e\mathbf{T} = \frac{AE}{l_e}\begin{bmatrix} l_{ij}^2 & l_{ij}m_{ij} & l_{ij}n_{ij} & -l_{ij}^2 & -l_{ij}m_{ij} & -l_{ij}n_{ij} \\ l_{ij}m_{ij} & m_{ij}^2 & m_{ij}n_{ij} & -l_{ij}m_{ij} & -m_{ij}^2 & -m_{ij}n_{ij} \\ l_{ij}n_{ij} & m_{ij}n_{ij} & n_{ij}^2 & -l_{ij}n_{ij} & -m_{ij}n_{ij} & -n_{ij}^2 \\ -l_{ij}^2 & -l_{ij}m_{ij} & -l_{ij}n_{ij} & l_{ij}^2 & l_{ij}m_{ij} & l_{ij}n_{ij} \\ -l_{ij}m_{ij} & -m_{ij}^2 & -m_{ij}n_{ij} & l_{ij}m_{ij} & m_{ij}^2 & m_{ij}n_{ij} \\ -l_{ij}n_{ij} & -m_{ij}n_{ij} & -n_{ij}^2 & l_{ij}n_{ij} & m_{ij}n_{ij} & n_{ij}^2 \end{bmatrix} \tag{5.22}$$

$$\mathbf{M}_e = \mathbf{T}^T\mathbf{m}_e\mathbf{T} = \frac{AEl_e}{6}\begin{bmatrix} 2l_{ij}^2 & 2l_{ij}m_{ij} & 2l_{ij}n_{ij} & l_{ij}^2 & l_{ij}m_{ij} & l_{ij}n_{ij} \\ 2l_{ij}m_{ij} & 2m_{ij}^2 & 2m_{ij}n_{ij} & l_{ij}m_{ij} & m_{ij}^2 & m_{ij}n_{ij} \\ 2l_{ij}n_{ij} & 2m_{ij}n_{ij} & 2n_{ij}^2 & l_{ij}n_{ij} & m_{ij}n_{ij} & n_{ij}^2 \\ l_{ij}^2 & l_{ij}m_{ij} & l_{ij}n_{ij} & 2l_{ij}^2 & 2l_{ij}m_{ij} & 2l_{ij}n_{ij} \\ l_{ij}m_{ij} & m_{ij}^2 & m_{ij}n_{ij} & 2l_{ij}m_{ij} & 2m_{ij}^2 & 2m_{ij}n_{ij} \\ l_{ij}n_{ij} & m_{ij}n_{ij} & n_{ij}^2 & 2l_{ij}n_{ij} & 2m_{ij}n_{ij} & 2n_{ij}^2 \end{bmatrix} \tag{5.23}$$

(b) Planar trusses

For a planar truss, the global coordinates *X*-*Y* can be employed to represent the plane of the truss. All the formulations of coordinate transformation can be obtained from the counterpart of those for spatial trusses by simply removing the rows and/or columns corresponding to the *z*- (or *Z*-) axis. The displacement at the global node *i* should have two components in the *X* and *Y* directions only: $D_{2i\text{-}1}$ and D_{2i}. The coordinate transformation, which gives the relationship between the displacement vector de based on the local coordinate system and the displacement vector $\mathbf{D_e}$, has the same form as Eq. (5.16), except that

$$\mathbf{D}_e = \begin{Bmatrix} D_{2i-1} \\ D_{2i} \\ D_{2j-1} \\ D_{2j} \end{Bmatrix} \tag{5.24}$$

and the transformation matrix **T** is given by

$$\mathbf{T} = \begin{bmatrix} l_{ij} & m_{ij} & 0 & 0 \\ 0 & 0 & l_{ij} & m_{ij} \end{bmatrix} \tag{5.25}$$

The force vector in the global coordinate system is

$$\mathbf{F}_e = \begin{bmatrix} F_{2i-1} \\ F_{2i} \\ F_{2j-1} \\ F_{2j} \end{bmatrix} \tag{5.26}$$

All the other equations for a planar truss have the same form as the corresponding equations for a space truss. The $\mathbf{K}_e$ and $\mathbf{M}_e$ for the planar truss have a dimension of 4 x 4 in the global coordinate system. They are listed as follows:

$$\mathbf{K}_e = \mathbf{T}^T \mathbf{k}_e \mathbf{T} = \frac{AE}{l_e} \begin{bmatrix} l_{ij}^2 & l_{ij}m_{ij} & -l_{ij}^2 & -l_{ij}m_{ij} \\ l_{ij}m_{ij} & m_{ij}^2 & -l_{ij}m_{ij} & -m_{ij}^2 \\ -l_{ij}^2 & -l_{ij}m_{ij} & l_{ij}^2 & l_{ij}m_{ij} \\ -l_{ij}m_{ij} & -m_{ij}^2 & l_{ij}m_{ij} & m_{ij}^2 \end{bmatrix} \tag{5.27}$$

$$\mathbf{M}_e = \mathbf{T}^T \mathbf{m}_e \mathbf{T} = \frac{AEl_e}{6} \begin{bmatrix} 2l_{ij}^2 & 2l_{ij}m_{ij} & l_{ij}^2 & l_{ij}m_{ij} \\ 2l_{ij}m_{ij} & 2m_{ij}^2 & l_{ij}m_{ij} & m_{ij}^2 \\ l_{ij}^2 & l_{ij}m_{ij} & 2l_{ij}^2 & 2l_{ij}m_{ij} \\ l_{ij}m_{ij} & m_{ij}^2 & 2l_{ij}m_{ij} & 2m_{ij}^2 \end{bmatrix} \tag{5.28}$$

5.2.4 Equation of Motion

The kinetic and potential energy of the truss frame can be expressed as:

$$\begin{aligned} T &= \frac{1}{2}\dot{Q}^T \left(\sum_{n=1}^{N_m} \mathbf{M}_e^n \right) \dot{Q} \\ U &= \frac{1}{2} Q^T \left(\sum_{n=1}^{N_m} \mathbf{K}_e^n \right) Q - Q^T P \end{aligned} \tag{5.29}$$

where Q is the whole global coordinates and N_m is the number of truss member. By applying the Lagrange principle and removing the freedom of constraints, the equation of motion for the damaged system is given as,

$$(M_c - M_d)\ddot{Q} + C_c\dot{Q} + (K_c - K_d)Q = P_c \tag{5.30}$$

where M_c, C_c, K_c is the constrained mass, damping and stiffness matrix respectively; M_d is the mass perturbation matrix induced by mass uncertainty and K_d is the stiffness perturbation matrix induced by stiffness uncertainty; P_c is the global nodal force vector.

5.3 Crack Model under Axial Load

Different from the flexural shaft, the truss bar is only forced by tension or compression without moment. Thus, the crack model is different from that built in Chapter 3.

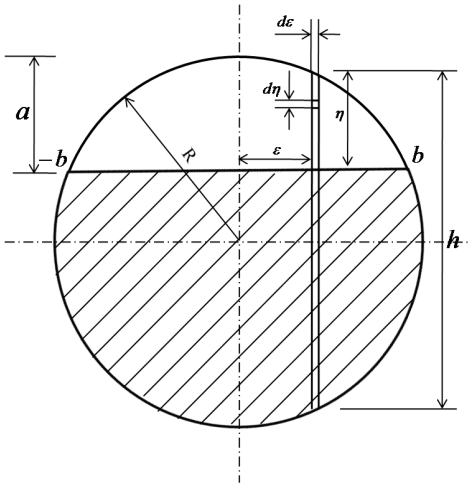

Fig. 5.3 Cracked bar cross-section

For a truss bar as shown in Fig. 2.9, $P_2 = P_3 = P_4 = P_5 = P_6 = 0$. Therefore, the crack energy equation (2.24) can be simplified as:

$$U_c = \frac{1}{E'}\int_A (K_{I1})^2 dA$$
$$K_{I1} = \sigma_1 \sqrt{\pi\eta} F_1(\eta / h) \tag{5.31}$$

where σ_1 is the axial stress of the bar which is,

$$\sigma_1 = \frac{P_1}{\pi R^2} = \frac{E}{l_e}(u_i - u_j) \tag{5.32}$$

Substituting Eq. (5.32) into crack energy equation, we have

$$U_c = \frac{\pi E^2}{E' l_e^2}(u_i - u_j)^2 \int_A \eta F_1^2(\eta / h) dA \tag{5.33}$$

The stiffness matrix for a truss bar element in the local coordinate system can be expressed as:

$$\mathbf{k}_c^e = \frac{\partial U_c}{\partial d_e} = \left[\frac{2E\pi}{E^{'}Al_e}\int_A \eta F_1^{\,2}(\eta/h)dA\right]\frac{EA}{l_e}\begin{bmatrix}1 & -1\\ -1 & 1\end{bmatrix} = d_b\mathbf{k}_e \tag{5.34}$$

where d_b is the damage parameter of the bar. After taking the coordinate transformation, the stiffness matrix in the global coordinate system is:

$$\mathbf{K}_c^e = \mathbf{T}^T\mathbf{k}_c^e\mathbf{T} = \left[\frac{2E\pi}{E^{'}Al_e}\int_A \eta F_1^{\,2}(\eta/h)dA\right]\frac{AE}{l_e}\begin{bmatrix} l_{ij}^2 & l_{ij}m_{ij} & -l_{ij}^2 & -l_{ij}m_{ij}\\ l_{ij}m_{ij} & m_{ij}^2 & -l_{ij}m_{ij} & -m_{ij}^2\\ -l_{ij}^2 & -l_{ij}m_{ij} & l_{ij}^2 & l_{ij}m_{ij}\\ -l_{ij}m_{ij} & -m_{ij}^2 & l_{ij}m_{ij} & m_{ij}^2\end{bmatrix} = d_b\mathbf{K}_e \tag{5.35}$$

The bar damage parameter d_b is studied with the increase of the crack depth. The non-dimensional form of d_b is given as:

$$d_b = \frac{2E\pi}{E^{'}Al_e}R^5\int_0^{\sqrt{\bar{a}^2-\bar{\varepsilon}^2}-(1-\bar{a})}\int_{-\bar{b}}^{\bar{b}}\overline{\eta}F_1^{\,2}(\overline{\eta}/\bar{h})d\bar{\varepsilon}d\overline{\eta} \tag{5.36}$$

where,

$$\bar{a} = \frac{a}{R}, \bar{b} = \frac{b}{R}, \bar{\varepsilon} = \frac{\varepsilon}{R}, \overline{\eta} = \frac{\eta}{R}, \bar{h} = \frac{h}{R} \tag{5.37}$$

5.4 Damage Identification: Mass and Stiffness Uncertainty

The truss system studied in this section is shown in Fig. 5.4. The truss parameters are shown is Table 5.1.

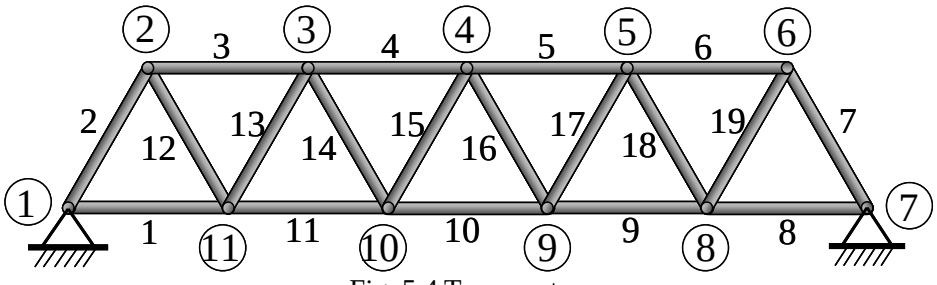

Fig. 5.4 Truss system

Table 5.1 Truss parameters

Parameter	Value	Units
Bar length, l_e	1	m
Bar radius, R	0.125	In
Bar density, ρ	2800	kg/m^3
Bar elastic modulus, E	75	GPa
Number of bar member	19	--

5.4.1 Stiffness Uncertainty Detection

Assuming that the truss has stiffness faults listed in Table 5.2, the FRF based damage detection method developed in Chapter 4 is used here to detect them.

Table 5.2 Truss Stiffness Faults

Bar No.	Stiffness Faults	Bar No.	Stiffness Faults
1	0	11	0
2	0	12	0
3	-7.5%	13	0
4	0	14	0
5	0	15	-10%
6	0	16	0
7	0	17	0
8	0	18	0
9	-5%	19	0
10	0		

Fig. 5.5 shows the actual and estimated stiffness faults of truss members. The blue and red bars denote the actual and estimated stiffness fault parameters, respectively. Fig. 5.6 shows the damage parameter iteration history. The real parts of estimates converge to the actual stiffness faults within several iterative steps and meanwhile the imaging parts of estimates go to zero.

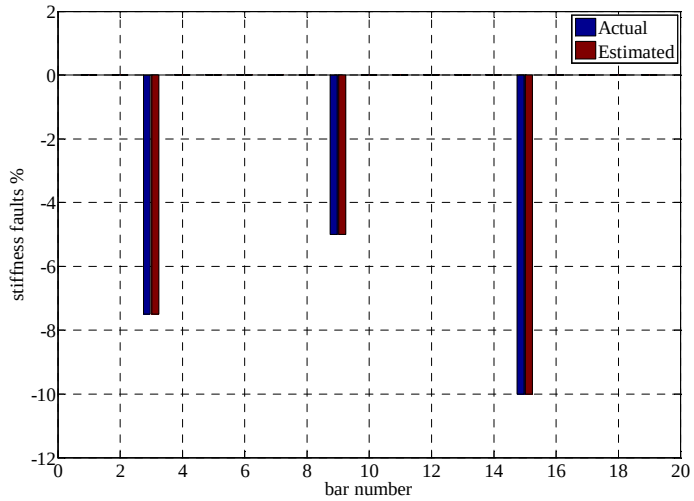

Fig. 5.5 stiffness faults; input: joint 5, sensor: joint 2 & 4

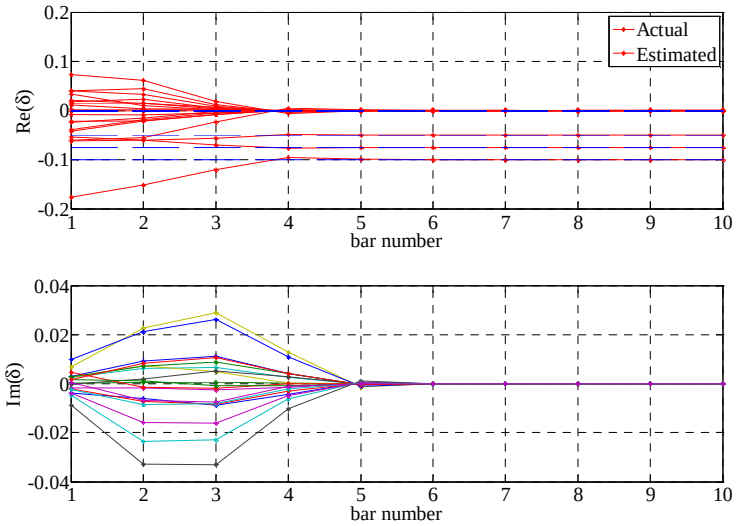

Fig. 5.6 Damage parameter iteration history; input: joint 5, sensor: joint 2 & 4

5.4.2 Stiffness and Mass Uncertainty Detection

Sometimes, the truss may have mass faults besides the stiffness faults which require the damage detection algorithm to be modified. If the mass fault is ignored during the damage identification process, estimated error would happen. Assuming that the truss has

the stiffness faults in Table 5.2 as well as mass faults listed in Table 5.3, the stiffness faults are revaluated using the original FRF based damage identification method.

Table 5.3 Truss mass Faults

Bar No.	Mass Faults	Bar No.	Mass Faults
1	0	11	-10%
2	0	12	0
3	0	13	0
4	-5%	14	0
5	0	15	5%
6	0	16	0
7	0	17	0
8	0	18	0
9	0	19	0
10	0		

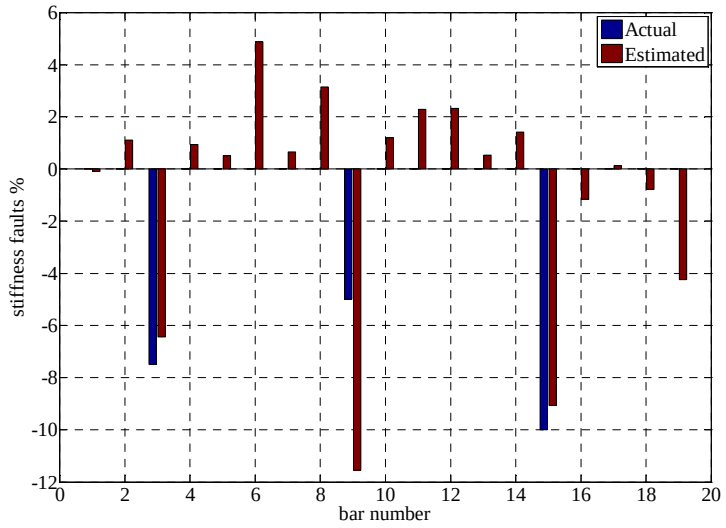

Fig. 5.7 Actual and estimated stiffness faults (ignoring mass faults); interrogation input: joint 5, sensor: joint 2 & 4

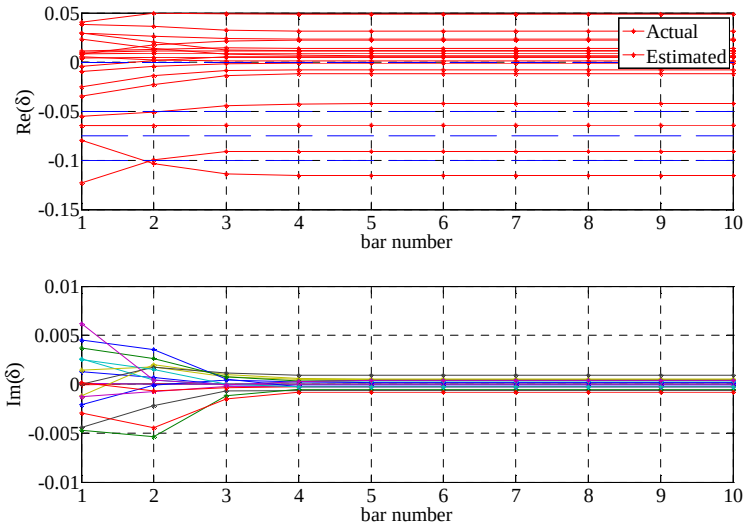

Fig. 5.8 Damage parameter iteration history (ignoring mass faults); interrogation input: joint 5, sensor: joint 2 & 4

Obviously, the existence of mass faults does have a great impact on the estimation accuracy of stiffness faults as shown in Fig. 5.7 and 5.8. Hence, a modified algorithm is proposed to include the mass uncertainty as desired estimated parameter.

The equations-of-motion are recast into the following state-space form with state vector $\mathbf{x} = [q^T \quad \dot{q}^T]^T$

$$\left(\mathbf{E} + \sum_{k=1}^{N_m} \Delta\mathbf{E}_k(t)\right)\dot{\mathbf{x}} = \left(\mathbf{A} + \sum_{k=1}^{N_m} \Delta\mathbf{A}_k(t)\right)\mathbf{x} + \mathrm{B}_u\mathbf{u}(t)$$
$$\mathbf{y} = \mathbf{C}_y\mathbf{x} \tag{5.38}$$

Here the external excitation is expanded in the complex exponential series as:

$$\mathbf{u}(t) = \mathbf{u}e^{j\omega t} \tag{5.39}$$

N_m is the number of bar members. The homogeneous solution of the time-invariant system can be expressed as

$$\mathrm{x}(t) = \mathrm{X}e^{j\omega t} \tag{5.40}$$

After performing harmonic balance, the damaged transfer function are given as a function of both mass and stiffness faults,

$$\tilde{\mathbf{T}} = \mathbf{C}_y[\, j\omega(\mathbf{E} + \sum_{k=1}^{N_{dm}} \Delta\mathbf{E}_k) - \mathbf{A} - \sum_{k=1}^{N_{dk}} \Delta\mathbf{A}_k \,]\mathrm{B}_u \tag{5.41}$$

Using the Taylor expansion on Eq. (5.41), the damage identification is formulated in terms of the following sensitivity matrix *S*,

$$\begin{aligned} \tilde{\mathbf{T}} - \mathbf{T} &\approx \mathbf{C}_y\mathbf{G}^{-1}(\sum_{k=1}^{N_m} \Delta\mathbf{A}_k - \sum_{k=1}^{N_m} \Delta\mathbf{E}_k)\mathbf{G}^{-1}\mathrm{B}_u \\ \ldots\ldots &= \mathbf{C}_y\mathbf{G}^{-1}(\sum_{k=1}^{N_m} \delta_{A,k}\mathbf{A}_k + \sum_{k=1}^{N_m} \delta_{E,k}\mathbf{E}_k)\mathbf{G}^{-1}\mathrm{B}_u \end{aligned} \tag{5.42}$$

$$\Downarrow$$

$$\Delta\mathbf{T}_{yu} = S\delta_{est} \tag{5.43}$$

Using the same procedure and following the iterative process shown in Fig. 5.9, the mass and stiffness faults can be detected by the modified algorithm.

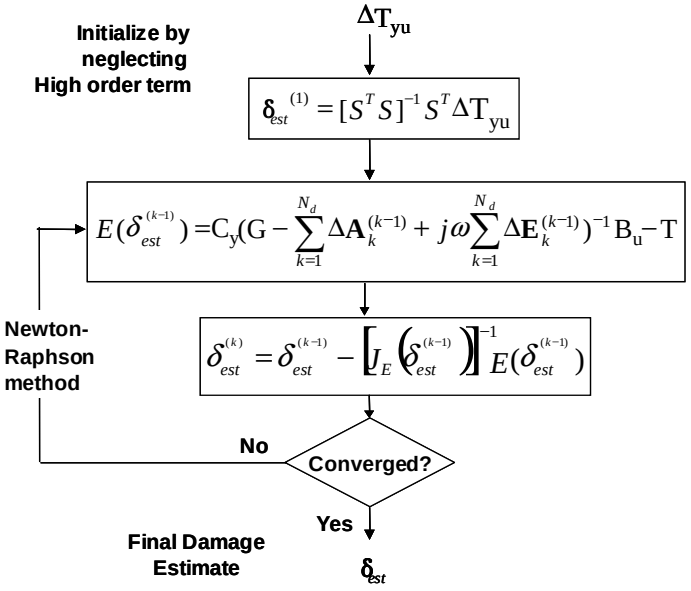

Fig. 5.9 Iterative damage identification process

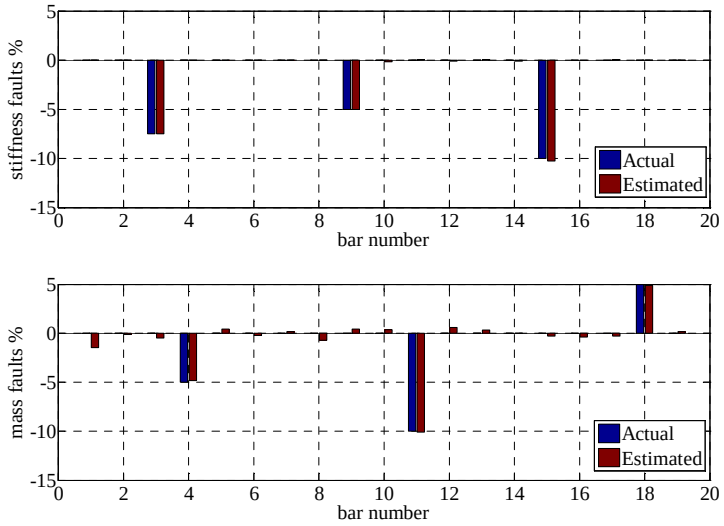

Fig. 5.10 Mass and stiffness fault estimates interrogation input: joint 5, sensor: joint 2, 3, 4 & 5

Fig. 5.10 shows the estimated mass and stiffness faults detected by the modified algorithm and both kinds of faults are able to be detected accurately.

5.5 Linear Damage Identification: Breathing Crack

When the stiffness fault is caused by a transverse crack on the truss, the crack will open and close with the variation of internal force. On the one hand, the crack is closed when the bar is compressed. On the other hand, it will open under tension. In this way, we call the crack is breathing. This breathing function is determined by the status of bar element force which can be obtained by computing the real-time distance of bar joints. Therefore, the breathing function is a nonlinear function which is dependent on the joint displacement.

In order to investigate the nonlinear behavior of the truss problem, we first assume that the breathing function is a function of time. In another words, we assume the excitation force drives the crack breathing with exciting frequency. Thus, the problem becomes a

nonlinear problem of time and we are able to linearize the problem by performing Fourier Expansion later.

5.5.1 Crack Breathing Function

Assuming that the crack opens and closes when the bar is stretched and compressed respectively, the crack breathing function $f_k(t)$ depends on the phase of bar internal force.

$$f_k(t) = \begin{cases} 1 & -\frac{\varphi_k}{\omega} < t < T/2 - \frac{\varphi_k}{\omega} \\ 0 & T/2 - \frac{\varphi_k}{\omega} \le t < T - \frac{\varphi_k}{\omega} \end{cases} \tag{5.44}$$

Here, φ_k is the phase of force for k^{th} member which is calculated through the following steady-state equation:

$$\begin{aligned} \dot{\mathbf{x}} &= \mathbf{A}\mathbf{x} + \mathrm{B}_u \mathbf{u}(t) \\ \mathbf{F} &= \mathbf{C}_F \mathbf{x} \end{aligned} \tag{5.45}$$

where $\mathbf{C}_F$ is the output matrix for bar internal force given as:

$$\mathbf{C}_F = \frac{EA}{l_e} \sum_{n=1}^{N_m} \mathbf{G}_\mathbf{p} \mathbf{T}_n^T \begin{bmatrix} 1 & -1 \\ -1 & 1 \end{bmatrix} \tag{5.46}$$

With $\mathbf{T}_n$ is the transformation matrix from local coordinate system to bar coordinate system and $\mathbf{G}_\mathbf{p}$ is the positioning matrix for placing the element matrix into the global matrix.

Note that the crack position is assumed not to affect the breathing phase, since the wave speed transmitted in the bar is much faster than the vibrating speed. For example, the 1st frequency for wave transmission is much larger than the excitation frequency,

$$\frac{\pi}{l_e}\sqrt{\frac{E}{\rho}} >> \omega \tag{5.47}$$

5.5.2 Damage Identification Algorithm in Frequency-domain

To develop the damage detection methodology for breathing cracked truss, the equations-of-motion are recast into the following state-space form with state vector $\mathbf{x} = [D_e^T \quad \dot{D}_e^T]^T$

$$\begin{aligned} \dot{\mathbf{x}} &= \left(\mathbf{A} + \sum_{k=1}^{N_d} \Delta\mathbf{A}_k f_k(t) \right)\mathbf{x} + \mathrm{B}_u \mathbf{u}(t) \\ \mathbf{y} &= \mathbf{C}_y \mathbf{x} \end{aligned} \tag{5.48}$$

Here $\mathbf{A}$ and $\Delta\mathbf{A}_k$ are the system matrix and damage matrices, and $f_k(t)$ is crack breathing function which switches between 0 and 1 periodically shown in the Fig. 5.11.

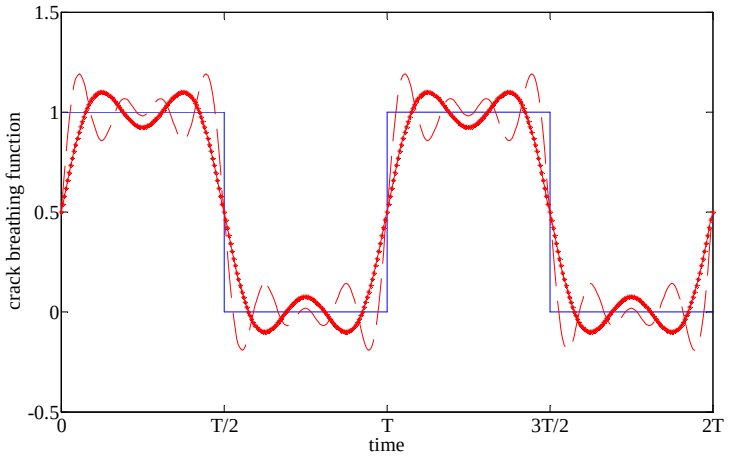

Fig. 5.11 Crack breathing function

The blue solid line is the actual breathing function; the red star line and dash line denotes the two-term and four-term Taylor expansions of the breathing function, respectively. In the damage identification algorithm, the three-term Taylor approximation is used to convert the nonlinear system to linear periodically time-varying system.

$$f_k(t) \approx \frac{1}{2} + \frac{2}{\pi}\sum_{n=1}^{\infty}\frac{\sin\left[(2n-1)(\omega t+\varphi_k)\right]}{2n-1} \tag{5.49}$$

The homogeneous solution of the linear periodically time-varying system can be expressed as

$$\mathbf{x}(t) = \sum_{k=-N_x}^{N_x} X_k e^{jk\omega t} \tag{5.50}$$

Where N_h is the number of system harmonics. After performing harmonic balance, the following hyper-dimensional problems whose solutions characterize the nominal and damaged system transfer function matrices are given as.

$$\hat{\tilde{\mathbf{T}}} = \hat{\mathbf{C}}_y[\hat{\mathbf{G}} - \sum_{k=1}^{N_m}\Delta\hat{\mathbf{A}}_k]^{-1}\hat{\mathbf{B}}_u \tag{5.51}$$

$\hat{\mathbf{G}}$ and $\Delta\hat{\mathbf{A}}_k$ are the hyper-dimensional nominal system matrix and damage perturbation matrix given by,

$$\hat{\mathbf{G}} = \begin{bmatrix} \ddots & & \vdots & & & \iddots \\ \cdots & -j2\omega\mathbf{I}-\mathbf{A}_0 & -\mathbf{A}_{-1} & -\mathbf{A}_{-2} & \cdots & \\ \cdots & -\mathbf{A}_{+1} & -j\omega\mathbf{I}-\mathbf{A}_0 & -\mathbf{A}_{-1} & -\mathbf{A}_{-2} & \cdots \\ \cdots & -\mathbf{A}_{+2} & -\mathbf{A}_{+1} & -\mathbf{A}_0 & -\mathbf{A}_{-1} & -\mathbf{A}_{-2} \\ & \cdots & -\mathbf{A}_{+2} & -\mathbf{A}_{+1} & j\omega\mathbf{I}-\mathbf{A}_0 & -\mathbf{A}_{-1} \\ & & \cdots & -\mathbf{A}_{+2} & -\mathbf{A}_{+1} & j2\omega\mathbf{I}-\mathbf{A}_0 \\ \iddots & & & \vdots & & \ddots \end{bmatrix} \tag{5.52}$$

$$\Delta\hat{\mathbf{A}}_k = \begin{bmatrix} \ddots & & \vdots & & & \iddots \\ \cdots & \Delta\mathbf{A}_{0,k} & \Delta\mathbf{A}_{-1,k} & \Delta\mathbf{A}_{-2,k} & \cdots & \\ \cdots & \Delta\mathbf{A}_{+1,k} & \Delta\mathbf{A}_{0,k} & \Delta\mathbf{A}_{-1,k} & \Delta\mathbf{A}_{-2,k} & \cdots \\ \cdots & \Delta\mathbf{A}_{+2,k} & \Delta\mathbf{A}_{+1,k} & \Delta\mathbf{A}_{0,k} & \Delta\mathbf{A}_{-1,k} & \Delta\mathbf{A}_{-2,k} \\ & \cdots & \Delta\mathbf{A}_{+2,k} & \Delta\mathbf{A}_{+1,k} & \Delta\mathbf{A}_{0,k} & \Delta\mathbf{A}_{-1,k} \\ & & \cdots & \Delta\mathbf{A}_{+2,k} & \Delta\mathbf{A}_{+1,k} & \Delta\mathbf{A}_{0,k} \\ \iddots & & & \vdots & & \ddots \end{bmatrix} \tag{5.53}$$

with

$$\begin{aligned}
&\Delta\mathbf{K}_{0,k} = \frac{1}{2}\delta_k \mathbf{K}_k \\
&\Delta\mathbf{K}_{2n-1,k} = \frac{1}{(2n-1)\pi}\left(\sin[(2n-1)\varphi_k] + \frac{1}{j}\cos[(2n-1)\varphi_k]\right)\delta_k \mathbf{K}_k \\
&\Delta\mathbf{K}_{-(2n-1),k} = \frac{1}{(2n-1)\pi}\left(\sin[(2n-1)\varphi_k] - \frac{1}{j}\cos[(2n-1)\varphi_k]\right)\delta_k \mathbf{K}_k \\
&n = 1,2,\ldots
\end{aligned} \tag{5.54}$$

and

$$\begin{aligned}
&\hat{\mathbf{B}}_u = [0 \quad 0 \quad \mathbf{B}_u \quad 0 \quad 0]^T \\
&\hat{\mathbf{C}}_y = (2n_h + 1) \otimes \mathbf{C}_y
\end{aligned} \tag{5.55}$$

The following steps are similar with the algorithm in section 4.5.1.

5.5.3 Damage Identification Algorithm in Time-domain

Previously, the damage identification methods were developed in frequency domain. For the practical damage detection, vibration signals are acquired and processed in time domain. Therefore, it is necessary to develop the damage detection algorithm in time domain.

The equations-of-motion are recast into the following state-space form with state vector $\mathbf{x} = [D_e^T \quad \dot{D}_e^T]^T$

$$\begin{aligned}
&\dot{\mathbf{x}} = \left(\mathbf{A} + \sum_{k=1}^{N_d} \Delta\mathbf{A}_k f_k(t)\right)\mathbf{x} + \mathrm{B}_u \mathbf{u}(t) \\
&\mathbf{y} = \mathbf{C}_y \mathbf{x}
\end{aligned} \tag{5.56}$$

Using 3-term approximation of Taylor expansion in Eq. (5.49), the crack breathing function can be expressed as:

$$f_k(t) \approx \frac{1}{2} + \frac{2}{\pi}\left[\sin(\omega t + \varphi_k) + \frac{\sin[3(\omega t + \varphi_k)]}{3}\right] \tag{5.57}$$

The input function u(t) and the homogeneous solution of the linear periodically time-varying system can be expressed as

$$\begin{aligned} \mathbf{u}(t) &= u\sin(\omega t) \\ \mathbf{x}_h(t) &= X_0 + \sum_{n=1}^{N_h}\left[X_n^s \sin(n\omega t) + X_n^c \cos(n\omega t)\right] \end{aligned} \tag{5.58}$$

Where N_h is the number of system harmonics. After performing harmonic balance, the following hyper-dimensional problems whose solutions characterize the nominal and damaged system transfer function matrices are given as.

$$\hat{\hat{\mathbf{T}}} = \hat{\mathbf{C}}_y[\hat{\mathbf{A}} - \sum_{k=1}^{N_m}\Delta\hat{\mathbf{A}}_k]^{-1}\hat{\mathbf{B}}_u \tag{5.59}$$

$\hat{\mathbf{G}}$ and $\Delta\hat{\mathbf{A}}_k$ are the hyper-dimensional nominal system matrix and damage perturbation matrix given by,

$$\hat{\mathbf{A}} = \begin{bmatrix} \mathbf{A} & \frac{\mathbf{A}_1^s}{2} & \frac{\mathbf{A}_1^c}{2} & & & \frac{\mathbf{A}_3^s}{2} & \frac{\mathbf{A}_3^c}{2} & \cdots & & \\ \mathbf{A}_1^s & \mathbf{A} & \omega\mathbf{I} & \frac{\mathbf{A}_1^c - \mathbf{A}_3^c}{2} & \frac{\mathbf{A}_3^s - \mathbf{A}_1^s}{2} & & & \frac{\mathbf{A}_3^c}{2} & -\frac{\mathbf{A}_3^s}{2} & \cdots \\ \mathbf{A}_1^c & -\omega\mathbf{I} & \mathbf{A} & \frac{\mathbf{A}_3^s + \mathbf{A}_1^s}{2} & \frac{\mathbf{A}_1^c + \mathbf{A}_3^c}{2} & & & \frac{\mathbf{A}_3^s}{2} & \frac{\mathbf{A}_3^c}{2} & \cdots \\ & \frac{\mathbf{A}_1^c - \mathbf{A}_3^c}{2} & \frac{\mathbf{A}_3^s + \mathbf{A}_1^s}{2} & \mathbf{A} & 2\omega\mathbf{I} & \frac{\mathbf{A}_1^c}{2} & -\frac{\mathbf{A}_1^s}{2} & \cdots & & \\ & \frac{\mathbf{A}_3^s - \mathbf{A}_1^s}{2} & \frac{\mathbf{A}_1^c + \mathbf{A}_3^c}{2} & -2\omega\mathbf{I} & \mathbf{A} & \frac{\mathbf{A}_1^s}{2} & \frac{\mathbf{A}_1^c}{2} & \cdots & & \\ \mathbf{A}_3^s & & & \frac{\mathbf{A}_1^c}{2} & \frac{\mathbf{A}_1^s}{2} & \mathbf{A} & 3\omega\mathbf{I} & \frac{\mathbf{A}_1^c}{2} & -\frac{\mathbf{A}_1^s}{2} & \cdots \\ \mathbf{A}_3^c & & & -\frac{\mathbf{A}_1^s}{2} & \frac{\mathbf{A}_1^c}{2} & -3\omega\mathbf{I} & \mathbf{A} & \frac{\mathbf{A}_1^s}{2} & \frac{\mathbf{A}_1^c}{2} & \cdots \\ \vdots & \frac{\mathbf{A}_3^c}{2} & \frac{\mathbf{A}_3^s}{2} & \vdots & \vdots & \frac{\mathbf{A}_1^c}{2} & \frac{\mathbf{A}_1^s}{2} & \mathbf{A} & 4\omega\mathbf{I} & \cdots \\ & -\frac{\mathbf{A}_3^s}{2} & \frac{\mathbf{A}_3^c}{2} & & & -\frac{\mathbf{A}_1^s}{2} & \frac{\mathbf{A}_1^c}{2} & -4\omega\mathbf{I} & \mathbf{A} & \cdots \\ & \vdots & \vdots & & & \vdots & \vdots & \vdots & \vdots & \ddots \end{bmatrix} \tag{5.60}$$

$$\Delta\hat{\mathbf{A}}_k = \begin{bmatrix} \Delta\mathbf{A}_{0,k} & \frac{\Delta\mathbf{A}^s_{1,k}}{2} & \frac{\Delta\mathbf{A}^c_{1,k}}{2} & & & \frac{\Delta\mathbf{A}^s_{3,k}}{2} & \frac{\Delta\mathbf{A}^c_{3,k}}{2} & \cdots & \\ \Delta\mathbf{A}^s_{1,k} & \Delta\mathbf{A}_{0,k} & 0 & \frac{\Delta\mathbf{A}^c_{1,k}-\Delta\mathbf{A}^c_{3,k}}{2} & \frac{\Delta\mathbf{A}^s_{3,k}-\Delta\mathbf{A}^s_{1,k}}{2} & & & \frac{\Delta\mathbf{A}^c_{3,k}}{2} & -\frac{\Delta\mathbf{A}^s_{3,k}}{2} & \cdots \\ \Delta\mathbf{A}^c_{1,k} & 0 & \Delta\mathbf{A}_{0,k} & \frac{\Delta\mathbf{A}^s_{3,k}+\Delta\mathbf{A}^s_{1,k}}{2} & \frac{\Delta\mathbf{A}^c_{1,k}+\Delta\mathbf{A}^c_{3,k}}{2} & & & \frac{\Delta\mathbf{A}^s_{3,k}}{2} & \frac{\Delta\mathbf{A}^c_{3,k}}{2} & \cdots \\ & \frac{\Delta\mathbf{A}^c_{1,k}-\Delta\mathbf{A}^c_{3,k}}{2} & \frac{\Delta\mathbf{A}^s_{3,k}+\Delta\mathbf{A}^s_{,k1}}{2} & \Delta\mathbf{A}_{0,k} & 0 & \frac{\Delta\mathbf{A}^c_{1,k}}{2} & -\frac{\Delta\mathbf{A}^s_{1,k}}{2} & \cdots & \\ & \frac{\Delta\mathbf{A}^s_{3,k}-\Delta\mathbf{A}^s_{1,k}}{2} & \frac{\Delta\mathbf{A}^c_{1,k}+\Delta\mathbf{A}^c_{3,k}}{2} & 0 & \Delta\mathbf{A}_{0,k} & \frac{\Delta\mathbf{A}^s_{1,k}}{2} & \frac{\Delta\mathbf{A}^c_{1,k}}{2} & \cdots & \\ \Delta\mathbf{A}^s_{3,k} & & & \frac{\Delta\mathbf{A}^c_{1,k}}{2} & \frac{\Delta\mathbf{A}^s_{1,k}}{2} & \Delta\mathbf{A}_{0,k} & 0 & \frac{\Delta\mathbf{A}^c_{1,k}}{2} & -\frac{\Delta\mathbf{A}^s_{1,k}}{2} & \cdots \\ \Delta\mathbf{A}^c_{3,k} & & & -\frac{\Delta\mathbf{A}^s_{1,k}}{2} & \frac{\Delta\mathbf{A}^c_{1,k}}{2} & 0 & \Delta\mathbf{A}_{0,k} & \frac{\Delta\mathbf{A}^s_{1,k}}{2} & \frac{\Delta\mathbf{A}^c_{1,k}}{2} & \cdots \\ \vdots & \frac{\Delta\mathbf{A}^c_{3,k}}{2} & \frac{\Delta\mathbf{A}^s_{3,k}}{2} & \vdots & \vdots & \frac{\Delta\mathbf{A}^c_{1,k}}{2} & \frac{\Delta\mathbf{A}^s_{1,k}}{2} & \Delta\mathbf{A}_{0,k} & 0 & \cdots \\ & -\frac{\Delta\mathbf{A}^s_{3,k}}{2} & \frac{\Delta\mathbf{A}^c_{3,k}}{2} & & & -\frac{\Delta\mathbf{A}^s_{,k1}}{2} & \frac{\Delta\mathbf{A}^c_{1,k}}{2} & 0 & \Delta\mathbf{A}_{0,k} & \cdots \\ & \vdots & \vdots & & & \vdots & \vdots & \vdots & \vdots & \ddots \end{bmatrix} \tag{5.61}$$

with

$$\hat{\mathbf{B}}_u = \begin{bmatrix} 0 & \overbrace{\mathbf{B}_u \quad 0 \quad \cdots}^{2n_h} \end{bmatrix}^T$$
$$\hat{\mathbf{C}}_y = (2n_h+1) \otimes \mathbf{C}_y \tag{5.62}$$

The following steps are similar with the algorithm in section 4.5.1.

5.5.4 Case Study

In order to ensure that all the damage parameters can be estimated from the measured transfer function shift information ΔT_{yu}, multiple sensors or/and excitation frequencies are utilized to enrich the data and make the problem over-determined as shown in equation (4.20). Two excitation frequency sets are used to detect the damage: one is near-resonance set and the other is far-off-resonance set as shown in Table 5.4 and 5.5. A pair of sensors are placed on joint 3 to measure the response in *x* and *y* directions (Table 5.6).

Table 5.4 Near-resonance excitation frequency set

	trial 1	trial 2
ω (Hz)	90	190

Table 5.5 Far-off-resonance excitation frequency set

	trial 1	trial 2
ω (Hz)	50	150

Table 5.6 Sensor position set

	Sensor (pair)
Joint No.	3

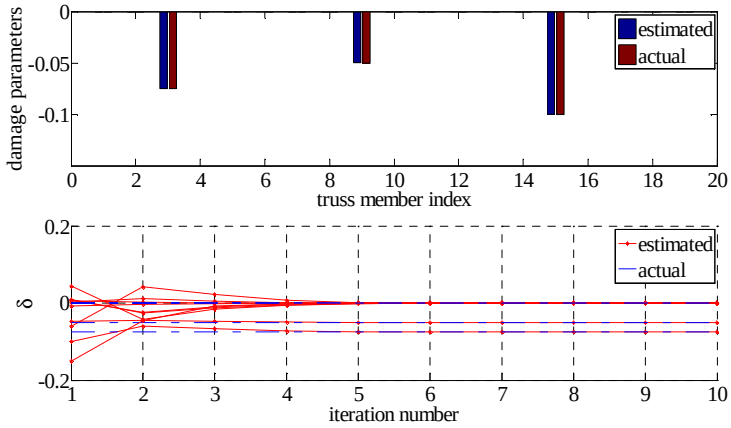

Fig. 5.12 Estimation results for near-resonance set; interrogation input: joint 5 in y dir.

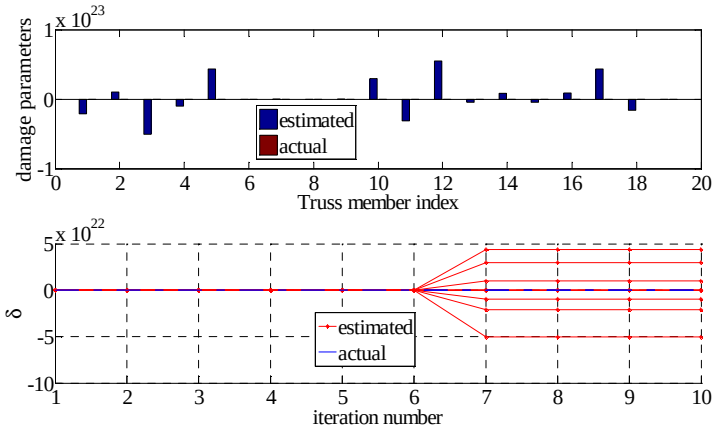

Fig. 5.13 Estimation results for far-off-resonance set; interrogation input: joint 5 in y dir.

Fig. 5.12 and 5.13 show the comparison of actual and estimated stiffness faults and damage parameter iteration history for near-resonance and far-of-resonance excitation

frequency set, respectively. The blue and red bar denotes the actual and estimated stiffness faults, respectively. These results again show the effectiveness of near-resonance excitation in damage detection process which was shown in Chapter IV.

5.6 Time-domain Simulation

In this section, truss model is simulated to get the nonlinear joint displacements and they are compared with those from simulation of simplified linear model.

5.6.1 Linear Simulation Diagram

Fig. 5.14 shows the simulation diagram of damage detection, which contains the excitation frequency switching block (Fig. 5.15), crack phase switching block (Fig. 5.16), damaged and nominal truss system block, convolution block (Fig. 5.17) and damage detection block. The excitation frequency switching block is used to get multiple sets of transfer function and enrich the dataset for damage detection. Crack phase switching block gives the system crack phases for the corresponding excitation frequency. The vibration response of damaged and nominal system is computed through S-functions in damaged and nominal truss system block. Then, the vibration response signals are processed in the convolution block to obtain Harmonic Fourier Coefficient (HFC). Finally, the damage detection block estimates the damage parameters using HFCs as input.

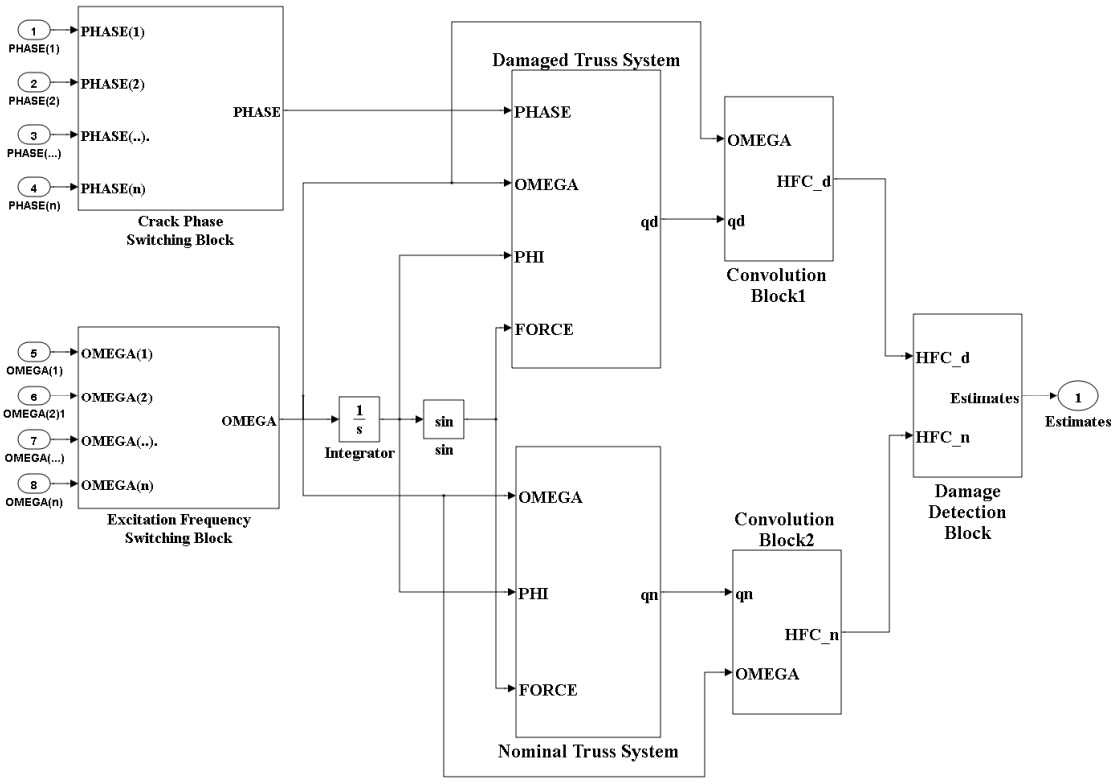

Fig. 5.14 Linear simulation diagram

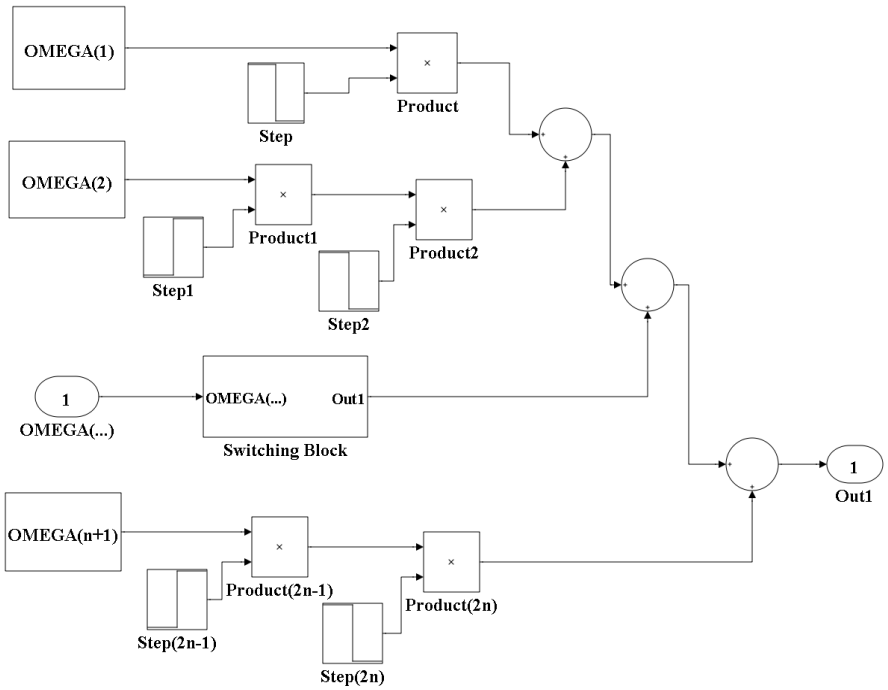

Fig. 5.15 Excitation frequency switching block

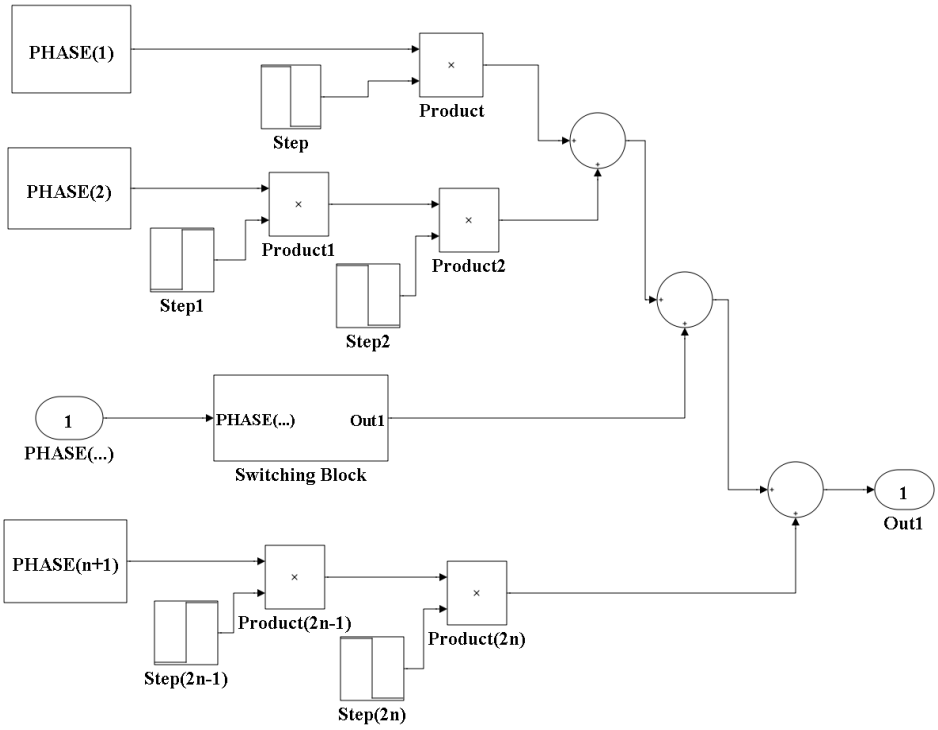

Fig. 5.16 Crack phase switching block

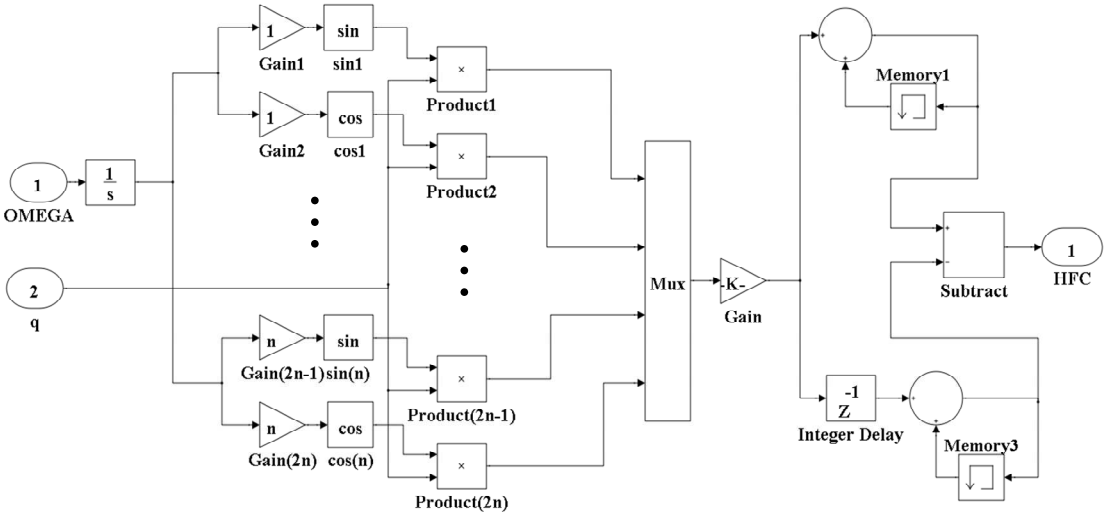

Fig. 5.17 Convolution block

5.6.2 Nonlinear Simulation Diagram

As mentioned at the beginning of this section, the damaged truss system is a nonlinear problem. The breathing function of crack is a nonlinear function of bar joint displacement. Hence, the system equation of motion is written as:

$$M_c\ddot{Q} + C_c\dot{Q} + (K_c - \sum_{k=1}^{N_d} K_{d,k} f_k(t,Q))Q = P_c \tag{5.63}$$

Here, $K_{d,k}$ is the stiffness reduction matrix on k^{th} truss bar member when the breathing crack is open; $f_k(t,Q)$ is a nonlinear function which can be expressed as:

$$f_k(t,Q) = \begin{cases} 1 & u(Q) > 0 \\ 0 & u(Q) \le 0 \end{cases} \tag{5.64}$$

with

$$u(Q) = \sqrt{\left(x_i + Q_{xi} - x_j - Q_{xj}\right)^2 + \left(y_i + Q_{yi} - y_j - Q_{yj}\right)^2} - \sqrt{\left(x_i - x_j\right)^2 + \left(y_i - y_j\right)^2} \tag{5.65}$$

where x_i, x_j, y_i and y_j are the coordinates of node i and j in x and y directions; Q_{xi}, Q_{xj}, Q_{yi} and Q_{yj} are the displacements of node i and j in x and y directions.

The full nonlinear vibration simulation of the damaged truss system is given in this section. Fig. 5.18 shows the nonlinear simulation diagram, which contains the excitation frequency switching block, damaged and nominal truss system block, damage feedback block (Fig. 5.19), convolution block (Fig. 5.17) and damage detection block. The excitation frequency switching block is used to get multiple sets of transfer function and enrich the dataset for damage detection. The vibration response of damaged and nominal system is computed through S-functions in damaged and nominal truss system block. For the nonlinear system, crack phase is not designated in advance because it can only be obtained by computing the distance of bar joints according to the response of every step.

Fig. 5.19 shows the details of damage feedback block which judges the status of damage and gives the feedback to the system for every step. Then, the vibration response signals are processed in the convolution block to obtain Harmonic Fourier Coefficient (HFC). Finally, the damage detection block estimates the damage parameters using HFCs as input.

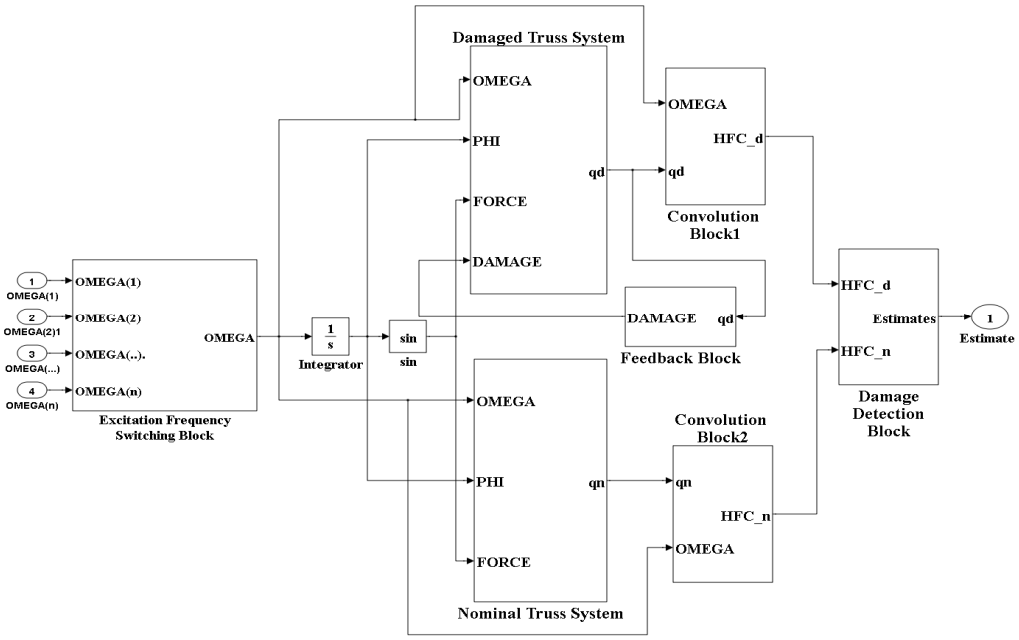

Fig. 5.18 Simulation diagram for nonlinear system

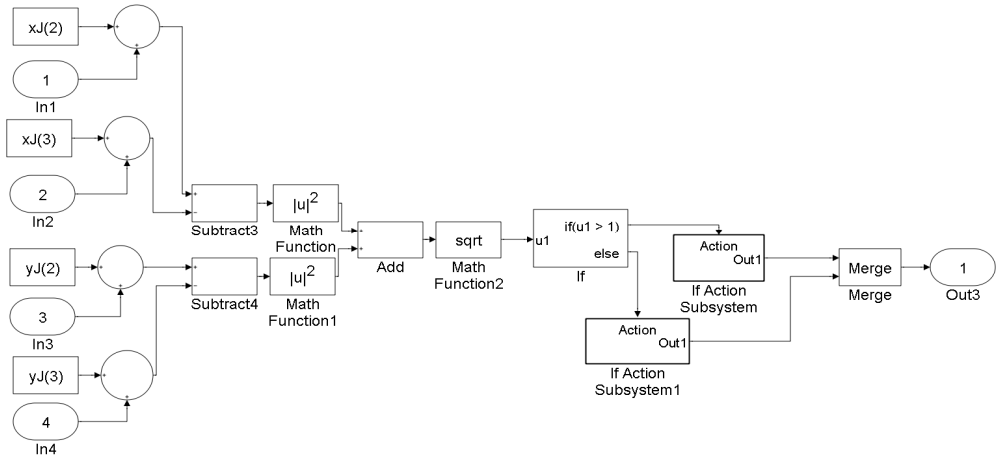

Fig. 5.19 Damage feedback block

5.6.3 Frequency Spectrum Comparison

For a linearly time-varying system, an excitation frequency leads to not only the frequency response at said frequency but also multiple sidebands. This feature benefits the process of damage detection, since the information of sidebands enriches the dataset for damage detection. However, it is a question that if we could be able to use this feature to detect the damage in a nonlinear system. Thus, we computed the joint displacements of time-varying and nonlinear system under the same damage condition and compared the frequency spectrum of the displacements.

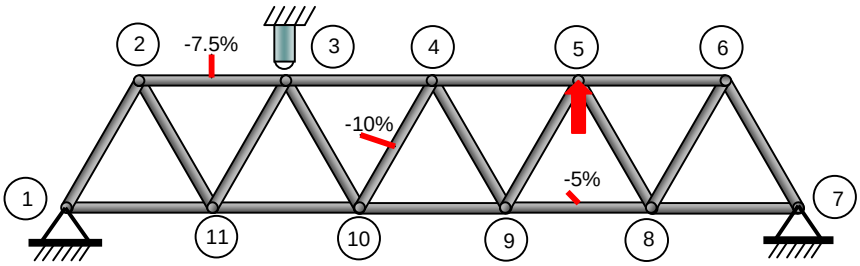

Fig. 5.20 Truss damage detection: nonlinear

The truss system shown in Fig. 5.20 is excited in y direction at joint 5 by four excitation trails with different frequency as shown in Fig. 5.21 and Table 5.7.

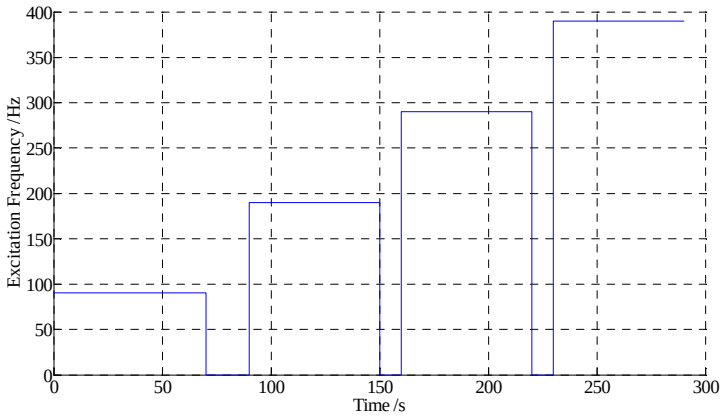

Fig. 5.21 Excitation frequency switching

Table 5.7 Excitation frequency set: nonlinear Truss

	trial 1	trial 2	trial 3	trial 4
ω (Hz)	90	190	290	390

The displacements of joints are calculated from the linear and nonlinear simulation in last section. Fig. 5.22 shows the displacement of damaged system at joint 3 in *x* direction. The red and blue lines denote the output from nonlinear and linear simulation, respectively.

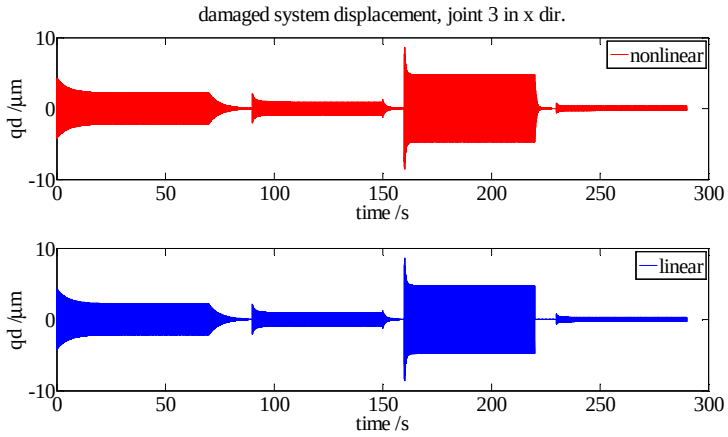

Fig. 5.22 Displacement of joint 3 in *x* direction

We can see from Fig. 5.22 that the vibration goes to steady state after a while for each harmonic input. The next step is to pick a segment of steady response and do Fast Fourier Transform so that the frequency components in the signal could be observed.

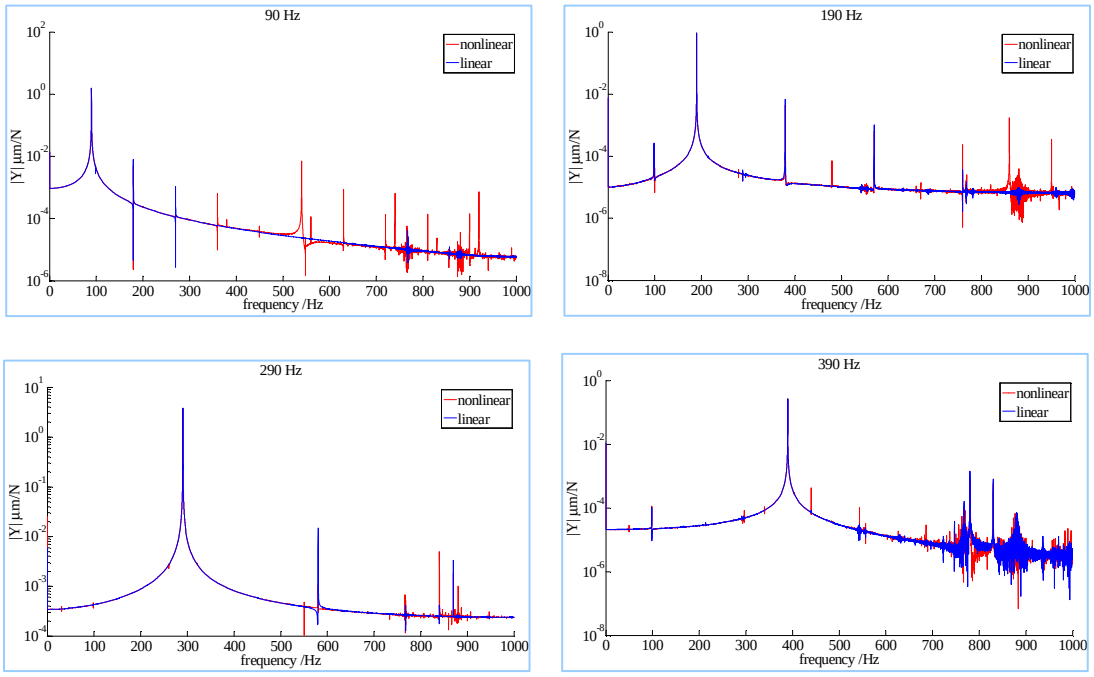

Fig. 5.23 Frequency spectrum for each harmonic input

Fig. 5.23 shows the linear and nonlinear frequency spectrums for each of harmonic inputs. The red and blue lines denote nonlinear and linear spectrum, respectively. The nonlinear response has a lot of irregular high-frequency harmonic components while the linear response is mainly composed of the primary and sideband harmonics. It can be seen that the curves match each other very well at the primary peak for all inputs. For lower excitation frequency such 90 Hz and 190 Hz, it looks like spectrum lines are close at 1st sideband location. For the higher order sidebands, the discrepancy can be seen obviously. To decide how many frequencies we can use for damage detection, we need to take a close look at the values at the primary peak and sidebands for both nonlinear and linear model. Fig. 5.24 shows Harmonic Fourier Coefficients (HFCs) for each of the harmonic inputs. They are calculated by convolution method and represent the specific values at primary peak and sidebands locations extracted from the frequency spectrum (Fig. 5.24).

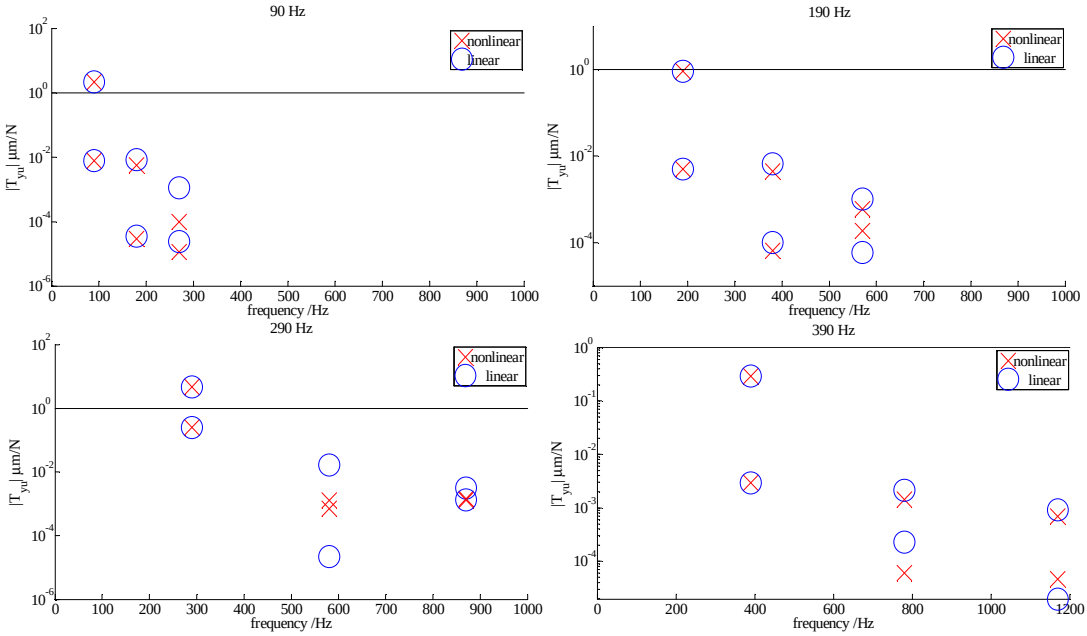

Fig. 5.24 Transfer function shifts data for each harmonic input

5.6.4 Damage Identification

In this section, the damage is estimated using different number of sensors and frequencies. Table 5.8 gives four cases which will be used for damage detection individually.

Table 5.8 Damage detection setup

	Sensor (pair)	Harmonics
Case I	Joint 2 &10	Primary
Case II	Joint 2 &10	Primary & 1st sideband
Case III	Joint 2	Primary
Case IV	Joint 2	Primary & 1st sideband

Fig. 5.25-5.28 show the damage detection results of four cases including the stiffness faults comparison and damage parameter iteration history. The blue and red bar denotes the actual and estimated stiffness faults, respectively. The blue dash line and red star line denotes the actual and estimated damage parameters, respectively.

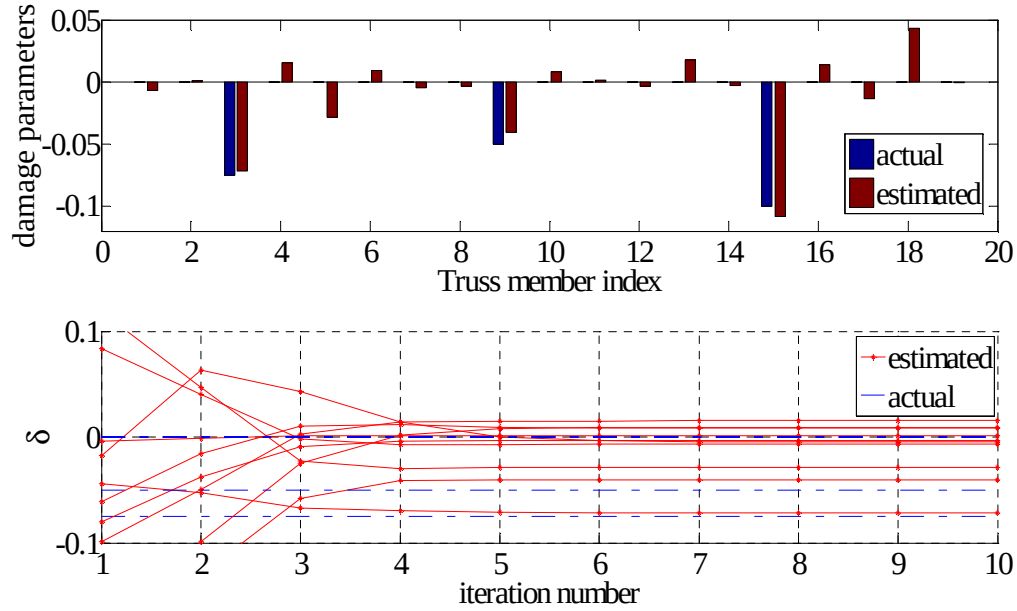

Fig. 5.25 Damage estimation results, Case I

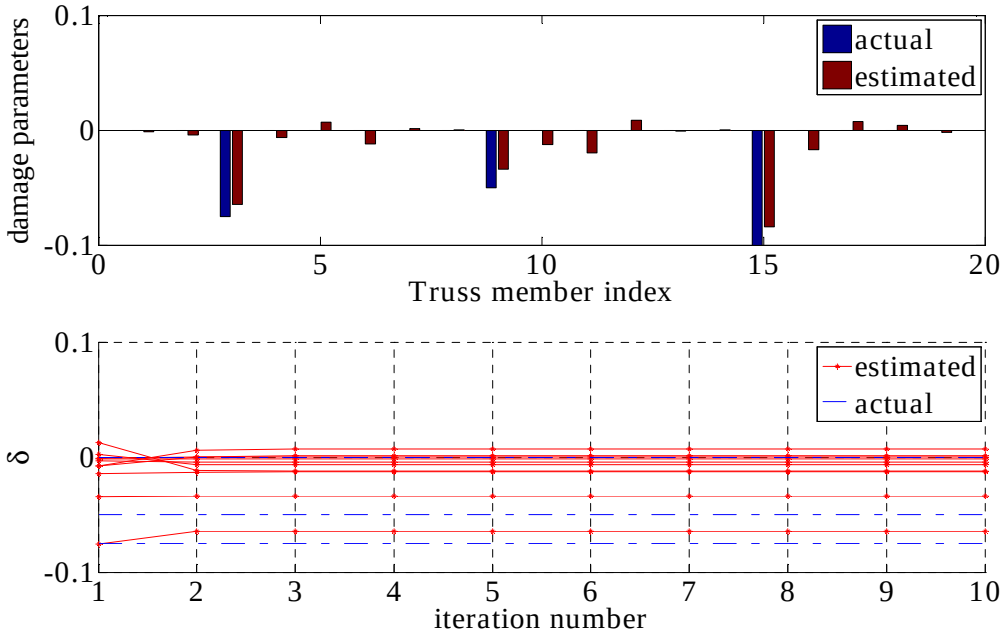

Fig. 5.26 Damage estimation results, Case II

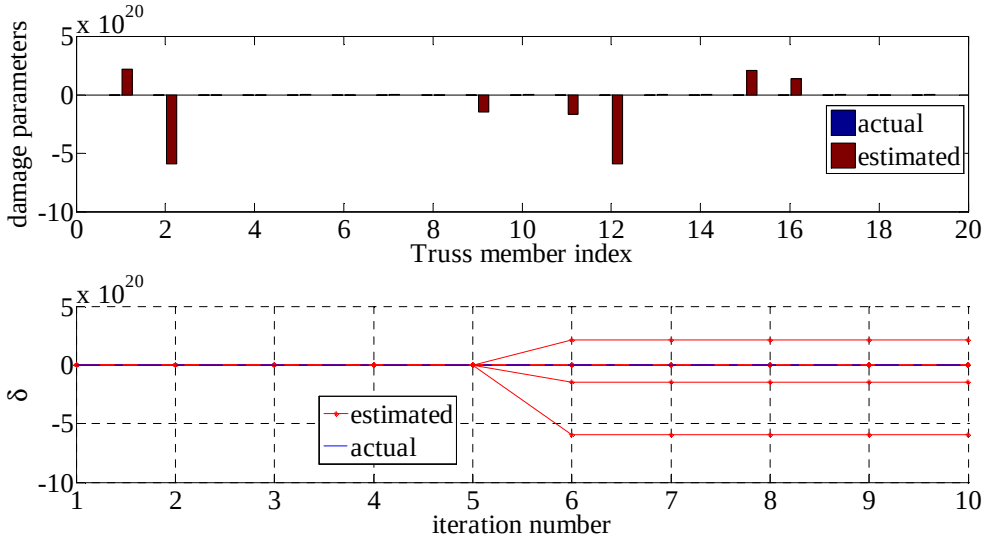

Fig. 5.27 Damage estimation results, Case III

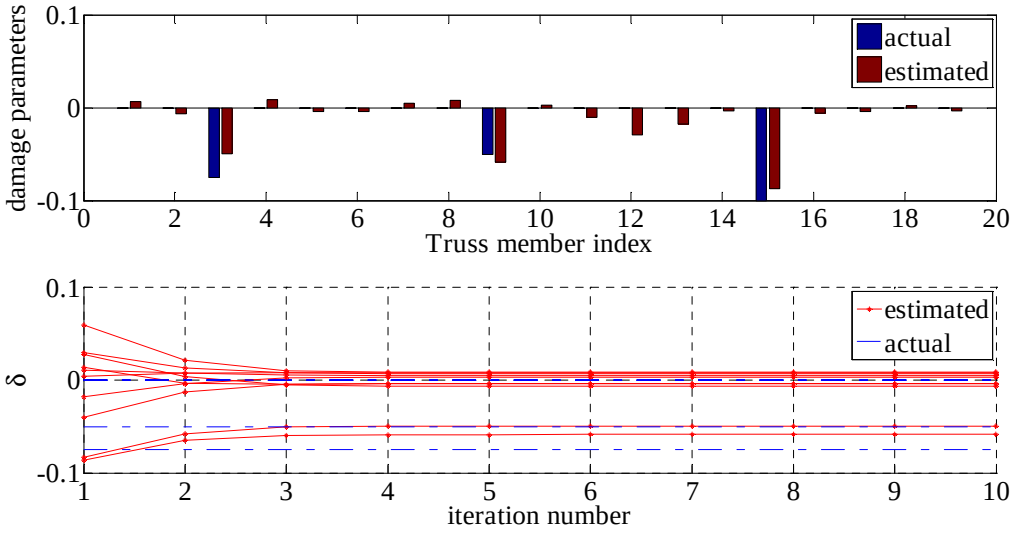

Fig. 5.28 Damage estimation results, Case IV

The results show that primary peak and 1st sideband interrogation is always better than just using primary peak interrogation regardless if we use 1 or 2 pairs of sensors. The data from primary peak is not enough to make the sensitivity matrix fully ranked if we use only one pair of sensors in case III. Therefore, the sensor should be increased or more excitation frequency should be applied which is not easy in the practical project.

However, the estimation results are much better if the information of 1st sideband is added in case IV. It shows that the sidebands data does benefit the damage detection even though some data are not perfect matched with the data of linear model.

5.7 Summary

In this Chapter, FRF based damage identification methodology is modified to identify the stiffness and mass uncertainties as well as the breathing cracks existed on a truss system. First, the truss model is built based on finite element methods and the crack model is rebuilt because the crack only endures tension and compression on a truss bar. Different from three damage parameters in rotor system, only one parameter is needed to represent the severity of damage. Meanwhile, the location of damage can only be targeted at bar element due to much faster wave transmission speed. For a practical truss, it may have stiffness reduction or mass uncertainty due to long-term usage and wear. Therefore, the method is used to detect both stiffness and mass uncertainties existed on a truss. It is shown that better estimation results can be achieved while including both kinds of uncertainty as unknown parameters.

When the truss has transverse cracks, the damage identification becomes a nonlinear problem due to the nonlinear behaviors of breathing cracks. For simplicity, the crack is assumed to be open and close with exciting frequency. With this assumption, the breathing function is a square wave and the damage detection algorithm is developed in frequency and time domain.

However, the crack does not open and close with a constant frequency in reality. To get the nonlinear vibration response, the nonlinear system model is built and the crack

status is determined by judging the distance of bar joints. The frequency spectrums are compared between the linear and nonlinear response and Harmonic Fourier Coefficients are computed by taking the response to the convolution block and moving average filter. Finally, the Harmonic Fourier Coefficients of primary and 1^{st} sidebands are used in damage detection and acceptable results are obtained.

Chapter VI

DAMAGE IDENTIFICATION OF BREATHING CRACKS IN ROTOR SYSTEM

6.1 Introduction

This chapter develops a damage detection method that is used to detect the breathing cracks on the rotordynamic system. It employs the change of transfer function between undamaged and damaged system to detect the cracks. The breathing crack model is built and compared with several classic breathing crack models. Then, the method is demonstrated by several numerical cases of damage detection using shaft sensors and laser scanner. Finally, the breathing cracked rotor system is simulated in the Simulink and the real-time vibration signal is processed and used for damage identification of breathing cracks.

6.2 Breathing Crack Model

In the rotor system, the existence of shaft cracks changes the shaft stiffness and impacts on the dynamical property of rotor system. We introduced several crack models in the Chapter I, such as square wave model and cosine model. In this chapter, Stress Intensity Factor (SIF) method is used to determine the open and close region of breathing cracks. Crack close line is calculated for every rotation angle while SIF is zero and then crack open region can be further determined.

6.2.1 Zero SIF Method

In the fracture mechanics, K_I, K_{II} and K_{III} are the stress intensity factors (SIF) corresponding to opening mode, sliding mode and shearing mode. When the crack is open, $K_I > 0$. Thus, we could compute K_I for every point in the crack region and determine the crack close line by $K_I = 0$ [150].

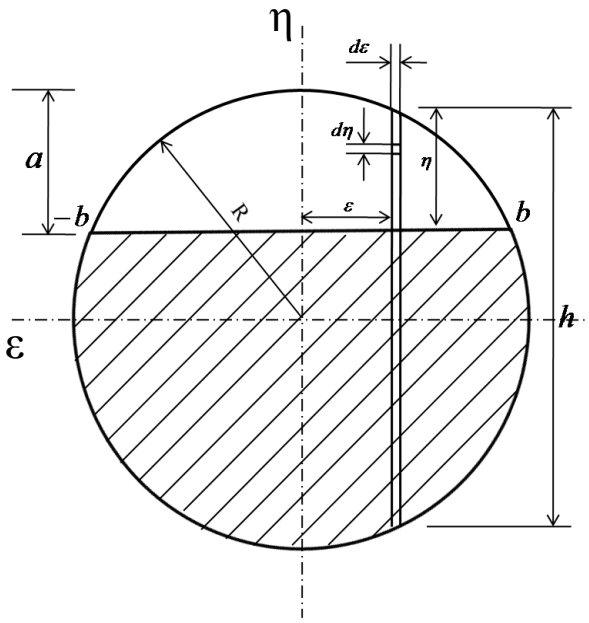

Fig. 6.1 Cracked shaft cross-section

Fig. 6.1 shows the cross-section at crack location. For a random position in crack region, the first SIFs in two directions are:

$$K_{I\eta} = \frac{Q_\eta L}{4} \frac{\sqrt{R^2 - \varepsilon^2}}{\frac{\pi R^4}{4}} \sqrt{\pi\eta} F_2(\eta/h)$$
$$K_{I\varepsilon} = \frac{Q_\varepsilon L}{4} \frac{\varepsilon}{\frac{\pi R^4}{4}} \sqrt{\pi\eta} F_1(\eta/h) \tag{6.1}$$

The total first stress intensity factor is

$$K_I = K_{I\eta} + K_{I\varepsilon} \tag{6.2}$$

6.2.2 Crack Open Region

In this section, we simulate the opening and closing of breathing crack while assuming that the breathing behavior is determined by gravity. Fig. 6.2 shows the coordinate transformation between crack and rotating-frame coordinates.

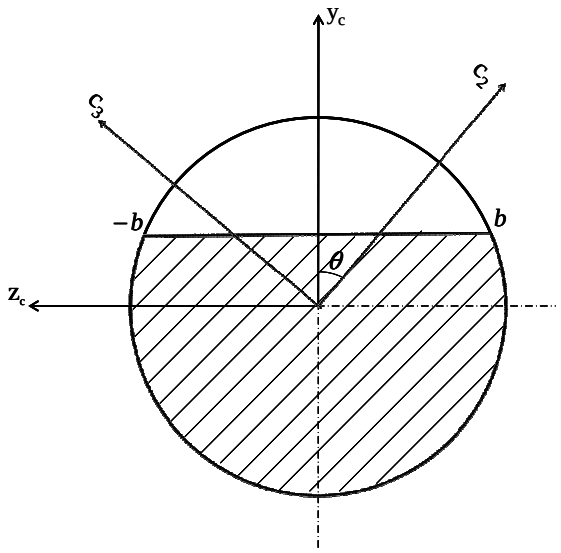

Fig. 6.2 Coordinate transformation: breathing crack

For simplicity, the angle between two coordinates θ = 0°. When the shaft is rotating with the speed Ω, the external forces in two directions of rotating-frame coordinate is,

$$\begin{aligned} Q_\eta &= -mg\cos(\Omega t) \\ Q_\varepsilon &= mg\sin(\Omega t) \end{aligned} \tag{6.3}$$

According to zero SIF method, we retrace the points with K_I = 0 in the entire crack region. Here, the crack depth is chosen be to R/2. Obviously, the crack is fully open when the rotation angle is 0°/360° and it is fully closed when the angle is 180°. Fig. 6.3 shows the cross-sections of breathing crack under different shaft rotation angles. The gray and white region denotes the closing and opening region of crack, respectively.

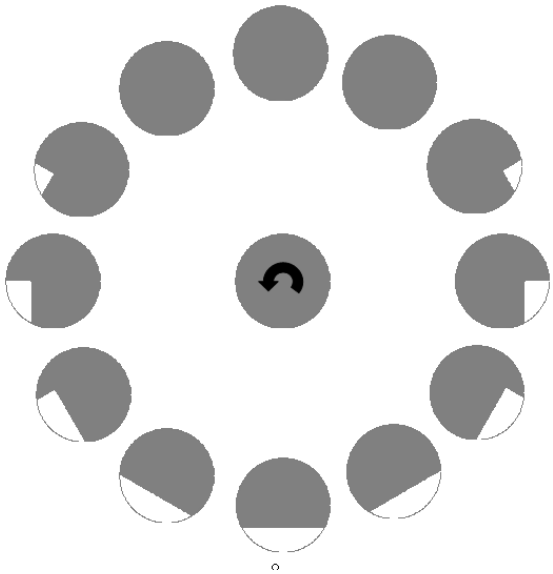

Fig. 6.3 Crack open region

For the crack with depth *R*/2, it keeps fully open and close for about 60 degrees for each state in one period. For other rotation angles, the crack is in transition state. Fig. 6.4 gives the area variation of crack open region versus the rotation angle.

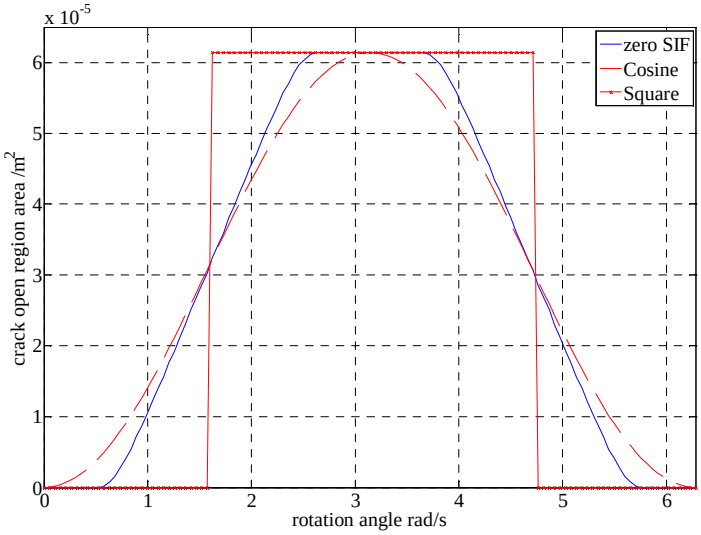

Fig. 6.4 Area variation of crack open region

The blue solid, red dash and red star line denotes the area calculated by zero SIF method, cosine and square model, respectively.

6.2.3 Breathing Crack Mechanism

Different from the open crack, the stiffness reduction parameters of breathing crack are function of rotation angle, $A_c^p(\Omega t)$, $B_c^p(\Omega t)$ and $C_c^p(\Omega t)$, which are shown in Fig. 6.5.

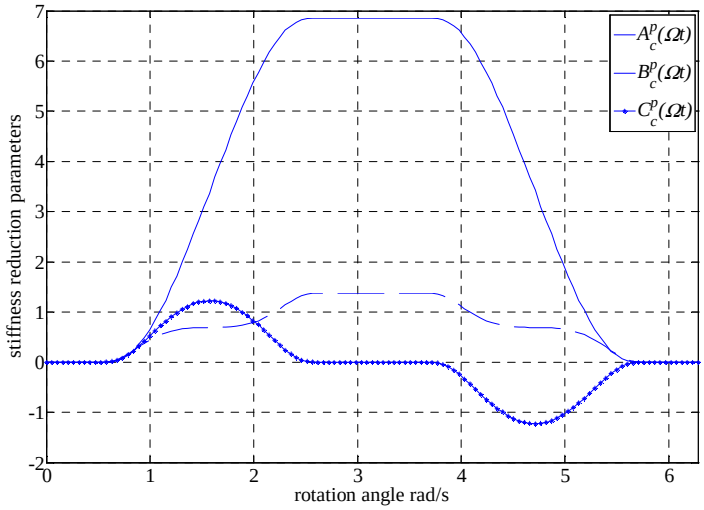

Fig. 6.5 Stiffness reduction parameters vs. rotation angle, a=R/2

Unlike the open cracks, the stiffness reduction parameters are not independent on the rotation angle any more for breathing cracks. For an open crack with any depth, the parameter in y_c direction is always much larger than the one z_c direction and the parameter in cross-coupling direction is always zero. However, the parameter in y_c direction (Fig. 6.2) is not dominant while the crack is opening in the early stage of transition. Furthermore, the crack leads to stiffness reduction in cross-coupling direction in crack coordinate because the crack open region is not symmetric with respect to the y_c axis.

Next, the stiffness variation in rotating coordinate {c} is expressed as a function of crack angle θ and rotation angle Ωt. Here, we define the stiffness reduction parameters in c_2, c_3 and the cross-coupling directions as $A_{c\theta}^p(\theta,\Omega t)$, $B_{c\theta}^p(\theta,\Omega t)$ and $C_{c\theta}^p(\theta,\Omega t)$:

$$
\begin{aligned}
A_{c\theta}^{p}(\theta,\Omega t) &= 2A_{c}^{p}(\Omega t)\cos^{2}\theta + 2B_{c}^{p}(\Omega t)\sin^{2}\theta - 2C_{c}^{p}(\Omega t)\sin 2\theta \\
B_{c\theta}^{p}(\theta,\Omega t) &= 2A_{c}^{p}(\Omega t)\sin^{2}\theta + 2B_{c}^{p}(\Omega t)\cos^{2}\theta + 2C_{c}^{p}(\Omega t)\sin 2\theta \\
C_{c\theta}^{p}(\theta,\Omega t) &= \left[A_{c}^{p}(\Omega t) - B_{c}^{p}(\Omega t)\right]\sin 2\theta + 2C_{c}^{p}(\Omega t)\cos 2\theta
\end{aligned}
\tag{6.4}
$$

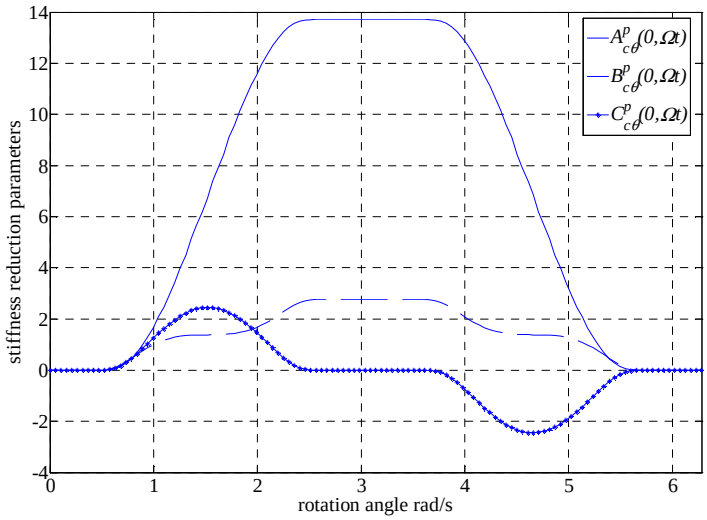

Fig. 6.6 stiffness reduction parameters vs. rotation angle, a=R/2, θ=0°

Fig. 6.6 shows the stiffness reduction parameters variation versus rotation angle (crack angle = 0°). When the crack angle is 0°, the stiffness reduction parameters in rotating-frame coordinate behave like those in crack coordinate. Fig. 6.7 shows the variation of $A_{c\theta}^{p}(\theta,\Omega t)$, $B_{c\theta}^{p}(\theta,\Omega t)$ and $C_{c\theta}^{p}(\theta,\Omega t)$ with the change of rotation angle when the crack angle is varying from 0° to 165° with an interval 15°. The solid, dash and star line denotes the stiffness reduction parameter in c_2, c_3 and cross-coupling direction, respectively.

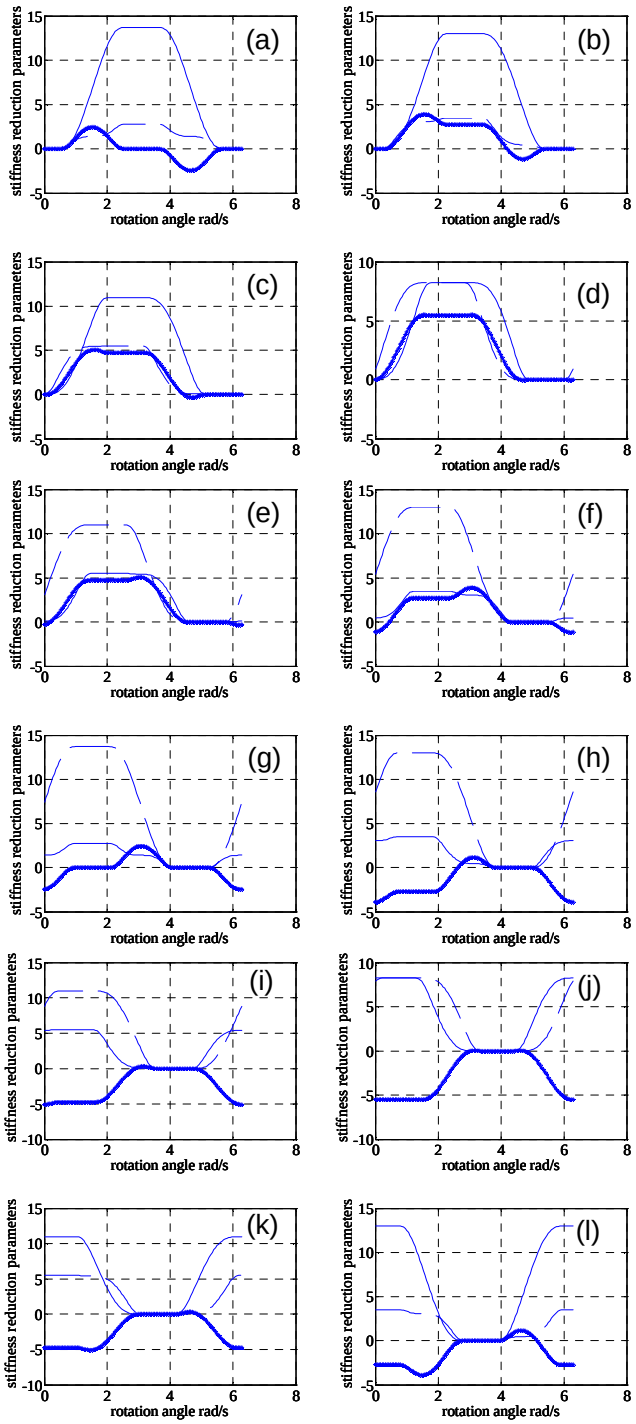

Fig. 6.7 stiffness reduction parameters variation, a=R/2; (a) Ωt=0; (b) Ωt=15°; (c) Ωt=30°; (d) Ωt=45°; (e) Ωt=60°; (f) Ωt=75°; (g) Ωt=90°; (h) Ωt=105°; (i) Ωt=120°; (j) Ωt=135°; (k) Ωt=150°; (l) Ωt=165°;

The maximum magnitudes of $A_{c\theta}^{p}(\theta,\Omega t)$, $B_{c\theta}^{p}(\theta,\Omega t)$ and $C_{c\theta}^{p}(\theta,\Omega t)$ vary periodically with period π. $Max\left(A_{c\theta}^{p}(\theta,\Omega t)\right)$ goes down in the range $0<\theta<\pi/2$ while $Max\left(B_{c\theta}^{p}(\theta,\Omega t)\right)$ rising up, and vice versa in the range $\pi/2<\theta<\pi$. $Max\left(C_{c\theta}^{p}(\theta,\Omega t)\right)$ is monotonously increasing in the range $0<\theta<\pi/4$ & $3\pi/4<\theta<\pi$ and monotonously decreasing in the range $\pi/2<\theta<3\pi/2$. Also, it can be observed that the phase of $A_{c\theta}^{p}(\theta,\Omega t)$, $B_{c\theta}^{p}(\theta,\Omega t)$ and $C_{c\theta}^{p}(\theta,\Omega t)$ shift left with the increase of the crack angle. Furthermore, the effect of cross-coupling stiffness reduction is dominant by the term $C_{c}^{p}(\Omega t)$ near the range $\theta=n\pi/2$ (n=0, 1, 2 …) and by the term $\left[A_{c}^{p}(\Omega t)-B_{c}^{p}(\Omega t)\right]$ near the range $\theta=n\pi/4$ (n=1, 3 …).

6.2.4 Crack Model Comparison

In this section, the stiffness reduction parameters are calculated by Dimarogonas method, Cosine and square model.

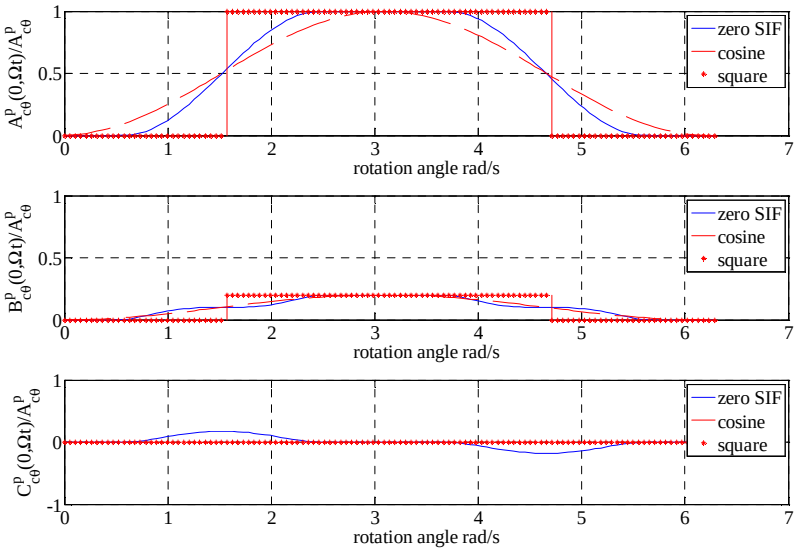

Fig. 6.8 Stiffness reduction parameters comparison, $a=R/2$

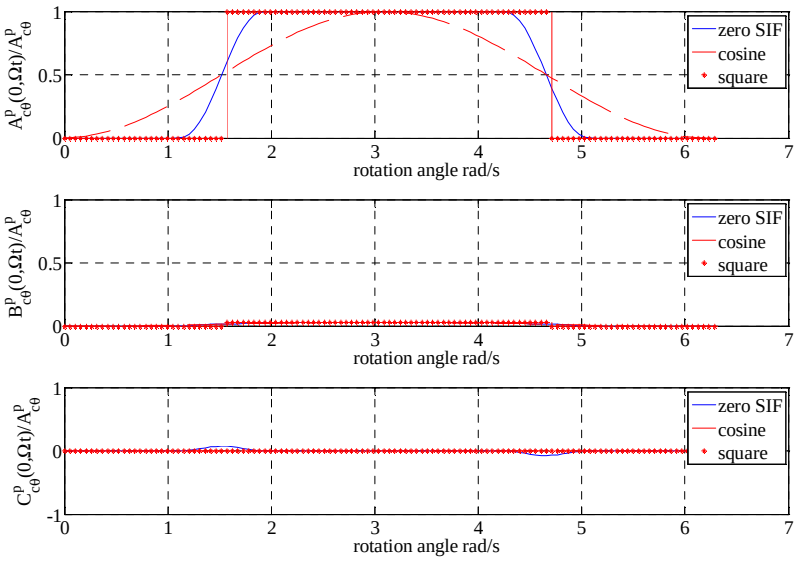

Fig. 6.9 Stiffness reduction parameters comparison, a=R/10

Fig. 6.8 shows the stiffness reduction parameters for a breathing crack with depth R/2 and crack angle 0°. Fig. 6.9 shows the parameters for a crack with depth R/10. After unifying $A^p_{c\theta}(0,\Omega t)$ to 1, it is easy to see that $\max\left(B^p_{c\theta}(0,\Omega t)\right)$ and $\max\left(C^p_{c\theta}(0,\Omega t)\right)$ become smaller with the decrease of crack depth. The ratio $\max\left(B^p_{c\theta}(0,\Omega t)/A^p_{c\theta}(0,\Omega t)\right)$ is 0.2 for a=R/2 and 0.04 for a=R/10 which means that $A^p_{c\theta}(0,\Omega t)$ is dominant for small cracks. The ratio $\max\left(C^p_{c\theta}(0,\Omega t)/A^p_{c\theta}(0,\Omega t)\right)$ is 0.2 for a =R/2 and 0.1 for a=R/10.

By comparing the different models, we found the cosine model is closer to the actual curve when the crack depth is large and square model is more accurate to describe the breathing behavior for small cracks. In addition, $C^p_{c\theta}(0,\Omega t)$ is assumed to be 0 in Cosine and Square crack models. This assumption approaches the real situation with the decrease of crack depth.

6.3 Damage Identification Algorithm

For the breathing cracked rotor system, the equation of motion is given as,

$$[M_s + M_d]\ddot{q} + [C_s + G_s + G_d]\dot{q} + \underbrace{[K_s - \sum_{k=1}^{n_e} f_k(t)\delta_k K_k]}_{\mathbf{K}(t)} q = 0 \tag{6.5}$$

Here, f_k is breathing function for k^{th} element. The cosine crack model is adopted in this chapter and f_k can be expressed as,

$$f_k(t) = \frac{1}{2}\left[1 - \cos(\Omega t + \theta_k)\right] \tag{6.6}$$

with θ_k is the angle of crack on k^{th} element. Then, the equation-of-motion is recast into the following state-space form with state vector $\mathbf{x} = \begin{bmatrix} q^T & \dot{q}^T \end{bmatrix}^T$

$$\begin{aligned} \dot{\mathbf{x}} &= \left(\mathbf{A} - \sum_{k=1}^{N_d} \Delta\mathbf{A}_k f_k(t) \right)\mathbf{x} + \mathrm{B}_u \mathbf{u}(t) \\ \mathbf{y} &= \mathbf{C}_y \mathbf{x} \end{aligned} \tag{6.7}$$

The external excitation and damage matrices, **u(t)**, and $\Delta\mathbf{A}_k(t)$, are expanded in the complex exponential series as:

$$\begin{aligned} \mathbf{u}(t) &= \mathbf{u}e^{j\omega t} \\ \Delta\mathbf{A}_k(t) &= \sum_{n=-N_h}^{N_h} \Delta\mathbf{A}_{n,k} e^{jn\Omega t} \end{aligned} \tag{6.8}$$

where N_h is the number of system harmonics. In the case of the shaft-disk system, N_h = 2. The homogeneous solution of the linear periodically time varying system can be expressed as

$$\mathbf{x}(t) = \sum_{n=-Nx}^{N_x} \mathbf{x}_n e^{jn\Omega t} e^{j\omega t} \tag{6.9}$$

After performing harmonic balance, the following hyper-dimensional problems whose solutions characterize the nominal and damaged system transfer function matrices are given as:

$$\mathbf{T} = \hat{\mathbf{C}}\hat{\mathbf{G}}^{-1}\hat{\mathbf{B}} \tag{6.10}$$

$$\tilde{\mathbf{T}} = \hat{\mathbf{C}}(\hat{\mathbf{G}} - \sum_{k=1}^{N_d} \Delta\hat{\mathbf{A}}_{\mathbf{k}})^{-1}\hat{\mathbf{B}} \tag{6.11}$$

Here, $\hat{\mathbf{G}}$ and $\Delta\hat{\mathbf{A}}_k$ are the hyper-dimensional nominal system matrix and damage perturbation matrix given by,

$$\hat{\mathbf{G}} = \begin{bmatrix} \ddots & & & \vdots & & & \iddots \\ \cdots & j(\omega-2\Omega)\mathbf{I}-\mathbf{A}_0 & -\mathbf{A}_{-1} & -\mathbf{A}_{-2} & \cdots & & \\ \cdots & -\mathbf{A}_{+1} & j(\omega-\Omega)\mathbf{I}-\mathbf{A}_0 & -\mathbf{A}_{-1} & -\mathbf{A}_{-2} & \cdots & \\ \cdots & -\mathbf{A}_{+2} & -\mathbf{A}_{+1} & j\omega\mathbf{I}-\mathbf{A}_0 & -\mathbf{A}_{-1} & -\mathbf{A}_{-2} & \cdots \\ & \cdots & -\mathbf{A}_{+2} & -\mathbf{A}_{+1} & j(\omega+\Omega)\mathbf{I}-\mathbf{A}_0 & -\mathbf{A}_{-1} & \cdots \\ & & \cdots & -\mathbf{A}_{+2} & -\mathbf{A}_{+1} & j(\omega+2\Omega)\mathbf{I}-\mathbf{A}_0 & \cdots \\ \iddots & & & \vdots & & & \ddots \end{bmatrix} \tag{6.12-a}$$

$$\Delta\hat{\mathbf{A}}_k = \begin{bmatrix} \ddots & & & \vdots & & & \iddots \\ \cdots & \Delta\mathbf{A}_{0,k} & \Delta\mathbf{A}_{-1,k} & \Delta\mathbf{A}_{-2,k} & \cdots & & \\ \cdots & \Delta\mathbf{A}_{+1,k} & \Delta\mathbf{A}_{0,k} & \Delta\mathbf{A}_{-1,k} & \Delta\mathbf{A}_{-2,k} & \cdots & \\ \cdots & \Delta\mathbf{A}_{+2,k} & \Delta\mathbf{A}_{+1,k} & \Delta\mathbf{A}_{0,k} & \Delta\mathbf{A}_{-1,k} & \Delta\mathbf{A}_{-2,k} & \cdots \\ & \cdots & \Delta\mathbf{A}_{+2,k} & \Delta\mathbf{A}_{+1,k} & \Delta\mathbf{A}_{0,k} & \Delta\mathbf{A}_{-1,k} & \cdots \\ & & \cdots & \Delta\mathbf{A}_{+2,k} & \Delta\mathbf{A}_{+1,k} & \Delta\mathbf{A}_{0,k} & \cdots \\ \iddots & & & \vdots & & & \ddots \end{bmatrix} \tag{6.12-b}$$

Using the Taylor expansion on Eq. (4.32), the damage identification is formulated in terms of the following sensitivity matrix *S*,

$$\tilde{\mathbf{T}} - \mathbf{T} \approx \hat{\mathbf{C}}\hat{\mathbf{G}}^{-1}(\sum_{k=1}^{N_d} \Delta\hat{\mathbf{A}}_{\mathbf{k}})\hat{\mathbf{G}}^{-1}\hat{\mathbf{B}} = \hat{\mathbf{C}}\hat{\mathbf{G}}^{-1}(\sum_{k=1}^{N_d} \delta_k \hat{\mathbf{A}}_{\mathbf{k}})\hat{\mathbf{G}}^{-1}\hat{\mathbf{B}} \tag{6.13}$$

$$\Downarrow$$

$$\Delta \mathbf{T}_{yu} = S\delta_{est} \tag{6.14}$$

With

$$S_k = \hat{\mathbf{C}}\hat{\mathbf{G}}^{-1}\hat{\mathbf{A}}_{\mathbf{k}}\hat{\mathbf{G}}^{-1}\hat{\mathbf{B}} \tag{6.15}$$

$\hat{\mathrm{B}}$ is hyper-dimensional input matrix and $\hat{\mathbf{C}}$ is hyper-dimensional output matrix.

$$\begin{aligned} \hat{\mathbf{B}} &= (2n_h + 1) \otimes \mathbf{B}_u^c \\ \hat{\mathbf{C}} &= (2n_h + 1) \otimes \mathbf{C}_y^c \end{aligned} \tag{6.16}$$

The following iterative process is similar with the process for time-invariant system. Note that the Jacobian and iterative error matrices are hyper-dimensional. The stiffness matrix of time-varying system is a function of time which can be expressed as:

$$\mathbf{K}(t) = \sum_{n=-N_h}^{N_h} \mathbf{K}^n e^{jn\Omega t} \tag{6.17}$$

with

$$\begin{aligned} \mathbf{K}^0 &= K_s - \frac{1}{2}\sum_{k=1}^{n_e}\left(\delta_{y,k}K_{y,k} + \delta_{z,k}K_{z,k} + \delta_{yz,k}K_{yz,k}\right) \\ \mathbf{K}^{-1} &= \frac{1}{4}\left(\sum_{k=1}^{n_e}\cos\theta_k\left(\delta_{y,k}K_{y,k} + \delta_{z,k}K_{z,k} + \delta_{yz,k}K_{yz,k}\right)_k - j\sum_{k=1}^{n_e}\sin\theta_k\left(\delta_{y,k}K_{y,k} + \delta_{z,k}K_{z,k} + \delta_{yz,k}K_{yz,k}\right)\right) \\ \mathbf{K}^{1} &= \frac{1}{4}\left(\sum_{k=1}^{n_e}\cos\theta_k\left(\delta_{y,k}K_{y,k} + \delta_{z,k}K_{z,k} + \delta_{yz,k}K_{yz,k}\right) + j\sum_{k=1}^{n_e}\sin\theta_k\left(\delta_{y,k}K_{y,k} + \delta_{z,k}K_{z,k} + \delta_{yz,k}K_{yz,k}\right)\right) \end{aligned} \tag{6.18}$$

6.4 Damage Identification: Shaft Sensors

In this section, the linear damage case in Table 3.6 is studied using FRF based damage identification method for time-varying shaft—disk system (note the damage is breathing). Using the conclusion obtained from Chapter 4, the system is given the excitation near resonances and sidebands (Table 6.1) at 3/4*L* and three pairs of sensor on the locations listed in Table 6.2.

Table 6.1 Excitation frequency set: rotor breathing crack

	trial 1	trial 2	trial 3	trial 4
ω (Hz)	160	120	220	890

Table 6.2 Sensor location set: rotor breathing crack

	Sensor 1	Sensor 2	Sensor 3
x_s (m)	1/8L	3/8L	5/8L

Figs 6.10 and 6.11 show the damage identification results for the damaged shaft system with single transverse open crack. Specifically, Fig. 6.10 shows the actual and converged estimates of the crack energy ratios and crack angles, wherein the blue and red bar denotes the actual and estimated values respectively. Fig. 6.11 shows the shaft damage parameter iteration history, wherein the blue dash line and red star line denotes the actual and estimated damage parameters respectively. Note that twice of crack angle can be estimated by Eq. (6.19),

$$2\theta = \tan^{-1}\frac{2\delta_{yz}}{(\delta_y - \delta_z)} \tag{6.19}$$

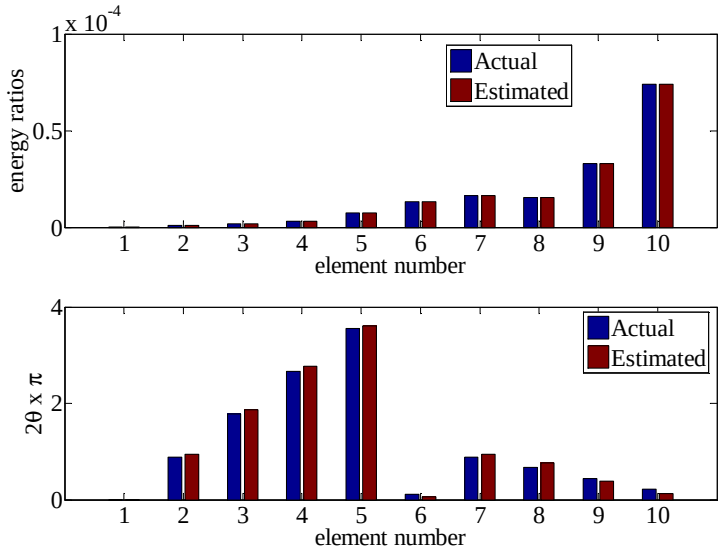

Fig. 6.10 Breathing crack energy ratio and angle estimates: linear case

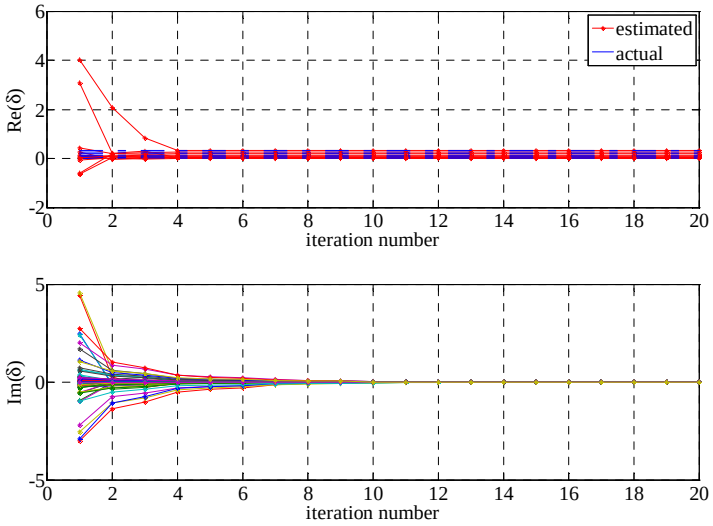

Fig. 6.11 Estimated breathing damage parameters vs. iteration number: linear case

It is known that three damage parameters are needed to estimate an open crack in the rotor system. However, nine damage parameters are required to represent a breathing crack. Besides the original three parameters $\delta_{y,k}$, $\delta_{z,k}$ and $\delta_{yz,k}$ representing the stiffness reduction in two lateral directions and their cross-coupling direction, extra estimated damage parameters $\delta_{y,k}\sin\theta_k$, $\delta_{z,k}\sin\theta_k$, $\delta_{yz,k}\sin\theta_k$, $\delta_{y,k}\cos\theta_k$, $\delta_{z,k}\cos\theta_k$ and $\delta_{yz,k}\cos\theta_k$ have to be estimated during the damage identification process of a breathing crack on k^{th} cell. As shown in Eq. (6.18). These parameters are associated with θ which enables us to estimate the crack angle rather than twice of crack angle. Table 6.3 gives the estimates of these 6 extra parameters. In this table, δ_1, δ_2, δ_3, δ_4, δ_5 and δ_6 denote the damage parameters $\delta_{y,k}\sin\theta_k$, $\delta_{z,k}\sin\theta_k$, $\delta_{yz,k}\sin\theta_k$, $\delta_{y,k}\cos\theta_k$, $\delta_{z,k}\cos\theta_k$ and $\delta_{yz,k}\cos\theta_k$, respectively.

Table 6.3 Estimated parameters related with crack angle

Cell number	Re(δ_1)	Re(δ_2)	Re(δ_3)	Re(δ_4)	Re(δ_5)	Re(δ_6)
1	-0.0000	0.0000	-0.0000	-0.0011	0.0000	-0.0000
2	0.0002	0.0057	0.0010	0.0000	0.0010	0.0002
3	0.0050	0.0007	-0.0018	-0.0136	-0.0019	0.0049
4	-0.0075	-0.0218	-0.0124	-0.0043	-0.0126	-0.0071
5	-0.0220	-0.0157	0.0180	0.0262	0.0187	-0.0215
6	0.0152	0.0007	0.0026	0.0862	0.0042	0.0149
7	0.0065	0.1256	0.0217	0.0012	0.0221	0.0038
8	0.0422	0.1190	0.0665	0.0244	0.0687	0.0384
9	0.0930	0.0667	0.0744	0.1108	0.0795	0.0887
10	0.0945	0.0154	0.0332	0.2598	0.0422	0.0913

Table 6.4 Sin(θ_k) calculated from estimated parameters

Cell number	sinθ_k		
	Re(δ_1)/Re(δ_y)	Re(δ_2)/Re(δ_z)	Re(δ_3)/Re(δ_{yz})
1	-0.0009	0.5388	-0.3891
2	0.9851	0.9848	0.9848
3	0.3420	0.3420	0.3420
4	-0.8660	-0.8660	-0.8660
5	-0.6428	-0.6428	-0.6428
6	0.1736	0.1736	0.1736
7	0.9848	0.9848	0.9848
8	0.8660	0.8660	0.8660
9	0.6428	0.6428	0.6428
10	0.3420	0.3420	0.3420

Table 6.5 Cos(θ_k) calculated from estimated parameters

Cell number	Cosθ_k		
	Re(δ_4)/Re(δ_y)	Re(δ_5)/Re(δ_z)	Re(δ_6)/Re(δ_{yz})
1	0.9976	-0.5291	-0.3947
2	0.1737	0.1736	0.1737
3	-0.9397	-0.9397	-0.9397
4	-0.5000	-0.5000	-0.5000
5	0.7660	0.7660	0.7660
6	0.9848	0.9848	0.9848
7	0.1736	0.1736	0.1736
8	0.5000	0.5000	0.5000
9	0.7660	0.7660	0.7660
10	0.9397	0.9397	0.9397

By calculating Re(δ_4)/ Re(δ_1), Re(δ_5)/ Re(δ_2), Re(δ_6)/ Re(δ_3), we have the sin(θ_k) and cos(θ_k) estimated from δ_y, δ_z and δ_{yz} listed in Table 6.4 and 6.5. For very small cracks

with zero crack angle, Re(δ_3)/Re(δ_{yz}) and Re(δ_6)/Re(δ_{yz}) may have very large error because Re(δ_{yz}) is very small and has the same level of magnitude as numerical error. Therefore, it is better to refer the estimation from the dominant crack parameters.

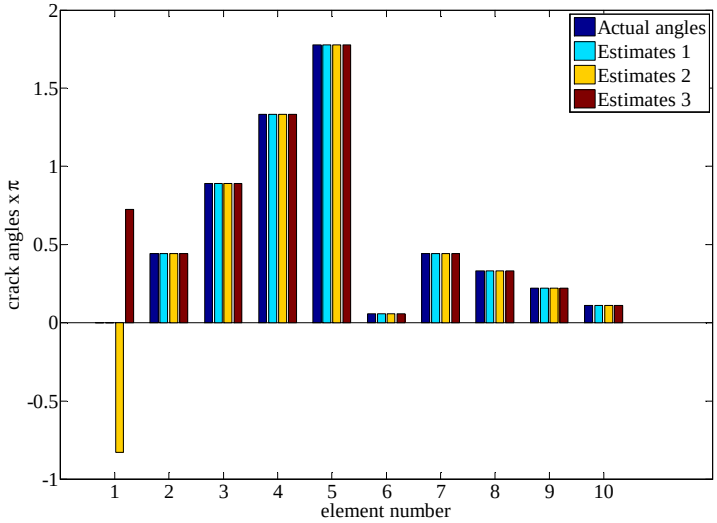

Fig. 6.12 Crack angle multiple estimates: linear case

Fig. 6.12 shows the comparison of actual crack angles and three trials of estimates. The blue, cyan, yellow and red bar denotes the actual, estimates from δ_y, estimates from δ_z and estimates from δ_{yz}, respectively. Table 6.6 gives the details of estimates.

Table 6.6 θ_k calculated from estimated parameters

Cell Number k	θ		
	$\delta_{y,k}$	$\delta_{z,k}$	$\delta_{yz,k}$
1	0.1887	-149.5690	130.3040
2	80.0001	80.0000	79.9998
3	160.0000	160.0001	160.0000
4	-120.0000	-120.0000	-120.0000
5	-40.0000	-40.0000	-40.0000
6	10.0000	10.0000	10.0000
7	80.0002	80.0000	79.9999
8	59.9999	59.9999	60.0001
9	40.0001	40.0002	39.9999
10	19.9999	19.9996	20.0001

6.5 Damage Identification: Laser Scanner

In this section, we utilize a laser scanner as a moving sensor which keeps sweeping the entire surface of the rotor instead of using sensors attached to shaft. The system is shown in Fig. 6.13.

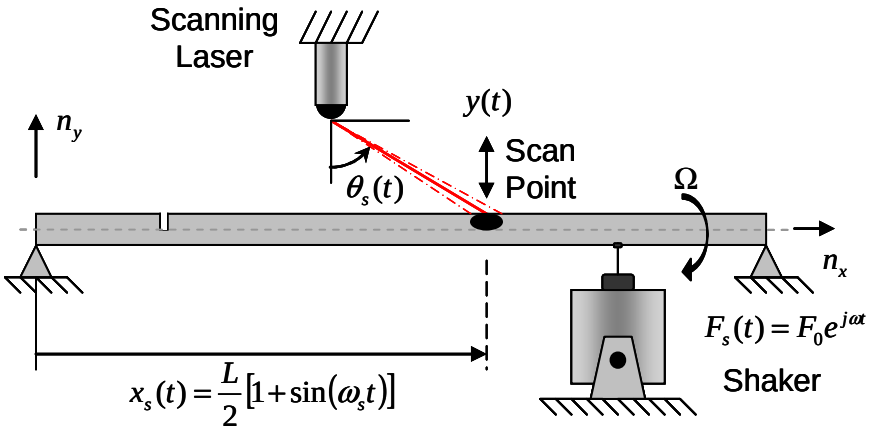

Fig. 6.13 laser scanning damaged system

6.5.1 Damage Identification Algorithm

Due to the scanning laser, the output matrix $\mathbf{C}_y$ is not time-invariant any more. The equations-of-motion becomes,

$$\begin{aligned}\dot{\mathbf{x}} &= \left(\mathbf{A}(t) + \sum_{k=1}^{N_d} \Delta\mathbf{A}_k(t)\right)\mathbf{x} + \mathrm{B}_u\mathbf{u}(t) \\ \mathbf{y}(t) &= \mathbf{C}_y(t)\mathbf{x}\end{aligned} \tag{6.20}$$

Assuming the output matrix $\mathbf{C}_y$ can be expressed as the summation of harmonics as the following equation,

$$\mathbf{C}_y(t) = \sum_{l=-N_f}^{N_f} \mathbf{c}_m e^{jl\omega_s t} \tag{6.21}$$

The external excitation and damage matrices, **u(t)**, and $\Delta\mathbf{A}_k(t)$, are expanded in the complex exponential series as:

$$\begin{aligned}\mathbf{u}(t) &= \mathbf{u}e^{j\omega t} \\ \Delta\mathbf{A}_k(t) &= \sum_{n=-N_h}^{N_h} \Delta\mathbf{A}_{n,k} e^{jn\Omega t}\end{aligned} \tag{6.22}$$

where N_h is the number of system harmonics. In the case of the shaft-disk system, $N_h = 2$. The homogeneous solution of the linear periodically time varying system can be expressed as

$$\mathbf{x}(t) = \sum_{n=-N_x}^{N_x} \mathbf{x}_n e^{jn\Omega t} e^{j\omega t} \tag{6.23}$$

Substituting Eq. (6.29) and (6.31) into Eq. (6.24), the output response y(t) becomes,

$$\mathbf{y}(t) = \sum_{n=-N_x}^{N_x} \sum_{l=-N_f}^{N_f} \mathbf{y}_{n,l} e^{j(\omega+n\Omega+l\omega_s)t} \tag{6.24}$$

The coefficient $\mathbf{y}_{n,l}$ is,

$$\mathbf{y}_{n,l} = \mathbf{c}_l \mathbf{x}_n \tag{6.25}$$

with

$$\mathbf{C}_y = \begin{bmatrix} \mathbf{c}_{-N_f} \\ \mathbf{c}_{-N_f+1} \\ \vdots \\ \mathbf{c}_{N_f} \end{bmatrix} \tag{6.26}$$

After performing harmonic balance, the following hyper-dimensional problems whose solutions characterize the nominal and damaged system transfer function matrices are given as:

$$\mathbf{T} = \hat{\mathbf{C}}\hat{\mathbf{G}}^{-1}\hat{\mathbf{B}} \tag{6.27}$$

$$\tilde{\mathbf{T}} = \hat{\mathbf{C}}(\hat{\mathbf{G}} - \sum_{k=1}^{N_d} \Delta\hat{\mathbf{A}}_{\mathbf{k}})^{-1}\hat{\mathbf{B}} \tag{6.28}$$

Here, $\hat{\mathbf{G}}$ and $\Delta\hat{\mathbf{A}}_k$ are the hyper-dimensional nominal system matrix and damage perturbation matrix given by,

$$\hat{\mathbf{G}} = \begin{bmatrix} \ddots & & & \vdots & & & \iddots \\ \cdots & j(\omega-2\Omega)\mathbf{I}-\mathbf{A}_0 & -\mathbf{A}_{-1} & -\mathbf{A}_{-2} & \cdots & & \\ \cdots & -\mathbf{A}_{+1} & j(\omega-\Omega)\mathbf{I}-\mathbf{A}_0 & -\mathbf{A}_{-1} & -\mathbf{A}_{-2} & \cdots & \\ \cdots & -\mathbf{A}_{+2} & -\mathbf{A}_{+1} & j\omega\mathbf{I}-\mathbf{A}_0 & -\mathbf{A}_{-1} & -\mathbf{A}_{-2} & \cdots \\ & \cdots & -\mathbf{A}_{+2} & -\mathbf{A}_{+1} & j(\omega+\Omega)\mathbf{I}-\mathbf{A}_0 & -\mathbf{A}_{-1} & \cdots \\ & & \cdots & -\mathbf{A}_{+2} & -\mathbf{A}_{+1} & j(\omega+2\Omega)\mathbf{I}-\mathbf{A}_0 & \cdots \\ \iddots & & & \vdots & & & \ddots \end{bmatrix} \tag{6.29-a}$$

$$\Delta\hat{\mathbf{A}}_k = \begin{bmatrix} \ddots & & & \vdots & & & \iddots \\ \cdots & \Delta\mathbf{A}_{0,k} & \Delta\mathbf{A}_{-1,k} & \Delta\mathbf{A}_{-2,k} & \cdots & & \\ \cdots & \Delta\mathbf{A}_{+1,k} & \Delta\mathbf{A}_{0,k} & \Delta\mathbf{A}_{-1,k} & \Delta\mathbf{A}_{-2,k} & \cdots & \\ \cdots & \Delta\mathbf{A}_{+2,k} & \Delta\mathbf{A}_{+1,k} & \Delta\mathbf{A}_{0,k} & \Delta\mathbf{A}_{-1,k} & \Delta\mathbf{A}_{-2,k} & \cdots \\ & \cdots & \Delta\mathbf{A}_{+2,k} & \Delta\mathbf{A}_{+1,k} & \Delta\mathbf{A}_{0,k} & \Delta\mathbf{A}_{-1,k} & \cdots \\ & & \cdots & \Delta\mathbf{A}_{+2,k} & \Delta\mathbf{A}_{+1,k} & \Delta\mathbf{A}_{0,k} & \cdots \\ \iddots & & & \vdots & & & \ddots \end{bmatrix} \tag{6.29-b}$$

$\hat{\mathbf{B}}$ is hyper-dimensional input matrix and $\hat{\mathbf{C}}$ is hyper-dimensional output matrix.

$$\begin{aligned} \hat{\mathbf{B}} &= (2n_h+1) \otimes \mathbf{B}_u \\ \hat{\mathbf{C}} &= (2n_h+1) \otimes \mathbf{C}_y \end{aligned} \tag{6.30}$$

The following iterative process is similar with the process for time-invariant system.

Next, the output matrix is derived in detail. According to the assumed mode method, we have

$$\mathbf{y}(t)=\sum_{m=1}^{n_m}\varphi_i(x_s(t))q_k(t)=\underbrace{\left[\varphi_1(x_s(t)) \quad \varphi_2(x_s(t)) \quad \cdots \quad \varphi_{n_m}(x_s(t))\middle| 0 \quad 0 \quad \cdots \quad 0\right]}_{\mathbf{C}_y(t)}\begin{bmatrix} q_1 \\ q_2 \\ \vdots \\ q_{n_m} \\ \dot{q}_1 \\ \dot{q}_2 \\ \vdots \\ \dot{q}_{n_m} \end{bmatrix} \tag{6.31}$$

with the m^{th} assumed mode,

$$\varphi_m(x_s(t))=\sin\frac{m\pi x_s(t)}{L} \tag{6.32}$$

Here, $x_s(t)$ is the scanning position which is assumed to be,

$$x_s(t)=\frac{L}{2}[1+\sin(\omega_s t)] \tag{6.33}$$

Taking Eq. (6.37) into Eq. (6.36), the assumed modes are expressed as,

$$\varphi_m(x_s(t))=\sin\frac{m\pi x_s(t)}{L}=\sin\left[\frac{m\pi}{2}+\frac{m\pi}{2}\sin(\omega_s t)\right] \tag{6.34}$$

Assuming the m^{th} mode can be expressed by Fourier expansion,

$$\varphi_m(x_s(t))=c_0^{(m)}+\sum_{n=1}^{N_f}\left[c_{cn}^{(m)}\cos n\omega_s t+c_{sn}^{(m)}\sin n\omega_s t\right] \tag{6.35}$$

The Fourier coefficients can be solved by the following integral,

$$c_0^{(m)}=\frac{1}{T_s}\int_0^{T_s}\varphi_m(x_s(t))dt=\frac{1}{T_s}\int_0^{T_s}\sin\left[\frac{m\pi}{2}+\frac{m\pi}{2}\sin(\omega_s t)\right]dt \tag{6.36}$$

$$c_{sn}^{(m)}=\frac{2}{T_s}\int_0^{T_s}\varphi_m(x_s(t))\sin n\omega_s t dt=\frac{2}{T_s}\int_0^{T_s}\sin\left[\frac{m\pi}{2}+\frac{m\pi}{2}\sin(\omega_s t)\right]\sin(n\omega_s t)dt \tag{6.37}$$

$$c_{cn}^{(m)} = \frac{2}{T_s}\int_0^{T_s} \varphi_m(x_s(t))\cos n\omega_s t dt = \frac{2}{T_s}\int_0^{T_s} \sin\left[\frac{m\pi}{2} + \frac{m\pi}{2}\sin(\omega_s t)\right]\cos(n\omega_s t)dt \qquad (6.38)$$

Let $\alpha = \omega_s t$, the coefficient are simplified as,

$$\begin{aligned} c_0^{(m)} &= \frac{1}{2\pi}\int_0^{2\pi} \phi_m(x_s(\alpha))d\alpha = \frac{1}{2\pi}\int_0^{2\pi} \sin\left[\frac{m\pi}{2} + \frac{m\pi}{2}\sin\alpha\right]d\alpha \\ c_{cn}^{(m)} &= \frac{1}{\pi}\int_0^{2\pi} \phi_m(x_s(\alpha))\cos(n\alpha)d\alpha = \frac{1}{\pi}\int_0^{2\pi} \sin\left[\frac{m\pi}{2} + \frac{m\pi}{2}\sin\alpha\right]\cos(n\alpha)d\alpha \\ c_{sn}^{(m)} &= \frac{1}{\pi}\int_0^{2\pi} \phi_m(x_s(\alpha))\sin(n\alpha)d\alpha = \frac{1}{\pi}\int_0^{2\pi} \sin\left[\frac{m\pi}{2} + \frac{m\pi}{2}\sin\alpha\right]\sin(n\alpha)d\alpha \end{aligned} \qquad (6.39)$$

Here gives the Fourier coefficients,

$$\begin{aligned} c_0^{(m)} &= (-1)^{\frac{m-1}{2}} J_0(\frac{m\pi}{2}), \mathrm{m} = 1,3,5,\cdots \\ c_0^{(m)} &= 0, \mathrm{m} = 2,4,6,\cdots \end{aligned} \qquad (6.40)$$

$$\begin{aligned} c_{c1}^{(m)} &= 0 \\ c_{s1}^{(m)} &= 0, \mathrm{m} = 1,3,5,\cdots \\ c_{s1}^{(m)} &= (-1)^{\frac{m}{2}} 2J_1(\frac{m\pi}{2}), \mathrm{m} = 2,4,6,\cdots \end{aligned} \qquad (6.41)$$

$$\begin{aligned} c_{s2}^{(m)} &= 0 \\ c_{c2}^{(m)} &= (-1)^{\frac{m-1}{2}} 2J_2(\frac{m\pi}{2}), \mathrm{m} = 1,3,5,\cdots \\ c_{c2}^{(m)} &= 0, \mathrm{m} = 2,4,6,\cdots \end{aligned} \qquad (6.42)$$

$$\begin{aligned} c_{c3}^{(m)} &= 0 \\ c_{s3}^{(m)} &= 0, \mathrm{m} = 1,3,5,\cdots \\ c_{s3}^{(m)} &= (-1)^{\frac{m}{2}} 2J_3(\frac{m\pi}{2}), \mathrm{m} = 2,4,6,\cdots \end{aligned} \qquad (6.43)$$

$$\begin{aligned} c_{s4}^{(m)} &= 0 \\ c_{c4}^{(m)} &= (-1)^{\frac{m-1}{2}} \frac{2}{(m\pi)^3}\left\{\left[-96m\pi + (m\pi)^3\right]J_0(\frac{m\pi}{2}) - \left[-384 + 16(m\pi)^2\right]J_1(\frac{m\pi}{2})\right\}, \mathrm{m} = 1,3,5,\cdots \\ c_{c4}^{(m)} &= 0, \mathrm{m} = 2,4,6,\cdots \end{aligned} \qquad (6.44)$$

$$c_{c5}^{(m)} = 0$$

$$c_{s5}^{(m)} = 0 \text{ , m} = 1,3,5,\cdots$$

$$c_{s5}^{(m)} = (-1)^{\frac{m}{2}} \frac{2}{\left(\frac{m\pi}{2}\right)^3} \left\{ \left[-48\frac{m\pi}{2} + \left(\frac{m\pi}{2}\right)^3 \right] J_1\left(\frac{m\pi}{2}\right) - \left[-192 + 12\left(\frac{m\pi}{2}\right)^2 \right] J_2\left(\frac{m\pi}{2}\right) \right\}, \text{m} = 2,4,6,\cdots \tag{6.45}$$

6.5.2 Damage Identification: Rotating Shaft-Disk System with Laser Scanner

In this section, the linear damage case in Table 3.6 is studied using FRF based damage identification method for time-varying shaft—disk system. Using laser scanner as moving sensor has obvious advantage that it can collect all of the information about the whole shaft by one sensor. Thus, the number of sensors is dramatically reduced. The excitation set in Table 6.1 is used here again.

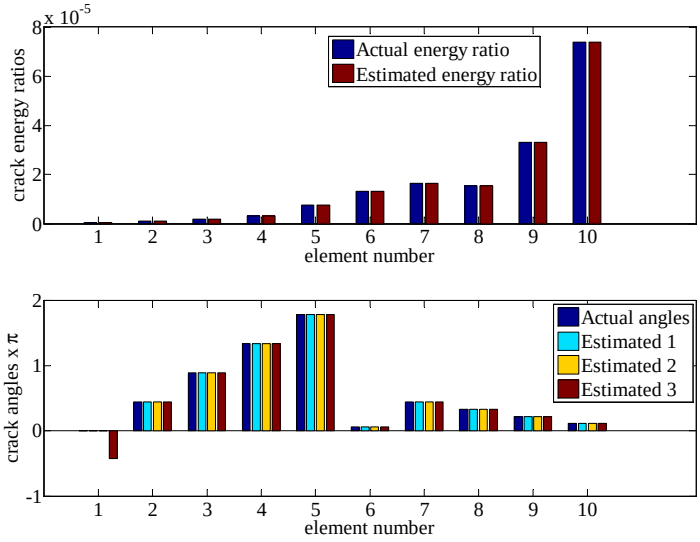

Fig. 6.14 Converged shaft crack damage energy ratio estimates: laser scanner

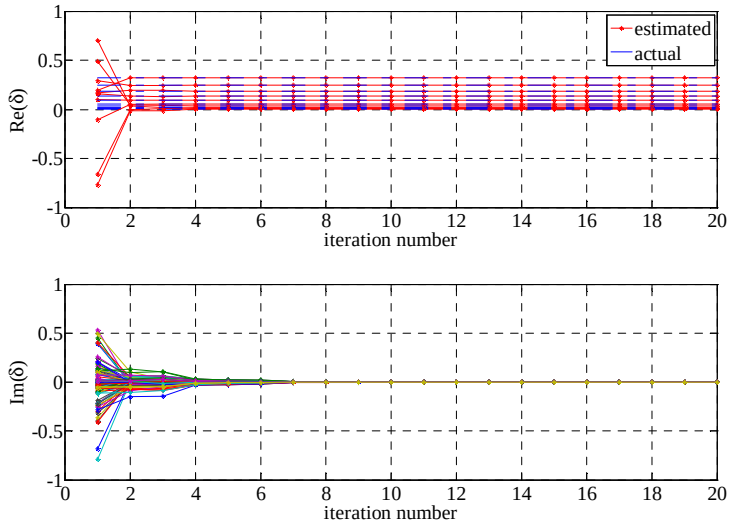

Fig. 6.15 Estimated shaft damage parameters vs. iteration number: laser scanner

The estimation is obtained using the first four harmonics of vibration response. Figs 6.14 and 6.15 show the damage identification results for the damaged shaft system with single transverse open crack. From Fig. 6.14, it can be observed that the crack angle estimates I and II are more accurate for 1st cell because they are corresponding to the dominant crack parameters δ_y and δ_z.

6.6 Time-domain Simulation

Previously, the damage identification methods were based on the frequency response function and developed in frequency domain. In this section, we simulate the vibration of shaft—disk system in Simulink and obtain the displacements of shaft using assumed mode method. Then, the Harmonic Fourier Coefficients are computed by convolution block and transfer function block and utilized by damage detection block to detect the damage.

6.6.1 Time-domain Damage Identification Algorithm

Different from the algorithm in frequency domain, the vibration signals are real numbers which requires the algorithm to be modified from exponential form to trigonometric form. The equations-of-motion are recast into the following state-space form with state vector $\mathbf{x} = [q^T \quad \dot{q}^T]^T$

$$\begin{aligned} \dot{\mathbf{x}} &= \left(\mathbf{A} - \sum_{k=1}^{N_d} \Delta\mathbf{A}_k \, f_k(t) \right) \mathbf{x} + \mathrm{B}_u \mathbf{u}(t) \\ \mathbf{y} &= \mathbf{C}_y \mathbf{x} \end{aligned} \tag{6.46}$$

Here, f_k is breathing function for k^{th} element. The cosine crack model is adopted in this chapter and f_c can be expressed as,

$$f_k(t) = \frac{1}{2}\left[1 - \cos(\Omega t + \theta_k)\right] \tag{6.47}$$

with θ_k is the angle of crack on k^{th} element. The input function u(t) and the homogeneous solution of the linear periodically time-varying system can be expressed as

$$\begin{aligned} \mathbf{u}(t) &= u \sin(\omega t) \\ \mathbf{x}_h(t) &= \sum_{n=-N_x}^{N_x} \left[X_n^s \sin(\omega t + n\Omega t) + X_n^c \cos(\omega t + n\Omega t) \right] \end{aligned} \tag{6.48}$$

Where N_x is the number of response harmonics. After performing harmonic balance, the following hyper-dimensional problem whose solution characterizes damaged system transfer function matrices are given as,

$$\hat{\hat{\mathbf{T}}} = \hat{\mathbf{C}}_y [\hat{\mathbf{A}} - \sum_{k=1}^{N_d} \Delta\hat{\mathbf{A}}_k]^{-1} \hat{\mathrm{B}}_u \tag{6.49}$$

$\hat{\mathbf{G}}$ and $\Delta\hat{\mathbf{A}}_k$ are the hyper-dimensional nominal system matrix and damage perturbation matrix given by,

$$\hat{\mathbf{A}}=\begin{bmatrix}
\ddots & \vdots & \vdots & \vdots & \vdots & & & \\
\cdots & \mathbf{A} & (\omega-\Omega)\mathbf{I} & \frac{\mathbf{A}_1^c}{2} & -\frac{\mathbf{A}_1^s}{2} & \cdots & & \\
\cdots & -(\omega-\Omega)\mathbf{I} & \mathbf{A} & \frac{\mathbf{A}_1^s}{2} & \frac{\mathbf{A}_1^c}{2} & \vdots & \vdots & \\
\cdots & \frac{\mathbf{A}_1^c}{2} & \frac{\mathbf{A}_1^s}{2} & \mathbf{A} & \omega\mathbf{I} & \frac{\mathbf{A}_1^c}{2} & -\frac{\mathbf{A}_1^s}{2} & \cdots \\
\cdots & -\frac{\mathbf{A}_1^s}{2} & \frac{\mathbf{A}_1^c}{2} & -\omega\mathbf{I} & \mathbf{A} & \frac{\mathbf{A}_1^s}{2} & \frac{\mathbf{A}_1^c}{2} & \cdots \\
 & \vdots & \vdots & \frac{\mathbf{A}_1^c}{2} & \frac{\mathbf{A}_1^s}{2} & \mathbf{A} & (\omega+\Omega)\mathbf{I} & \cdots \\
 & & \cdots & -\frac{\mathbf{A}_1^s}{2} & \frac{\mathbf{A}_1^c}{2} & -(\omega+\Omega)\mathbf{I} & \mathbf{A} & \cdots \\
 & & & \vdots & \vdots & \vdots & \vdots & \ddots
\end{bmatrix} \tag{6.50}$$

$$\Delta\hat{\mathbf{A}}_k=\begin{bmatrix}
\ddots & \vdots & \vdots & \vdots & \vdots & & & \\
\cdots & \Delta\mathbf{A}_{0,k} & 0 & \frac{\Delta\mathbf{A}_{1,k}^c}{2} & -\frac{\Delta\mathbf{A}_{1,k}^s}{2} & \cdots & & \\
\cdots & 0 & \Delta\mathbf{A}_{0,k} & \frac{\Delta\mathbf{A}_{1,k}^s}{2} & \frac{\Delta\mathbf{A}_{1,k}^c}{2} & \vdots & \vdots & \\
\cdots & \frac{\Delta\mathbf{A}_{1,k}^c}{2} & \frac{\Delta\mathbf{A}_{1,k}^s}{2} & \Delta\mathbf{A}_{0,k} & 0 & \frac{\Delta\mathbf{A}_{1,k}^c}{2} & -\frac{\Delta\mathbf{A}_{1,k}^s}{2} & \cdots \\
\cdots & -\frac{\Delta\mathbf{A}_{1,k}^s}{2} & \frac{\Delta\mathbf{A}_{1,k}^c}{2} & 0 & \Delta\mathbf{A}_{0,k} & \frac{\Delta\mathbf{A}_{1,k}^s}{2} & \frac{\Delta\mathbf{A}_{1,k}^c}{2} & \cdots \\
 & \vdots & \vdots & \frac{\Delta\mathbf{A}_{1,k}^c}{2} & \frac{\Delta\mathbf{A}_{1,k}^s}{2} & \Delta\mathbf{A}_{0,k} & 0 & \cdots \\
 & & \cdots & -\frac{\Delta\mathbf{A}_{1,k}^s}{2} & \frac{\Delta\mathbf{A}_{1,k}^c}{2} & 0 & \Delta\mathbf{A}_{0,k} & \cdots \\
 & & & \vdots & \vdots & \vdots & \vdots & \ddots
\end{bmatrix} \tag{6.51}$$

with

$$\hat{\mathbf{B}}_u=\begin{bmatrix}0 & 0 & \overbrace{\mathbf{B}_u \quad 0 \quad \cdots \quad 0}^{2n_h}\end{bmatrix}^T$$
$$\hat{\mathbf{C}}_y=(2n_x+2)\otimes\mathbf{C}_y \tag{6.52}$$

The following steps are similar with the algorithm in section 4.5.1.

6.6.2 Simulation Diagram

Fig. 6.16 shows the simulation diagram of damage detection, which contains the excitation frequency switching block, Cosine crack model block, damaged and nominal

rotor system block, displacement block, convolution block, HFC computing block and damage detection block.

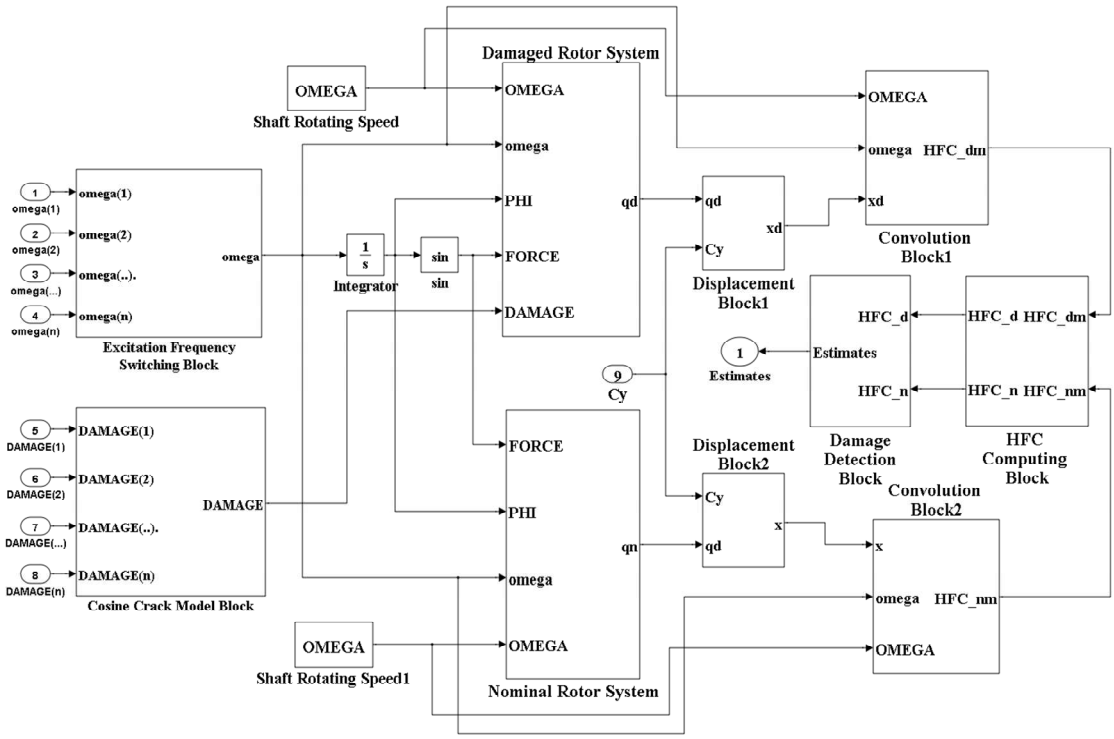

Fig. 6.16 Simulation diagram: rotor system

The excitation frequency switching block is used to get multiple sets of transfer function and enrich the dataset for damage detection. This block not only changes the excitation frequency but also varies the amplitudes of inputs for every excitation frequency. Cosine crack model block gives the system the information of damage approximated by Cosine crack model. The vibration response of damaged and nominal system in modal coordinate is computed through S-functions in damaged and nominal shaft system block. Then, the displacements observed by laser scanner are obtained by assumed mode method in the displacement block. Passing through the convolution block, Harmonic Fourier Coefficient (HFC) are obtained. Note that these HFCs are not the

transfer function data we need, because the system is driven by multiple inputs simultaneously. Therefore, these HFCs are needed to go through the HFC computing block and transform to HFCs for single input. Finally, the damage detection block estimates the damage parameters using HFCs as input.

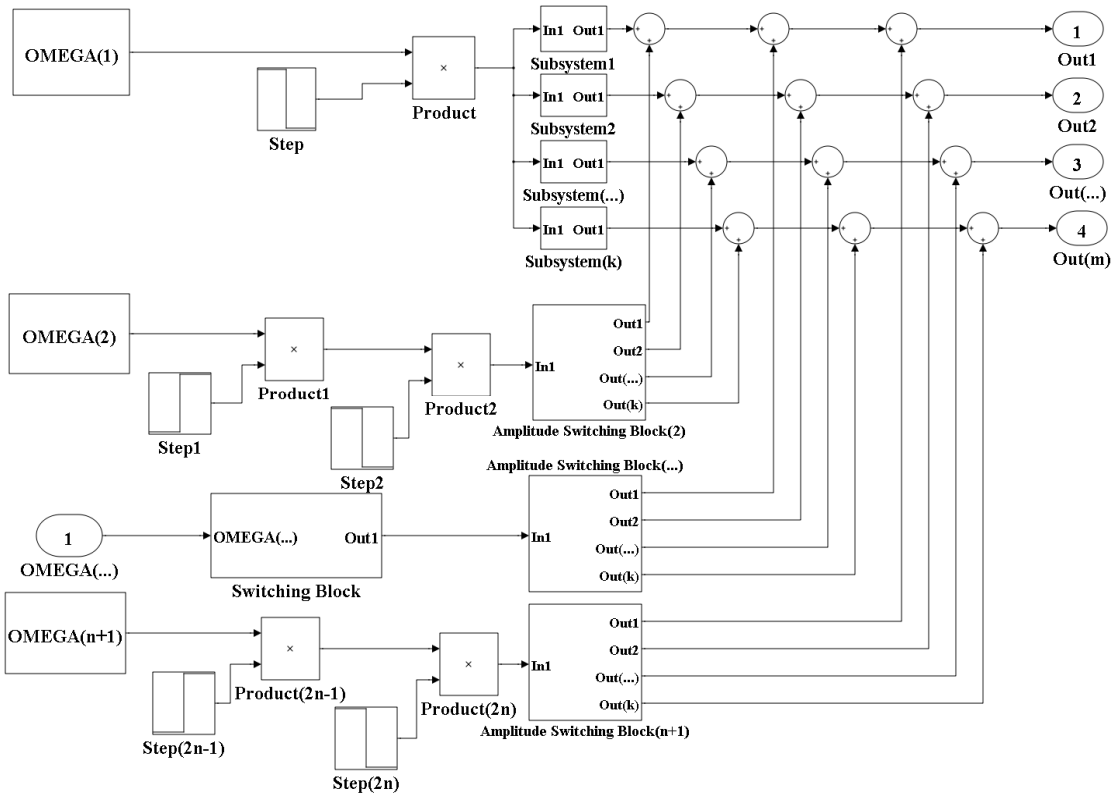

Fig. 6.17 Excitation frequency switching block

Fig. 6.17 shows the excitation frequency switching block which has the function of changing excitation frequency and force amplitude. The reason of changing excitation frequency is that more sets of transfer function could be obtained to enrich the dataset for damage detection. The amplitude switching block is used to change the amplitudes of multiport inputs so that multiple trails of vibration response could be obtained for different combination sets of inputs. Later, they will be transformed to the data for each single input by HFC computing block.

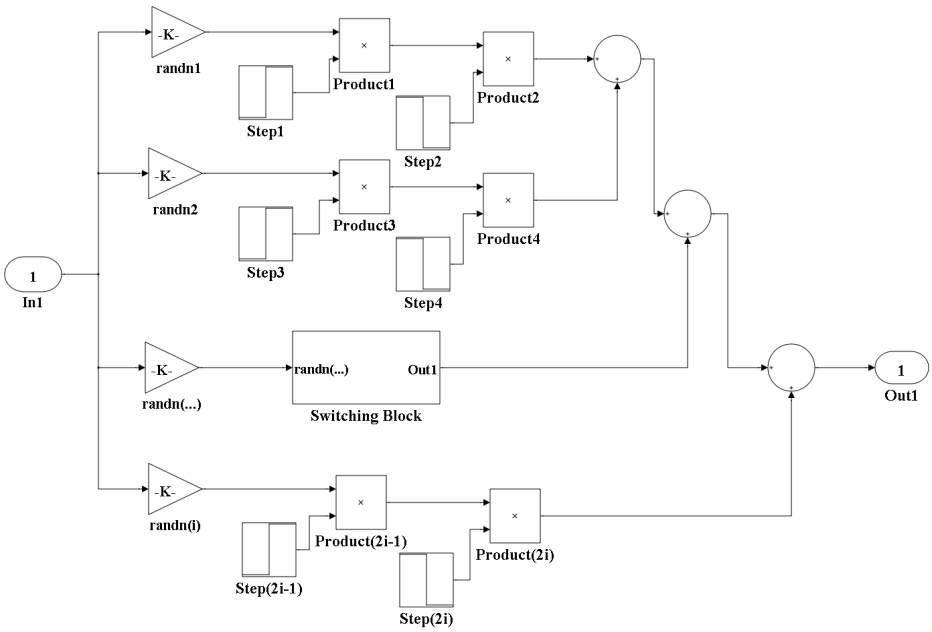

Fig. 6.18 Amplitude switching block

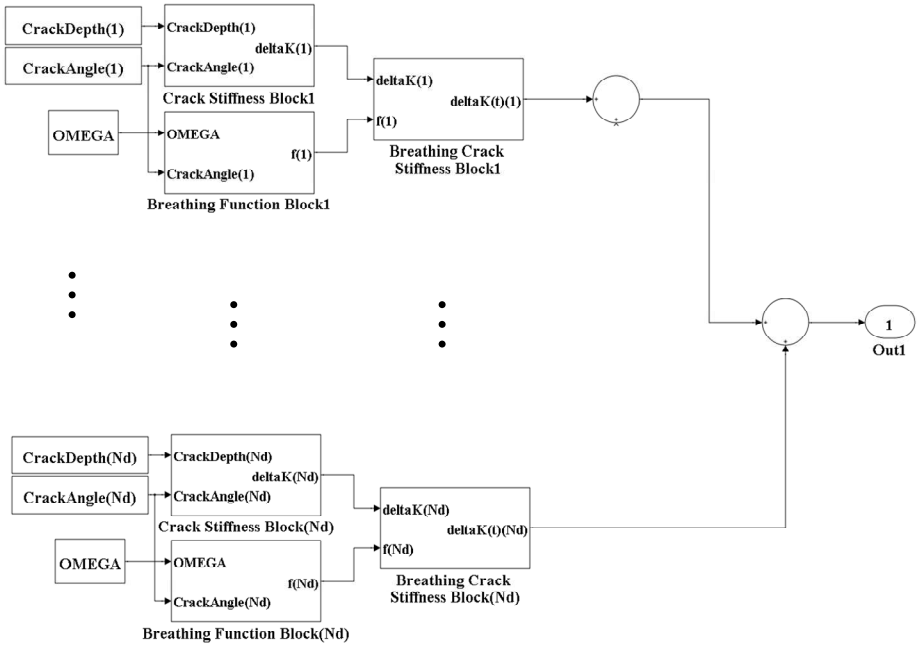

Fig. 6.19 Cosine Crack Model Block

Cosine crack model block is shown in Fig. 6.19. This block is using Cosine crack model to simulate the breathing behavior of damage. The time-varying damage stiffness matrix is,

$$\Delta \mathbf{K}_k(t) = \frac{1}{2}\left[1 - \cos\left(\Omega t + \theta_k\right)\right]\Delta \mathbf{K}_k \tag{6.53}$$

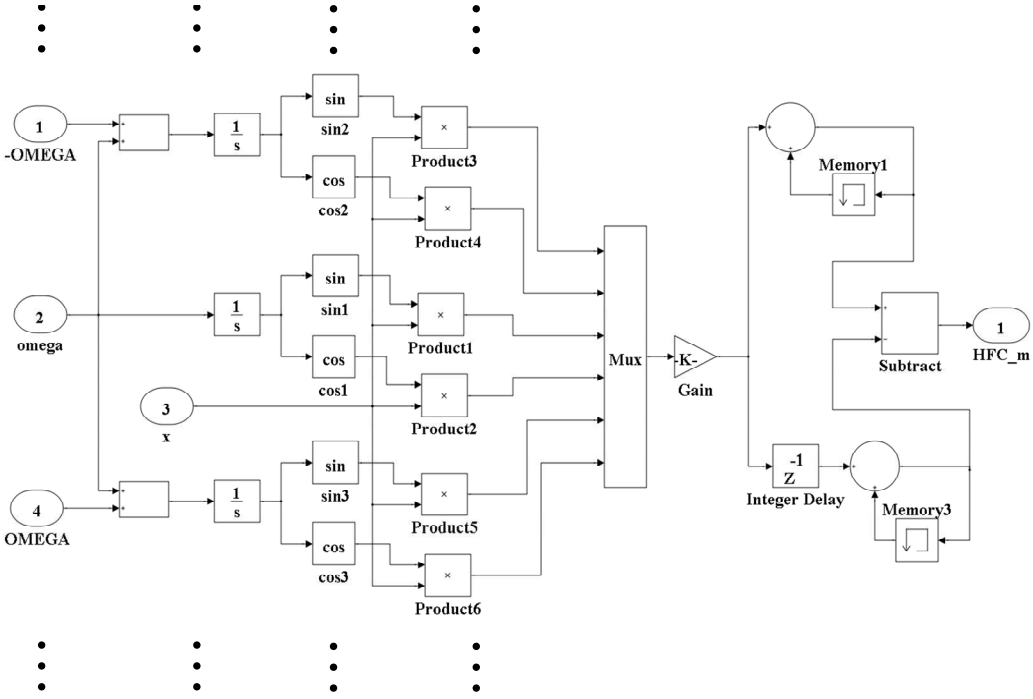

Fig. 6.20 Convolution block

Fig. 6.20 shows the convolution block which computes the HFCs for multiple inputs. To get the transfer function for single input, HFC computing block is employed to convert the HFCs for multiport inputs to HFCs for single input. Define y_1, y_2 … y_i are the vibration response of inputs u_1, u_2 … u_i,

$$\begin{bmatrix} y_1 & y_2 & \cdots & y_i \end{bmatrix} = \mathbf{T}\begin{bmatrix} u_1 & u_2 & \cdots & u_i \end{bmatrix} \tag{6.54}$$

Assuming the transfer functions for k input ports are needed and we have i trails of inputs, the transfer function matrix T could be solved when $i \geq k$,

$$\mathbf{T} = \mathbf{Y}\mathbf{U}^{\mathbf{T}}\left(\mathbf{U}\mathbf{U}^{\mathbf{T}}\right)^{-1} \tag{6.55}$$

Here, if **U** is unit matrix (not necessarily square)

$$\mathbf{U}=\begin{bmatrix}\overbrace{\begin{matrix}1 & 0 & \cdots & 0\\ 0 & 1 & \cdots & 0\\ \vdots & \vdots & \ddots & \vdots\\ 0 & 0 & \cdots & 1\end{matrix}}^{i}\\ \\ \end{bmatrix}\Bigg\}k \tag{6.56}$$

The measured vibration response **Y** matrix is transfer function matrix **T**. When we need the transfer functions of many input ports, it is more convenient to assign random number to the amplitude of force,

$$\mathbf{U}=\begin{bmatrix} u_{11} & u_{12} & \cdots & u_{1i}\\ u_{21} & u_{22} & \cdots & u_{2i}\\ \vdots & \vdots & \ddots & \vdots\\ u_{k1} & u_{k1} & \cdots & u_{ki}\end{bmatrix} \tag{6.57}$$

Then, HFCs are computed by Eq. (6.55) and used in damage detection block to detect the damage.

6.6.3 Damage Identification Results

Similarly, multiple excitation frequencies are utilized to enrich the data and make the problem over-determined. The excitation frequency set is given in Table 6.7 and laser scanner is used for damage detection.

Table 6.7 Excitation frequency set: rotor simulation

	trial 1	trial 2
ω (Hz)	170	900

Fig. 6.21 shows two excitation frequencies which are used for damage detection. The input lasts 30 seconds for each frequency and has a 10s interval between two trials. The amplitudes variation of force is shown in Fig. 6.22.

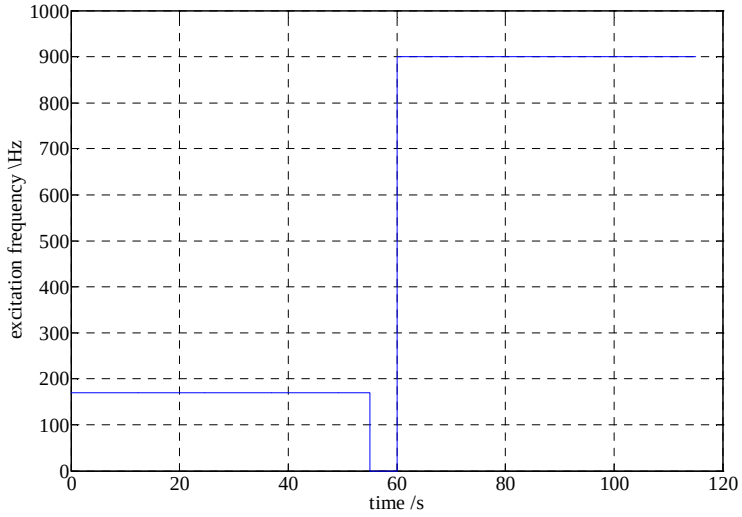

Fig. 6.21 Excitation frequency: rotor simulation

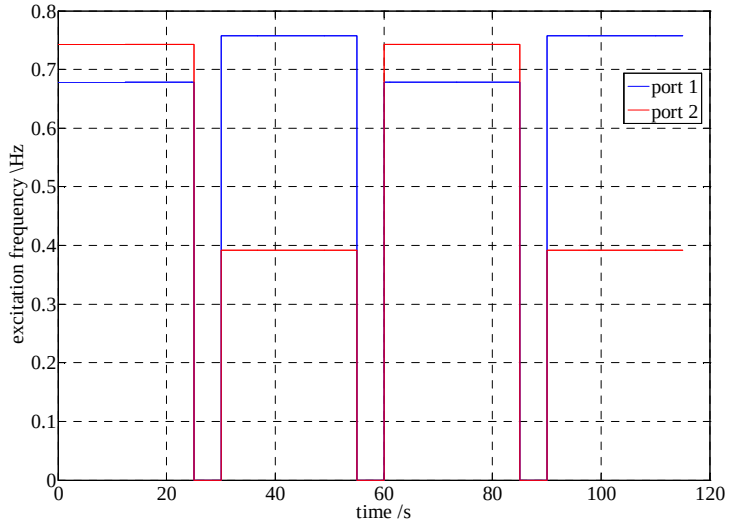

Fig. 6.22 Force amplitudes for 2 input ports

Fig. 6.23-6.25 show Harmonic Fourier Coefficients of multiport inputs for DC term, 1st and 2nd harmonics collected by laser scanner in c_2 direction, respectively. We could see that HFCs oscillate at the beginning stage of excitation and converge with the increase of time while the vibration response goes to stable. However, these HFCs are not able to be using for damage detection. We need to calculate the HFCs for single input from Eq. (6.55).

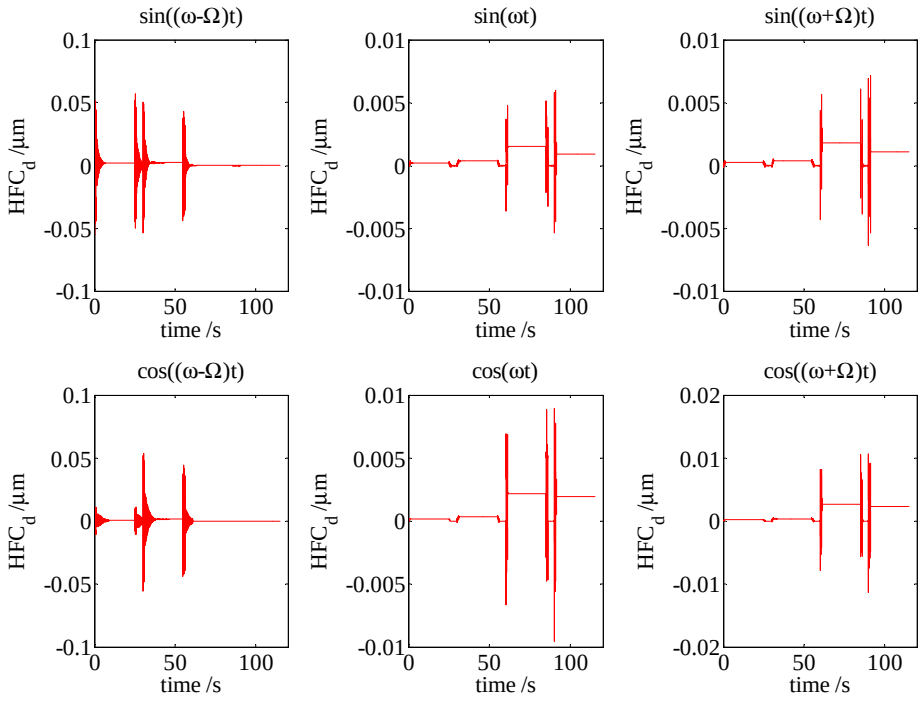

Fig. 6.23 Harmonic Fourier Coefficients of multiport inputs for DC term, c_2 dir.

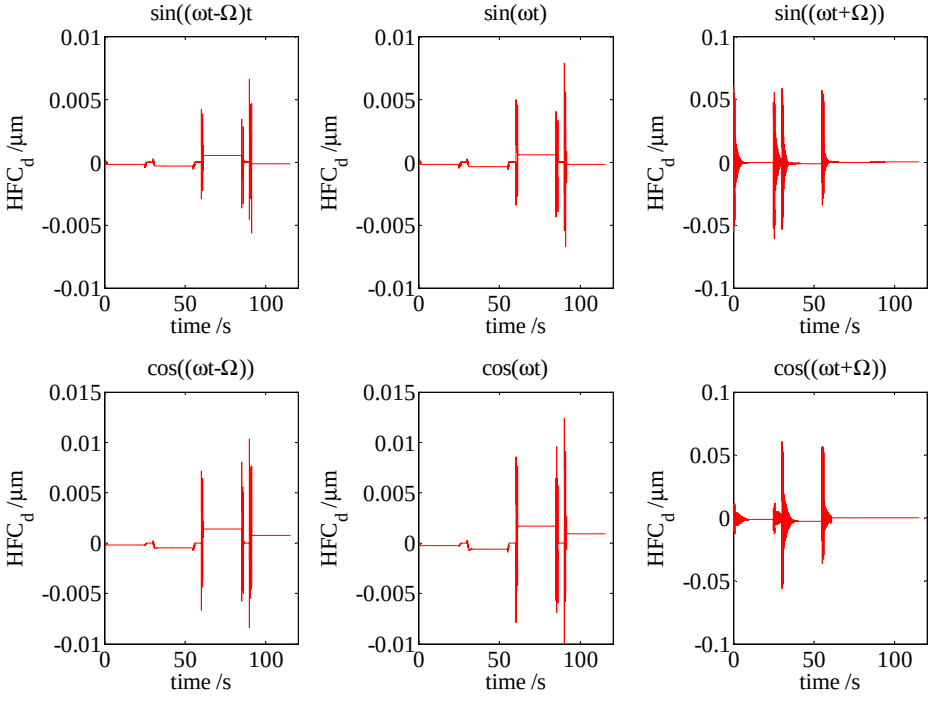

Fig. 6.24 Harmonic Fourier Coefficients of multiport inputs for 1st harmonic, c_2 dir.

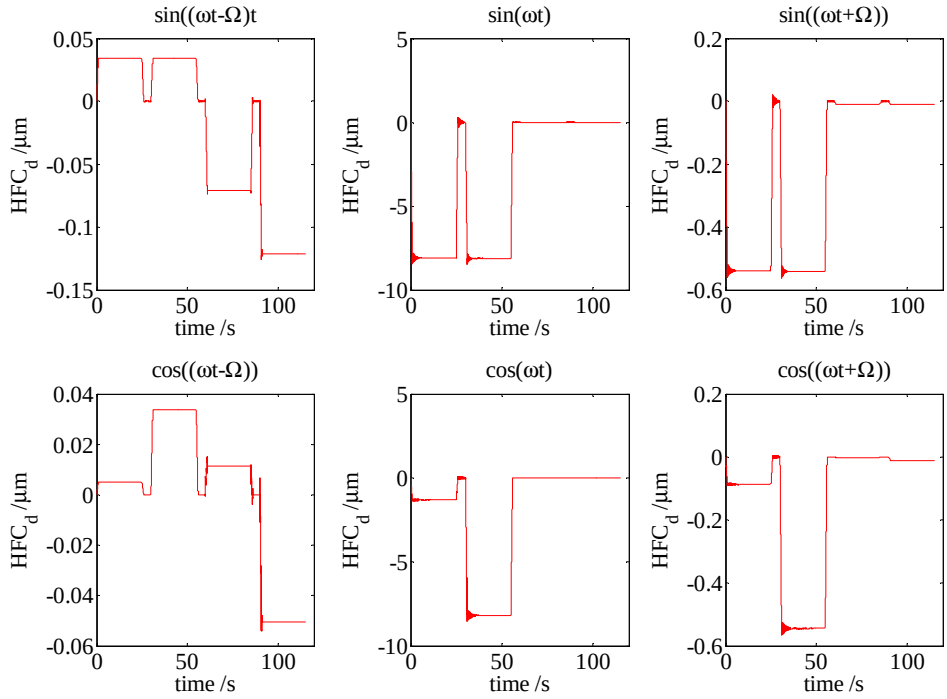

Fig. 6.25 Harmonic Fourier Coefficients of single port inputs for 2nd harmonic, c_2 dir.

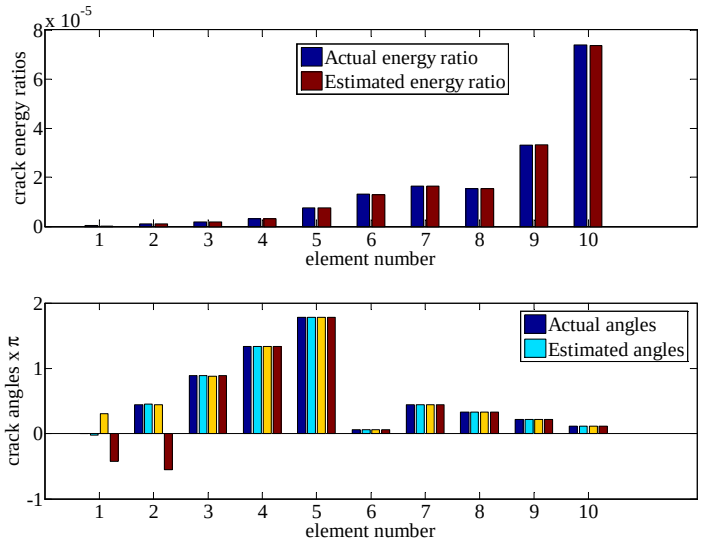

Fig. 6.26 Crack depth and angle comparison

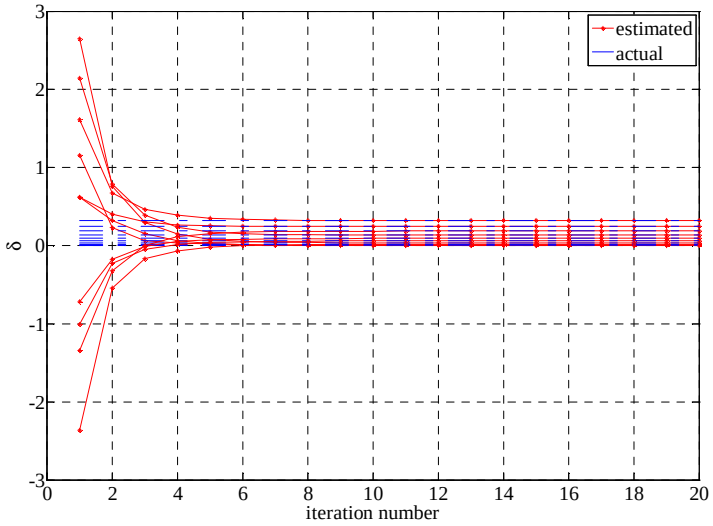

Fig. 6.27 Damage parameter iteration history

Using the HFCs computing by left least square method as the input of damage detection block in time domain, the estimation results are obtained in Fig. 6.26 and 6.27. Fig. 6.26 shows crack energy ratio and angle comparison and Fig. 6.27 gives damage parameter iteration history. The blue dash line and red star line denotes the actual and estimated damage parameters respectively.

6.7 Summary

The crack is assumed to be breathing during operation due to the effect of gravity or imbalance weight. Zero-SIF (Stress Intensity Factor) method is employed to determine the close line of open crack area. It is found that the crack parameter is a function of both crack phase and rotation angle and this function can be approximated by a cosine function. In Chapter III, we know that 3 damage parameters are needed for damage detection of open cracks. For breathing cracks, 6 more parameters are needed to estimate $\delta_i \sin(\theta)$ and $\delta_i \cos(\theta)$ terms ($i=y, z, yz$). The transfer function can be obtained from the

vibration response measured by sensors attached on shaft or laser scanner. After validating the algorithm in frequency domain, time-domain simulation is conducted and Harmonic Fourier Coefficients (HFC) of vibration response is calculated by convolution and left least square techniques and then filtered by an average moving window filter. Finally, the damage detection is processed by using HFCs for single input channel as the input of time-domain damage detection block.

Chapter VII

CONCLUSIONS AND RECOMMENDATIONS FOR FUTURE WORK

7.1 Summary and Conclusions

This thesis explores two kinds of new vibration-based damage identification methodologies: Floquet based method (Methodology I) and Frequency Response Function (FRF) based method (Methodology II). Based on the open cracked rotor system, Floquet based method is developed using Floquet theory, least square method and eigenvector updating method. It is found that this method is able to detect the crack location and severity effectively with the assistance of Active Magnetic Bearing (AMB). The adjustable stiffness or virtual mass of AMB benefits the damage identification by proper tuning. The introduction of AMB breaks the symmetric structure of rotor system along the axial direction as long as the AMB is not placed in the midpoint of shaft. In addition, the asymmetric stiffness of AMB plays an important role in breaking modal symmetry and distinguishing multiple cracks. Though Floquet based method works well to identify the crack depth and location, it could not tell the crack angle since the mapping from natural frequency shift to crack angle is not unique.

To overcome this problem, FRF based method is subsequently developed which utilizes the magnitude and phase of transfer function shifts induced by damage. FRF based method provides the advantages of random interrogating frequency and multiple inputs/outputs which greatly increase the variety of adjustable parameters. The damage detection algorithm is derived based on Taylor Expansion, least square method and Newton-Raphson method. It is found that the transfer function shifts are more sensitive

when the system is excited near resonances or sidebands. Consequently, the damage estimation results are much better while using near-resonance or near sidebands excitation. For time-varying system, sidebands appear at frequencies: $\omega \pm n\Omega$ and they drift away from the resonance with the increase of rotation speed. The information of sidebands enriches the database for damage detection and also helps to reduce the number of sensors. Armed with this method, two kinds of breathing cracked system are studied: breathing cracked truss system and rotor system.

For the breathing cracked truss system, the crack model is rebuilt because the crack is driven open and close by axial force. According to Strain Energy Released Rate (SERR) concept in fracture mechanics, only one damage parameter is needed to represent and estimate one crack on a truss bar. For the damaged time-invariant system with stiffness and mass uncertainties, FRF based method is modified to include both kinds of uncertainties as the desired estimated parameters and yields very good results. For the damaged truss system with breathing cracks, several assumptions are made to convert the breathing function $f_k(t,Q)$ to pure function of time $f_k(t)$ in the first step. Then, $f_k(t)$ can be approximated by Fourier expansion and the linear damage detection algorithm is developed in time-domain. The second step is to get the vibration response of joints through simulation without any assumptions. By doing Fast Fourier Transform (FFT), the frequency components contained in the response can be observed from frequency spectrum. Finally, Harmonic Fourier Coefficients (HFCs) for primary peak and sidebands are used for damage detection after comparing the frequency spectrum of nonlinear and linear vibration response. It is concluded that the sidebands do improve the damage detection results and meanwhile reduce the number of sensors.

For the breathing cracked rotor system, the presented work is using Cosine crack model to approximate the nonlinear behavior of breathing cracks. Assuming the breathing crack is driven by gravity, the nonlinear model is built based on zero stress intensity factor method and compared with Cosine and Square Wave crack models. An important discovery in this part is that nine damage parameters are needed to represent a breathing transverse crack in rotor system. Similar as open crack, the first three damage parameters are able to detect the crack depth and twice of crack angle. The other six parameters are related to crack angle and can give three sets of crack angle estimates. It is recommended that the crack angle estimates are more accurate while being estimated by dominant terms. In frequency domain, distributed damage is identified using different kinds of sensor, such as sensor attached to shaft or laser scanner. In time domain, the vibration of damaged and nominal rotor systems is simulated and HFCs for multiple input channels are computed by convolution method and filter by moving averaging window. As the input of damage detection block, HFCs of single input channel are obtained from HFCs for multiple channels by left least square method.

7.2 Recommendations for Future Work

One of the continued topics will be more parametric study of damage detection using laser scanner. As we known from previous study, laser scanner is able to provide much information of multiple harmonics if the scanning function is decomposed by Fourier Expansion. Compared with damage detection using shaft sensor, the number of sensors can be dramatically reduced with the usage of laser scanner. Fig. 7.1 shows the Frequency Response Function (FRF) of damaged system with distributed damage case

which is observed from multiple shaft sensors. Fig. 7.2 plots FRF of damaged system with distributed damage case obtained from laser scanner.

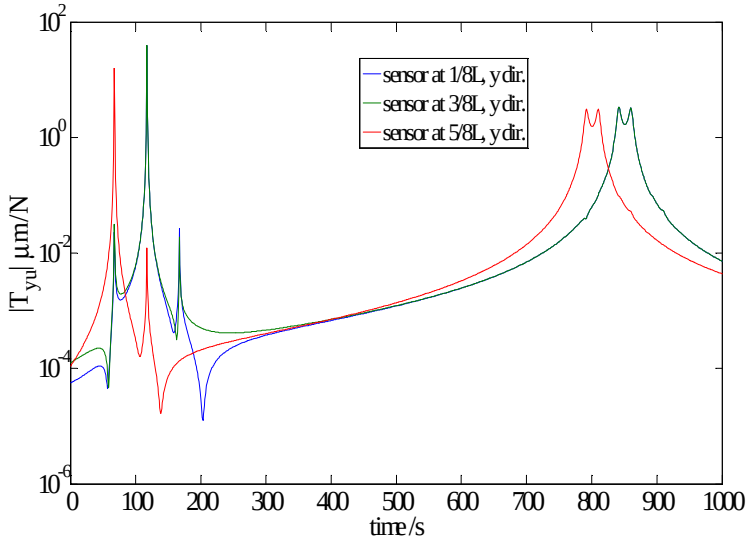

Fig. 7.1 Damaged FRF: shaft sensors

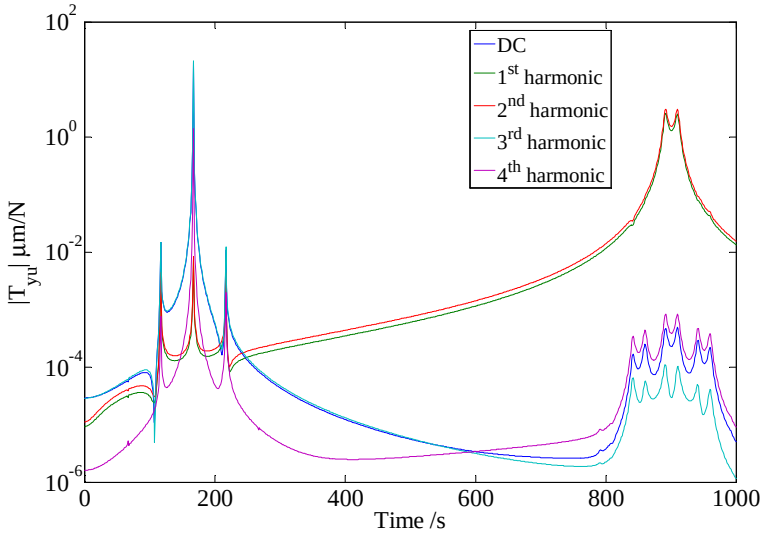

Fig. 7.2 Damaged FRF: laser scanner

The further investigation will be done to explore the impact of scanning frequency ω_s on the output matrix C_y and frequency response functions.

Another recommended research is the damage detection of real breathing cracked rotor system by including the nonlinear crack model into the simulation diagram. The crack

open area is determined by calculating the bending moments in two lateral directions according to the vibration response in real-time. The proposed simulation diagram is shown in Fig. 7.3.

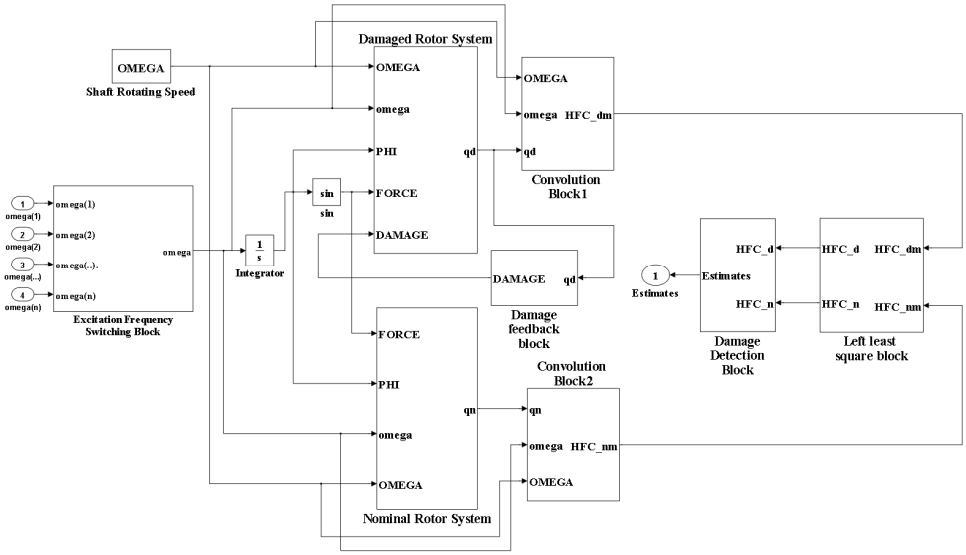

Fig. 7.3 Breathing cracked rotor system nonlinear simulation

Here, the damage feedback block take the vibration response of damaged system to compute the bending moments in real time. Then the real-time crack open area can be determined by taking the bending moments to zero SIF (Stress Intensity Factor) method.

There are more research topics we would like to explore such as:

(1) Damage identification based on torsional vibration of rotor system

Unlike the bending moment and axial force, torque will induce the sliding and shearing deformation of transverse crack. Therefore, different SIFs will be involved in the calculation of crack released strain energy. It is very interesting to explore the characteristics of torsional vibration and the damage detection based on it.

(2) Experiment verification of damage identification method

A lot of theoretical damage detection methods have been done and demonstrated via numerical examples and simulations. The next step is to implement the experiments and test these theories. Of course, there will be many technical difficulties encountering in the experimental work, such as the measurement of higher natural frequencies, the installation of sensors, the noise cancellation of vibration signals, etc. Once all of these works is done, it will provide a comprehensive guidance of damage identification including theory, application and experiments.

LIST OF REFERENCES

[1] Shahab A. S., and Thomas J., Coupling effects of disc flexibility on the dynamic behavior of multi disc-shaft systems, J of Sound and Vibration, 1987, I 14(3): 435-452.

[2] Wu F., Flowers G. T., A transfer matrix technique for evaluating the natural frequencies and critical speeds of a rotor with multiple flexible disks, ASME. J of Vibration and Acoustics, 1992, 114:242-248.

[3] Sakata M., Kimura K., Park S.K. and Ohnabe H., Vibration of bladed flexible rotor due to gyroscopic moment, J of Sound and Vibration, 1989,113(3): 417-430.

[4] Wu F., Flowers G. T., An experimental study of the influence of disk flexibility and rubbing on rotor dynamics, ASME Vibration of Rotating Systems, 1993, 60:19-26.

[5] Chun S. B. and Lee C. W., Vibration analysis of shaft-bladed disk system using substructure synthesis and assumed modes method J of Sound and Vibration, 1996, 189(5): 587-608.

[6] Loewy R. G. and Khader N., Structural dynamics of rotating bladed-disk assemblies coupled with flexible shaft motions, AIAA J, 1984, 22(9):1319-1327.

[7] Foiles W. C., Allaire P. E., Gunter E.J., Review: Rotor balancing, J. of Shock and Vibration, 1998, 5(5):325-336.

[8] Parkinson A. G., Schneider H., Balancing of flexible rotors-some considerations on modal convergence, In: Proc. 5th International Conf. on Rotor Dynamics, Germany, Sep. 1998, 653-663.

[9] McLaclan N. W., Theory and Application of Mathieu Functions, Dover Publications, lnc., New York, 1964

[10] Bolotin V. V., The Dynamic Stability of Elastic Systems, Holden-Day, Inc., 1964.

[11] Floquet G., Sur les equations differentielles lineaires，Ann. De L'ecole Normale Superieure, Vol. 12, 1883, pp. 47-88.

[12] A. Unger and M. A. Brull, Parametric Instability of a Rotating Shaft Due to Pulsating Torque, Transaction of the ASME, Vol. 48, December 1981，pp.948-958.

[13] J. W. Lund and F. K. Orcutt, Calculations and Experiment on the Unbalance Response of a Flexible Rotor, Transactions of the American Society of Mechanical Engineers, Journal of Engineering for Industry, Vol. 89, 1967, pp785-796.

[14] R. L. Ruhl, Dynamics of Distributed Parameter Rotor System: Transfer Matrix and Finite Element Technique, Ph. D. Thesis, Cornell University, 1970.

[15] R. L. Ruhl and J.F. Booker, A Finite Element Model for Distributed Parameter Turbo rotor System, Transactions of the American Society of Mechanical Engineers, Journal of Engineering for Industry, Vo1.94, 1972, pp128-132.

[16] C. A. Papadopoulos, A. D. Dimarogonas, Coupled Longitudinal and Bending Vibrations of a Rotating Shaft with an Open Crack. Journal of Sound and Vibration, 1987, 117(1):81-93.

[17] S. C. Huang, Y. M. Huang, S. M. Shieh, Vibration and Stability of a Rotating Shaft Containing a Transverse Crack, Journal of Sound and Vibration, 1993, 162(3): 387-401.

[18] A. S. Sekhar, B. S. Prbhu, Vibration and stress Fluctuation in Cracked Shafts. Journal of Sound and Vibration, 1994, 169(5): 655-667.

[19] Y. B. Kim, A Multiple Harmonic Balance Method for the Internal Resonant Vibration of a Non-linear Jeffcott Rotor, Journal of Sound and Vibration, 1997,208(5): 745--761.

[20] Z. Ji, J. W. Zu, Method of Multiple Scales for Vibration Analysis of Rotor-Shaft Systems with Non-linear Bearing Pedestal Mode. Journal of Sound and Vibration, 1998, 218(2): 293-305.

[21] C. O. Chang, J. W. Cheng, Non-linear Dynamics and Instability of a Rotating Shaft-disk System, Journal of Sound and Vibration, 1993,160(3): 433--454.

[22] Friswell M. I., Penny J. E. T. Crack Modeling for Structural Health Monitoring. Structural Health Monitoring, 2002, 1(2): 139-148.

[23] Dimarogonas A.D., Vibration of cracked structures: a state of the art review, Engineering Fracture Mechanics, 1996, 55(5): 831-857.

[24] Wu N.X., Wu K.Q., You M.Y., Dynamical simulation of cracked beam, J. of Engineering Design, 2006, 04: 236-240.

[25] Hu J.S., Feng X., Li X, Review of vibration analysis of cracked beam and crack diagnosis , Vibration and Shock, 2007, 26(11): 146-152.

[26] Kirmsher P.G., The effect of discontinuities on the natural frequency of beams, Proc. American Society of Testing and Materials, 1944, 44:897-904.

[27] Thomson W J. Vibration of slender bars with discontinuities in stiffness. Journal of Applied Mechanics, 1943, 17: 203-207.

[28] Isalik A.M., Free vibrations of reinforced concrete bars with crack in flexure. SOVIET APPLIED MECHANICS, 1967, 3: 71-73.

[29] Petroski H.J, Simple static and dynamic models for the elastic beam. International Journal of Fracture, 1981, 17: 71-76.

[30] Ku D.M., Chen L.W., Dynamic stability of a shaft disk system with flaws, Computers & Structures, 1992, 43: 306-311.

[31] Wendtland D, Aenderung der Biegeeigen frequenzen Einer Idealisierten Schaufel Durch Risse, vol. PhD: University of Karlsruhe, 1972.

[32] Cawley P., Ray R., A comparison of natural frequency changes produced by cracks and slots. Journal of Vibration and Acoustics, Stress, Reliability in Design, Transactions of the ASME, 1988, 110: 366-370.

[33] Silva J.M.M., Gomez A.J.M.A., Experimental dynamic analysis of cracked free-free beams, Experimental Mechanics, 1990, 30: 20-25.

[34] Gomez A.J.M.A., Silva J.M.M., Theoretical and experimental data on crack depth effects in the dynamic behavior of free-free beams, Int. Modal Analysis Conference, IMAC, 1991:274-283.

[35] Irwin G.R., Fracture mechanics Structural Mechanics, 1960:557.

[36] Liebowitz H., Claus W.D., Failure of notched columns, Engineering Fracture Mechanics, 1968, 1: 379-383.

[37] Liebowitz H.,, Vanderveldt H., Harris D.W., Carrying capacity of notched column, International Journal of Solids and Structures, 1967, 3: 489-500.

[38] Ocamura H., Liu H.W., Chu C.S., et al, A cracked column under compression, Engineering Fracture Mechanics, 1969, 1:547-564.

[39] Gudmunson P., The dynamic behavior of slender structures with cross-sectional cracks, Journal of Mechanics and physics Solids, 1983, 31:329-345.

[40] Rice J.R., Lew N., The part-through surface crack in an elastic plate. Journal of Applied Mechanics, 1972, 39: 185-194.

[41] Dimarogonas A.D., Stephen A.P., Analytical methods in rotor dynamics, Applied Science Publishers, 1983.

[42] Dimarogonas A.D., Vibration Engineering, St. Paul: West Publishers, 1976.

[43] Chondros T.G., Dimarogonas A.D., Identification of cracks in welded joints of complex structures. Journal of Sound and Vibration, 1980, 69: 531-538.

[44] Papadopoulos C.A., Dimarogonas A.D., Coupling of bending and torsional vibrations of a cracked Timoshenko shaft, Ingenieur Archiv, 1987, 57: 257-266.

[45] Ostachowicz W.M., Krawczuk M., Analysis of the effect of crack on the natural frequency of a cantilever beam, Journal of Sound and Vibration, 1991, 150(2): 191-201.

[46] Krawczuk M., Zak A., Ostachowicz W., Elastic beam finite element with a transverse elasto-plastic crack, Finite Elements in Analysis and Design, 2000, 34(1): 61-73.

[47] Christides S., Barr A.D.S., One-dimensional theory of cracked Bernoulli-Euler beams, International Journal of Mechanical Sciences, 1984, 26: 639-648.

[48] Christides S., Barr A.D.S., Torsional vibration of cracked beams of non-circular cross-section, International Journal of Mechanical Sciences, 1986, 28(7): 473-490.

[49] Shen M.H.H., Pierre C., Free vibration of beams with a single edge crack, Journal of Sound and vibration, 1994, 170(2): 237-259.

[50] Shen M.H.H., Pierre C., Natural modes of Bernoulli — Eider beams with symmetric cracks, Journal of Sound and Vibration, 1990, 138(1): 115-134.

[51] Chondros T.G., Dimarogonas A.D., Yao J., A consistent cracked bar vibration theory, Journal of Sound and Vibration, 1997, 200(3): 303-313.

[52] Chondros T.G., Dimarogonas A.D., Yao J., Longitudinal vibration of a continuous cracked bar, Engineering Fracture Mechanics, 1998, 61(5-6): 593-606.

[53] Chondros T.G., Dimarogonas A.D., Yao J., A continuous cracked beam vibration theory, Journal of Sound and Vibration, 1998, 215(1): 17-34

[54] Chondros T.G., Dimarogonas A.D., Vibration of a cracked cantilever beam, Journal of Vibration and Acoustics, 1998, 120: 742-746.

[55] Chondros T.G., The continuous crack flexibility model for crack identification, Fatigue and Fracture of Engineering Materials and Structures, 2001, 24(10): 643-650.

[56] Chondros T.G., Variational formulation of a rod under torsional vibration for crack identification, Theoretical and applied fracture mechanics, 2005, 44: 95-104.

[57] Chondros T.G., Labeas G.N., Torsional vibration of a cracked rod by Variational formulation and numerical analysis, Journal of Sound and Vibration, 2007, 301(3-5): 994-1006.

[58] Carneiro S.H.S., Inman D.J., Continuous model for the transverse vibration of cracked Timoshenko beams, Journal of Vibration and Acoustics, Transactions of the ASME, 2002, 124(2): 310-320.

[59] Swamidas A.S.J., Yang X., Seshadri R., Identification of Cracking in Beam Structures using Timoshenko and Euler Formulations, Journal of Engineering Mechanics, 2004, 130(11): 1297-1308.

[60] Yang X.F., Swamidas A.S.J., Seshadri R., Crack identification in vibrating beams using the energy method, Journal of Sound and Vibration, 2001, 244(2): 339-357.

[61] Ibrahim A., Ismail F., R. Martin H., Modeling of the dynamics of a continuous beam including nonlinear fatigue crack, International Journal of Analytic and Experimental Modal Analysis, 1987, 2: 76-82.

[62] Pugno N., Surace C., Ruotolo R., Evaluation of the non-linear dynamic response to harmonic excitation of a beam with several breathing cracks, Journal of Sound and Vibration, 2000, 235(5): 749-762.

[63] Ruotolo R., Surace C., Crespo C., et al, Harmonic analysis of the vibrations of a cantilevered beam with a closing crack, Computers & Structures, 1996, 61(6): 1057-1074.

[64] Chondros T.G., Dimarogonas A.D., Yao J., Longitudinal vibration of a bar with a breathing crack, Engineering Fracture Mechanics, 1998, 61(5-6): 503-518.

[65] Chondros T.G., Dimarogonas A.D., Yao J., Vibration of a beam with a breathing crack, Journal of Sound and Vibration, 2001, 239(1): 57-67.

[66] Shen M.H.H., Chu Y.C., Vibration of beams with a fatigue crack, Computers & Structures, 1992, 45(1):79-93.

[67] Cheng S.M., Wu X.J., Wallace W., et al, Vibrational response of a beam with a breathing crack. Journal of Sound and Vibration, 1999, 225(1): 201-208.

[68] Douka E., Hadjileontiadis L.J., Time-frequency analysis of the free vibration response of a beam with a breathing crack, NDT and E International, 2005, 38(1): 3-10.

[69] Loutridis S., Douka E., Hadjileontiadis L J. Forced vibration behavior and crack detection of cracked beams using instantaneous frequency, NDT and E International, 2005, 38(5): 411-419.
[70] Kisa M., Brandon J., The effects of closure of cracks on the dynamics of a cracked cantilever beam, Journal of Sound and Vibration, 2000, 238(1): 1-18.
[71] Andreaus U., Casini P., Vestroni F., Non-linear dynamics of a cracked cantilever beam under harmonic excitation, International Journal of Non-Linear Mechanics, 2007, 42(3): 566-575.
[72] Kogl M., Hurlebaus S., Gaul L., Finite element simulation of non-destructive damage detection with higher harmonics, NDT and E International, 2004, 37: 195-205.
[73] Hirose S., Achenbach J.D., Higher harmonics in the far field due to dynamic crack-face contacting, Journal of the Acoustical Society of America, 1993, 93(1): 142-147.
[74] Lele S.P., Maiti S.K., Modeling of transverse vibration of short beams for crack detection and measurement of crack extension, Journal of Sound and Vibration, 2002, 257(3): 559-583.
[75] Patil D.P., Maiti S.K., Detection of multiple cracks using frequency measurements, Engineering Fracture Mechanics, 2003, 70(12): 1553-1572.
[76] Rizos P.F., Aspragathos N., Dimarogonas A.D., Identification of crack location and magnitude of a cantilever beam from the vibration mode, Journal of Sound and Vibration, 1990, 138(3): 381-388.
[77] Narkis Y., Elinalah E., Crack identification in a cantilever beam under uncertain end conditions, International Journal of Mechanical Sciences, 1996, 38(5): 499-507.
[78] Chaudhari T.D., Maiti S.K., A study of vibration of geometrically segmented beams with and without crack, International Journal of Solids and Structures, 2000, 37: 761-779.
[79] Chaudhari T.D., Maiti S.K., Modeling of transverse vibration of beam of linearly variable depth with edge crack, Engineering Fracture Mechanics, 1999, 63: 425-445.
[80] Nandwana B.P., Maiti S.K., Modeling of vibration of beam in presence of inclined edge or internal crack for its possible detection based on frequency measurements, Engineering Fracture Mechanics, 1997, 58(3): 193-205.

[81] Kasper D.G., Swanson D.C., Reichard K.M., Higher-frequency wave number shift and frequency shift in a cracked, vibrating beam, Journal of Sound and Vibration, 2008, 312(1-2): 1-18.

[82] Lin H.P., Chang S.C., Wu J.D., Beam vibrations with an arbitrary number of cracks, Journal of Sound and Vibration, 2002, 258(5): 987-999.

[83] Khiem N.T., Lien T.V., A simplified method for natural frequency analysis of a multiple cracked beam, Journal of Sound and Vibration, 2001, 245(4): 737-751.

[84] Khiem N.T., Lien T.V., Multi-crack detection for beam by the natural frequencies, Journal of Sound and Vibration, 2004, 273: 175-184.

[85] Khiem N.T., Lien T.V., The dynamic stiffness matrix method in forced vibration analysis of multiple-cracked beam, Journal of Sound and Vibration, 2002, 254(3): 541-555.

[86] Khiem N.T., Crack detection for structure based on the dynamic stiffness model and the inverse problem of vibration, Inverse Problems in Science and Engineering, 2006, 14(1): 85-96.

[87] Ricci P., Viola E., Stress intensity factors for cracked T-sections and dynamic behavior of T-beams, Engineering Fracture Mechanics, 2006, 73(1): 91-111.

[88] Viola E., Ricci P., Aliabadi M.H., Free vibration analysis of axially loaded cracked Timoshenko beam structures using the dynamic stiffness method, Journal of Sound and Vibration, 2007, 304(1-2): 124-153.

[89] Gounaris G., Dimarogonas A., A finite element of a prismatic beam for structure analysis, Computers & Structures, 1988, 28(3): 309-313.

[90] Chinchalkar S., Determination of crack location in beams using natural frequencies, Journal of Sound and Vibration, 2001, 247(3): 417-429.

[91] Kisa M., Free vibration analysis of a cantilever composite beam with multiple cracks, Composites Science and Technology, 2004, 64(9): 1391 — 1402.

[92] Kisa M., Arif Gurel M., Modal analysis of multi-cracked beams with circular cross section, Engineering Fracture Mechanics, 2006, 73(8): 963-977.

[93] Kisa M., Arif Gurel M., Free vibration analysis of uniform and stepped cracked beams with circular cross sections, International Journal of Engineering Science, 2007, 45(2-8): 364-380.

[94] Kisa M., Brandon J., Topcu M., Free vibration analysis of cracked beams by a combination of finite elements and component mode synthesis methods, Computers & Structures, 1998, 67(4): 215-223.

[95] C.A. Papadopoulos, A.D. Dimarogonas, Stability of cracked rotors in the coupled vibration mode, Journal of Vibration and Acoustics, Stress and Reliability in Design, 110:356-359.

[96] C.A. Papadopoulos, Torsional vibration of rotors with transverse surface cracks, Computers and Structures, 1994, 51(6): 713-718.

[97] S.C. Huang, etc, Vibration and Stability of a rotating shaft containing a transverse crack, journal of Sound and Vibration, 1993, 162(3):387-401.

[98] Lee Y.S., Chung M.J., A study on crack detection using engenfrequency test data, Computers & structures, 2000, 77:327-342.

[99] B.S. Prabhu, A.S. Sekhar, Severity estimation of cracked shaft vibration with film bearings, Tribology Transactions, 1995, 38(3): 583-588.

[100] G.T. Zheng, Vibration of a rotor system with a switching crack and detection of the crack, Journal of Engineering for Gas Turbines and Power, 1998, 120(1): 149-154.

[101] A.S. Sekhar, B.S. Prabhu, Transient analysis of cracked rotor passing through critical speed, Journal of Sound and Vibration, 1994, 173(3): 415-421.

[102] A.S. Sekhar, Vibration Characteristics of a cracked rotor with two open cracks, Journal of Sound and Vibration, 1999, 223(4): 497-512.

[103] S.D. Panteliou, T.G. Chondros, V.C. Argyrakis, Damping factor as an indicator of crack severity, Journal of Sound and Vibration, 2001, 241(2): 235–245.

[104] W. Zhang, R.B. Testa, Closure effects on fatigue crack detection, Journal of Engineering Mechanics, 1999, 125(10): 1125–1132.

[105] N. Bachschmid, P. Pennacchi, E. Tanzi, Transverse crack modeling and validation in rotor systems, including thermal effects, International Journal of Rotating Machinery, 2003, 9 (2): 113–126.

[106] A.P. Bovsunovsky, The mechanisms of energy dissipation in the non-propagating fatigue cracks in metallic materials, Engineering Fracture Mechanics, 2004, 71(16–17): 2271–2281.

[107] R.K. Behera, D.R.K. Parhi, S.K. Sahu, Vibration analys is of a cracked rotor surrounded by viscous liquid, Journal of Vibration and Control, 2006, 12(5): 465–494.
[108] D.R. Parhi, A.K. Behera, Vibration analysis of cantilever type cracked rotor in viscous fluid, Transactions of the Canadian Society for Mechanical Engineering, 2003, 27(3): 147–173.
[109] D.R. Parhi, A.K. Behera, Vibrational analysis of cracked rotor in viscous medium, Journal of Vibration and Control, 2000, 6(3): 331–349.
[110] G. Sabnavis, R.G. Kirk, M. Kasarda, Cracked shaft detection and diagnostics: A literature review, Shock and Vibration Digest, 2004, 36(4).
[111] Salawu O.S., Detection of structural damage through changes in frequency: A review, Engineering Structures, 1997, 19(9): 718-723.
[112] Cawley P., Admas R.D., The location of defects in structures from measurements of natural frequencies, Journal of Strain Analysis, 1979, 14(2): 49-57.
[113] Dharmaraju N., Sinha J.K., Some comments on use of anti-resonance for crack identification in beams, Journal of Sound and Vibration, 2005, 286(3): 669-671.
[114] Dilena M., Morassi A., The use of anti-resonances for crack detection in beams, Journal of Sound and Vibration, 2004, 276: 195-214.
[115] Dilena M., Morassi A., Damage detect ion in discrete vibrating systems, Journal of Sound and Vibration, 2006, 289(4-5): 830-850.
[116] P.G. Nikolakopoulos, D.E. Katsareas, C.A. Papadopoulos, Crack Identification in Structures, in: M. Papadrakakis, B.H.V. Topping (Eds.), Computational Structural Engineering for Practice, Civil-Comp Press, 1994, pp. 1–8.
[117] P.G. Nikolakopoulos, D.E. Katsareas, C.A. Papadopoulos, Crack identification in frame structures, Computers and Structures, 1997 64(1–4): 389–406.
[118] S.P. Lele, S.K. Maiti, Modelling of transverse vibration of short beams for crack detection and measurement of crack extension, Journal of Sound and Vibration, 2002 257 (3): 559–583.
[119] S. Ratan, H. Baruh, J. Rodriguez, On-line identification and location of rotor cracks, Journal of Sound and Vibration, 1996, 194 (1): 67–82.

[120] P.F. Rizos, N. Aspragathos, A.D. Dimarogonas, Identification of crack location and magnitude in a cantilever beam from the vibration modes, Journal of Sound and Vibration , 1990, 138(3): 381–388.

[121] I. Imam, S.H. Azzaro, R.J. Bankert, Development of an on-line rotor crack detection and monitoring system, Journal of Vibration, Acoustics, Stress, and Reliability in Design, 1989, 111(3): 241–250.

[122] S. Seibold, K.Weinert, A time domain method for the localization of cracks in rotors, Journal of Sound and Vibration, 1996, 195(1): 57–73.

[123] G.M. Dong, J. Chen, J. Zou, Parameter identification of a rotor with an open crack, European Journal of Mechanics—A: Solids, 2004, 23(2): 325–333.

[124] M. Karthikeyan, R. Tiwari, S. Talukdar, Crack localisation and sizing in a beam based on the free and forced response measurements, Mechanical Systems and Signal Processing, 2007, 21(3): 1362–1385.

[125] G.D. Gounaris, C.A. Papadopoulos, Analytical and experimental crack identification of beam structures in air or in fluid, Computers and Structures, 1997, 65(5): 633–639.

[126] Y. Ishida, T. Ikeda, T. Yamamoto, Vibrations of a rotating shaft containing a transverse crack (1st report, variations of a resonance curve due to the angular position of an unbalance at the major critical speed), Nippon Kikai Gakkai Ronbunshu, C Hen/Transactions of the Japan Society of Mechanical Engineers, Part C, 1987, 53(488): 925–932.

[127] H.Y. Hwang, C. Kim, Damage detection in structures using a few frequency response measurements, Journal of Sound and Vibration, 2004, 270(1–2): 1–14.

[128] G.D. Gounaris, C.A. Papadopoulos, A.D. Dimarogonas, Crack identification in beams by coupled response measurements, Computers and Structures, 1996, 58(2): 299–305.

[129] G.D. Gounaris, C.A. Papadopoulos, Crack identification in rotating shafts by coupled response measurements, Engineering Fracture Mechanics, 2002, 69(3): 339–352.

[130] A.K. Darpe, A. Chawla, K. Gupta, Analysis of the response of a cracked Jeffcott rotor to axial excitation, Journal of Sound and Vibration, 2002, 249(3): 429–445.

[131] A.K. Darpe, K. Gupta, A. Chawla, Experimental investigations of the response of a cracked rotor to periodic axial excitation, Journal of Sound and Vibration, 2003, 260(2): 265–286.

[132] M.H.F. Dado, O. Abuzeid, Coupled transverse and axial vibratory behaviour of cracked beam with end mass and rotary inertia, Journal of Sound and Vibration, 2003, 261(4): 675–696.

[133] S.M. Al-Said, M. Naji, A.A. Al-Shukry, Flexural vibration of rotating cracked Timoshenko beam, Journal of Vibration and Control, 2006, 12(11) :1271–1287.

[134] P.N. Saavedra, L.A. Cuitino, Vibration analysis of rotor for crack identification, Journal of Vibration and Control, 2002, 8(1): 51–67.

[135] P.N. Saavedra, L.A. Cuitino, Crack detection and vibration behavior of cracked beams, Computers and Structures, 2001, 79(16): 1451-1459.

[136] Suh M.W., Yu J.M., Lee J.H., Crack detection using classical optimization technique, Key Engineering Materials, 2000, 183-187: 61-66.

[137] He Y., Guo D., Chu F., Using genetic algorithms and finite element methods to detect shaft crack for rotor-bearing system, Mathematics and Computers in Simulation, 2001, 57: 95-108.

[138] R. Isermann, Model based fault detection and diagnosis methods, Proceedings of the American Control Conference, 1995, 3: 1605-1609.

[139] N. Bachschmid, R. Dellupi, Non linear behaviour of oil film bearings and its relevance in force identification procedures, Paper, American Society of Mechanical Engineers, 1997.

[140] N. Bachschmid, P. Pennacchi, E. Tanzi, Identification of transverse crack position and depth in rotor systems, Meccanica, 2000, V35 (6): 563-582.

[141] R. Markert, R. Platz, M. Seidler, Model based fault identification in rotor systems by least squares fitting, International Journal of Rotating Machinery, 2001, 7(5): 311-321.

[142] N. Dharmaraju, R. Tiwari, S. Talukdar, Identification of an open crack model in a beam based on force–response measurements, Computers and Structures, 2004, 82(2–3): 167-179.

[143] N. Dharmaraju, R. Tiwari, S. Talukdar, Development of a novel hybrid reduction scheme for identification of an open crack model in a beam, Mechanical Systems and Signal Processing, 2005, 19(3): 633–657.

[144] A.S. Sekhar, Identification of unbalance and crack acting simultaneously in a rotor system: Modal expansion versus reduced basis dynamic expansion, Journal of Vibration and Control, 2005, 11(9): 1125–1145.

[145] A.S. Sekhar, Crack identification in a rotor system: a model-based approach, Journal of Sound and Vibration, 2004, 270(4–5): 887–902.

[146] P. Pennacchi, N. Bachschmid, A. Vania, A model-based identification method of transverse cracks in rotating shafts suitable for industrial machines, Mechanical Systems and Signal Processing, 2006, 20(8): 2112–2147.

[147] J. Ginsberg, Engineering Dynamics, Cambridge University Press: 2007.

[148] F. Amirouche, Fundamentals of multibody dynamics: Theory and Applications, Birkhauser, 2006.

[149] M. Janssen, J. Zuidema, R. Wanhill, Fracture mechanics, Spon Press: 2004.

[150] A.K. Darpe, K. Gupta, A.Chawla, Coupled bending, longitudinal and torsional vibrations of a cracked rotor, Journal of sound and vibration, 2004, 269: 33-60.

[151] H. DeSmidt and J. Zhao, Extension-Twist Coupled Graphite/Epoxy Composite Driveshafts for Gear-Mesh Vibration Suppression, Proceedings of American Helicopter Society 66th Annual Forum, Phoenix, AZ, May 11-13, 2010.

[152] M. Peng and H. A. DeSmidt, Torsional Stability of a Face-Gear Drive System, Proceedings of American Helicopter Society 68th Annual Forum, Fort Worth, Texas, May 1-3, 2012.

[153] H. DeSmidt and M. Peng, Structural Damage Identification of Periodically Time-Varying Bladed-Disk/Rotor System, Proceedings of 2009 NSF Engineering Research and Innovation Conference, Honolulu, Hawaii, June 22-25, 2009.

[154] J. Zhao, H. DeSmidt, Cracked Shaft Damage Identification via Symmetry Breaking Active Magnetic Bearing Control and Interrogation, Proceedings of the ASME 2011 International Design Engineering Technical Conferences & Computers and Information in Engineering Conference IDETC/CIE 2011, Washington, DC, August 29-31, 2011

[155] www.math.ubc.ca/~anstee/math184/184newtonmethod.pdf

[156] S.S. Quek, G.R. Liu, Finite Element Method: A practical course, Butteworth & Heinemann, 2003.

VITA

Jie Zhao was born in Shanxi, China. He received his Bachelor and Master degree with the major of automotive engineering at Beihang University. Then, he worked as a patent examiner at State Intellectual Property Office, P.R.C for over one year. In 2008, he began to pursue his Doctor of Philosophy degree under the supervision of Dr. Hans A. DeSmidt in department of Mechanical, Aerospace and Biomedical Engineering at The University of Tennessee-Knoxville. His research interest includes vibration analysis and damage detection of time-invariant and time-varying systems.